

ON THE INVESTIGATION OF LIGHT-MATTER INTERACTIONS IN SLAB PHOTONIC CRYSTAL CAVITIES

THÈSE N° 6092 (2014)

PRÉSENTÉE LE 21 FÉVRIER 2014

À LA FACULTÉ DES SCIENCES DE BASE
LABORATOIRE D'OPTOÉLECTRONIQUE QUANTIQUE
PROGRAMME DOCTORAL EN PHOTONIQUE

ÉCOLE POLYTECHNIQUE FÉDÉRALE DE LAUSANNE

POUR L'OBTENTION DU GRADE DE DOCTEUR ÈS SCIENCES

PAR

Ulagalandha Perumal DHARANIPATHY

acceptée sur proposition du jury:

Prof. N. Grandjean, président du jury
Prof. R. Houdré, directeur de thèse
Prof. R. Baets, rapporteur
Prof. T. Krauss, rapporteur
Prof. V. Savona, rapporteur



ÉCOLE POLYTECHNIQUE
FÉDÉRALE DE LAUSANNE

Suisse
2014

*Where the mind is without fear and the head is held high
Where knowledge is free
Where the world has not been broken up into fragments by narrow domestic walls
Where words come out from the depth of truth
Where tireless striving stretches its arms towards perfection
Where the clear stream of reason has not lost its way into the dreary desert sand of dead habit
Where the mind is led forward by thee into ever-widening thought and action
Into that heaven of freedom, my Father, let my country awake.*

— *“Gitanjali”*
Rabindranath Tagore (1861-1941)

Abstract

Photonic crystal nanocavities are promising and versatile systems, with applications in telecommunications, quantum computing, cavity quantum electrodynamics, and optical biosensing. However, the realization of these cavities tailored to specific experimental requirements continues to be a formidable challenge. In this thesis, the physics and radiation loss mechanisms in slab photonic crystal cavities are explored theoretically through Bloch mode expansion and finite element methods. The fundamental limitations behind the realization of high quality factors in the presence of disorder are identified and a novel fast evolutionary method of cavity design is explored for tailoring photonic crystal cavities. Such tailored cavities were designed and optically characterized for achieving unique experimental conditions. In the first case, a specifically designed hollow circular cavity with high quality factor (2000) in water is used for demonstrating μW power on-chip optical trapping of nanometre sized dielectric particles for tens of minutes. The strength of the perturbation due to a single particle is of the order of a few line widths of the cavity mode that results in interesting back-action effects, which are theoretically and experimentally confirmed in this thesis. This new phenomenon paves the way for several interesting experiments concerning the dynamics of the trap, single particle cooling and non-conservative force fields. This successful resonant trapping mechanism is also extended to a lab-on-a-chip type integrated optical device for single particle detection, manipulation, and analysis. In the second case of tailoring the cavities, new designs are proposed for obtaining very high quality factors in extremely small modal volumes. These designs possess significantly high experimental quality factors (418,000) and also display nonlinear operations such as optical bistability at extremely low (μW) input powers. In addition to these experiments, the thesis also reports the design and characterization of photonic crystal devices on a gallium nitride substrate. The spectral advantages offered by gallium nitride allow for placing the operating wavelength of cavities anywhere from visible (400 nm) to near infrared (1600 nm), which can be utilized to perform various light-matter interaction experiments. In this context, cavities with quality factors more than 5000 were shown for both visible and near infrared wavelengths. The dispersion and propagation characteristics of ridge waveguides and photonic crystal waveguides in gallium nitride are also studied and shown in detail.

Keywords

Photonic crystals, Finite element methods, High-Q cavities, Optical trapping, Nonlinear optics, Light-matter interaction

Abstract (Tamil)

ஆய்வுச்சுருக்கம்

ஒளியனின் படிக நானோ உட்குழிவு, இன்று தொலைத்தொடர்பு துளியன் தகவல் நுட்பம், க்வாண்டம் கணிப்பு, உட்குழிவு துளியன் மின் இயக்கவியல் மற்றும் ஒளிசார் உயிர் உணர்வு போன்ற பல்வேறு துறைகளில் பயனளிக்கக் கூடிய ஒரு வியத்தகு சாதனமாகும். எனினும், இத்தகைய நானோ உட்குழிவு, பல்வேறு குறிப்பிட்ட ஆய்வுகளுக்கு ஏற்றவாறு உற்பத்தி செய்தல் என்பது மிகவும் கடினமான செயலாகக் கருதப்படுகிறது. இந்த ஆய்வேட்டில், ஒளியனின் படிக நானோ உட்குழிவுகளில் இயற்பியல் மற்றும் கதிர்வீச்சு இழப்பு வழிமுறைகள் ப்ளாக் முறை விரிவாக்கம் மற்றும் ப்ஹைநைட் எலிமென்ட் விதிமுறைகள் மூலமாக ஆராயப்பட்டுள்ளன. இப்படிக்கங்களில் சீர்குலைவு செயல்பாட்டினால் அதிக கொள்திறன் கொண்ட உட்குழிவுகள் வடிவமைப்பதில் உள்ள அடிப்படை வரம்பெல்லைகள் கண்டறியப்பட்டுள்ளன. மேலும் இவ்வுட்குழிவுகளை வேண்டியபடி வடிவமைக்க பரிணாம அடிப்படையில் செயல்படும் ஒரு புதிய செயல்முறை ஆய்வுசெய்யப்பட்டுள்ளது. இத்தகைய குறிப்பிட்டவாறு வடிவமைக்கப்பட்ட உட்குழிவுகள் தனித்தன்மை பொருந்திய ஆராய்ச்சிகளில் ஈடுபடுத்தப்பட்டன. முதல் எடுத்துக்காட்டாக, இவ்வாறு குறிப்பிட்ட வகையில் வடிவமைக்கப்பட்ட அதிக கொள்திறன் (2000) உள்ள வட்ட உட்குழிவினை தண்ணீரில் சோதனை செய்து பார்த்ததில், மைக்ரோவாட் சக்தி கொண்ட ஒளியியல் பிடிபடல் மூலமாக நானோமீட்டர் அளவு கொண்ட மின்கடத்தா தனித்துகள் ஒன்றை பல்வேறு நிமிடங்களுக்கு வட்ட உட்குழியின் உள்ளே பிடித்து வைக்க முடியும் என்று உறுதி செய்யப்பட்டுள்ளது. அத்தகைய துகளின் உலைவானது உட்குழிவு வரிதடிப்பின் அளவில் சில மடங்கு முறை இருப்பதினால் வியத்தகு இணைத்த-செயல்பாடுகள் கொள்கைமுறை மூலமாகவும் செயல்முறை மூலமாகவும் இவ்வாய்வேட்டில் உறுதி செய்யப்பட்டுள்ளன. இத்தகைய ஒளியியல் பிடிபடல் நிகழ்வானது பல்வேறு பிடிபடல் இயக்கவிசையியல், தனித்துகள் குளிர்ந்த மற்றும் மரபு சாரா விசை இயக்க ஆராய்ச்சிகளுக்கு வழிவகுக்கும் என்று எதிர்பார்க்கப்படுகின்றது. இப்பரிவுள்ள ஒளியியல் பிடிபடல் பொறிநுட்பம் மூலமாக மேலும் ஒரு லேப்-ஆன்-எ-சிப் போன்ற ஒரு சாதனம் தனித்துகள் கண்டறிதல், கையாளுதல் மற்றும் பகுப்பாய்வு செயல்பாடுகளுக்காக வெற்றிகரமாக வடிவமைக்கப்பட்டுள்ளது. இரண்டாவது எடுத்துக்காட்டாக, மிகச் சிறிய மின்கொள்பரப்பளவு மற்றும் மிக உயர்ந்த கொள்திறன் மிக்க உட்குழிவுகள் உருவாக்கப்பட்டுள்ளன. இவ்வுட்குழிவுகள் ஆய்வரையில் மிக உயர்ந்த கொள்திறன் கொண்டதோடு (418,000) மட்டுமல்லாமல் மிகக் குறைந்த உள்ளீடு ஒளி ஆற்றல்களில் (மைக்ரோ வாட் அளவில்) ஒளியியல் ஈடுருதி விளைவுகள் போன்ற நேர்பாங்கற்ற ஒளிவிளைவுகளை காட்டியுள்ளன. கேலியம் நைற்றைடின் நிறமாலை மேம்பாடுகளினால் இப்படிக்கங்களின் அலைநீளத்தை கண்ணுருவி 400 nm லிருந்து அகச்சிவப்பு அருகில் 1600 nm வரை எந்த அலைநீளத்திலும் பயன்படுத்தலாம். இத்தகைய தனிப்பட்ட சாதனங்களைக் கொண்டு சடப்பொருளுக்கும் ஒளிக்கும் இடையேயான பல உள்வினை சோதனைகள் மேற்கொள்ளப்பட இயலும். இதன் பொருட்டு 5000 க்கும் மேற்பட்ட கொள்திறன் கொண்ட ஒளியனின் படிக உட்குழிவுகள் கண்ணுருவியில் இருந்து அகச்சிவப்பு வரை செய்து காட்டப்பட்டுள்ளது. மேலும், கேலியம் நைற்றைடில் கட்டுருவாக்கப்பட்ட முகட்டு அலைவழிகாட்டி மற்றும் ஒளியனின் படிக அலைவழிகாட்டிகளின் ஒளிபரப்பல் மற்றும் நிறப்பிரிகை தன்மைகள் விரிவாக ஆய்வுசெய்யப்பட்டுள்ளன.

திறவுச் சொற்கள்

ஒளியனின் படிக உட்குழிவுகள், ப்ஹைநைட் எலிமென்ட் விதிமுறைகள், அதிக கொள்திறன் உட்குழிவுகள், ஒளியியல் பிடிபடல், நேர்பாங்கற்ற ஒளிவிளைவுகள்

Résumé

Les nanocavités à cristaux photoniques sont des structures prometteuses et polyvalentes pouvant avoir des applications pour les télécommunications, le calcul quantique, l'électrodynamique quantique en cavité et la biodétection optique. Cependant, la mise en oeuvre de ces cavités, adaptées à un besoin expérimental spécifique, constitue un défi formidable. Dans cette thèse, la physique et les mécanismes de pertes par radiation au sein des cavités à cristaux photonique planaires sont explorés à l'aide de développement en mode de Bloch et de méthodes numérique par éléments finis. Les limites fondamentales derrière la réalisation de cavités à fort facteur de qualité en présence de désordre sont identifiées. De telles cavités ont été développées et caractérisées optiquement pour atteindre des conditions expérimentales uniques. Dans le premier cas, une cavité circulaire spécialement ajustée avec un fort facteur de qualité lorsque il est immergé dans l'eau (2000) est utilisée pour démontrer le piégeage optique de nanoparticules diélectriques sur puce à des puissances de l'ordre du μW . L'amplitude de la perturbation due à une particule unique est de l'ordre de quelques largeurs de raie du mode de cavité. Cette perturbation donne lieu à d'intéressants effets de rétroaction, qui sont confirmés de manière théorique et expérimentale dans cette thèse. Ce nouveau phénomène permet d'entrevoir une série d'expériences novatrices concernant la dynamique du piège, le refroidissement de particule unique et les champs de force non-conservatives. Ce mécanisme de piégeage résonant est aussi appliqué sous la forme d'un dispositif optique de type "Lab-on-Chip" pour la détection, manipulation et l'analyse de particules uniques. Dans le deuxième cas de développement de cavités, de nouvelles structures sont proposées pour obtenir de très forts facteurs de qualités, combinés à de très petits volumes de mode. Ces cavités possèdent des facteurs de qualités expérimentaux très élevés (418,000) et permettent la mise en évidence d'effets non-linéaires, tels que la bistabilité optique, à des puissances extrêmement faibles (μW). En plus de ces expériences, cette thèse discute les conception et la caractérisation de structures à cristaux photoniques en nitrure de gallium. Les avantages offerts par le nitrure de gallium dans le domaine spectral permettent de choisir la longueur d'onde d'opération des cavités indifféremment entre le proche ultra violet (400 nm) et le proche infrarouge (1600 nm). Cette propriété peut-être particulièrement utile pour la réalisation de diverses expériences relevant de l'interaction matière-rayonnement. Dans ce contexte, des cavités possédant les facteurs de qualité supérieurs à 5000 ont été obtenues aussi bien dans le domaine visible que dans le domaine infrarouge. Les propriétés de dispersion et de propagation de guides d'ondes de type ruban ainsi que de guides d'ondes à cristaux photoniques ont aussi été étudiées en détails.

Mots-clefs

Cristaux photoniques, méthodes d'éléments finis, cavités à fort Q, piégeage optique, optique non-linéaire, interaction lumière-matière.

Contents

Abstract (English)	v
Abstract (Tamil)	vii
Abstract (French)	ix
Table of contents	xiii
List of figures	xvii
List of tables	xix
List of acronyms	xxiii
Introduction	xxvi
1 Photonic crystals and light-matter interactions	1
1.1 Photonic crystals: Historical progress	2
1.2 Mathematical treatment of light propagation in PhCs	4
1.3 Defects in 2D photonic crystals: Cavities and waveguides	8
1.4 The notion of Q-factor in photonic crystal cavities	12
1.5 Light-matter interaction experiments with 2D photonic crystals	13
1.5.1 Chemical and biological sensing	13
1.5.2 Nonlinear optical effects	15
1.5.3 Quantum electrodynamics	17
1.5.4 Photonic integrated circuits	19
2 Numerical investigations of PhC cavities	21
2.1 A historical walk	22
2.2 Numerical methods for photonic crystals	23
2.3 Numerical methods used in this thesis	24
2.3.1 Mode expansion methods	24
2.3.2 Finite Element Methods (FEM)	29
2.4 Some numerical results obtained during this thesis	34
2.4.1 Dispersion and slow light	34
2.4.2 Cavity mode evolution in PhC lattice	37

Contents

2.4.3	Quality factors and modal volumes	38
2.4.4	Disorder in PhC cavities and the influence on Q-factor	41
2.5	Summary and outlook	44
3	Resonant optical trapping in hollow PhC cavities	45
3.1	Optical trapping: The physics and the history	46
3.2	Calculation of optical forces in an optical trap	50
3.2.1	Optical forces: Ray optics approximation	50
3.2.2	Optical forces: The dipole force approximation	51
3.2.3	Optical forces: The Maxwell Stress Tensor Formalism	52
3.2.4	Optical trapping dynamics	53
3.3	Hollow photonic crystal cavities for integrated optical trapping	56
3.3.1	Circular cavity	56
3.3.2	The slot cavity	62
3.4	Resonant optical trapping in a circular cavity	64
3.4.1	The optofluidic sample and light coupling	64
3.4.2	Ultra low power resonant optical trapping	67
3.4.3	Particle-cavity perturbation	69
3.4.4	Particle-cavity back-action	73
3.4.5	Single particle analysis and manipulation	78
3.5	Discussions and outlook	81
3.5.1	Summary of developments from this work	81
3.5.2	A comparison with other integrated platforms	81
3.5.3	Future directions	82
4	Ultrahigh Q-factor H0 nano cavity and nonlinear effects	85
4.1	Optimization of photonic crystal cavities for high Q-factors	86
4.1.1	Optimizing leaky light cone components	86
4.1.2	Tuning the mode-gap of PhC waveguides	87
4.1.3	Analytic or semi-analytic designs of cavity mode	88
4.2	Evolutionarily optimized ultrahigh-Q H0 cavity	89
4.2.1	Design optimization	89
4.2.2	Coupling to the cavity	91
4.2.3	Fabrication of the cavities	92
4.3	Experimental characterization results	93
4.3.1	Q-factor measurement	93
4.3.2	Nonlinear behaviour in the H0 cavity	98
4.3.3	Optical bistability	101
4.4	Discussion and summary	103

5 Integrated photonic devices in GaN for light-matter interactions	105
5.1 Gallium nitride semiconductor technology	106
5.1.1 GaN for high power electronics	106
5.1.2 GaN for light emission and optoelectronics	107
5.2 Integrated photonics with GaN: A brief overview	109
5.3 GaN photonic devices in the near-IR: Experimental results	110
5.3.1 Single mode operation	110
5.3.2 Growth and fabrication of samples	110
5.3.3 Examination of structures with SEM and AFM	112
5.3.4 Comparison of process flows: SOI vs GaN on Si in the near-IR	114
5.3.5 Optical characterization of the devices	115
5.4 GaN photonic crystal cavities in the visible: Experimental results	123
5.4.1 Growth and fabrication	123
5.4.2 Optical characterization and analysis	124
5.5 Summary and perspectives	126
Conclusions and Outlook	130
Bibliography	155
Acknowledgements	157
Curriculum Vitae	159

List of Figures

1.1	The first predictions of a photonic bandgap effect from 1987	3
1.2	Illustration of the dispersion diagram for a simple planar waveguide	5
1.3	Illustration of bandgap effect in a 1D photonic crystal	6
1.4	Photonic bandgap for a triangular lattice and formation of a cavity mode	8
1.5	Cavity mode types in a 2D photonic crystal	9
1.6	Slab photonic crystal linear defect band diagrams	10
1.7	Waveguide modes within a line defect photonic crystal	11
1.8	Photonic crystals for biological and chemical sensing	13
1.9	Error-free optical sensing in photonic crystal cavities	14
1.10	Third harmonic generation in a photonic crystal waveguide	16
1.11	A basic schematic describing cavity quantum electrodynamics	17
1.12	Photonic crystals and quantum dot coupling	18
1.13	Photonic integrated circuits	19
1.14	All optical random access memory with photonic crystal cavities	20
2.1	An ancient numerical method from Babylon	22
2.2	Finite element model for the farfield profile of a slit cross section	30
2.3	Mesh evolution of a single hole in a slab	31
2.4	Meshing cross-sections of a photonic crystal slab	32
2.5	Meshing of single particle motion inside hollow cavities	33
2.6	Group index engineered slow light W1 waveguide: Numerical simulation	34
2.7	Experimental demonstration of a slow light W1 waveguide	35
2.8	Group index engineered slot coupled cavity waveguide	36
2.9	Calculation of bandgap and the electric field distributions in a PhC lattice	37
2.10	Evolution of cavity mode profile and position for different defects	38
2.11	Calculation of cavity Q-factors with different approaches	39
2.12	Guided mode expansion computation of field profiles of high-Q cavities	41
2.13	Dependence of standard deviation value versus magnitude of disorder	42
2.14	Histograms of quality factors with disorder for high-Q cavities	43
3.1	Radiation pressure witnessed in a comet tail	46
3.2	Evolution of the single beam gradient trap	47
3.3	Overview of integrated trapping platforms from the literature	48

List of Figures

3.4	Ray optics description of trapping forces	50
3.5	Illustration of the trapping potential and forces	54
3.6	Power spectral density of a trapped particle's motion	55
3.7	The circular cavity for resonant trapping	56
3.8	Electric field distributions of the multiple modes of a circular cavity	57
3.9	Water infiltration over the circular cavity	59
3.10	Initial experiments of water infiltration in the circular cavity	60
3.11	Finite element analysis of the neighboring modes	61
3.12	The properties of the slot photonic crystal cavity mode	62
3.13	The slot cavity for resonant trapping	63
3.14	The optofluidic trapping chip	64
3.15	The two layers microfluidic membrane and photonic crystal sample	65
3.16	Coupling configuration of the circular cavity	66
3.17	Snapshots of resonant optical trapping in a hollow cavity	67
3.18	Illustration of the optical interfaces with the cavity to estimate the guided power	68
3.19	Calculation of the resonance shift due to vertical displacement of particle	70
3.20	In-plane displacement and resonance shifts in circular cavity	71
3.21	Experimental setup to probe particle cavity perturbation	71
3.22	Measured resonance shift due to particle cavity perturbation	72
3.23	Numerical emission spectra corresponding to particle position	73
3.24	Computation of trapping forces within the hollow circular cavity	74
3.25	Escape energy calculation for the particle in the resonant trap	75
3.26	Two different trapping regimes and total escape energy	75
3.27	Behaviour of trapping forces with respect to position of particle	76
3.28	Experimental measurement of the wavelength dependent escape power	77
3.29	An all-optical single particle detector	78
3.30	Calculation of array of optical traps with circular cavity	78
3.31	Wavelength selective resonant trapping scheme	79
3.32	Effect of refractive index and size variation of particles	80
3.33	Variation of the hollow circular cavity design	83
4.1	Schematic and Fourier transform optimization of L3 cavity	86
4.2	Schematic of mode-gap cavity confinement based cavities	87
4.3	Schematic and electric field distribution of optimized H0 cavity	89
4.4	Influence of disorder on the Q-factors	90
4.5	Various cavity-waveguide coupling schemes for H1-type cavity	91
4.6	Coupling optimization for the L3 cavity	92
4.7	Scanning electron micrograph of H0 cavity with different coupling schemes	92
4.8	Schematic of the end-fire measurement setup	93
4.9	Initial measurement of Q-factors for various coupling schemes	94
4.10	Q-factor vs. waveguide separation	94
4.11	Measured Q-factors of optimized H0 cavity through side coupling	95

4.12 Transmission measurements of H0 cavity through side coupling	96
4.13 Numerical study of transmission in H0 cavity through side coupling	97
4.14 Variation of resonance wavelength in a PhC cavity due to nonlinear effects . . .	99
4.15 Device used for measuring nonlinearity	99
4.16 Nonlinear absorption and dispersion in the H0 nanocavity	100
4.17 Optical bistability in a PhC cavity based on a two-port transmission model . . .	101
4.18 Optical bistability in the H0 nanocavity	102
5.1 LED technology history	107
5.2 Bandgap energies for various LED materials	108
5.3 Single mode operation for near-IR wavelengths	110
5.4 Schematic of the fabrication process in the near-IR	111
5.5 Scanning electron micrograph images of the wires and PhCs	112
5.6 Atomic force microscope measurement of the PhC slab	113
5.7 Comparison of SOI and GaN process flows	114
5.8 Light scattering from the tethers holding the wire waveguide	115
5.9 Propagation loss in a tethered nanowire	116
5.10 Experimental and numerical dispersion of wire waveguides	117
5.11 Light propagation through a GaN PhC waveguide	118
5.12 Dispersion and transmission through a PhC W1	119
5.13 Fourier transform spectra of cavity modes	121
5.14 L3 cavity: Coupling and Q-factor measurement	121
5.15 Experimental measurement of a heterostructure PhC cavity	122
5.16 Schematic cross section of the 2D GaN PhC L7 cavity	123
5.17 SEM images of the PhC L7 cavity	124
5.18 Optical characterization of L7 cavities	125

List of Tables

2.1	Comparison of analytical and FEM solutions for farfield	31
2.2	Mesh cases comparison for a single hole in a photonic crystal	32
2.3	Mode volume definition comparisons	40
3.1	Infiltration of water in the circular cavity	58
3.2	Quality factors of modes in the proximity	61
3.3	Finite element analysis summary of circular cavity	61
3.4	Finite element analysis summary of slot cavity	63
3.5	Parameters used for the estimation of guided power	69
3.6	A comparison of various integrated single-particle trapping platforms	82
4.1	Optimized parameters for H0 cavity	90
4.2	Comparison of Q-factors recently demonstrated in ultra-small photonic crystal cavities	97
4.3	Nonlinear processes in silicon and order of susceptibility	98
4.4	Comparison of optical bistability threshold in 2D Si PhC cavities	102
4.5	Ultrahigh-Q 2D PhC cavities	103
4.6	Summary of evolutionarily optimized H0 cavities	104
5.1	Comparison of electrical properties of semiconductors	106
5.2	Comparison of optical storage media	108
5.3	Cavity designs for GaN PhC	120

List of Acronyms

AFM	Atomic Force Microscopy
AlN	Aluminium Nitride
BHF	Buffered Hydrofluoric acid
BME	Bloch Mode Expansion
CAMFR	CAvity Modelling FRamework
CMOS	Complementary Metal Oxide Semiconductor
CPU	Central Processing Unit
DWDM	Dense Wavelength Division Multiplexing
EDFA	Erbium Doped Fiber Amplifier
FCA	Free Carrier Absorption
FCD	Free Carrier Dispersion
FDTD	Finite-Difference Time-Domain
FEM	Finite Element Methods
FSC	Fine Scanning mode
FWM	Four Wave Mixing
GaAs	Gallium Arsenide
GaN	Gallium Nitride
GB	Giga Byte
GME	Guided Mode Expansion
HPhC	Hollow Photonic Crystal
ICP	Inductively Coupled Plasma
InP	Indium Phosphide
IR	InfraRed
MOVPE	Metal Organic Vapour Phase Epitaxy
MST	Maxwell Stress Tensor
PEVCD	Plasma Enhanced Chemical Vapour Deposition
PhC	Photonic Crystal
PIC	Photonic Integrated Circuits
PWE	Plane Wave Expansion
QED	Quantum Electro Dynamics
RAM	Random Access Memory
RIE	Reactive Ion Etching
RMS	Root Mean Square
SEM	Scanning Electron Micrograph

List of Tables

SOI	Silicon On Insulator
SPM	Self Phase Modulation
TE	Transverse Electric
THG	Third Harmonic Generation
TM	Transverse Magnetic
TPA	Two Photon Absorption
UV	UltraViolet
WDM	Wavelength Division Multiplexing
XPM	Cross Phase Modulation

Introduction

The tailoring of electromagnetic radiation within a sub-wavelength periodic structure has ushered a wide spectrum of investigations over the past two and half decades. These investigations primarily began with the understanding of physics behind the formation of bandgaps for various lattice parameters and dielectric materials during the late eighties and early nineties. The photonic bandgap effect has been understood by drawing heavy parallels with the electronic bandgap properties from solid state physics. In a similar fashion to electronics, impurity states (perturbation in the periodic lattice) leading to light localization was revealed in the early nineties leading to the development of extremely small optical microcavities using the photonic bandgap effect. Following this, various investigations have been performed to localize light in one, two and three dimensional photonic crystal structures.

Meanwhile, the compatibility with standard microelectronics fabrication technologies lead to the rise of a special type of photonic crystal fabricated on a silicon-on-insulator wafer. These devices were termed “slab photonic crystals” as they were made on a planar slab with a two dimensional photonic crystal pattern inscribed on them although they were truncated to a finite thickness in the vertical direction. Within these slab photonic crystal devices, a waveguiding mechanism was also demonstrated with the formation of a line defect in a perfect crystal lattice. This waveguide mode had the ability to confine light using both the index guided mechanism and the photonic bandgap effect exhibiting very interesting dispersion properties near the band edge, which is popularly known as “slow light” owing to the reduction in the group velocity of the propagating mode.

The slab photonic crystal devices offer a number of exciting features such as: extremely high spatial and temporal confinement of light and extremely small modal volumes apart from their direct compatibility with standard microelectronics fabrication processes. The design of cavities with high quality factors has been pursued through various semi-analytical methods and through parametric optimization of the position or radii of holes in the photonic crystal lattice. These high quality factor cavities and waveguides have been thoroughly investigated and characterized during the past decade, which has unravelled their properties such as slow light, energy transport, self-collimation effects, Anderson localization and enhanced nonlinear light-matter interactions. These devices have also been used as a platform to investigate a plethora of novel physical phenomena spanning the domains of quantum information, cavity quantum electrodynamics, photonic integrated circuits and optical sensors.

List of Tables

This thesis aims to further the above-mentioned understanding of slab photonic crystal devices in order to extend their applicabilities to specific light-matter interaction experiments.

In this context, elaborate numerical modelling of photonic crystal cavities is performed with a combination of finite element methods, plane wave, guided mode and Bloch mode expansion methods. These methods are crucial for calculating quality factors, effects of infiltration of liquids or single particles, mode overlap ratios, band edge states, electric field distributions and waveguide dispersions. These calculations were important to the design of photonic crystal devices tailored to specific experimental requirements.

In the first experiment, optical trapping of sub- μm sized dielectric particles is addressed. Single particle optical trapping originated in the 1970s using strong gradient forces at the waist of a laser beam. The challenges imposed by diffraction limit and the prohibitive input powers required to trap smaller particles has propelled researchers towards several integrated on-chip optical tweezer systems. In this thesis, for maximizing the interaction of a 500 nm sized particle with the trapping field, a 700 nm sized hollow circular cavity is chosen and is used to demonstrate resonant optical trapping successfully. Finite element methods are extensively used in order to assist the design of the cavities and for analyzing the particle perturbation and back-action effects. As predicted by calculations, the strong perturbation due to a single particle in the cavity is measured along with particle-cavity back-action phenomena that eventually leads to the existence of two distinct trapping regimes based on input wavelength. Exclusivity and wavelength selective trapping are also demonstrated subsequently.

In the second experiment, a fast evolutionary method in conjunction with mode expansion methods is used to address the problem of global optimization of cavity quality factors. This thesis proposes a new ultrahigh quality factor (1.95 million) H0 nanocavity design that has an extremely small modal volume ($0.34 (\frac{\lambda}{n})^3$). These cavities are experimentally characterized resulting in loaded quality factors of up to 418,000. In addition to this, nonlinear optical effects leading to optical bistability are observed for μW input optical powers.

The above-described experiments use a silicon-on-insulator platform for fabricating the structures. It is well-known that the spectral absorption of silicon acts as a hurdle in achieving cavities at visible wavelengths. Moreover, the two photon absorption at near-infrared wavelengths acts detrimentally when high optical power applications are envisaged. In order to address both these issues, gallium nitride is chosen as an alternate platform on which photonic crystal cavities and waveguides are fabricated using a unique approach. Experiments confirming quality factors of up to 5000 are reported for both visible and near infrared wavelengths. In addition to cavities, fully suspended ridge waveguides and photonic crystal waveguides were used in the near infrared wavelengths on gallium nitride and first measurements of loss and dispersion are reported.

The text is organized in five self-consistent chapters in the following manner.

Chapter 1 introduces the basic concepts related to this thesis in a brief manner. Photonic bandgap effects, cavity defect mode formation and waveguide defects are explained and illustrated. It also mentions the important historical developments in the progress of 2D photonic crystals. Finally, a few specific light-matter interaction experiments involving 2D photonic crystal cavities are surveyed in the broader context of this thesis.

Chapter 2 constitutes the numerical analysis work related to this thesis. The different numerical methods that were utilized during the progress of the work are clearly explained from their basic principles. The application of these methods is then shown with results including cavity designs, quality factors, dispersion diagrams and mode volume calculations that were collected during the course of the thesis. A conclusive numerical study on the influence of disorder in high-Q factor photonic crystal cavities is also elaborated.

Chapter 3 explains the first light-matter interaction experiment conducted in this thesis. It assembles all the results regarding the resonant optical trapping phenomena performed with specifically designed hollow circular photonic crystal cavities. The calculations and design of the cavities is explained and the experimental results pertaining to trapping, particle cavity perturbation are detailed. The physics of back-action and the existence of unique trapping regimes is revealed. The integrated nature of the traps is used to demonstrate wavelength selective on-chip traps.

Chapter 4 reports the second light-matter interaction experiment from this thesis. It proposes a novel ultrasmall H0 nanocavity design that comes from a global evolutionary optimization technique. The design and optical characterization of these cavities is reported in detail including the coupling mechanisms. The application of the cavity to ultralow power nonlinear optical effects is also presented.

Chapter 5 extends the photonic crystal effects through the scaling of Maxwell's equations to a second semiconductor platform using Gallium Nitride as a substrate. The novel fabrication procedure for making this device is elaborated and the detailed numerical and experimental results pertaining to both the visible and near-infrared gallium nitride photonic crystal devices are presented.

The conclusions and future outlook obtained from the course of this work are summarized at the end of this thesis. The projects in this thesis are supported by the Swiss National Science Foundation (SNSF) and the National Center for Competence in Research - Quantum Photonics framework.

1 Photonic crystals and light-matter interactions

This chapter serves as the introductory chapter to this thesis and will attempt to introduce all the necessary concepts in a concise fashion. Section 1 introduces the concept of photonic crystals and briefly surveys its historical development. Section 2 follows up with the mathematical treatment of light propagation in these devices. Section 3 elaborates on the physics behind the formation of optical cavities and waveguide modes in photonic crystals. Section 4 talks about the notion of a quality factor and its relevance in photonic crystal cavities. Section 5 is dedicated to showcase the broad range of light-matter interaction experiments performed with the aid of photonic crystal devices.

1.1 Photonic crystals: Historical progress

The path of scientific and technological progress from time immemorial has based itself mostly on the understanding and manipulation of matter enveloping us. This manipulation was reserved to macroscopic objects such as wood, steel and iron for centuries until the advancements of twentieth century opened the doors towards microscopic manipulation of condensed matter. The electrical and electronic properties of solid-state matter have given rise to a variety of new materials such as superconductors, semiconductors and ceramics. The conduction of electrons within any solid material is possible owing to the existence of a specific property that does not scatter the flow of electrons. This property can be understood by deriving the band structure of a material medium, which is formed due to the overlap of all discretized energy levels of individual atomic orbitals. The energy bands also have gaps between them leading to forbidden energy levels for the passage of the electrons. These bandgaps can cover all the directions of the crystal lattice if this potential is sufficiently strong. In a similar manner to electrons, an omnidirectional bandgap for light propagation would require a periodic dielectric potential in order to fully suppress the propagation of light through the medium. This requires a detailed understanding of the physics of electromagnetic radiation. The propagation of electromagnetic radiation has been analyzed ever since the days of the advent of Maxwell's equations in 1861. These equations have given a profound insight into the mechanism of the nature of light and electromagnetic wave propagation. Similar to the control of electrons in semiconductor circuits, the controlled manipulation of light in small dimensions has been a long pursuit but has remained elusive due to the complex nature of optical confinement in microscopic dimensions. The first attempts of such confinement go back to 1887 when Lord Rayleigh discovered the effect of light propagation through a one-dimensional periodic structure giving rise to stop bands for specific frequencies. However, these one dimensional structures had neither an omnidirectional bandgap nor a very large refractive index contrast.

Incidentally, 100 years after Lord Rayleigh's discovery, two theoretical papers [1, 2] appeared in the Physical Review Letters in 1987 referring to the creation of the photonic bandgap as is known currently. John explained this effect from the point of view of localizing photons inside an index modulated lattice while Yablonovitch proposed a scheme to use the electromagnetic bandgap to inhibit spontaneous emission inside a lattice (Figure 1.1). The term *photonic crystals* was originally coined by Yablonovitch in his article in 1989 [3] where he refers to this structured dielectric medium as a photonic crystal. The article read "Furthermore, this has enabled us to use sophisticated microwave homodyne detection techniques to measure the phase and amplitude of the electromagnetic Bloch wave functions propagating through the *photonic crystal* [3]". This term since then broadly refers to the area of 2D or 3D periodic structures that have a very large refractive index contrast (> 2), which is considerably different from the well-established field of one dimensional layered structures of the past 125 years. The two above-mentioned works kick-started a flurry of attempts for demonstrating the effect experimentally at microwave wavelengths using face-centred-cubic crystals [3]. In

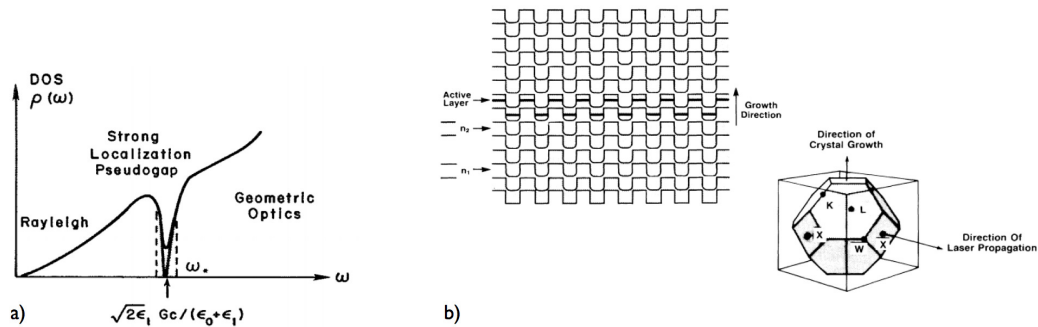


Figure 1.1: The first predictions of a photonic bandgap effect from 1987. a) John showing a pseudogap of strongly localized photons in a lattice with permittivity modulation [1]. b) Yablonovitch proposing a scheme to have an electromagnetic bandgap to have inhibited spontaneous emission [2].

the very same period during the early nineties, there was an inconsistency in the theoretical understanding of the bandgap in the face-centred-cubic structures leading to contradicting claims of presence or absence of this effect [4–8]. However, this issue was put to rest with detailed analysis and further numerical calculations that followed. The first experimental measurement of photonic bandgaps arrived in the early 1990s with the demonstration of bandgaps at microwave frequencies for 2D photonic crystal structures [9–11]. For instance, in the experiment of [11], 0.74 mm diameter and 100 mm long alumina ceramic rods were arranged in a square lattice with a lattice constant of 1.87 mm. The measurements for both TE and TM polarizations were performed confirming the presence of a bandgap predicted by plane wave expansion calculations. In addition to these initial structures, newer designs based on a woodpile photonic crystal were proposed and demonstrated successfully for infrared wavelengths [12]. The extension of the effect to smaller wavelengths, though exciting, was rather prevented by the absence of relevant fabrication techniques. This led to the interest in the self-assembled opal structures fabricated from colloidal solutions [13–17]. The first fabrication and measurement of 2D photonic crystals operating at near-infrared wavelengths was reported by Krauss and co-workers [18, 19] and by Lin and co-workers for the case of 3D photonic crystals [12]. The bandgap effect was also implemented in optical fibres leading to a new type of fibres called *photonic crystal fibres (PCF)* [20]. The effect of impurity states in a perfectly periodic lattice also leads to interesting properties in the bandgap similar to the case of electronic states, which opened up the possibility of optical cavities that confine light in the photonic crystal [21]. All the above-mentioned woodpile, photonic crystal fibre and opal structures, in spite of possessing interesting characteristics were quite challenging to implement in integrated applications. In view of this issue, the concept of planar 2D photonic crystals was introduced [22, 23]. These devices are referred to as 2D photonic crystals because they have the photonic crystal effect acting in two dimensions and total internal reflection acting along the vertical direction. This slab photonic crystal structure is the main focus of this thesis and all the following chapters concentrate on furthering the understanding of these devices. The historical developments concerning the development of 2D planar photonic crystals will be introduced contextually in the later sections of this chapter.

1.2 Mathematical treatment of light propagation in PhCs

The properties of light inside a photonic crystal can be understood with the help of solutions to the Maxwell's equations in a periodic medium that is given by the Bloch's theorem. In the case of a medium with no charges and currents, the Maxwell's equations describing light propagation are given by

$$\nabla \cdot \mathbf{D} = 0 \quad (1.1)$$

$$\nabla \cdot \mathbf{B} = 0 \quad (1.2)$$

$$\nabla \times \mathbf{E} = -\frac{\partial \mathbf{B}}{\partial t} \quad (1.3)$$

$$\nabla \times \mathbf{H} = \frac{\partial \mathbf{D}}{\partial t} \quad (1.4)$$

where \mathbf{E} and \mathbf{H} are the electric and magnetic fields in the medium, \mathbf{D} and \mathbf{B} are displacement and magnetic induction fields respectively. If the field strengths are small enough and if the dielectric function is scalar, the linear isotropic formulation can be used. Ignoring frequency dependence of the dielectric function, we can write the following constitutive relations:

$$\mathbf{D}(\mathbf{r}) = \epsilon_0 \epsilon(\mathbf{r}) \mathbf{E}(\mathbf{r}) \quad (1.5)$$

$$\mathbf{B}(\mathbf{r}) = \mu_0 \mu(\mathbf{r}) \mathbf{H}(\mathbf{r}) \quad (1.6)$$

$$n(\mathbf{r}) = \sqrt{\epsilon(\mathbf{r}) \mu(\mathbf{r})} \quad (1.7)$$

where n is the refractive index, ϵ_0 is the free space permittivity, μ_0 is the free space magnetic permeability, $\mu(\mathbf{r})$ and $\epsilon(\mathbf{r})$ are the magnetic permeability distribution and electric permittivity distribution in the medium respectively. Taking into account all the above equations and by assuming harmonic propagation (frequency ω and wavevector \mathbf{k}) and transverse electromagnetic waves ($\nabla \cdot \mathbf{H}(\mathbf{r}) = \mathbf{0}$), the last two of the Maxwell's equations can be decoupled to obtain the well-known linear eigenvalue Helmholtz equation that is given by

$$\left[\nabla \times \frac{1}{\epsilon(\mathbf{r})} \nabla \times \right] \mathbf{H}(\mathbf{r}) = \frac{\omega^2}{c^2} \mathbf{H}(\mathbf{r}) \quad (1.8)$$

The knowledge of the magnetic field can then be used to derive the electric field components at any eigenfrequency ω_0 as

$$\mathbf{E}(\mathbf{r}) = \frac{i}{\omega_0 \epsilon_0 \epsilon(\mathbf{r})} \nabla \times \mathbf{H}(\mathbf{r}) \quad (1.9)$$

Equation 1.8 has to be solved for finding the modes $\mathbf{H}(\mathbf{r})$ and their corresponding frequencies for a given permittivity distribution $\epsilon(\mathbf{r})$. The left hand side is a differential operator acting on a function, whose eigenvalues are proportional to the square of their mode frequencies. Since the operator is linear, the superposition of modes is also part of the solution set.

1.2. Mathematical treatment of light propagation in PhCs

In order to visualize the solution space for any propagation medium, such as a simple dielectric waveguide, the dispersion diagram is often used as shown in figure 1.2b. This diagram plots the eigenmodes that are obtained for various frequencies with respect to the wavevector ($k_{||}$) along the propagation direction. The slab structure for the reasons of symmetry can have both Transverse Electric (TE) and Transverse Magnetic (TM) modes. TE modes are those that have in-plane electric field plane components and a vertical magnetic field component.

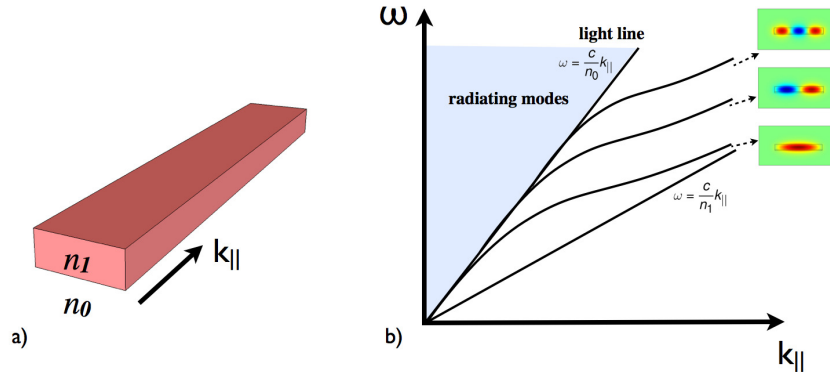


Figure 1.2: Illustration of the dispersion diagram for a simple planar waveguide. a) The optical waveguide with the refractive indices for the core (n_1) and cladding (n_0). b) The dispersion diagram with the in-plane wave vector and frequency (ω) showing the different orders of modes and electric field mode profiles (vertical cross section) and the radiating continuum outside the cladding light line.

Figure 1.2b shows the first, second and third order TE modes that can propagate inside the slab structure. Other higher order modes are also possible and are not shown here. It can also be seen that at each frequency, there can be more than one possible spatial mode present in the structure depending on the frequency. The specific mode cut-off frequencies are determined by the thickness of the slab structure. The shaded area in blue corresponds to the modes that are present in the light cone that represent the continuum of radiating modes. The line separating these modes from the discrete guided modes is referred to as the *light line*.

In order to extend the understanding of this simple dispersion diagram to a periodic structure, symmetry and periodicity arguments have to be invoked. A simple case of dielectric modulation is illustrated in figure 1.3. In the first case, where there is no dielectric modulation, the dispersion is linear for such a homogenous medium and the artificial periodicity induced by a period " a " folds the modes at every periodic boundary. This also means that the line from the negative side of the wavevector axis gets folded from $\frac{2\pi}{a}$. The negative axis physically means that there is a forward and backward propagating solution for the same k value. This backward line crosses the forward line at $\frac{\pi}{a}$ as shown in figure 1.3a that corresponds to the positive half of the Brillouin zone. There is no bandgap possible in this type of structure, when there is no perturbation. However, if the dielectric guide is modulated with a perturbation in refractive index, the situation at the Brillouin zone edge at $k = \frac{\pi}{a}$ starts to change. It can be

Chapter 1. Photonic crystals and light-matter interactions

seen in figure 1.3b that there exists a set of frequencies for which no real solutions can exist for all k , meaning that there are no allowed propagating states in the system. All these solutions are imaginary and hence purely evanescent. It can be imagined as if the reflections occurring from each of the interfaces of the modulated media lead to a constructive interference and results in a complete reflection of the input light.

The variational theorem and the principle of orthogonality need to be applied to further understand the spatial profiles of the modes. In order to not violate the symmetry of the system, only two standing waves are possible at the crossing point ($k = \frac{\pi}{a}$). These modes can be localized only either in the high or low dielectric medium. As the variational principle tries to minimize the energy, it localizes the low frequency modes in high dielectric regions and vice versa. This results in two different frequencies for these modes resulting in the formation of a bandgap as shown in figure 1.3b. The next higher eigenvalue corresponds to the higher harmonic mode that can satisfy the variational principle but also simultaneously satisfy orthogonality with the previous mode and so on.

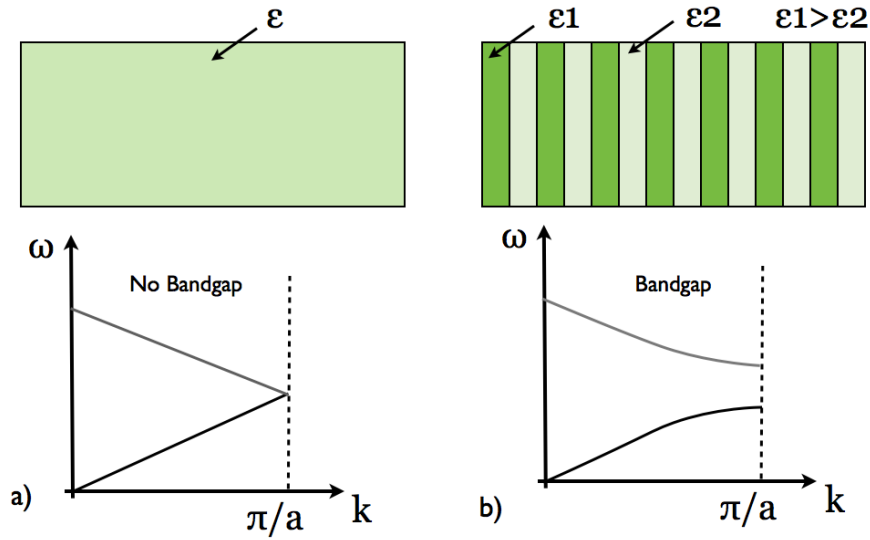


Figure 1.3: Illustration of bandgap effect in a 1D photonic crystal. a) In the absence of perturbation, the modes can be artificially folded at the $\frac{\pi}{a}$ point but with no bandgap. b) In the presence of a periodic perturbation in index, a splitting of the modes occur that results in the opening of a bandgap.

In the case of a periodic perturbation like inside a photonic crystal medium, the field $\mathbf{H}(\mathbf{r})$ can be expanded by the well-known Bloch's formalism. This gives us

$$\mathbf{H}(\mathbf{r}, t) = e^{i(\mathbf{k}\mathbf{r} - \omega t)} \mathbf{H}_{\mathbf{k}}(\mathbf{r}) \quad (1.10)$$

This translates to the fact that the wave vector is periodic in the direction of the periodicity such that $\mathbf{k} = \mathbf{k} + \frac{2\pi}{a}$. The periodicity allows the bands to be folded by a period equivalent to $\frac{2\pi}{a}$, where a is the periodicity of the perturbation in dielectric distribution. In this context, the

1.2. Mathematical treatment of light propagation in PhCs

two modes that were degenerate in figure 1.3a at the crossing are going to be split when there is the introduction of periodicity. The lower state is going to be localized in the high refractive index dielectric while the higher state will be localized in the low refractive index dielectric. This periodicity can also be extended to multiple dimensions and the Bloch theorem applies in the same manner. This means that only the computations pertaining to the primitive cell that repeats itself needs to be performed in order to obtain the complete band diagram. The region in the dispersion diagram that is between $\mathbf{k} = -\frac{\pi}{\mathbf{a}}$ and $\mathbf{k} = \frac{\pi}{\mathbf{a}}$ in the case of a one dimensional periodicity represents the first Brillouin zone. In the presence of additional symmetries in the crystal, more redundant regions can be identified leaving the so called *irreducible Brillouin zone*. The exact solutions for this problem can only be computed through numerical techniques and are presented in chapter 2 in detail.

In a surprising similarity with solid state physics, the behaviour of electrons in a semiconductor crystal is governed by a similar eigenvalue equation that is obtained from the Schrödinger equation

$$\left[\frac{-\hbar^2}{2m} \nabla^2 + V(\mathbf{r}) \right] \phi(\mathbf{r}) = E\phi(\mathbf{r}) \quad (1.11)$$

where \hbar is the reduced Planck's constant, m is the mass of the electron, $V(r)$ is the crystal field, $\phi(r)$ denotes the wave function of the electron and E gives the total energy. In this case the solutions to $\phi(r)$ are in the form of Bloch waves. These waves have an amplitude modulated function given by the same periodicity as the lattice under study. Equations 1.8 and 1.11 are in similar form and are looking for solutions representing the distribution of a function in space. The solutions exist in a periodically modulated material function (crystal field in the electronic case and dielectric permittivity in the photonic case). The operators preceding the left hand side of the equations are normally called the Maxwell operator and Hamiltonian operator respectively. The Hermitian nature of these operators results in real eigenvalues which are the electron energy and the square of the mode frequency respectively. The understanding of the physics of solid-state electronics has highly favoured the development of photonic bandgap physics as the formation of bandgaps, doping of defect states in bandgaps and the behaviour of reciprocal spaces give rise to a variety of analogies between the two systems.

In the case of quantum mechanics, the lowest eigenstates are found in the low potential region while in photonic crystals, the lowest modes will have their electric fields concentrated in the region of high dielectric constant. One of the primary differences between the two systems is the fact that the Maxwell's equations allow for the scaling of the dimensions of the lattice parameters and the corresponding eigenfrequencies are scaled accordingly, which is not the case with the Schrödinger equation. This feature allows for the translation of the bandgap effects in a variety of materials and to a range of frequencies that can prove useful to a number of exciting experiments. For example, the fabrication of near-infrared photonic crystals would require sub micrometer features but a microwave photonic crystal would only need a millimetre size feature to observe similar effects.

1.3 Defects in 2D photonic crystals: Cavities and waveguides

Cavities

As explained in the previous section, a periodic dielectric modulation results in a bandgap for one or both polarizations of the electric field. 2D photonic crystals are very interesting because of the established fabrication techniques for the case of planar waveguide structures. In this context, in order to obtain a complete bandgap for both TE and TM polarizations, a triangular lattice photonic crystal is used as illustrated in figure 1.4a. In this thesis, all the reported devices follow this configuration, i.e, a triangular lattice of air holes embedded on a freestanding dielectric membrane. The associated bandgap is also shown in the figure showing

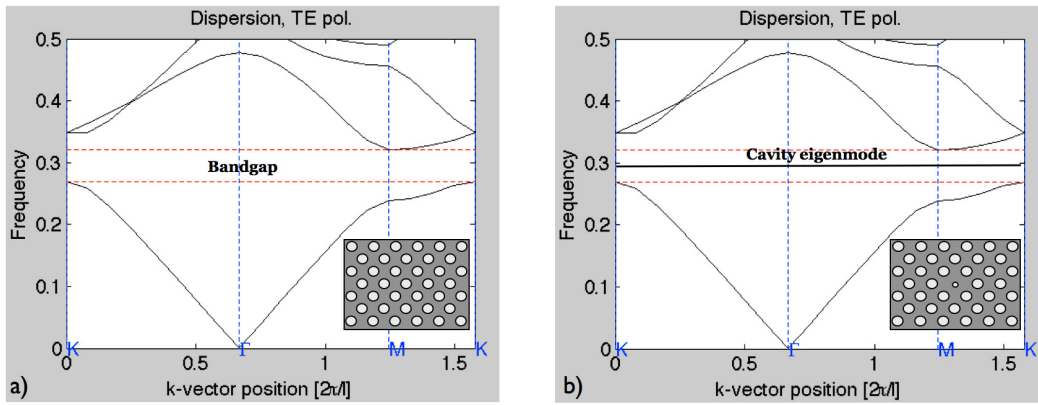


Figure 1.4: Photonic bandgap for a triangular lattice and formation of a cavity mode. a) A bulk photonic crystal with the air and dielectric bands enclosing the bandgap. b) The creation of a small defect by reducing the hole radius that results in a discrete state formation in the bandgap.

the lower dielectric band and the higher air band at low and high frequencies respectively. The creation of a defect such as removing a single hole creates a perturbation in the bulk periodicity resulting in a localized eigenmode in this spatial region. This leads to the presence of one or more discrete states in the bandgap of the bulk dispersion. This can also be intuitively understood by imagining the holes around the defect creating a reflecting mirror for the confined mode. This “point-like” defect can be created by two ways. One example is illustrated in figure 1.4b. The first possibility is through removal of a hole from a perfect triangular lattice in a slab as shown in figure 1.4b. This results in an increase in the presence of dielectric media, i.e., a positive value for $\Delta\epsilon$. Perturbation theory shows that for such a positive value, the corresponding frequency shift is negative and a discrete mode can fall into the bandgap from the bottom of the upper air band. The second possibility is through an increase in the size of a single hole in the periodic lattice. This results in a decrease in the presence of dielectric content leading to a negative value of for $\Delta\epsilon$. Perturbation theory shows that for such a negative value, the corresponding frequency shift is positive and a discrete mode arises out of the top of the lower dielectric band. The creation of a defect in the lattice breaks the translational symmetry of the crystal but also has its local symmetries. The strength of light localization often depends on the size of the bandgap and where the mode is localized. An

1.3. Defects in 2D photonic crystals: Cavities and waveguides

intuitive understanding of localization was presented by Stanley and co-workers [24] where a one dimensional Bragg reflector made of alternating layers of GaAs and AlAs was used. In the case of insertion of a $\frac{1}{2}$ impurity layer, a transmission peak is found in the exact center of the band gap with the highest finesse. Further increase in the layer thickness results in the moving of this peak towards either of the bands with lower finesse. It was also shown that this mid-gap impurity could have the lowest gain threshold for a laser resonator. The larger the defect, the more the higher order modes are pulled into the band gap leading to multiple mode cavities. The different type of cavity modes are also visualized in the following figure 1.5. A slow increase in the defect hole radius can lead to the formation of different mode profiles namely, the monopole, dipole, quadrupole and hexapole cavities [23, 24]. The

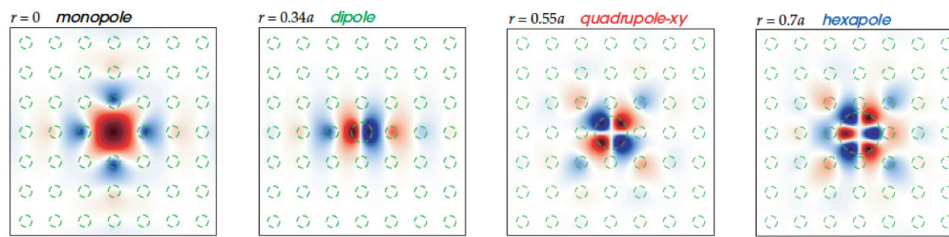


Figure 1.5: Different types of cavity modes in a 2D photonic crystal with square lattice of dielectric pillars in air. The increase in the defect radius brings the higher order modes into the bandgap leading to the creation of dipole, quadrupole and hexapole modes respectively. Reprinted from [25].

complete understanding of the spatial mode formation in photonic crystals involves group theory and symmetry and can be referred here [26–28]. In the case of higher order modes such as hexapole modes, there is the formation of degenerate pairs and non-degenerate modes. When two modes are degenerate, they have exactly the same frequency. However, this is not possible to find in the experiment owing to the fact that there is a splitting of these states due to disorder in fabrication. It is also not possible with plane wave expansions (as will be explained in chapter 2) to obtain the degenerate modes with exactly the same frequency as the number of plane waves used for computation limits this. In the case of a triangular lattice, point like defect cavities have a C_{6v} symmetry, denoting rotational invariance by 60 degrees from the center of the cavity. According to group theory, doubly degenerate modes must be present in such a symmetric system [26]. In simpler words, the degeneracy of modes and the rotational properties are very closely related. If the modes are monopole or hexapole, then their shapes with respect to the centre are invariant under rotational operations and hence they are non-degenerate [28]. This will be explained in the case of a hexapolar circular cavity in chapter 3. Meanwhile, the dipole and quadrupole like eigenstates end up having doubly degenerate modes. In this case, a given state can be rotated by an angle and added with a second rotated state in order to obtain a pair of degenerate states whose combination preserves the C_{6v} symmetry. If a cavity defect has multiple modes, they can then be grouped into nondegenerate monopole or hexapole and doubly degenerate dipole or quadrupole modes respectively.

Waveguides

Guiding of optical radiation is possible with planar integrated waveguides that work on the basis of total internal reflection. In order to create a waveguide mode in a PhC, a row of holes can be removed creating a line defect. This results in the creation of a mode that is guided through this spatial region from one end of the photonic crystal to the other end akin to an optical waveguide but confined by the photonic crystal lattice [29, 30]. This discrete guided band falls inside the band gap and is popularly known as a *photonic crystal waveguide*. Depending on the number of rows that are removed, it can be labelled as a W1, W2 or Wn waveguide. These multiple rows removal might result in the appearance of more than one guided mode resulting in a multimodal PhC waveguide. The biggest difference between the point defect and the line defect is the behaviour with respect to wave vector k . This is made possible by preserving the translational symmetry in the propagation direction. This mechanism can be interesting for various applications, for example, to be able to couple light into a photonic crystal cavity leading to completely integrated photonic crystal devices as will be shown in the later chapters of this thesis. It can also be imagined that in the case of pillar type photonic crystals, this mode can be localized in air and hence can be very useful for light-matter interaction applications with its enhanced overlap and for making sharp bends with low losses [31, 32]. The various possible waveguide modes present in a photonic crystal slabs

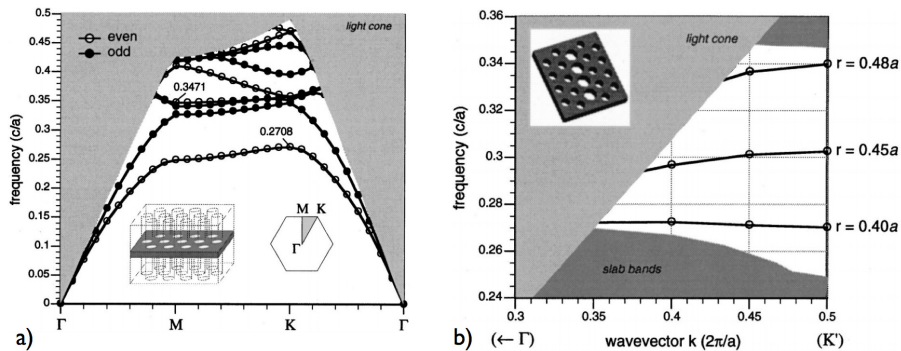


Figure 1.6: Slab photonic crystal linear defect band diagrams. *a)* Band diagram of slab photonic crystal showing light cone and discrete states that are fully delocalized in the slab. *b)* Band diagram of line defect in the slab photonic crystal giving rise to slab bands and discrete guided modes lying in the band gap. Their mechanism depends on whether dielectric is added or removed from the system. Reprinted from [33].

were studied and reported in detail by Johnson and co-workers [33]. It is easily understood that conventional waveguides in integrated optics use total internal reflection for confinement. Their thickness can be optimized to make them single mode as multiple modes can lead to lossy propagation. The light that is guided in such a waveguide is limited by radiation losses. One possible way to have a waveguide with no radiation losses would be to use a three dimensional photonic crystal effect and confine light in all directions, which is challenging to fabricate eventhough some have been studied [34–36]. The truncation of the waveguide in the vertical direction brings up an interesting concept called the “light cone” or “light line” as

1.3. Defects in 2D photonic crystals: Cavities and waveguides

shown in figure 1.6a. This region constitutes the continuum of radiation modes that pervade the structure. The allowed modes in the slab are the discrete modes that are below the light cone. These modes are fully contained by the slab due to its higher effective index than the surrounding air and decay exponentially far away from the slab. The bandgap in this slab band diagram (figure 1.6a) is not a true band gap as there are still radiation modes present in those frequencies. It is exactly this reason as to why cavity modes that were introduced before decay because they are coupled to these radiation modes. The horizontal axis of these band diagrams represent the wavevector along the symmetry points Γ , M and K in the irreducible Brillouin zone and the vertical axis correspond to reduced frequency scaled by the lattice parameter. It is important to remember that increasing the thickness of the slab gives rise to the presence of higher order modes that could prevent the bandgap from occurring completely for one or both polarizations. In the case of having a substrate below the slab, the bandgap

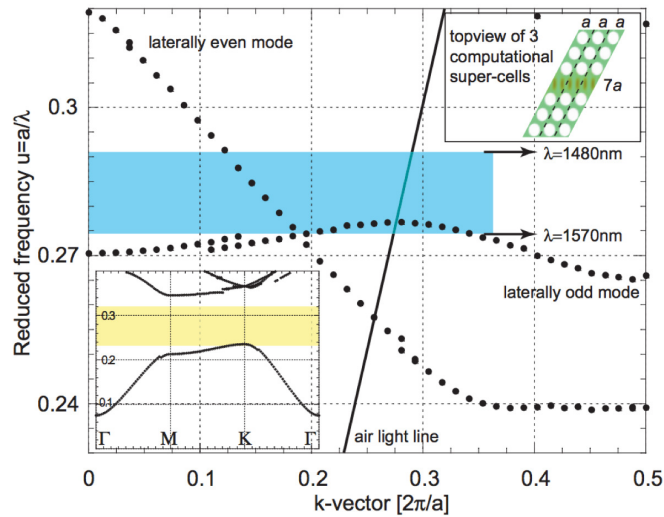


Figure 1.7: Waveguide modes within a line defect photonic crystal. 3D calculations of the corresponding W1 waveguide dispersion relation. The shaded region in blue corresponds to the near-infrared wavelength range. The laterally even and odd modes can be seen. Lower inset: band structure of the corresponding bulk structure (shaded region in yellow shows the bandgap of a perfect bulk photonic crystal slab). Upper inset: overhead view of the computational super-cell that constitutes the W1 waveguide. Reprinted from [37].

properties might not be altered as long as a sufficient buffer region is created [38]. It must be noted that asymmetry can completely alter the bandgap properties as will be explained in the section on disorder in chapter 2. The difference between figure 1.6a and figures 1.6b is that the creation of the linear defect changes the slab band diagram resulting in slab bands, which is a projection of the bands of the unperturbed slab on that of the Brillouin zone of the linear defect. The guided modes can only exist in the bandgap and they can be truly guided. They can be of two types just like in the case of cavities, by adding or removing dielectric material. In the case of a standard W1 waveguide with one row of holes removed, the spatially even-like mode falls into the bandgap from the air band as shown in the computed W1 band diagram in figure 1.7 [37].

1.4 The notion of Q-factor in photonic crystal cavities

The quality factor Q is a dimensionless number that is used to denote the losses present in any resonant cavity. The term was widely used in the context of electronic tank circuits and microwave resonances and later has also migrated into optical cavities. This quantity will be repeatedly used in the rest of this thesis for differentiating light confinement in various cavities.

In the formal definition, it denotes the ratio of energy stored in the system to the energy lost per cycle in the system at the resonance frequency ω_0

$$Q = \frac{\omega_0 E_{\text{stored}}}{P_{\text{dissipated}}} \quad (1.12)$$

The physical interpretation is that the cavity can sustain “ Q ” number of oscillations before decaying by a factor of $1/e$. If a finite amount of energy is input into the system, the total energy decay can be monitored in time and the number of oscillations for this decay can be ascertained. This is also one of the preferred methods used in certain numerical methods such as FDTD as will be explained in chapter 2. The Fourier transform of such a time decaying field resembles a Lorentzian function whose shape is given by

$$F(\omega) = \frac{1}{(\omega - \omega_0)^2 + (\frac{\omega_0}{2Q})^2} \quad (1.13)$$

This means that in the case of the light radiated from a cavity, the full width at half maximum of the cavity-radiated spectrum can be used to directly estimate the Q . It has to be noted that several factors can affect the Q -factor of a slab photonic crystal cavity through the different possible loss mechanisms. This can be defined in a simplistic sense as:

$$\frac{1}{Q} = \frac{1}{Q_{\text{intrinsic}}} + \frac{1}{Q_{\text{disorder}}} + \frac{1}{Q_{\text{coupling}}} \quad (1.14)$$

where $Q_{\text{intrinsic}}$ denotes the radiative and absorptive losses associated to the cavity and material system and Q_{disorder} denotes the increase in the losses due to the presence of structural disorder that will be explained further in chapter 2. Q_{coupling} on the other hand depends on how light can be non-invasively input into the cavity mode. A waveguide, for instance, can be used to couple the light into the microcavity through evanescent coupling and this coupling strength can also influence the measured Q -factors. This issue will be treated in detail in chapter 4.

The ability to obtain tuneable and robust high Q -factor cavities has been of tremendous importance for various experiments involving photonic crystals. A very high- Q cavity ensures a long photon life time in wavelength-scale spatial dimensions that opens up exciting frontiers for light-matter interaction experiments as will be overviewed in the following section.

1.5 Light-matter interaction experiments with 2D photonic crystals

Planar photonic crystal devices have been used in a plethora of experiments in the past two decades since their inception. This spans from enhancing light extraction in LEDs [39–42], increasing efficiency in solar cells [43–47] to performing optomechanics experiments with photonic crystal cavities [48, 49]. However, in the context of the contributions in this thesis, a subset of relevant experimental domains are reviewed in detail in the following subsections.

1.5.1 Chemical and biological sensing

CMOS integration has paved way to a number of devices that can be potentially made into "Lab-on-a-chip" style systems that can offer both compactness and elevated performance in sensitivity to analyte detection [50]. The principle revolves around integrating a number of sensor elements in the same platform in a cost-effective manner that can then be used to multiplex a variety of sensing operations. The basic biosensor device for biological applications uses biochemistry and physics in order to identify the specimen under study while in chemical detection; a specific physical property can be tracked. There are numerous transduction mechanisms such as piezoelectric, electrochemical, mass sensitive and optical. In most optical sensors, the detection mechanism is based on a refractive index shift and this has been exploited in a number of methods as reviewed in [51]. In an initial work by Chow and

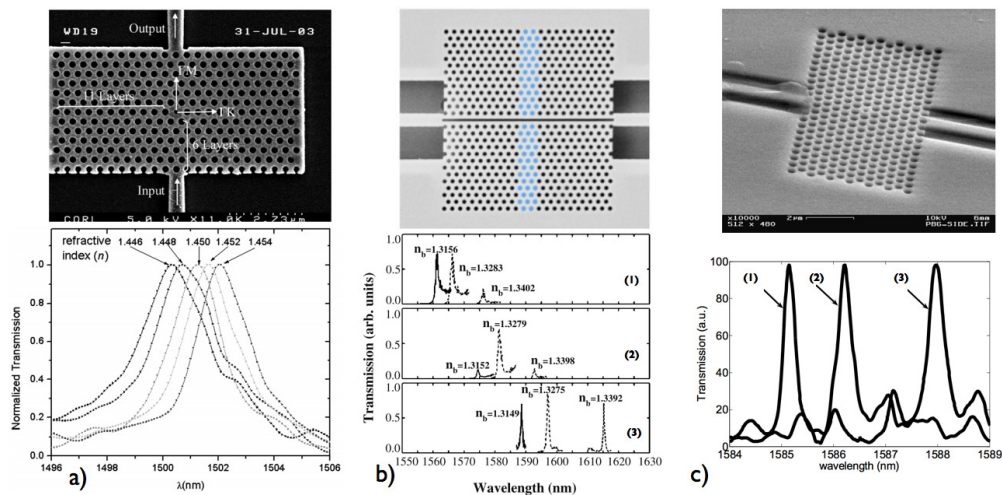


Figure 1.8: Photonic crystals for biological and chemical sensing. Transmission measurements indicating the resonance shift of the cavity mode a) PhC cavity used for detecting difference in refractive index of optical fluid [52]. b) Slotted photonic crystal cavity used for detecting chemical concentration. The variation with respect to slot sizes 171 nm (1), 166 nm (2) and 152 nm (3) is shown [53]. c) PhC cavity transmission showing red shift after oxidation and silanization (1), after glutaraldehyde attachment (2) and infiltration of bovine serum albumin (BSA) molecules (3) [54].

co-workers as shown in figure 1.8a [52], a microcavity was formed by reducing the diameter of a hole and this cavity mode was used to detect the changes in the refractive index due to

Chapter 1. Photonic crystals and light-matter interactions

an optical silicone fluid up to an index difference of 0.002. This value has been considerably increased by adapting structures that can have a larger overlap with the medium as demonstrated by Di Falco and co-workers by employing a slotted photonic crystal cavity shown in figure 1.8b [53]. There was also a report of extending the sensing experiments to the scale of detecting single proteins within a photonic crystal microcavity by Lee and co-workers [54].

The sensitivity of such a refractive index based optical sensor is quantified by the number S

$$S = \frac{\Delta\lambda}{\Delta n} = \Gamma \frac{\lambda_0}{n_{eff}} \quad (1.15)$$

where n_{eff} is the effective index of the cavity mode, λ_0 is the resonance wavelength, Γ is the overlap of the mode with the medium, $\Delta\lambda$ is the shift of the resonance wavelength and Δn is the associated change in refractive index. PhC cavities due to their increased confinement of radiation interact with the analyte and the change in the mode property can be tracked leading to a very sensitive measurement system. Various implementations of optical sensors based on photonic crystals can be found here [55]. As many other physical parameters

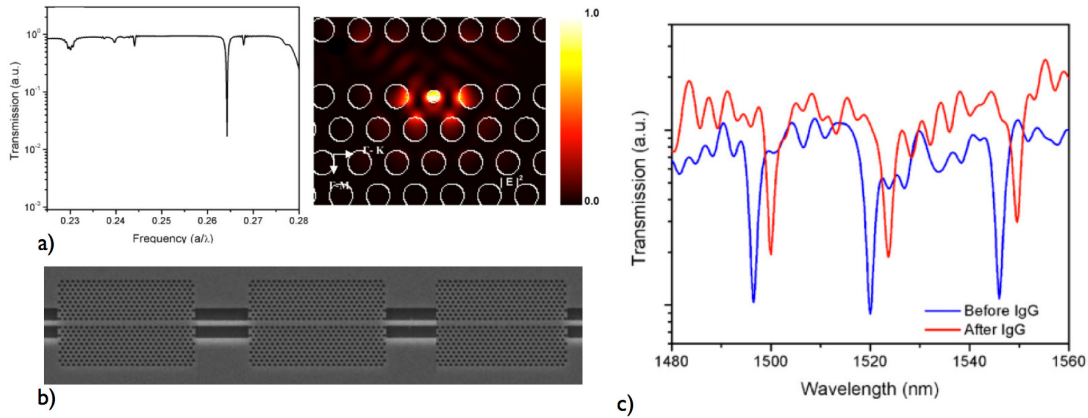


Figure 1.9: Error-free optical sensing in photonic crystal cavities. *a)* FDTD calculations showing the transmission spectrum and cavity field profile. *b)* SEM image of fabricated device with the three cavities placed one after another. *c)* The spectrum before and after immunoglobulin binding. Reprinted from [56].

such as temperature and pressure can also simultaneously act on the refractive index of the medium [57], it is important to decouple these influences with the help of a reference system to eliminate erroneous measurements. One way of doing this is to have multiple cavities on the same device, which was explored by Pal and coworkers for detecting the binding of human immunoglobulin [56] as shown in figure 1.9. In most cases, the signal to noise ratio determines the detection limit achievable by the system and this problem has to be addressed by a careful design of the measurement apparatus [58]. The advantages offered by the photonic crystals include high sensitivity and small footprint and this is being combined with the emergence of novel microfluidic systems that can bring very small concentrations of analyte to the measurement area [59, 60].

1.5.2 Nonlinear optical effects

Historically, experiments concerning nonlinear optics had to wait until the invention of the ruby laser in 1960 by Maiman and co-workers [61]. The initial work in experimental nonlinear optics started with the demonstration of second-harmonic generation by Franken and co-workers in 1961 [62]. In this work, with an intense excitation at a wavelength of 694.3 nm, second harmonic generation at 347.2 nm in crystalline quartz was demonstrated. The conversion efficiency was rather low in this work but this was increased over the following years with the aid of higher intensity lasers and appropriate phase matching techniques. This was also followed by the reporting of third harmonic generation in calcite by Terhune and co-workers in 1962 [63]. These experiments were quite important at that time as they were able to generate a coherent light output with a coherent light input. The demonstration of stimulated raman scattering also came in 1962 through Woodbury and co-workers where they used a ruby laser and nitrobenzene as the gain medium [64].

In an other seminal work in 1976, Gibbs and co-workers reported an interesting development regarding optical bistability inside a sodium-filled Fabry-Perot interferometer [65]. The system was constructed using a 11-cm long FP interferometer with Sodium vapour at 10^{-4} to 10^{-5} Torr pressure in the 2.5 cm region midway between the mirrors. The optical beam diameter was about 1.65 mm and a maximum power of 13 mW. The mirror reflectivities were around 90 percent. In the presence of a nonlinear medium within the cavity, the round trip phase shift $\phi = \frac{4\pi nL}{\lambda}$ carried the refractive index term which had the contribution of the nonlinear index. This resulted in a hysteresis plot with respect to input power. This behaviour was explained using the fact that there was the effect of both nonlinear dispersion and nonlinear absorption inside the medium. In this experiment, it was envisioned that optical memories, limiters and amplifiers were possible in the future. This work also set the note for the plethora of research work that followed for studying these effects in various integrated optical devices. An exhaustive discussion of the experiments and analytical models used for studying optical bistability can be referred from the comprehensive textbook on this topic by Gibbs [66]. The achievement of nonlinearities were extended to smaller systems for lowering the threshold powers required to achieve these effects. The first demonstration of such microoptical nonlinearities was performed with liquid microdroplets. A droplet can be regarded as an optical microcavity in a dielectric due to the whispering gallery mode that it exhibits. This was studied by Ching and co-workers in 1987 [67]. Following this work, several groups attempted to recreate the nonlinear effects inside these microdroplets and silica microspheres and succeeded [68, 69]. These systems were very interesting, nevertheless, they were quite impractical as they could only be used in research environments. Since the beginning of the 1990s, cavities that were of the size of the order of one wavelength of light were starting to be fabricated. In a significant work by Armani and co-workers [70], a process for producing silica toroid-shaped microresonators-on-a-chip with Q-factors in excess of 100 million was reported. These devices with their extremely high confinement of optical energy made possible the lowering of nonlinearity thresholds to the tens of μW power range. Ring resonator devices have also been widely studied in order to enhance the nonlinearities [71–74]. In the context of the previously mentioned arguments,

Chapter 1. Photonic crystals and light-matter interactions

a photonic crystal cavity is also expected to have a high density of optical energy stored in very small volumes leading to enhancement of intensity dependent nonlinear effects. This enhancement can be of several orders of magnitude larger than the classical devices. The highly integrable nature of these devices along with the ease of coupling light into them makes them a strong candidate for observing enhanced nonlinear optical phenomena.

The interest in the photonic crystal community was spurred with several theoretical studies and predictions since the 2000s, particularly from the group of Joannopoulos [75–83]. Following these predictions, a seminal work by Barclay and co-workers [84] showed the various nonlinearities present in a 2D PhC device in silicon. Further investigations were also reported

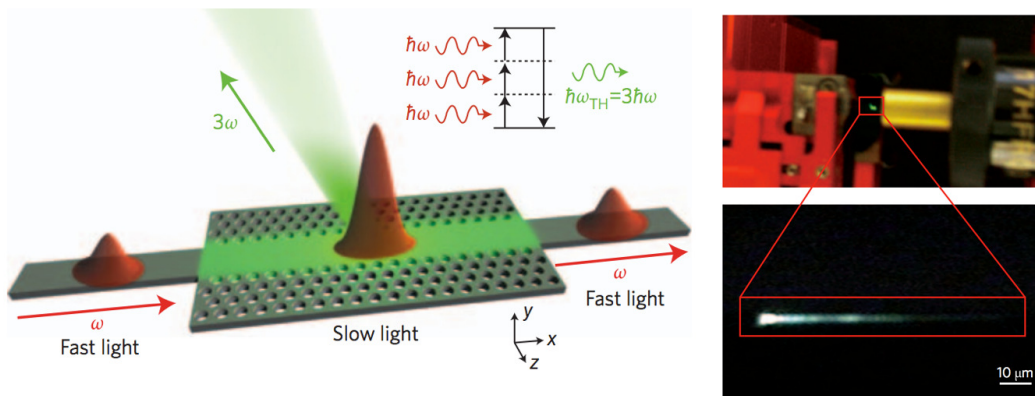


Figure 1.10: Green light emission illustrated in a slow light photonic crystal waveguide showing a pulse at frequency ω getting spatially compressed when it enters the waveguide and a third harmonic signal is extracted out of the device at a specific angle. The right side photographs show the emission visible to the naked eye during the experiment. Reprinted from [85].

concerning nonlinear and adiabatic control of cavities [86], optical bistability and all-optical switching [87–94], all-optical modulation [95] and third harmonic generation [96]. In the case of silicon, the picture is quite complex due to several processes. When two photons are absorbed at infrared wavelengths, they enable an electron to leave the valence band to reach the conduction band. This electron-hole pair that has been created by Two Photon Absorption (TPA) is later absorbed leading to Free Carrier Absorption (FCA) and subsequently results in a change in the refractive index of the system. Meanwhile, the optical Kerr effect has a third order dependence with respect to incident intensity that also creates a change in the refractive index of the system. It has been found that the sign of the change in refractive index is negative for free carrier related dispersion and positive for thermal and optical Kerr effect related dispersion [84]. The creation of phonons due to both TPA and FCA eventually leads to thermal expansion and a thermal refractive index change. These counter occurring phenomena also lead to several interesting features at high powers including pulsating behaviors [97]. Some of these effects can be utilized to achieve novel and compact nonlinear optical systems while some of the effects detrimental to the smooth operation of the device.

1.5.3 Quantum electrodynamics

The field of cavity quantum electro dynamics (cQED) broadly deals with the various possible mechanisms to tailor the emission of a single atom or a quantum dot ever since the days of Purcell, who proposed that the environment of an emitter can change the emission rate [98]. It deals with the interaction of quantized matter with a quantized electromagnetic field (photon) in a cavity. As has been explained before, photonic crystal devices can offer such a precise environment with strong confinement of light(Q) over small modal volumes(V) both in cavities and waveguides. Many such devices have been proposed and demonstrated as promising test beds for performing cQED experiments since the year 2001 [27, 99–101]. Two main aspects before proceeding towards the experiments are to make sure that quality factor is very high and also that the quantum dot is placed in a region where there is a maximum field overlap. Apart from using cavities, in a recent work by Lund and co-workers [102], quantum dots have been coupled in a broadband of frequencies by utilizing the modes in the slow light window of a photonic crystal waveguide near the band edge where they observed enhancement. The basic idea of cQED is to be able to couple an atom to a confined optical field as shown in the schematic in figure 1.11. The strength of this coupling can be quantified by a parameter $g(r)$

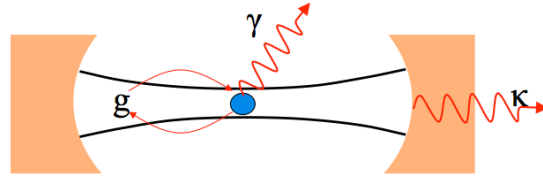


Figure 1.11: A basic schematic describing cavity quantum electrodynamics showing the atom decay rate (γ), cavity loss rate (κ) and coupling parameter g .

which is given by [27] as

$$g(r) = g_0 \frac{\epsilon(r)|E|}{\max(\epsilon(r)|E|')} \quad (1.16)$$

$$g_0 = \gamma \sqrt{\frac{V_0}{V_{mode}}} \quad (1.17)$$

where g_0 is the vacuum Rabi frequency, V_{mode} is the modal volume and γ is the decay rate for the excited state of the atoms. The basic ingredients required for an efficient quantum electrodynamics experiment is the maximization of the coupling parameter $g(r)$. In an ideal case, this is possible by designing a cavity with a very high Q factor and a very small modal volume as will be demonstrated in this thesis in chapter 4. When such a cavity is coupled with a quantum dot system, the photon from the cavity mode will form a quasiparticle known as a *polariton* when it is bound by the electron-hole pair in the quantum dot system. The strength of the coupling determines two possible regimes:

Chapter 1. Photonic crystals and light-matter interactions

- **Weak coupling:** This is the case when the interaction of the emitter is incoherent and is dominated by the damping states of the system. Spontaneous emission rates of single quantum dots embedded in a photonic crystal cavity can be modified significantly depending on if they are near cavity resonance or not [103]. Single-photon sources are envisaged in this regime.
- **Strong coupling:** This is a coherent interaction of the emitter with the cavity field where the cavity and the quantum dot system cannot be treated separately as it is a superposition state where the energy is being exchanged between the two at the rate of the coupling parameter. The stronger the coupling, the higher the rate of this energy exchange. Single photon nonlinearities and quantum information processing can be envisaged in this regime [104].

In addition to the coupling strength, accurate lithographic alignment steps are necessary in order to align the quantum dot with the microcavity field maximum which could drastically alter this coupling strength. Moreover, the tuning of the nanocavity resonance with respect to the quantum dot can also maximize the coupling acquired. For example, in this work [101], a precise technique was implemented that could position a quantum dot accurately on the field maximum and spectral tuning of the cavity mode with the emission line was reported successfully. The controlled tuning was performed by enlarging the holes and by thinning the PhC membrane. While the advantages of quantum dot-cavity coupling in the weakly

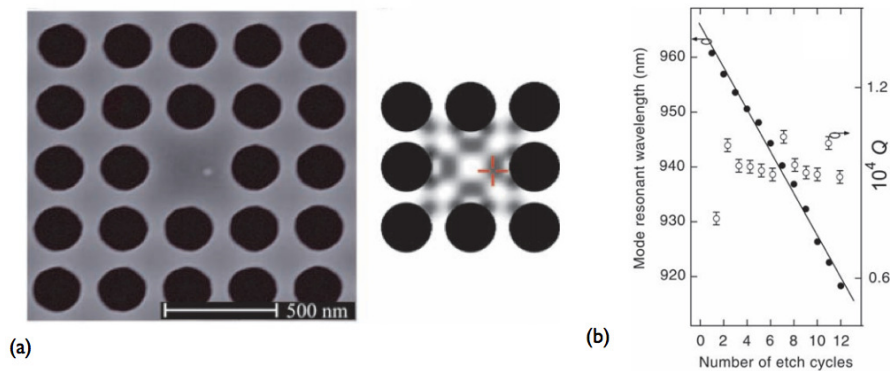


Figure 1.12: Photonic crystals and quantum dot coupling. a) Scanning electron micrograph image of the S1 defect cavity with a small dot indicating the top quantum dot of the stack. Electric field distribution is shown next to the image showing the maximum overlap with the QD. Shift of resonance wavelength of the mode with the number of etch cycles. Reprinted from [101].

coupled regime brings in the possibility of single photon sources [103], the advantages of strongly coupled systems would allow the placement of a large number of such systems in a mm^2 area opening the door towards quantum information networks. In the same system, the interconnections between these individual elements can also be facilitated by appropriately designed photonic crystal waveguides [99].

1.5.4 Photonic integrated circuits

Electronic integrated circuits pervade many aspects of human life today from communications to computation and the fundamental reason for this success lies in the ability to package millions of smaller building blocks (transistors) inside a single IC (Integrated Circuit). For example, the Xeon microprocessor from Intel released in 2012 has approximately 5 billion transistors within a single IC package. The surge in microprocessor speeds combined with the internet and mobile phone network usage has pushed the classical electronic communication links to their limits. In order to cope with this “bandwidth crunch”, photonic-electronic integration is seen as a best possible solution for the near future. Following the footsteps of the microelectronics predecessor, microphotonic chips intend to pack multiple photonic components within a single “Photonic Integrated Circuit (PIC)” [105] especially for their use in WDM (Wavelength Division Multiplexing) systems as shown in figure 1.13a. These photonic components include a number of functionalities such as lasers, waveguides, couplers, cavities, photodetectors and modulators and are expected to serve Tb/s communication links in the near future [106]. Amongst the different material technologies, InP has been

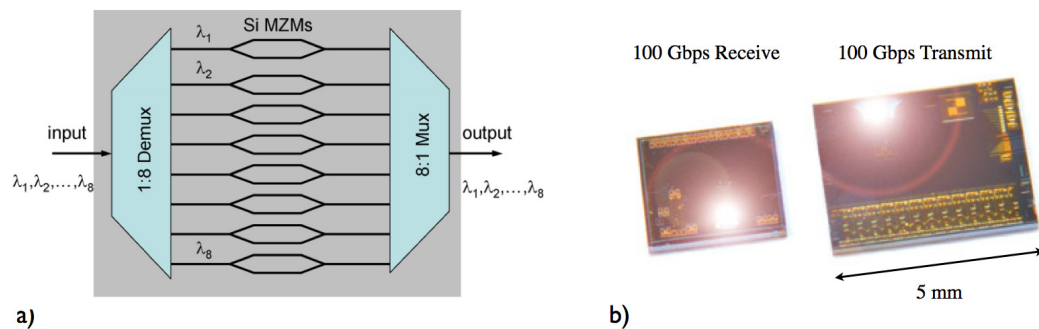


Figure 1.13: Photonic integrated circuits. a) Schematic showing various components of a silicon PIC including a demultiplexer, high speed silicon Mach Zehnder modulators and a multiplexer. Reprinted from [107]. b) 100 Gbps transmitter receiver chips forming a DWDM system commercialized by Infinera corporation. Reprinted from [108].

widely used to make these devices while recently silicon is being considered a preferred material given the higher refractive index contrast and superior processing technologies that are adopted from the CMOS industry [105, 109, 110]. As a highlight in the development of PICs for communication, Infinera corporation had introduced the first “DWDM system on chip” with a capacity of 100 Gb/s with InP technology in 2004 [108] as shown in figure 1.13b. In the development of PICs for communication systems, photonic crystals have been explored extensively for new designs of lasers [111, 112] and high speed modulators [113–115]. Apart from this, there has also been considerable interest in pursuing miniaturization of components required for processors such as on-chip optical memories and chip-chip optical switches [116, 117]. The energy cost for a single bit data transport is expected to be around fJ/bit in order to achieve low power transport channels. In a recent work by Nozaki and coworkers [118], an ultralow power all optical RAM was realized based on high-Q nanocavities in silicon with 2.5 fJ/bit in a very small area. A low switching energy, small device footprint and a fast switching

Chapter 1. Photonic crystals and light-matter interactions

time would be the preferred characteristics of such a system.

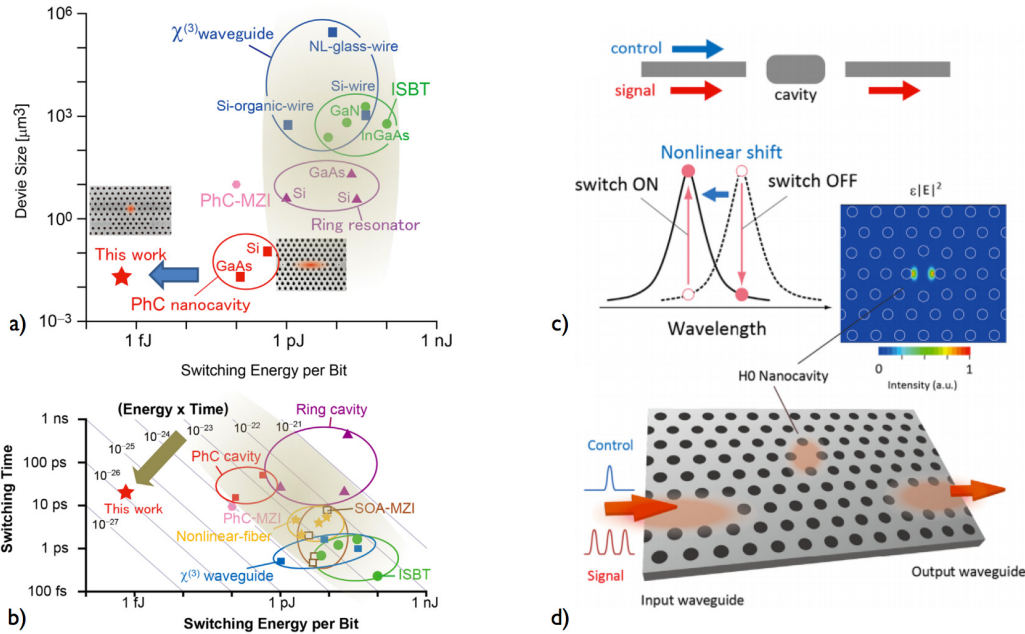


Figure 1.14: All optical random access memory with photonic crystal cavities. *a)* Comparison of various optical switches including the photonic crystal result from Nozaki and coworkers. *b)* Comparison of device footprint and switching energy showing the ultra low power switching energy of a photonic crystal based switching device. *c)* The switching principle based on nonlinear shift in the cavity system. *d)* Illustration of the H0 nanocavity and the electric field distribution. Reprinted from [119].

A recent comparison of various integrated optical switching devices by Notomi and coworkers [119] indicates that the large Q/V enhancement plays a crucial role in reducing the switching energy to the femtojoule level as seen in figure 1.14. An H0 nanocavity as implemented in this work [118] brings down the footprint by a large amount when compared to other ring resonator based devices facilitating the addition of several devices in the same waveguide chain. However, the problems in wafer-scale fabrication of these devices with a high yield ratio is one of the major concerns limiting widespread implementations. It is expected that in the light of novel standardized fabrication procedures for photonic crystals, a photonic network-on-chip architecture can be envisaged that can be used to implement an all-optical transport layer between microelectronic components.

In summary, it has clearly emerged from the sections outlined in this chapter that a simple two-dimensional slab photonic crystal device can be put to a variety of experimental scenarios for furthering the understanding of nanoscale phenomena. In most of the above-mentioned cases, either the cavity parameters or the quality factor or the modal volume are primarily the key factors for being able to conduct these experiments successfully. The rest of this thesis will focus on optimizing these parameters for various cavities, exploring their fundamental limitations and demonstrating novel light-matter interaction experiments.

2 Numerical investigations of PhC cavities

This chapter details the various numerical methods used and explains the calculations performed during the course of this thesis. Section 1 gives a historical overview of numerical methods. Section 2 introduces the numerical methods used for investigating photonic crystals. Section 3 details the mode expansion methods and finite element methods in length. Section 4 surveys the numerical results obtained during the course of thesis including dispersion properties, cavity mode analysis and effects of structural disorder. Section 5 provides a brief summary and outlook.

Contributions:

All the calculations shown in this chapter were performed using in-house developed mode expansion tools [120, 121] and a commercially available finite element solver [122]. This chapter also includes a work on disorder in photonic crystal cavities, which is a collaborative effort with the group of Prof. Vincenzo Savona (LTPN). In this work, the results using the finite elements were computed by myself while the results from the mode expansion tools were computed by Momchil Minkov (LTPN).

Publication of results:

The calculations shown in this chapter are complementary to the experiments that are reported in chapters 3, 4 and 5 of this thesis. These results are published alongside their respective experimental results in [123–129]

2.1 A historical walk

Any technique in mathematical physics obtains a prefix “numerical”, if it uses an approximate solution to solve any given problem. The usage of such numerical estimations goes back to the times of ancient civilizations when approximations were used to calculate the square roots of numbers that were required for construction and carpentry. One such example was found in an ancient Babylonian clay tablet as shown in figure 2.1. This tablet dates back to 1700 BC and shows the impressive evaluation of the square root of 2 over a diagonal of a square on a hexagesimal base and is interpreted as $1 + \frac{24}{60} + \frac{51}{60^2} + \frac{10}{60^3} \approx 1.414$.

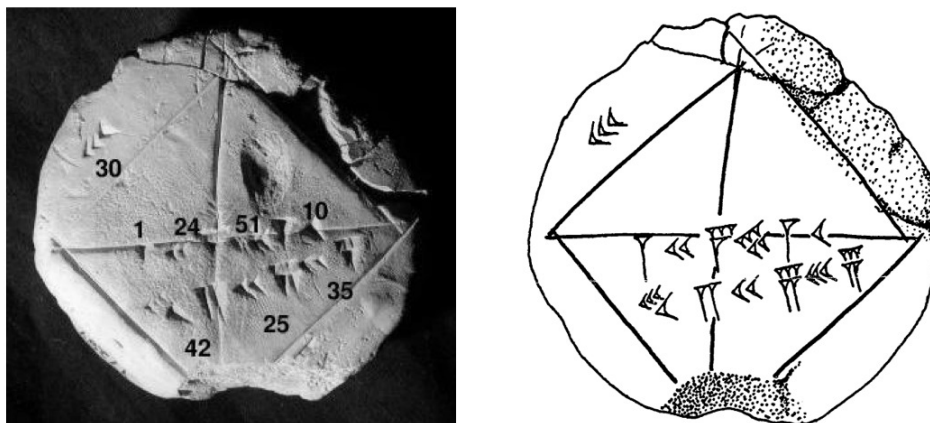


Figure 2.1: An ancient numerical method from Babylon. The expansion of the diagonal is described on the tablet with a sexagesimal basis using the inscriptions that has been decoded. Reprinted from [130].

This approach was developed for solving numerous day-to-day problems over the following centuries in both physics and astronomy. Newton introduced his famous “polynomial” fitting in the 17th century followed by noteworthy contributions on iterative techniques by Gauss, Legendre, Jacobi, Euler and others. In the beginning of the 20th century, two seminal papers were published by Richardson [131] and Courant [132] explaining the usage of finite differences for obtaining numerical solutions to partial differential equations. Courant also published his work on variational techniques in 1943 [133] that set the basis for the field of the modern version of finite element methods. In this work, he introduced the idea of minimizing a functional using linear elements in the calculation domain leading to the notion of mesh elements.

At this juncture, Von Neumann ushered a new wave of modern linear algebra with his influential paper on inverting matrices numerically in 1947 [134]. Since then, this field of applied mathematics has benefitted largely from the development of powerful computing machines starting from the 1940s followed by the invention of distributed computing algorithms over the end of the last century. These are presently employed to solve several large-scale physical problems involving massive systems of linear equations, optimization of functions with several variables and for solving complex systems of partial differential equations.

2.2 Numerical methods for photonic crystals

In most problems involving electromagnetism, the accurate solution to the problem lies in rigorously solving the Maxwell's equations, which are a pair of coupled differential equations as introduced in chapter 1. Solving these equations with the appropriate boundary conditions pertaining to a specific problem leads to a physical solution. Analytical formulation to this set of equations can be only performed on very simple systems such as a simple planar interface. For complex structures, such as a photonic crystal, it is highly cumbersome to obtain such formulations and hence numerical techniques have to be relied upon. The calculation of electromagnetic modes within a photonic crystal has always been a time demanding and a computationally intensive task. In this regard, it is important to understand the structures that we want to study in our experiments before fabricating them. This enables the tailoring of the structure accordingly in order to maximize the favourable characteristics pertaining to the experiment. Ideally, it would be beneficial to know the dispersion properties, spatial distributions of field profiles, cavity mode overlap ratios, losses and Q-factor estimates of cavity modes, nature of optical forces and absorption effects. As different numerical methods have their own advantages and disadvantages, a suitable choice must be made so as to use the appropriate method for specific properties. The variety of methods used to understand photonic crystals have broadly fallen into the following categories even though several lesser known methods can also be found in the literature [135–138] and in this review [139].

1. **Expansion methods:** The modes corresponding to the photonic crystal are decomposed into a set of known basis functions. These basis functions can be based on either a set of plane waves or guided waves of the slab or the Bloch modes of the periodic lattice. These methods will be explained in detail in the later sections of this chapter.
2. **Scattering matrix methods:** A set of scattering elements are placed periodically inside a layer that represents the modulation of dielectric permittivity. The propagation of light through these layers can be then described by using the well-known scattering matrix formalism [140].
3. **Finite difference time domain:** This is a time domain computation of the Maxwell's equations where the computational domain is first split into a number of smaller cells [132, 141]. The derivatives are represented by discrete difference formalisms and the electric and magnetic field components are determined inside these cells by an updating mechanism that uses the knowledge of the past fields in time. The computation then evolves the fields over time leading to a solution until a convergence obtained.
4. **Finite element methods:** Any complex structure or problem is subdivided into smaller and simpler elements called mesh elements. The method is based on the fact that an approximate solution is assumed for the function to be solved. The parameters of this approximate solution are then iteratively updated based on reducing the error in the solution. This method is also detailed in the next section of this chapter.

2.3 Numerical methods used in this thesis

The expansion methods (PWE, GME and BME) are used in this thesis primarily to understand bulk dispersion diagrams and to locate defect mode profiles inside the bandgap. Three dimensional finite element methods were used to understand the Q-factors of the cavities, refractive index sensitivities and the behaviour of optical forces. The formulations of these techniques are elaborated in detail below.

2.3.1 Mode expansion methods

Plane Wave Expansion (PWE)

The PWE method was proposed in the early 1990s [7, 8, 26] as a standard tool to study the physics of photonic crystals. In the case of a monochromatic field with angular frequency ω , the Maxwell's equations can be decoupled and are written as:

$$\frac{1}{\epsilon(\mathbf{r})} \nabla \times \frac{1}{\mu(\mathbf{r})} \nabla \times \mathbf{E}(\mathbf{r}) = \frac{\omega^2}{c^2} \mathbf{E}(\mathbf{r}) \quad (2.1)$$

$$\frac{1}{\mu(\mathbf{r})} \nabla \times \frac{1}{\epsilon(\mathbf{r})} \nabla \times \mathbf{H}(\mathbf{r}) = \frac{\omega^2}{c^2} \mathbf{H}(\mathbf{r}) \quad (2.2)$$

In the case of a photonic crystal with a periodic lattice, the eigenstate (ψ) inside the structure can be written using Bloch's theorem as

$$\psi(\mathbf{k}, \mathbf{r}) = e^{i\mathbf{k}\mathbf{r}} u_{\mathbf{k}}(\mathbf{r}) \quad (2.3)$$

where the $u_{\mathbf{k}}(\mathbf{r})$ denotes a periodic function with similar periodicity as the lattice and \mathbf{k} denotes the Bloch vector. This periodic function can then be represented as a summation of plane waves in the reciprocal lattice as

$$u_{\mathbf{k}}(\mathbf{r}) = \sum_m u_m(\mathbf{k}) e^{i\mathbf{G}_m \mathbf{r}} \quad (2.4)$$

It is important to note that in the case of a completely 2D photonic crystal light propagation, TE polarized light has only the in-plane electric field components and vice versa for the TM polarized light. Nevertheless, this is not true for slab 2D photonic crystals as there is a truncation in the vertical direction and refractive index based confinement is required. The presence of translational and vertical symmetry leads to the presence of even or odd modes that can be regarded as TE like and TM like modes [38]. These modes can be expanded as [120]:

$$E_z(\mathbf{r}) = \sum_m A_m e^{i(\mathbf{k}+\mathbf{G}_m)\mathbf{r}} \quad (2.5)$$

$$H_z(\mathbf{r}) = \sum_m B_m e^{i(\mathbf{k}+\mathbf{G}_m)\mathbf{r}} \quad (2.6)$$

Moreover, from the same argument of periodicity and symmetry, the permittivity and permeability distributions can also be approximated by the following expansions [120]:

$$\frac{1}{\epsilon(\mathbf{r})} = \sum_m \theta_m e^{i\mathbf{G}_m \mathbf{r}} \quad (2.7)$$

$$\frac{1}{\mu(\mathbf{r})} = \sum_m \eta_m e^{i\mathbf{G}_m \mathbf{r}} \quad (2.8)$$

All the above expansions in equations 2.3 to 2.8 can be used to expand the operator $\frac{1}{\epsilon(\mathbf{r})} \nabla \times \frac{1}{\mu(\mathbf{r})} \nabla \times$ and the electric field distributions appearing in equations 2.1 and 2.2. This leads to the final formulation of the expansions based on plane waves for both TM and TE polarizations as [120]:

$$\sum_n A_n \cdot [(\mathbf{k} + \mathbf{G}_m) \cdot (\mathbf{k} + \mathbf{G}_n)] \cdot \theta_{m-n} = \frac{\omega^2}{c^2} A_m \quad (2.9)$$

$$\sum_n B_n \cdot [(\mathbf{k} + \mathbf{G}_m) \cdot (\mathbf{k} + \mathbf{G}_n)] \cdot \theta_{m-n} = \frac{\omega^2}{c^2} B_m \quad (2.10)$$

The above expressions constitute the form of a Hermitian eigenvalue problem. An operator θ acting on two vector functions $\mathbf{H1}, \mathbf{H2}$ is termed as Hermitian if it satisfies the condition $\langle \mathbf{H1}, \theta \mathbf{H2} \rangle = \langle \theta \mathbf{H1}, \mathbf{H2} \rangle$ where $\langle \cdot, \cdot \rangle$ denotes the inner product between the two functions. This condition means it is independent of which function is operated upon before taking the inner product. The general properties of such a Hermitian operator gives real and positive eigenvalues and ensures orthogonality between modes that do not have the same frequency.

The number of plane waves used for computation determines the accuracy of the method as the computational complexity increases. The maximum magnitude of the set of wave vectors is referred to as G_{max} and it can be gradually increased during the computation until convergence is obtained. The number of plane waves used is generally proportional to G_{max}^2 . It can be seen that the above-mentioned expansions take the form of a Fourier expansion inevitably bringing up the issue of Gibbs phenomenon for discontinuous functions.

In the case of 2D photonic crystals, the dielectric permittivity distribution shows abrupt transitions at the edge of the holes leading to a discontinuous function. These discontinuities lead to the presence of the Gibbs phenomenon in the approximations that eventually degrades the accuracy of the PWE based solutions. This problem has been resolved in this method by using the technique of using an inversion rule method involving the Toeplitz matrix.

A second method to reduce this phenomenon is the use of a finite filter that can smoothen out this phenomenon. The permittivity and permeability distributions have to be accurate because they are also used to compute the displacement field (\mathbf{D}) and magnetic induction field (\mathbf{B}) based on the constitutive relations.

Guided Mode Expansion (GME)

As explained in the previous section, an ideal 2D PhC structure with holes embedded in a dielectric medium would support the existence of either TE or TM polarizations. However, the devices that have been studied in the course of this thesis are fabricated over a thin slab, resulting in a truncation of symmetry in the vertical direction. This can be compounded with the fact that there can be different materials above and beneath the dielectric layer, for example a system with silica, silicon and air. In this sense, the light confinement is achieved in the vertical direction with an index contrast based total internal reflection. The field distribution of such guided modes inside a membrane of dielectric media is not similar to that of the plane wave used in the previous expansion technique. In order to get a closer approximation to a real structure, the guided modes of such a dielectric waveguide structure must be used in the basis expansion instead of a set of plane waves. This was first explored and reported by Andreani and Gerace in 2006 [142] where the Bloch modes of the PhC structure are expanded over guided modes of the slab. The method in a nutshell is explained below.

In the case of a simple planar dielectric slab surrounded by a lower index medium, the one dimensional Helmholtz equation can be represented as

$$\frac{\partial^2 \phi(z)}{\partial z^2} + (\epsilon(z) \frac{\omega^2}{c^2} - k_x^2) \phi(z) = 0 \quad (2.11)$$

where the allowed modes can be computed through implicit trigonometric equations showing the dispersion relation between wave vector and frequency as explained in chapter 1 in figure 1.2 where the light line, the guided modes and the radiative modes were indicated. These are as a result of total internal reflection at the slab interface. The addition of photonic crystal structure to such a slab brings in additional complexity of periodicity. This modifies the dispersion diagram shown in figure 1.2. In a sense, every guided mode allowed in the slab gets altered due to the periodic nature of this crystal resulting in an extremely complex landscape. The guided mode expansion is a fast algorithm that can be used to calculate this complex landscape. The solution to the Maxwell's equations from 2.2 concerning the magnetic field can be expanded using the orthonormal set of basis vectors as [142]:

$$\mathbf{H}(\mathbf{r}) = \sum_v c_v \mathbf{H}_v(\mathbf{r}) \quad (2.12)$$

and the Helmholtz equation can be written as:

$$\sum_v c_v \mathbf{H}_u^* \nabla \times \frac{1}{\epsilon} \nabla \times \mathbf{H}_v = \frac{\omega^2}{c^2} \sum_v c_v \mathbf{H}_u^* \mathbf{H}_v \quad (2.13)$$

The above expression when integrated over the system volume leads to a linear eigenvalue problem of the form:

$$\sum_{uv} H_{uv} c_v = \frac{\omega^2}{c^2} c_u \quad (2.14)$$

The basis states $\mathbf{H}_u(\mathbf{r})$ are basically the guided modes of a slab with the permittivity taken on average depending on the filling factor. The above matrix is also Hermitian and that ensures that the eigenvalues are positive and hence are the real Bloch modes of the photonic crystal. When the photonic crystal periodicity is taken into account, only guided modes with wave vector $\mathbf{g} = \mathbf{k} + \mathbf{G}$ are allowed where \mathbf{G} is the vector of reciprocal lattice. This leads to the expansion of the magnetic field inside the photonic crystal as:

$$\mathbf{H}_{\mathbf{k}} = \sum_{\mathbf{G}} \sum_l c(\mathbf{k} + \mathbf{G}, l, s) \mathbf{H}_{\mathbf{k} + \mathbf{G}, l, s}^{guided} \quad (2.15)$$

where l corresponds to the index of the mode for a wave vector $\mathbf{k} + \mathbf{G}$ and s denotes the polarization. The spatial distribution of modes can be further understood from the symmetry planes present in the structure. A breaking of symmetry in the plane of the photonic crystal structure can lead to the mixing of TE and TM polarized modes and this is important with respect to the presence of disorder, which will be touched upon in a later section of this chapter. This expression in equation 2.15 does not include the lossy radiative modes in the basis set. The radiation losses of the Bloch modes can also be treated with the GME approach but by following the Fermi golden rule from quantum mechanics [143]. These losses can then be represented as the imaginary part of their frequency as

$$-Im\left(\frac{\omega_{\mathbf{k}}^2}{c^2}\right) = \pi |H_{leaky, guided}|^2 \rho\left(\mathbf{k}; \frac{\omega_{\mathbf{k}}^2}{c^2}\right); \quad (2.16)$$

where $\rho\left(\mathbf{k}; \frac{\omega_{\mathbf{k}}^2}{c^2}\right)$ represents the one dimensional photonic density of radiating states at a fixed in-plane wave vector. This imaginary part is then used to calculate the Q-factor of cavities that will be explained later in this chapter. In both the PWE and GME methods, the calculation of a bulk PhC structure is achieved by computing a primitive cell along with periodic conditions. In the case of waveguides and cavities, a ‘‘supercell’’ approach is required where a larger area is used as a primitive cell that encloses the defect. The size of the supercell is chosen in a manner so as to fully capture the physical properties of the defect structure. The supercell size can be increased until convergence is obtained for specific cavity properties such as resonance wavelength or Q-factor. However, a larger supercell with a very high G_{max} increases the computational cost considerably (from a few minutes to a few hours in a personal computer).

The PWE method is a simple technique and works well for regular crystals with infinite thickness whereas the GME method is naturally suited for the case of slab photonic crystal devices. The additional mathematical complexities in GME render it computationally more demanding than the PWE method, nevertheless it allows for an accurate and reliable computation of dispersion diagrams of waveguides. This is possible because of the difference in the vertical profile of the mode of a guided mode and a plane wave. In addition to this, the GME is advantageous as it allows for the calculation of radiative losses and hence quality factors accurately without having the need for the usage of full field calculations. This advantage will be highlighted in the section on computing quality factors for huge sets of disorder realizations in the later part of this chapter.

Bloch Mode Expansion (BME)

The before-mentioned methods derive the final dispersion map of a photonic crystal structure on the basis of a perfectly linear dielectric medium. However, it is important to note that disorder plays a huge role due to the inconsistencies arising from the fabrication process. This disorder appears as a slight perturbation on top of the regular periodic modulation of the dielectric medium and can lead to interesting properties such as Anderson localization of mode profiles and light losses as will be explained in detail in the later section of this chapter.

In order to take this into account, Savona proposed a technique based on Bloch modes that represent the PhC lattice [121] that was also inspired by the earlier work of John [1]. The basic idea is to compute the Bloch modes of a PhC by using other methods such as GME and then expand the “disordered PhC” on the basis of these modes. In this context, only the Bloch modes close to the frequency of interest need to be considered that reduces the complexity and computation time significantly. In the limit of considering all the Bloch modes in the crystal, this technique becomes formally equivalent to a GME computation. The formalism is as follows [121]. The disorder in the system can be written as

$$\epsilon'(\mathbf{r}) = \epsilon(\mathbf{r}) + \delta\epsilon(\mathbf{r}) \quad (2.17)$$

The eigenmodes of the disordered lattice are calculated by expanding on the basis of the Bloch modes of the regular PhC. The actual eigen mode including disorder can be represented as \mathbf{E}_β , where β is the index of the actual mode. This expansion is then written as [121]

$$\mathbf{H}_\beta(\mathbf{r}) = \sum_{\mathbf{k}n} U_\beta(\mathbf{k}, n) \mathbf{H}_{\mathbf{k}n}(\mathbf{r}) \quad (2.18)$$

Using equation 2.1 and the above expressions, it is possible to write

$$\sum_{\mathbf{k}n} U_\beta(\mathbf{k}, n) \left[\nabla \times \frac{1}{\epsilon(\mathbf{r})} \nabla \times \mathbf{H}_{\mathbf{k}n}(\mathbf{r}) - \frac{\omega_\beta^2}{c^2} \mathbf{H}_{\mathbf{k}n}(\mathbf{r}) \right] = \mathbf{0} \quad (2.19)$$

By taking a scalar product of equation 2.19 with $\mathbf{E}_{\mathbf{k}'n'}^*(\mathbf{r})$ and integrating on \mathbf{r} in order to normalize the modes over the total volume just like in the case of the GME, we can finally obtain the generalized eigenvalue problem using BME as:

$$\sum_{\mathbf{k}'n'} \left[\frac{\omega_{\mathbf{k}n}^2 - \omega_\beta^2}{c^2} \delta_{\mathbf{k}\mathbf{k}'} \delta_{nn'} + V_{\mathbf{k}n, \mathbf{k}'n'} \right] U_\beta(\mathbf{k}', n') = 0 \quad (2.20)$$

The above expression also contains the information of the disorder present in the system in the matrix $\mathbf{V}_{\mathbf{k}n, \mathbf{k}'n'}$. In order to check the convergence of the method, the number of bands can be increased and eigenvalues can be checked. If the perturbation is relatively small, only a small subset of Bloch bands is required to find the solution. This advantage can also be exploited in computations involving photonic crystal cavities based on a waveguide structure, such as the width-modulated cavities from Kuramochi and coworkers [144].

2.3.2 Finite Element Methods (FEM)

Physical phenomena are generally represented by mathematical formalisms that further help to understand the underlying mechanisms involved. Phenomena such as motion of water waves, propagation of electromagnetic radiation or transfer of heat in a medium, all of these phenomena can eventually be described via partial differential equations involving variables to be solved for. These variables can also be coupled from one physical equation to the other using coupling coefficients. Finite element methods allows for the accurate calculation of the physical variables involved in such systems by solving the partial differential equations inside a discretized grid, often referred to as a *mesh*. The system of differential equations is then reduced to a system of algebraic equations that can be solved in a numerical machine such as a powerful computer in order to obtain the final results. In this thesis, such a finite element solver [122] was used to obtain the solution of the modes in photonic crystals. This solver is based on a variational formulation that is defined as a minimization of a functional. The method is as follows

1. Define the function with a set of basis functions $\phi(x, y) = \sum_{i=1}^M u_i b_i(x, y)$.
2. Write an expression J in terms of the above basis functions, for example in the case of the wave equation as $J = \int \left(\left(\frac{\partial \phi}{\partial x} \right)^2 - k^2 \phi^2 \right) dx$.
3. Find the coefficients of u_i such that J is minimized, for example using the condition $\frac{\partial J}{\partial x} = 0$.

A second method is also possible from the various implementations of the Galerkin method. This is a method based on weighted residuals where an approximate solution is assumed for the given problem under study. The error resulting from this approximate solution is the residual error and is minimized with iteratively optimizing the weighting functions. There are various parameters in the finite element method that can affect the accuracy of the solution. This can be:

- Choice of type of elements used in the mesh that can alter the degrees of freedom significantly.
- Choice of basis functions: Linear, quadratic or cubic.
- Choice of solver used: Direct or iterative solvers.

In most cases, it is important to optimize the parameters mentioned before depending on the particular physics involved. In order to illustrate the applicability of FEM to electromagnetic problems, a simple case involving the calculation of the far-field distribution from a rectangular slit is described below.

Chapter 2. Numerical investigations of PhC cavities

The analytical form of Fraunhofer diffraction integral for the far field calculation of a field on an aperture is given as:

$$U(x_0, y_0) = -\frac{e^{-jkz}}{j\lambda z} e^{\frac{-jk}{2z}(x_0^2+y_0^2)} F.T(U(x_1, y_1)) \quad (2.21)$$

Here, the field intensity U is calculated at a point (x_0, y_0) far from the aperture at a distance z . This expression suggests that the far field intensity observed at the far field plane is directly the Fourier transform of the aperture function itself. In the case of a rectangular slit, this will translate to the *sinc* function and in the case of a circular aperture, it is an *Airy* disc. The first zeros of the *sinc* function can be analytically written as $\frac{\lambda z}{D}$ where D is given by the slit size.

This particular simple case was modelled using the FEM solver and the results are shown in figure 2.2. A plane wave is impinged on a slit and a far-field calculation is made on a surface far away from the aperture. The figure also shows the extremely dense discretization of the computation volume through triangular mesh elements.

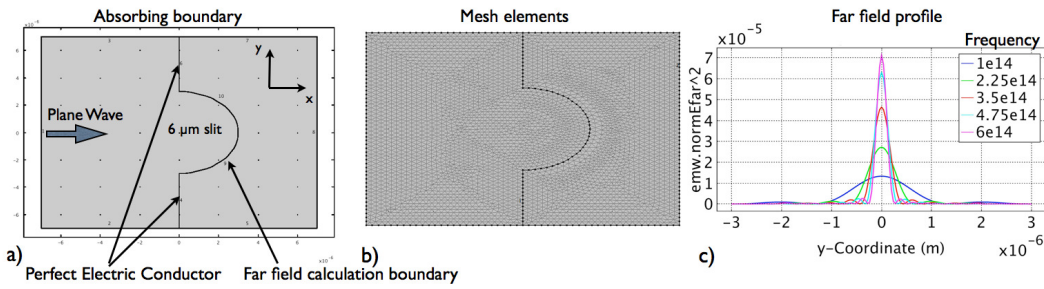


Figure 2.2: Finite element model for the farfield profile of a slit cross section. a) The geometry under consideration showing the slit of $6 \mu\text{m}$ impinged by a plane wave. b) The discretization of computational space by triangular mesh elements. c) The far field profile obtained for different input frequencies.

This computation uses triangular mesh elements and edge mesh elements. The total number of mesh elements is close to 7000 and the solution takes only a few seconds for solving the wave equation in this domain on a personal computer. The refractive index is set to 1 and the boundary conditions are shown in the figure. Two different boundary conditions are used, the perfect electric conductor, for the case of the slit wall, while the surrounding boundaries are absorbing boundaries. A plane wave is launched onto the slit from the boundary and frequency domain analysis is performed.

The far field is then computed by using the near-far field transformation method. The intensity of the field distribution and also the intensity of the field components are also shown in the figure. The far field profile is the expected pattern of a sinc profile and the zeros of this function are compared with that of the analytical formulation and is displayed in table 2.1 that clearly shows the agreement with the two methods.

2.3. Numerical methods used in this thesis

Frequency	Position of zero (Analytical)	Position of zero (FEM)
100 THz	3.5 μm	3.6 μm
225 THz	1.55 μm	1.6 μm
350 THz	1 μm	1.03 μm
475 THz	0.74 μm	0.78 μm
600 THz	0.58 μm	0.6 μm

Table 2.1: Comparison of analytical and FEM solutions for farfield.

In the three-dimensional modelling of most of the photonic crystal devices presented in this thesis, tetrahedron mesh elements were employed. In order to have an estimate of mesh quality in such tetrahedral meshes, a parameter referred to as q is defined as

$$q = \frac{72\sqrt{3}V}{((h_1)^2 + (h_2)^2 + (h_3)^2 + (h_4)^2 + (h_5)^2 + (h_6)^2)^{\frac{3}{2}}} \quad (2.22)$$

where V is the volume of the tetrahedron element and $h_1...h_6$ are the respective lengths of each sides. It is preferred to have this parameter to be greater than 0.1 for a better mesh convergence while solving electromagnetic problems. It is also imperative to keep the elements in other regions such as the volume of air lesser in q so that the computation time does not explode. Nevertheless, it is also not practical to mesh all the domains in the same fashion. The convergence of the solution depends heavily on the individual mesh elements. In the case of the photonic crystal slab, the meshing of the holes is of a high importance given the fact that it is responsible for the perturbation of the slab. To show this, four different cases of hole-mesh are considered on a single hole in a PhC as shown in figure 2.3.

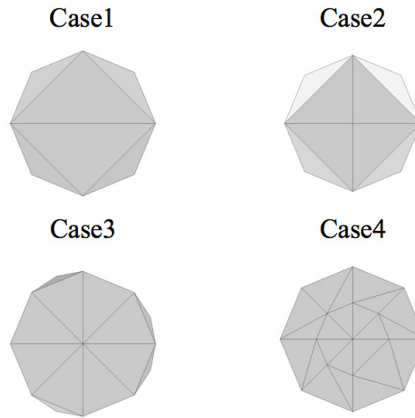


Figure 2.3: Mesh evolution of a single hole in a slab showing the increase in number of elements that invariably changes the shape of the hole perceived by the solver and hence the solution accuracy.

In a crude first order, these mesh elements can also alter the lattice shape and symmetry. For example, case1 shown in figure 2.3 starts to resemble a square hole rather than the intended circular hole. The difference in the shape of the hole might also result in the breaking of

Chapter 2. Numerical investigations of PhC cavities

symmetry as will be explained in the last section of the chapter. All these four cases are then used to compute the Q-factor of a photonic crystal cavity that is based on the A3 design reported here [144]. In the original paper, this cavity design is reported to have a FDTD numerical quality factor of 1 million. It can be seen from table 2.2 and figure 2.3 as the mesh is progressively made denser, the Q-factor starts to converge to its expected value. Such a stark increase in the convergence of solution is not seen for the case of the increase in elements for the “less important” domains like the volume of air above and below the membrane.

Case	Number of 2D elements	Number of 3D elements	Q-factor
1	2	18	4700
2	4	42	36000
3	8	69	750000
4	22	90	1150000

Table 2.2: Mesh cases comparison for a single hole in a photonic crystal.

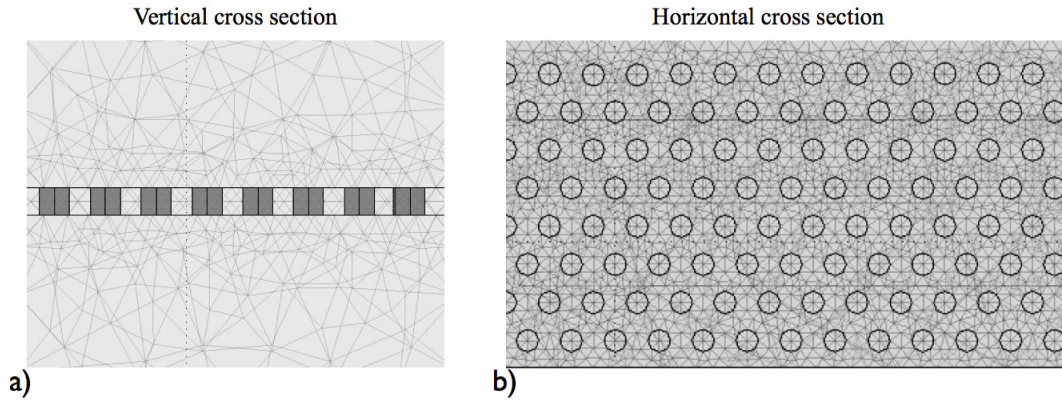


Figure 2.4: Meshing cross-sections of a photonic crystal slab showing the density of mesh elements in the vertical (a) and horizontal (b) cross sections.

The PhC model includes three main subdomains. The first is the volume of air above and below the slab structure as shown in figure 2.4a. This thickness of this domain is generally of the order of the wavelength of operation, for the case of silicon and near-IR wavelengths, $2 \mu\text{m}$ is found to be sufficient. The ratio of the size of the smallest structure to the size of the largest structure determines the complexity of the meshing. In this example, a hole of radius 250 nm and the air volume of $2 \mu\text{m}$ makes it impossible to create a uniform mesh as the number of elements tend to become unmanageable. Hence, adaptive meshes as shown in figure 2.4 are implemented. It can be clearly seen in figure 2.4 that the air volume is sparsely meshed and the density grows as it reaches the surface of the slab. The slab boundaries and the surface are meshed densely and the holes are meshed with the highest density of mesh elements.

The optimum adaptive meshing sizes have been repeatedly refined depending on various mesh refinement computations. In the presence of a small nanoparticle in the computation domain, such as in the case of a single dielectric particle in the cavity, as shown in figure 2.5,

a second problem arises as the particle is free to be placed in the air domain close to the cavity. In order to smoothen this abrupt transition of mesh densities, a constant mesh density cylinder was placed around the particle as can be seen in figure 2.5 that encloses the motion volume. In this manner, the effect of the motion of the particle can be truly captured and the inaccuracies due to mesh inconsistencies can be safely discarded.

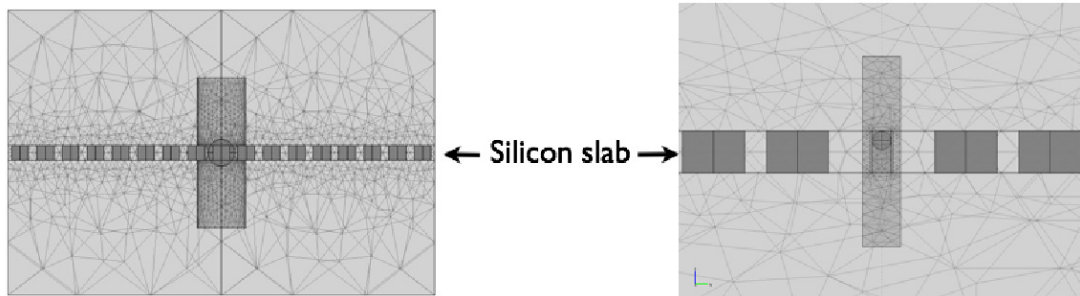


Figure 2.5: Meshing of single particle motion inside hollow cavities by creating constant mesh density cylinders in order to discard mesh inaccuracies.

All the computations performed in this thesis used three-dimensional modelling of complex photonic crystal geometries. These geometries resulted in mesh structures comprising of close to a million mesh elements, which are impractical to solve in any personal computer due to memory constraints and hence a cluster computing platform was used. A computing cluster is a group of linked computers, networked together in order to form a single “super” computer. It is generally referred to as a *poor man’s super computer* and is vastly employed in many heavy computing environments. The simple tasks involved in handling a cluster computing platform is enumerated as follows:

1. Prepare the jobfile that includes the commands to execute the computation sequence in a local machine.
2. Submit the jobfile to the cluster batching system that queues the job, allocates resources and completes computation.
3. Retrieve solutions and log files back to local machine for post processing the results.

The advantages of parallel computing come in two flavours. It can be used by operating on multiple cores of a single machine, generally termed as the *number of processors* or it can be used by using multiple machines, generally termed as *number of nodes*. However, in this thesis, the single machine, multiple processor parallelism was more extensively used. This was also due to the fact the PARDISO (*PARallel sparse Direct and multi-recursive Iterative linear SOLver*) type solver was used which is a fast, robust solver that can work on multiple cores inside a single machine. Further information on this solver can be found here [145].

2.4 Some numerical results obtained during this thesis

In the course of this thesis, several investigations were conducted to probe possible enhancement effects predicted due to the slow light property of photonic crystal waveguides [146]. In order to exploit this enhancement offered by an increased group index of the propagating mode, highly bandwidth specific slow-light structures were designed, fabricated and optically characterized. The mode expansion methods outlined in this chapter (PWE and GME) were crucial to these experiments and some of the results obtained are additionally highlighted in this section. Apart from this, other numerical results regarding cavity designs, Q-factor calculations and the influence of disorder are also presented in this section.

2.4.1 Dispersion and slow light

As introduced in chapter 1, photonic crystal waveguides are extremely important for various applications involving slow light enhancement and on-chip light coupling to cavities [77, 85, 146, 147]. In this context, the modelling of their propagation properties was important to most of the experiments performed in this thesis. In the case of applications requiring slow light, the bandwidth over which the light is slowed down also becomes extremely important. For example, to measure the enhancement of the absorption lines of acetylene, it is important to have the slow light group index to be linear over a range of 1500 nm to 1540 nm. In order to achieve this, the position of the first rows on either side of the standard W1 waveguide can be tuned as previously reported here [148]. Taking this as a starting point, by shifting the first row of holes by $0.13a$, a slow light waveguide with group index in the expected bandwidth was designed and is shown in figure 2.6. The supercell based GME is used to perform this computation. The left side of the figure shows the supercell that is highlighted in green involving 5

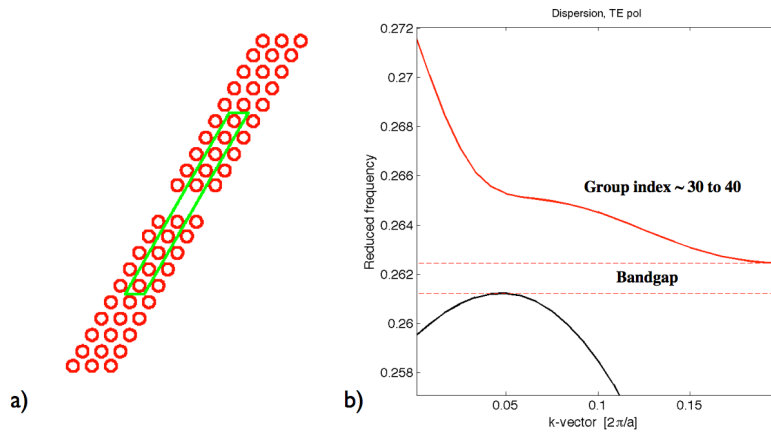


Figure 2.6: Group index engineered slow light W1 waveguide: Numerical simulation with 2D GME, a) Supercell for the simulation b) Dispersion of the even mode of the W1 guided mode (shown in red) and the band gap shown in dotted red line. The horizontal axis is plotted by taking into account band folding due to the applied grating.

2.4. Some numerical results obtained during this thesis

rows on both sides of the defect waveguide and a single repeatable column in the propagation direction. This supercell is repeated in the simulation with periodic boundary conditions. The maximum length of the reciprocal lattice vector used in this case was $G_{max} = 4\frac{2}{\sqrt{3}}\frac{2\pi}{a}$. The right side of figure 2.6 shows the calculated dispersion diagram of such a shifted waveguide. The group index is indeed modified as predicted here [148] and flat regions of group index with slow light propagation characteristics are found. The falling of the W1 even mode from the air band also shortens the bandgap width, nevertheless, a small bandgap still persists in the structure. The usable region of the slow light bandwidth is debatable as it is strongly influenced by disorder and by the presence of Anderson localization that has been extensively studied [149–153]. The above-discussed design was fabricated and the SEM image of

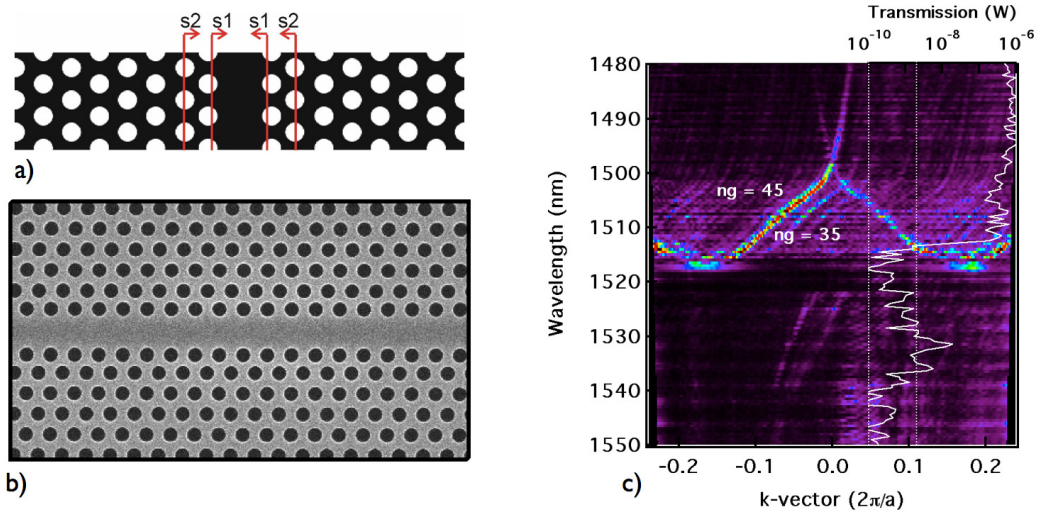


Figure 2.7: Experimental demonstration of a slow light W1 waveguide. a) The schematic of the modification of the position of holes for achieving this effect [148]. b) Scanning electron micrograph of the fabricated structure. c) Dispersion and transmission measurement indicating the group index and flat band region close to the band edge along with a very improved slow light transmission signal.

the sample fabricated is shown figure 2.7b. The dispersion measurements using the grating scattering approach [154] were performed and presented in figure 2.7c. It can be seen that the transmission characteristics of the slow light region are also significantly improved due to the implementation of slow-light tapering in the photonic crystal structure and by the design of an in-line grating for non-invasively measuring dispersion. This new design helps to achieve a "linear slow light" regime with a good transmission spectrum. It can also be seen that the measured data is in close agreement with the predicted dispersion profile provided by the calculations. This method takes less than a few minutes to design and parametrically tune the properties of the waveguide using a personal computer. The PWE method can also be used to compute the same curves but there are subtle differences between the two methods. The guided mode cross section profile in the slab along the vertical direction shows an exponential decay into the top layer and this modifies the effective interaction of the light and perturbation in the case of the GME. The interaction of higher order modes also plays a significant role in the

Chapter 2. Numerical investigations of PhC cavities

case of the guided mode that results in a slight compression of the bandgap when compared to the PWE method. It is in general more accurate to use the GME method as it is closer to depicting the experimental situation and this has also been verified with measurements as in this case of the slow waveguide. This device is a perfect illustration of a ready-to-use, bandwidth specific, slow-light waveguide that can be used for a number of applications. There are also

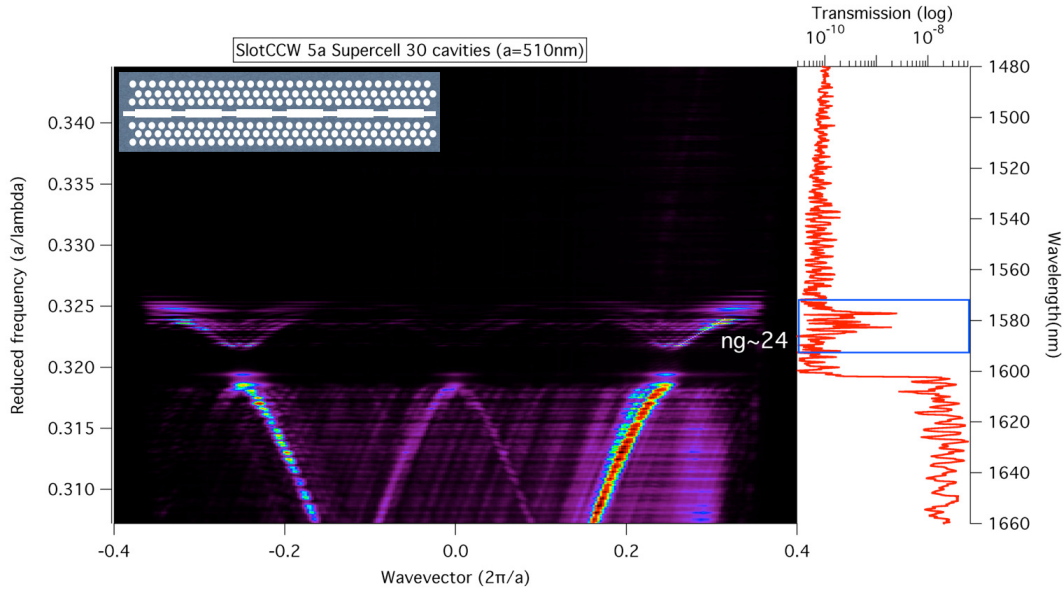


Figure 2.8: Group index engineered slot coupled cavity waveguide. The inset shows the schematic of the structure measured. The dispersion of the coupled cavity waveguide is clearly shown exhibiting the sinusoidal pattern with a slow light bandwidth. The transmission measurement on the right confirming the same.

applications in which the light in the waveguide is preferred to be propagating in the low-index medium. Slotted photonic crystal waveguides and slotted coupled-cavity waveguides (CCW) have been investigated for achieving this purpose [114, 154, 155]. A case of slotted coupled cavity waveguides was designed and fabricated during this thesis to create a slow light window for these devices to use in light-matter interaction experiments and is shown in figure 2.8. This device is a concatenation of a number of individual slot photonic crystal cavities placed in an in-line arrangement. The distance between the cavities and the coupling strength together determines the dispersion curve for these devices. It was also shown previously that a chain of eight cavities can support a slow-light bandwidth of 0.33 THz (2.6 nm) with a group index of approximately 100 [154]. It can be shown with the so-called "tight binding approximation" that for a chain of finite length of N cavities, the dispersion curve sampled with a constant spacing k is given by $\omega_i \approx \omega_0 + \kappa \cos(k_i \Lambda)$ where ω is the frequency, ω_0 is the resonance frequency of each cavity, Λ is the CCW periodicity, and κ is the coupling strength between the cavities. This equation shows the dispersion curve will have a sinusoidal shape as can be also clearly seen in the experimental measurement of figure 2.8. The increase in coupling will lead to an increase in bandwidth and also a decrease in group velocity of guided light.

2.4.2 Cavity mode evolution in PhC lattice

The formation of cavity modes has been briefly discussed in chapter 1. In order to visualize it more clearly, the PWE method was used to understand how the field localization in cavities evolve with respect to the air band and dielectric bands.

To perform this analysis, a triangular lattice with filling factor of 40 percent in a slab with holes configuration is chosen. The dispersion diagram along the Γ , M and K points is shown in figure 2.9a. The electric field localization is shown at the M and K points in figure 2.9b and c respectively. It can be seen that the mode in the air band (top band) has a field fully localized in air and the vice-versa at the bottom band chosen at K-point. In the case of making cavities that localize light in air, it will be beneficial to work with the modes falling from the top band. This is in context of the hollow-cavities that will be seen in chapter 3 for optical trapping experiments. For example, as it was explained in chapter 1 regarding the creation of cavity

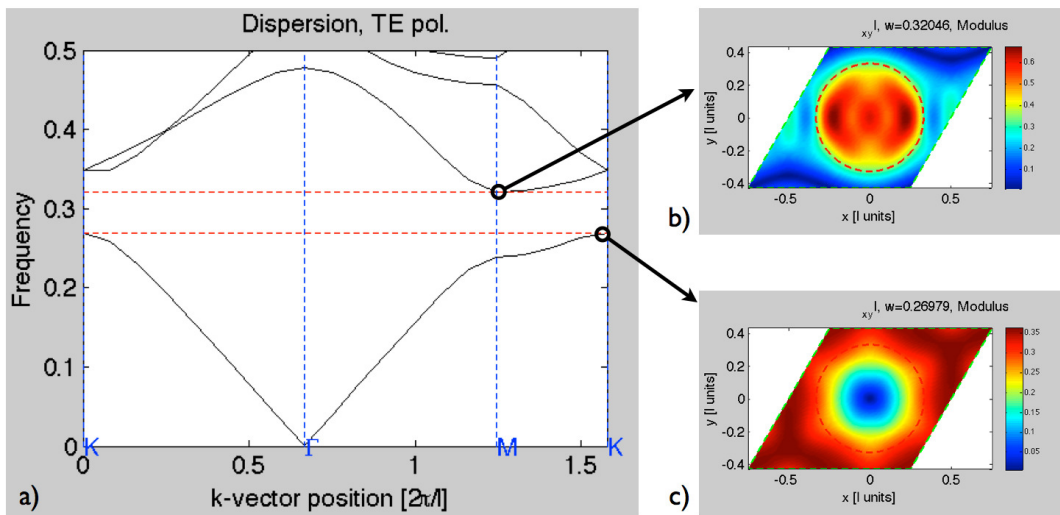


Figure 2.9: a) PWE based calculation of bandgap and the electric fields showing the two states from the bottom and top bands at K and M points respectively. b) and c) The localization of electric fields as seen in the unit cell. The field is localized in air for the top band and in dielectric for the bottom band.

modes, a slight perturbation results in the breaking of symmetry and allows for localization of light. A state in the otherwise photonic crystal bulk is delocalized all over the crystal area. In figure 2.10, the evolution of the cavity modes with respect to this perturbation is visually explored with the aid of the PWE method. In figure 2.10, the central three holes are changed to a different filling factor (30%). In figure 2.10b, the filling factor of five central holes are changed (35%, 24%, 20%, 25% and 35%). In figure 2.10c, an elliptical hole is created in the centre and the surrounding holes are decreased in their filling factor (indicated in green and pink). The fourth figure shows the circular cavity that is used in chapter 3, where the central hole is enlarged and six other holes are removed from the lattice.

In all the cases, the position of the cavity frequency with respect to the bulk bandgap is

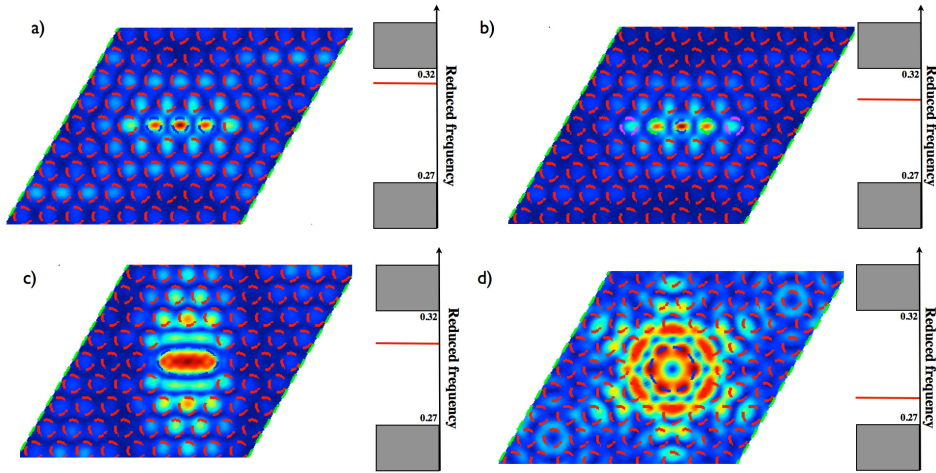


Figure 2.10: Evolution of cavity mode profile and position for different defects showing the position of the cavity mode in the bandgap relative to the air and dielectric bands. It is seen that for increased localization in silicon, the mode is much closer to the dielectric band and vice versa.

indicated with a red line next to the figures. It is intuitively easy to understand that with the removal of further and further dielectric material; the cavity mode starts moving closer and closer to the lower band. The localization in silicon also generally favours higher Q-factors and this is one of the reasons that most high-Q cavities have their field localized in silicon as total internal reflection allows a better confinement in this case. The accurate estimation of Q-factors of these modes must however, be calculated with a 3D method in order to understand the radiation losses.

2.4.3 Quality factors and modal volumes

The computation of quality factors has remained a challenge for a number of reasons mostly owing to the differences in the experimental samples and ideal theoretical structures. However, in most cases, the calculation of the intrinsic Q is required which comes from the radiation loss mechanism due to the slab nature of the photonic crystal. In the guided mode expansion method formulation, an approximation was used by not taking into account the radiative modes outside the light cone. It is exactly this coupling that leads to the radiation losses in the cavity. This radiative decay leads to an imaginary part in the eigenvalue solutions which can be calculated via the Fermi golden rule [143] as shown in the previous section of GME [142, 156]. By calculating the imaginary part of the frequency of the defect mode with perturbation theory, the Q-factor can then be quantified as

$$Q_{factor} = \frac{\omega}{2Im(\omega)} \quad (2.23)$$

In order to show the various methods used to compute the Q-factors, a comparison with respect to four well-known 2D PhC cavity designs is presented in figure 2.11. Mode expansion

2.4. Some numerical results obtained during this thesis

methods can also be used to derive the Q-factor of the cavities in a faster way compared to the full simulation methods. Cavities that have a distribution similar to a PhC waveguide can be considered as a perturbation on the waveguide mode and the previously explained BME method can be used to expand the cavity modes. The BME method relies on the fact that the Bloch modes of a disorder-less waveguide can be used to expand cavity modes with and without disorder. In the limit of the inclusion of all the Bloch bands, it is equivalent to a GME simulation. The advantage of BME is that only modes that are closer to the frequency of interest need to be included and this computation can be only a few minutes on a personal computer. The BME computations have been verified for high Q cavities with increasing

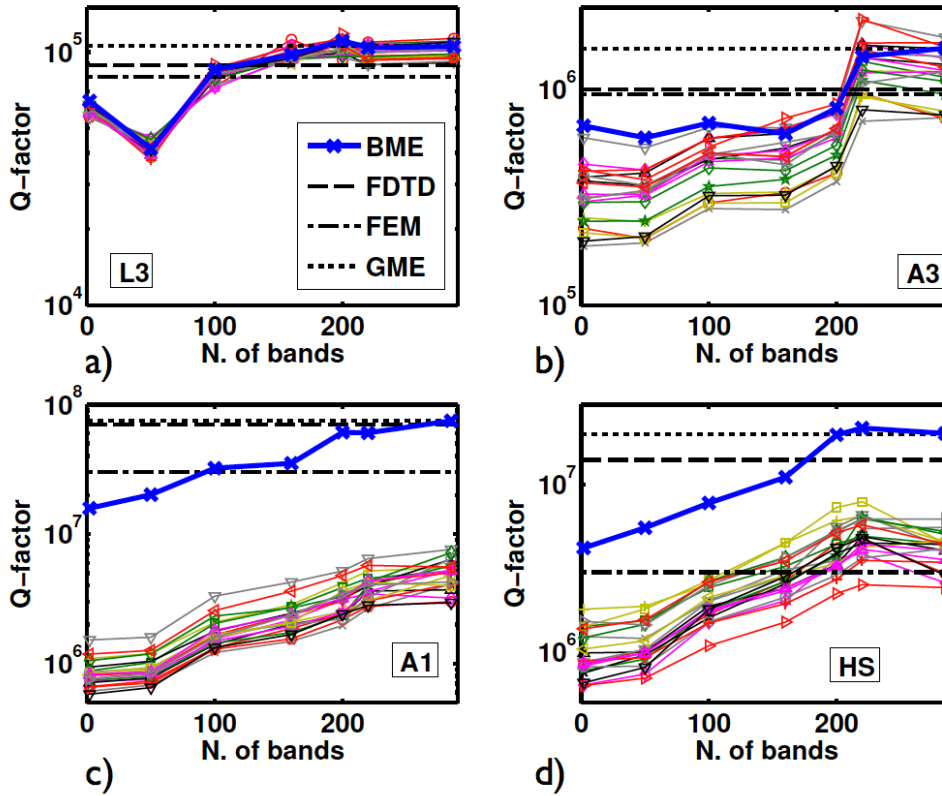


Figure 2.11: Calculation of cavity Q-factors with different numerical tools for four different cavity designs. a) L3 b) A3 c) A1 d) Heterostructure. *Reprinted from a publication from this thesis [129].*

number of Bloch bands as can be seen in figure 2.11. In the case of high Q-cavities, the BME method has to be used with caution, as there is an extremely delicate situation due to various interferences of the radiating modes. The figure shows GME and FDTD values taken from the corresponding publications of the cavities. FEM and BME values are compared against them. The BME and GME results were obtained for a supercell of length $32a$ ($24a$ for L3 cavity) in the x-direction and length $16\sqrt{3}/2a$ in the y-direction ($10\sqrt{3}/2a$ for the L3 cavity). As expected, when all bands are included, it can be seen that the BME and GME yield almost the same Q value, which is also in good agreement with the FEM and FDTD full simulation methods.

Chapter 2. Numerical investigations of PhC cavities

It is to be noted that only radiation loss based calculations are performed here and this has to be taken as the “ideal” Q-factor of the cavity. There is however, a similar trend in all the computations shown in this figure. The values of FEM are always more conservative than the FDTD and GME/BME. This effect is attributed primarily to the difference in calculation methodology and the application of boundary conditions. The FEM uses a first order scattering boundary condition, while the FDTD uses a perfectly matched layer condition that absorbs all incident radiation. The GME and BME methods use a periodic boundary condition as they are mode expansion methods.

In terms of computational cost, in order to obtain a converged Q-value using 3D FEM, when running on a single-core of a multiprocessor CPU, takes of the order of tens of hours and more than 100 GB or memory. The same computation with a 3D FDTD technique and GME is expected to take around 5 to 15 hours and several tens of GB of memory. On the contrary, a BME computation with only a few bands takes of the order of only several minutes with a memory of 1GB (on a personal computer), illustrating the potential of this method for large variety of problems. This is extremely useful especially in the case of disorder realizations that will be explained in a later section and in the case of cavity optimization to which, chapter 4 is dedicated to.

The knowledge of modal volumes is quite important to calculate various physical parameters. The definition of effective modal volume of a cavity is generally given as [157]

$$V_{eff} = \frac{\int \epsilon(r) |E(r)|^2 d^3r}{\max[\epsilon(r) |E(r)|^2]} \quad (2.24)$$

A second definition inspired from the inverse participation ratio that is more appropriate in some cases where the definition of mode volume is less sensitive to field distribution discontinuities but results in a larger value than the previous definition is given as:

$$V_{effnew} = \frac{(\int f(r) d^3r)^2}{\int f^2(r) d^3r} \quad (2.25)$$

where $f(r)$ denotes a positive valued function such as $\epsilon(r) |E(r)|^2$. The two definitions are compared for three cavity designs in table 2.3 where the difference is highest for the case of the slot cavity as it has the discontinuous field distribution at the slot boundaries.

Cavity	V_{eff} in μm^3	V_{effnew} in μm^3
Circular cavity [158]	0.21	0.36
Slot cavity [159]	0.053	0.51
Modified L3 cavity [160]	0.11	0.50

Table 2.3: Mode volume definition comparisons for a few PhC cavities.

2.4.4 Disorder in PhC cavities and the influence on Q-factor

The results presented in this section are originally published in “Statistics of the disorder-induced losses of high-Q photonic crystal cavities”, *Optics Express*, **21**, 28233 (2013) [129]

In many applications using photonic crystal cavities as explained in chapter 1, high quality factors are desired. Several ultra-high Q designs have been proposed in this context [144, 161–164] with numerical quality factors ranging from 10^5 to 10^9 . In all these works, the experimentally measured Q-factors have considerably fallen below the numerically computed value and this is attributed to the “disorder” present in the PhC lattice that arises due to fabrication imperfections. This disorder can manifest itself in the size of the air holes, shape of the holes, surface texturing of the slab and the position of the holes with respect to the cavity and this has been extensively studied previously [165–169]. It has been shown that the disorder induced cavity losses scale as σ^2 , where σ is the magnitude of the random fluctuations and is dependent on fabrication methods. It is also being agreed that this average value depends marginally on specific cavity designs. In the case of difference between shape disorder and area disorder, previous studies indicate that the shape dependence is much lesser than the size or position of holes [170, 171].

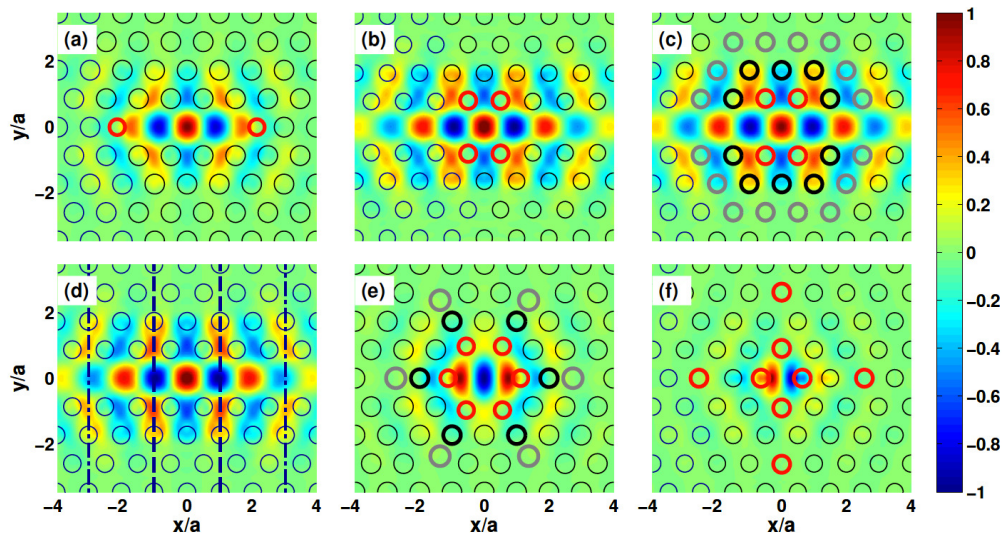


Figure 2.12: Guided mode expansion computation of field profiles of high-Q cavities. a) L3 design with the adjacent holes modified. b) A3 where the red coloured holes are shifted outward. c) A1 with the red, black and grey holes shifted outwards. d) Heterostructure where the dashed region corresponds to a squeezed lattice constant compared to the exterior part. e) Optimized H1: the holes marked in red are shifted outward. f) Optimized H0 where the eight holes marked in red are shifted symmetrically. **Reprinted from a publication from this thesis [129].**

In this context, the influence of disorder on six well-known cavity designs was investigated: L3 [161], A3 and A1 [144], Heterostructure (HS) [162], H1 and H0 [172, 173]. All the devices are based on the triangular lattice with holes etched in a silicon slab. GME computed field profiles are shown in figure 2.12 for all the parameters taken from their respective sources. For understanding disorder, random fluctuations were artificially introduced into the models on

the positions and radii of holes with an underlying Gaussian distribution with zero mean and standard deviation σ . There were no correlations between the disorder magnitudes of each hole in this model. The measured Q can be written as:

$$\frac{1}{Q} = \frac{1}{Q_i} + \frac{1}{Q_d} + \frac{1}{Q_a} \quad (2.26)$$

where Q_i is the ideal Q -factor of the cavity, Q_d is associated to disorder and Q_a accounts for absorption dependent losses. In the presence of disorder, there is additional light scattering into the light cone although there is also a possibility for the destructive interference of two disorder channels scattering light resulting in a negative value of Q_d . This leads us to believe that controlled and deterministic structural modifications can also dramatically increase the Q -factor post fabrication of the sample. The GME based Q calculation method allows to

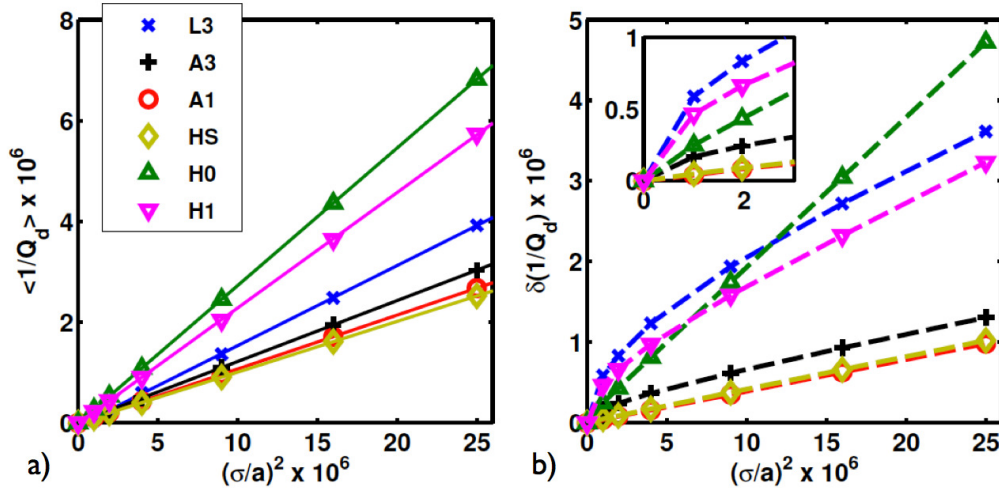


Figure 2.13: a) Dependence of standard deviation in ω on the magnitude of disorder σ . b) Dependence of the expectation value of $1/Q_d$ on σ^2 . **Reprinted from a publication from this thesis [129].**

drastically increase the amount of combinations of disorder that could be implemented in the calculation. This capacity is way beyond the reach of 3D finite difference or finite element solvers. For instance, in this case, 400 disorder realizations for each cavity were computed for each σ value of $0.001a$, $0.0014a$, $0.002a$, $0.003a$, $0.004a$, and $0.005a$. It was found that the frequency distribution was deviating slightly but centred around the ideal cavity frequency. The mean $\langle 1/Q_d \rangle$ and standard deviation $\delta(1/Q_d)$ are related as

$$\delta\left(\frac{1}{Q_d}\right) = \left(\left\langle \left(\frac{1}{Q_d}\right)^2 \right\rangle - \left\langle \frac{1}{Q_d} \right\rangle^2 \right)^{\frac{1}{2}} \quad (2.27)$$

This standard deviation is plotted against σ^2 for different cavities and is shown in figure 2.13. The results confirm the scaling $\langle 1/Q_d \rangle \propto \sigma^2$ that has been established before and this is confirmed for all the six cavities in study. The slope of the lines in figure 2.13 can be interpreted as the measure of the robustness of the cavity to disorder effects. It can be seen

2.4. Some numerical results obtained during this thesis

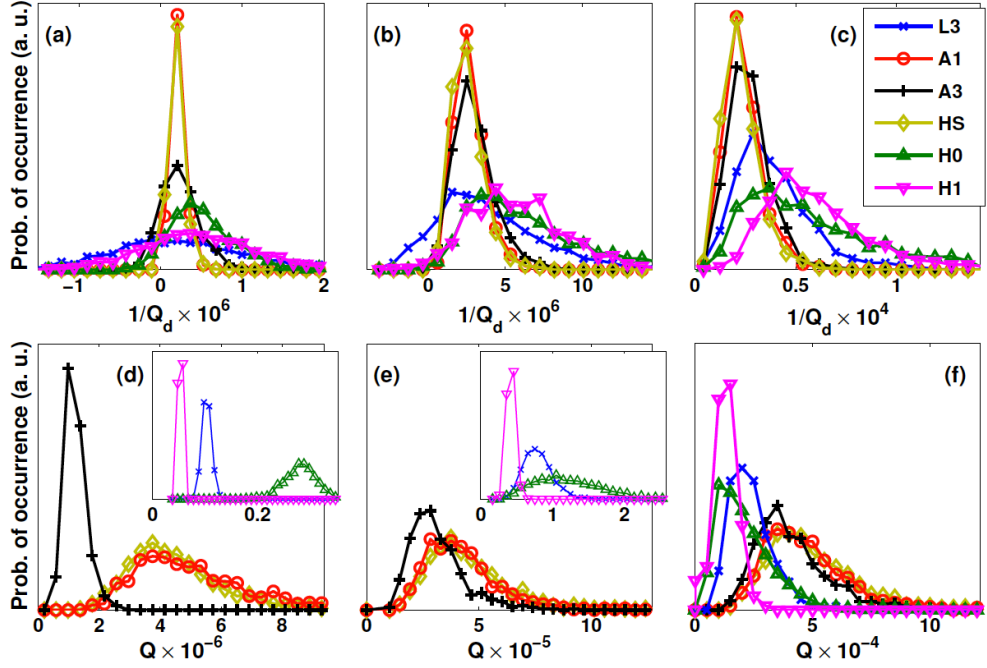


Figure 2.14: Histograms of quality factors with disorder for six different cavities computed with GME for 1000 disorder realizations with different values for σ . *Reprinted from a publication from this thesis [129].*

that this measure is inverse proportional to cavity mode volume. This leads us to affirm that if disorder induced losses are dominating, the full statistical distribution of those losses starts being design independent as can be seen in figure 2.14. The higher the disorder, the more similar all these cavities start behaving in terms of Q-factors. These results are quite important for the optimization of PhC cavity designs. The findings can be summarized as follows.

1. In the regime where the disorder induced losses are dominating ($Q_d < Q_i$), the statistics of $1/Q_d$ are approximately design-independent.
2. Theoretically optimizing Q_i is relevant only if the measured Q is not much smaller than Q_i .
3. The way to improve Q-factors in the above case is to rely on decreasing disorder or by exploring the high-Q tail of the probability distribution.
4. It must also be kept in mind that for extremely high nominal Q values, the measured value is limited by nonlinear effects and absorption.

In terms of purely optimizing the cavity for a better Q, it is imperative to consider all the positions of the holes and their respective radii, as they are inseparable. An ideal tool for optimizing cavities would be a global optimization tool that can evaluate all the weighting parameters. This will be explored in further detail in chapter 4.

2.5 Summary and outlook

The mode expansion methods were useful in the accurate prediction of band gaps, waveguide cut-offs, filling factor variations and slab thickness variations. These results allowed for accurate mask designs for the fabrication process resulting in measured wavelength variations less than 10 nm from the designed value in a large set of samples throughout this thesis. Such predictable accuracies allowed for the fabrication of only a minimum number of samples required for experimentation saving a great deal of time, cost and stress. A feedback loop from the fabricated structures also helped in predicting the etch-induced filling factor variations and diameter variations of the air holes.

The finite element methods on the other hand was very useful for computing cavity Q-factors, modal volumes and resonance wavelengths to a high degree of accuracy that matched experimental measurements. It allowed for realistic simulations of systems such as a motion of a single dielectric particle within a PhC cavity structure that assisted the understanding of perturbative effects and optical forces. The FEM was used in tandem with the mode expansion methods as a cross checking mechanism for the Q-factors obtained with the GME method in cases where ultrahigh Q-factor cavities (greater than a million) were computed. The usage of symmetry planes reduced the computational cost significantly and in combination with a cluster computing platform, a large number of parametric studies were also made possible.

In summary, this chapter has detailed the use of various algorithms and has showcased some of the results computed during this thesis. There is a strong criticism in the scientific community regarding the usage of numerical tools for the understanding of physical phenomena. As most of these methods have a “black-box” approach, the user has to take the additional responsibilities of cross-validating the results using first order analytical methods or phenomenological calculations. In the case of a possibility of experimental validation, this is the best preferred situation. A strong balance between numerical prediction and experimental validation is required for performing purposeful research especially in complex physical systems (like photonic crystals) where analytical formulations are simply not feasible.

3 Resonant optical trapping in hollow PhC cavities

This chapter describes the resonant optical trapping phenomena in 2D photonic crystal cavities. Section 1 outlines the physical basics and the historical development of optical trapping. Section 2 gives a concise description of the calculation of mechanical forces exerted on a particle placed in an electromagnetic field and introduces some concepts defining the optical trapping dynamics. Section 3 introduces the hollow cavities within the photonic crystal domain that could potentially be used for optical trapping. Section 4 shows all the numerical and experimental results obtained during this work including resonant trapping, particle-cavity perturbation and particle-cavity back-action in a hollow circular photonic crystal cavity. Section 5 offers additional insights into the contributions from this chapter and compares the results with other trapping platforms.

Contributions:

This work was performed as an in-house collaborative effort between the students of my research group. I contributed to the finite element modelling of the cavity Q-factors, device layout design for the sample and the optical trapping force computations. The experimental apparatus along with the microfluidic circuit was conceived and constructed by Dr. Nicolas Descharmes assisted by Mario Tonin. Dr. Zhaolu Diao fabricated the silicon photonic crystal devices.

Publication of results:

The results obtained during the course of this research work are published in [123–125].

3.1 Optical trapping: The physics and the history

Light, in all forms, including the form that we receive from the sun carries both energy and momentum. This energy can be felt through the warmth that we feel in our body or in the case of plants, this energy is used to initiate the process of photosynthesis. It was not very well understood until recently that light also carried momentum. The initial observation and postulation of this effect is generally credited to Johannes Kepler, who in 1619 offered an explanation to the presence of comet tails that were pointed away from the sun as can be seen in a recent photograph of the ISON comet tail acquired by NASA (figure 3.1). In this picture, a combination of solar radiation and solar wind pushes the smaller disintegrated particles from the comet's surface forming this tail. However, this explanation was incomplete until 1873, when Maxwell predicted the existence of the so-called "radiation pressure" from his electromagnetic field equations. Radiation pressure is the pressure exerted upon any surface upon which there is an electromagnetic radiation. It can be visualized as the change in momentum when a photon strikes a surface on its path. Lebedev achieved the first experimental validation of this concept in 1901 by using light from a focused arc lamp. The quantity of radiation pressure possible at this time was quite limited due to the absence of intense light sources for experimentation. For example in a simple case of a reflecting mirror, for 1 Watt of light, the force experienced by the mirror are of the order of a few nanonewtons that makes it extremely small to measure.

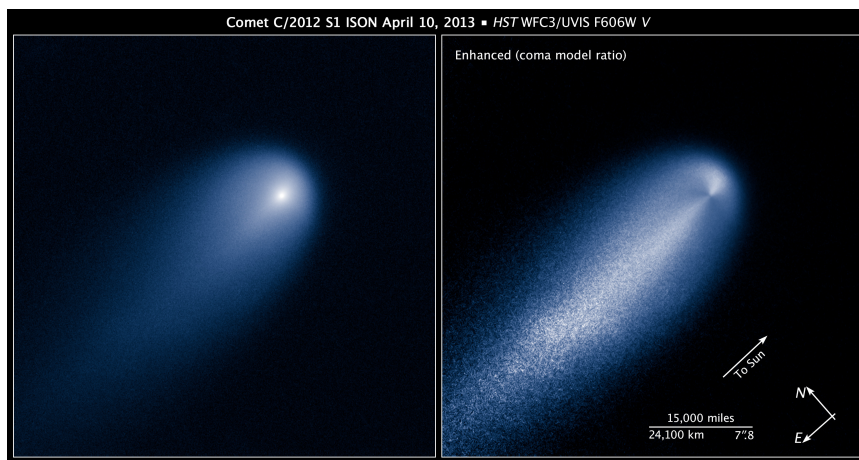


Figure 3.1: Radiation pressure witnessed in a comet tail. The tail of the comet ISON is seen pointed away from the sun in clearly captured file photograph from NASA [174] indicating the radiation pressure induced by the optical energy of the sun. The image on the right is an enhanced version of the left side image.

The goal of extending this phenomena to microscopic dimensions required the use of a highly focussed beam of light and this was only possible after the achievement of the laser in the 1960s [61]. Following this development, Ashkin showed in his first seminal work in 1971 [175] that radiation pressure from a laser could be used to accelerate micrometer sized dielectric particles. In his initial experiments, the particles were guided by the effect of radiation pressure. The particles were suspended in water to avoid heating issues. Along with this effect, it was

3.1. Optical trapping: The physics and the history

also seen that the particles near the exterior of the laser beam were pulled towards the center. It was understood that there were two force components under play in this phenomenon, a scattering force (F_{scat}) along the direction of the incident beam and a gradient force (F_{grad}) along the intensity gradient of the laser beam. The vector sum of these forces allowed for either acceleration or deceleration of these microscopic particles. This was the case for particles whose refractive index was larger than the surrounding environment and also whose size was larger than few times the wavelength of light. In the case of particles whose index was smaller than that of the surrounding medium, the gradient force direction was inverted and pushed the particles towards the periphery of the beam. To demonstrate this effect, μm sized air bubbles in a solution of glycerine were used [176]. They also later showed that these particles can also be confined in three dimensions using two opposing laser beams. The opposing signs of the scattering force components was used to hold the particle axially while the gradient forces of the beams that were also symmetric helped restoring the particle in the transverse direction.

A second breakthrough work [177] was reported by Ashkin and co-workers where a particle was stably held with the aid of a single focussed laser beam as shown in figure 3.2a. This was the first time when a single particle was stably held in free space in a stable position through optical means. This phenomena was termed as "Optical Tweezing" or "Optical Trapping" and has revolutionized the field of micro-manipulation ever since, particularly for the handling of biological specimen such as viruses, bacteria and cell-organelles [178, 179].

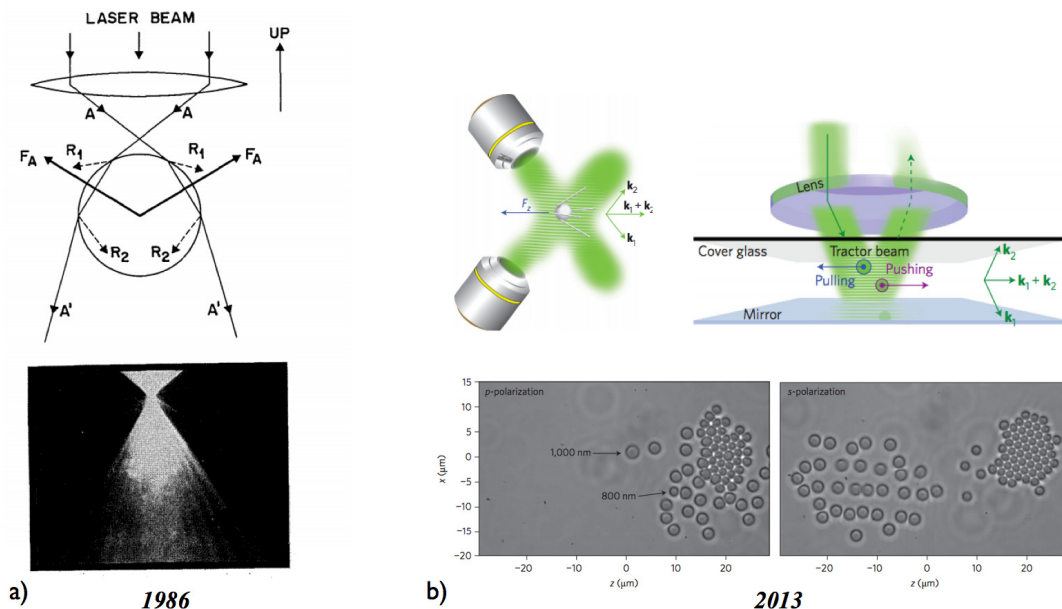


Figure 3.2: Evolution of the single beam gradient trap. a) The illustration of the first gradient trap by Ashkin along with the experimental photograph of a $10 \mu\text{m}$ sphere trapped in water from 1986 [177]. b) The illustration of a tractor beam trap showing the polarization dependent forces and the sorting of dielectric particles from 2013 [180].

Chapter 3. Resonant optical trapping in hollow PhC cavities

This formed the basis of a large spectrum of trapping studies that lead to the development of laser cooling of atoms by Steven Chu [181] and the subsequent creation of Bose Einstein condensates by Wolfgang Ketterle [182]. Both these achievements lead to the winning of the Nobel prize in physics for 1997 and 2001 respectively. Since then, the single beam gradient trap has been investigated and developed extensively. The evolution of this exciting field of study starting from the first work in 1986 to a recent development in 2013 where novel tractor beam traps have been used for polarization dependent sorting and separation of dielectric particles can be seen in figure 3.2. A detailed review of various possible tweezers techniques and their applications can be found here [183].

In order to obtain a stable three-dimensional trap, the axial gradient force must exceed the scattering force component. In standard optical tweezers, this is achieved by increasing the focusing of the trapping laser as much as possible through the incorporation of high numerical aperture objectives. It was observed that the trapping of small particles became cumbersome, as prohibitive input powers were required as the diffraction limit was reached. This was also the juncture during which the technologies for fabricating well defined micro and nano-optical structures emerged. This opened the possibility to engineer highly intense fields in these structures with very low optical powers. The sub-wavelength spatial dimensions allowed for increasing the gradient force while not augmenting the scattering components in comparison with a standard optical tweezer. It also opened up the path for making highly integrated optical trapping platforms leading to lab-on-chip type systems primarily involving either plasmonic devices, integrated waveguides or optical microcavities as shown in figure 3.3.

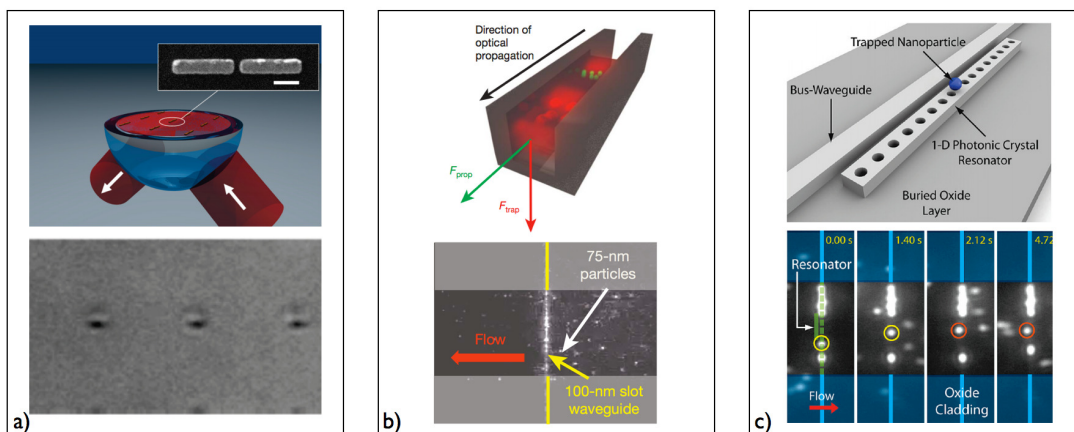


Figure 3.3: Overview of integrated trapping platforms from the literature. a) Plasmonics based trap where gold nanoantennas are periodically arranged. Light is coupled through a hemispherical glass lens. Bottom image shows the trapping of E-coli bacteria. [184]. b) Slot waveguide illustrating the transport of particles using the radiation pressure force. Bottom image shows the trapping of 75 nm sized polystyrene particles over 100 nm slot waveguides. Reprinted from [185]. Optical microcavity trap based on a 1D photonic crystal nanobeam cavity along with a coupling waveguide for the transport of particles is illustrated. Bottom image shows the trapping of a 500 nm-sized particle on the cavity (red circle) after it was transported by the bus waveguide. Reprinted from [186].

Plasmonics based traps

In earlier works regarding plasmonic traps [187–189], it was predicted that trapping of dielectric objects sized less than 100 nm was possible near sharp metallic tips or nano-apertures using the evanescent waves from the near-field landscape. The first experimental studies were based on gold based surface plasmon polariton modes that were used to trap micron size dielectric particles [190, 191]. The integration of microfluidic circuit to the plasmonic structures [192] was followed by experiments involving biological particles such as bacteria as shown in figure 3.3a [184] and proteins [193].

Waveguide based traps

Nanophotonic waveguides have the capacity to confine light in the higher index dielectric while the evanescent radiation is still present in the low index cladding medium. This was first investigated in a report by Kawata and co-workers [194] where they showed trapping of both metallic particles (0.5 to 1 μm in size) and dielectric particles (1 to 5 μm). The light in the waveguide was also used for the propulsion of the particles and transporting them within the structures as shown in subsequent works [195–197]. The limited overlap of the evanescent mode with the surrounding medium prompted the use of slotted nanostructures as introduced by Almeida and co-workers [198]. The slotted waveguide was implemented and used for trapping 75 nm-sized particles by Yang and co-workers [185] as shown in figure 3.3b. They also showed the trapping of DNA strands using the same device. This was a first demonstration where a hollow structure in the integrated form was used to achieve optical trapping.

Optical microcavity based traps

Optical cavities made from micro and nanostructured materials have the ability to confine electromagnetic radiation in sub wavelength dimensions resonantly. In the case of standard optical tweezers, the particles do not influence the tweezers beam frequency, which is not the case when a resonant trap is involved. This property is expected to give rise to interesting physical mechanisms and trapping behaviours, which is the subject of the investigation of this thesis as will be reported in the next few sections. The initial demonstration of such a microcavity based trapping came from Lin and co-workers [199] where a silicon microring resonator and the corresponding whispering gallery mode was used to trap 500 nm sized particles with input powers as low as 5 mW. Similar ring resonator cavities integrated with microfluidic channels transporting and trapping micro particles were also reported [200, 201]. The first report of using a 1D PhC cavity in the form of a nanobeam was published by Mandal and co-workers [186] where they could trap particles of 48 and 62 nm in diameter. This device is also illustrated in figure 3.3c. A similar nanobeam cavity trap was reported by Renaut and co-workers [202] to study a cluster of microspheres.

3.2 Calculation of optical forces in an optical trap

The various ways to determine the optical forces acting on a particle in an optical field depend primarily on the diameter of the particle and the wavelength of electromagnetic radiation. In all cases, the understanding of the scattering and gradient components of the forces is crucial.

3.2.1 Optical forces: Ray optics approximation

In the case of particles whose diameter is much larger than the wavelength of light ($D > 10\lambda$), the ray optics approximation is sufficient to describe the forces. This was also the detailed explanation offered by Ashkin in the case of the first trapping experiment [203]. The input laser beam can be broken down into several individual rays with their own intensity and momentum. Each of these rays can then be treated in a separate manner. In a linear and non-dispersive medium, the rays can propagate as a straight line and their behaviour can be well described by the rules of geometric optics and the particle can be considered as a weak lens. If a light beam carries a linear momentum h/λ , the refraction of light by the weak lens will cause a change in momentum and hence a corresponding reaction force described by the Newton's third law acts on the object as illustrated in figure 3.4.

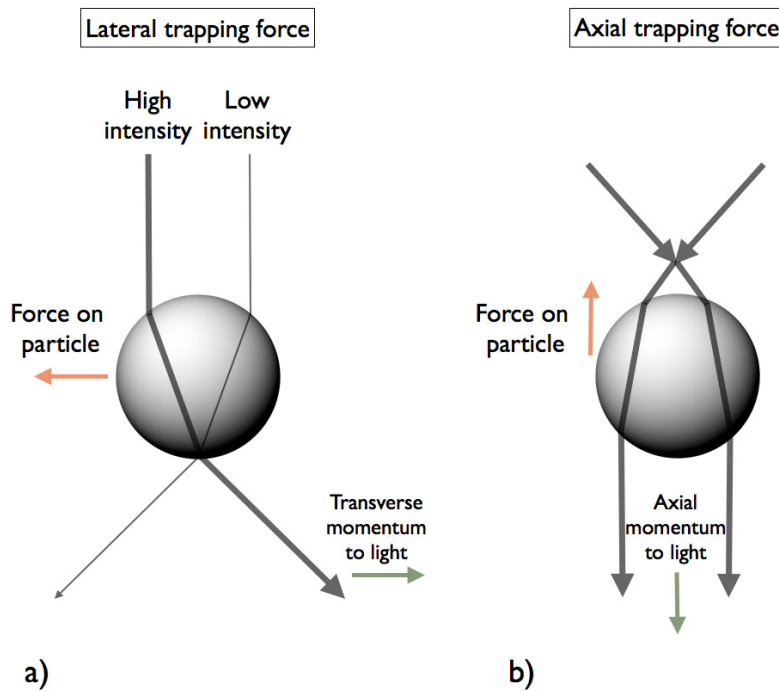


Figure 3.4: Ray optics description of trapping forces. a) The direction of the force on the particle when there is a gradient in the input beam intensity and the lateral trapping force is shown acting in opposite direction of the momentum imparted to light b) The direction of the force on the particle when a particle beyond the focus of a beam finds an axial momentum imparted to light that causes a reaction force, which in turn pushes the particle towards the focal point.

3.2. Calculation of optical forces in an optical trap

The light reflected from the particle, on the other hand will push the particle forward. The reflection depends on the relative refractive index between the particle and the surrounding medium. In the case of a dielectric particle, it is sometimes easier to trap in water than in the air because of the fact the stronger reflections between the particle and air can cause a stronger scattering component. The effect of the multiple rays can then be summed vectorially in order to obtain the total force. It has to be noted that the scattering force acts in the beam direction while the gradient force acts towards the beam focus and so in the case of a beam directed downwards, the stable optical trapping lies just below the focus of the beam. By taking into account all the angles of reflection and refraction of the incident beam, a trigonometric evaluation of the scattering (F_{scat}) and gradient force (F_{grad}) components for each individual ray can be performed [203].

$$F_{scat} = \frac{nP}{c} \left(1 + R_F \cos(2\theta_R) - \frac{T_F^2 (\cos(2\theta_R - 2\theta_T) + R_F \cos(2\theta_R))}{1 + R_F^2 + 2R_F \cos(2\theta_T)} \right) \quad (3.1)$$

$$F_{grad} = \frac{nP}{c} \left(1 + R_F \sin(2\theta_R) - \frac{T_F^2 (\sin(2\theta_R - 2\theta_T) + R_F \cos(2\theta_R))}{1 + R_F^2 + 2R_F \cos(2\theta_T)} \right) \quad (3.2)$$

where θ_R is the angle of reflection, θ_T is the angle of transmission, n is the refractive index of the medium, P is the optical power of the beam, c is the velocity of light and R_F and T_F are Fresnel coefficients. As mentioned before, the ray optics approach works very well for a spherical particle in a non-dispersive medium whose size is much larger than the wavelength of light used. For non-spherical shapes of particles, several additional approximations are required to take these additional scatterings into account.

3.2.2 Optical forces: The dipole force approximation

If the particle diameter is much smaller than the wavelength of light, the dipole approximation is used to describe the forces. In this case, the beam is uniform all over the particle and it can be considered as a collection of dipoles. When a single dipole is placed in a uniform electromagnetic field \vec{E} , it creates a response due to the polarizability of the material (α). This response is an induced dipole moment \vec{p} and is given as

$$\vec{p} = \alpha \vec{E} \quad (3.3)$$

Taking the polarizability from the Clausius-Mossotti relations, this dipole moment can then be written as

$$\vec{p} = 4\pi n_{medium}^2 \epsilon_0 r^3 \left(\frac{N^2 - 1}{N^2 + 2} \right) \vec{E} \quad (3.4)$$

where N is the refractive index ratio given by $n_{particle}/n_{medium}$ and ϵ_0 is the free space permittivity. This dipole will experience a Lorentz force that eventually gives rise to the

gradient force component, which is written as [204]

$$\vec{F}_{grad} = (\vec{p} \cdot \nabla) \vec{E} \quad (3.5)$$

$$\vec{F}_{grad} = \pi n_{medium}^2 \epsilon_0 r^3 \left(\frac{N^2 - 1}{N^2 + 2} \right) \nabla |\vec{E}|^2 \quad (3.6)$$

In the case of the scattering force component, the induced dipole moment oscillates with the field and the particle acts like an antenna radiating waves in all directions. These scattering events can influence the magnitude and direction of the total field. The corresponding changes in momentum are then exerted as a scattering force on the particle. This can be found by taking the scattering cross section of the dipole and the intensity of the incident field whose wavenumber $k = 2\pi/\lambda$ and can be written as [204]

$$\vec{F}_{scat} = \frac{8\pi n_{medium} k^4 r^6}{3c} \left(\frac{N^2 - 1}{N^2 + 2} \right) I \quad (3.7)$$

It can be seen from the above expressions for the gradient and scattering forces that they scale very differently with the radius of the particles. In addition, in a standard Gaussian beam trap, the scattering component is a non-conservative force while the gradient component arises from a conservative potential. This has significant implications on the physics of the system in this thesis that will be touched upon in the discussion section.

3.2.3 Optical forces: The Maxwell Stress Tensor Formalism

The ray optics formalism works well for particles whose size is $\gg \lambda$ and the dipole force approximation works well for particles whose size is $\ll \lambda$. However, in practical experiments, it is rather hard to fall in either of these two regimes and hence a full field analysis is the only solution to obtain an accurate description of the optical forces. This is indeed the case of our experimental study where 500 nm-sized polystyrene particles are used at a wavelength of 1.55 μm and hence the maxwell stress tensor formalism needs to be used.

The formalism can be derived as follows. Starting from the Maxwell's equations in a linear isotropic material system as shown in chapter 1, we can write the Lorentz force acting on a distribution of charges with density ρ in a volume V as

$$\vec{F} = \int_V [\rho \vec{E} + \vec{j} \times \vec{B}] dV \quad (3.8)$$

This force law connects the electromagnetic field to the mechanical properties, most importantly the momentum. After performing standard vector calculus substitutions on the Maxwell's equations, we can write the expression [205]

$$\nabla \cdot [\epsilon_0 \vec{E} \vec{E} - \mu_0 \vec{H} \vec{H} - \frac{1}{2} (\epsilon_0 E^2 + \mu_0 H^2) \hat{I}] = \frac{d}{dt} \frac{1}{c^2} [\vec{E} \times \vec{H}] + \rho \vec{E} + \vec{j} \times \vec{B} \quad (3.9)$$

3.2. Calculation of optical forces in an optical trap

The expression on the left hand side of the above equation is termed as the Maxwell's Stress Tensor (MST) and is given by T . Integrating this tensor over a volume V surrounding the particle and after applying the Gauss's law of integration, we can obtain

$$\int_V \nabla \cdot T dV = \int_{\partial V} T \cdot \hat{n} ds \quad (3.10)$$

From here, we can define the mechanical and electromagnetic field momenta as

$$\vec{F} = \frac{d\vec{P}_{mech}}{dt} \quad (3.11)$$

$$\vec{P}_{field} = \frac{1}{c^2} \int_V [\vec{E} \times \vec{H}] dV \quad (3.12)$$

This allows us to write the conservation law for linear momentum as

$$\int_{\partial V} T \cdot \hat{n} ds = \frac{d}{dt} [\vec{P}_{field} + \vec{P}_{mech}] \quad (3.13)$$

The electromagnetic field momentum vanishes when averaged over time. The average force can then be written from equations 3.11 and 3.13 as

$$\langle F \rangle = \int_{\partial V} \langle T \rangle \cdot \hat{n} ds \quad (3.14)$$

The above equation is very powerful as it can allow the calculation of mechanical forces acting on any arbitrary body within this closed volume. The time averaged force is entirely the result of the electric and magnetic fields on the surface enclosing this volume. The material properties of the particle surprisingly do not appear in this formulation. However, it does indirectly appear while taking the full field that includes the incident and scattering fields. This fact is important in order for this calculation to work properly. Several numerical methods have been developed for this purpose including the FDTD and FEM. In the case of our experiment, the fields of the photonic crystal cavity along with a particle are calculated in detail with a finite element solver. The MST is then evaluated on the surface of the sphere that is present within the cavity volume in order to obtain the optical forces present in the system.

3.2.4 Optical trapping dynamics

When the focus of the laser input beam is increased, the intensity gradient increases and the axial gradient force becomes stronger than the scattering force component, resulting in a stable optical trap. It is not the case always as there is an additional force due to the Brownian motion of the particle. The thermal kinetic energy associated with Brownian motion is given by $k_B T$, where k_B is the Boltzmann's constant and T the temperature.

This energy has to be overcome by the depth of the optical trapping potential well as illustrated

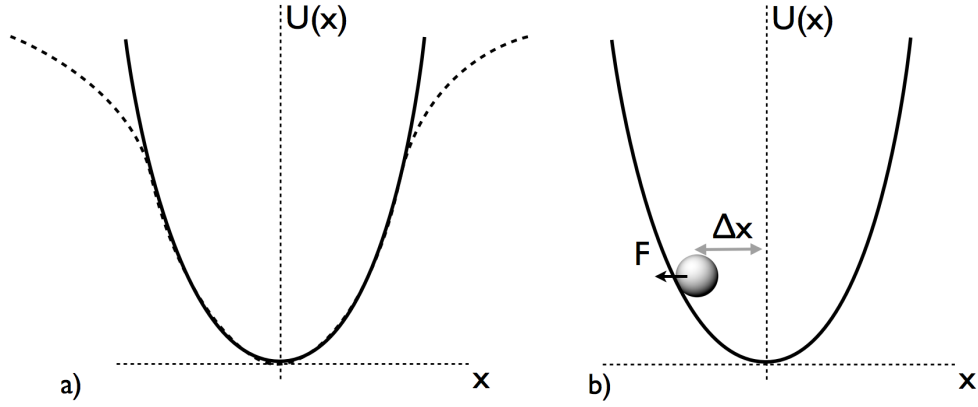


Figure 3.5: Illustration of the trapping potential and forces. a) In typical circumstances, the potential can be approximated by a harmonic potential well as illustrated. b) The harmonic potential gives a linear relationship between the trapping forces and the particle displacement as indicated. A steeper potential well results in a an increase in the slope of the linear force-distance curve and hence stiffness.

in figure 3.5, which is generated by a conservative gradient force. This potential energy of the trap can be derived by integrating equation 3.5. The trapping potential (U) is then given by [204]

$$U = \frac{-2\pi n_{medium} r^3}{c} \left(\frac{N^2 - 1}{N^2 + 2} \right) I + C \quad (3.15)$$

where C is an arbitrary integration constant. In the context of the Brownian motion of the particle, the effect of the drag force is also to be overcome by the trapping potential well. This viscous drag force due to the dynamic viscosity η and particle velocity v is given as

$$F_{drag} = -6\pi\eta r v \quad (3.16)$$

The physical influence of the trapping potential resulting in the constraining of the Brownian motion of the particle. The equation of motion describing the particle in a trap is given as

$$m \frac{dx^2}{dt^2} + \gamma \frac{dx}{dt} + \kappa x = \zeta \quad (3.17)$$

where m is the particle mass, γ is the friction coefficient coming from the drag force ($6\pi\eta r$) and ζ representing the forces due to Brownian motion due to the thermal collisions. The third term on the left hand side represents the influence of the optical trap. By neglecting the contribution of inertial effects in these spatial scales, an expression for power spectral density (PSD) of the particle's motion is given by [206]

$$PSD(\omega) = \frac{2k_B T / \pi \gamma}{\omega_c^2 + \omega^2} \quad (3.18)$$

3.2. Calculation of optical forces in an optical trap

The PSD is shown as a function of frequency for the case of an optically trapped bead in figure 3.6. The two different regimes (trapping and diffusive) are clearly seen. The low frequencies are flat due to the stiffness of the trap and the transition point is determined by the cut-off frequency(ω_c) which comes from the stiffness of the trap that is derived from the potential well. The higher frequencies are dominated by diffusion of the particle and later by high frequency noise. This plot is often used as a primary means of calibration and characterization of an

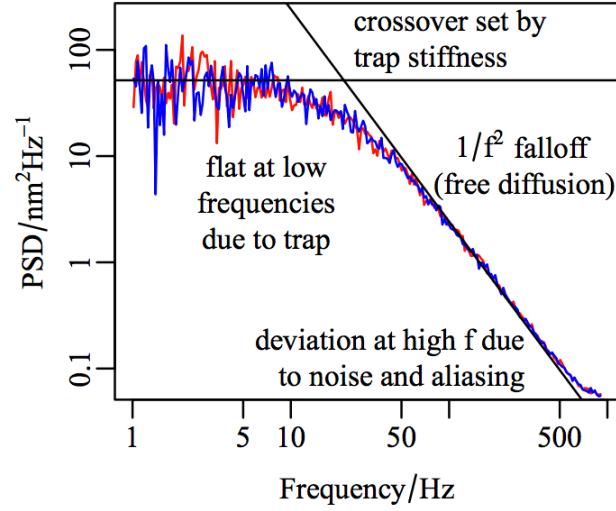


Figure 3.6: Power spectral density of a trapped particle's motion indicating the different regimes and the cut-off frequency that is set by the stiffness of the trap (κ). Reprinted from [206].

optical trap. This method allows for the estimation of trapping stiffness by using the relation:

$$\kappa = \omega_c \gamma \quad (3.19)$$

The stiffness information can be gathered only knowing the viscosity and particle size in this case and not the actual displacements involved, which can be challenging to measure in the case of smaller particles. In cases where the absolute position of the particle is tracked (for example, centroid method), the equipartition theorem can be used to estimate the stiffness as:

$$\kappa = \frac{k_B T}{\langle x^2 \rangle} \quad (3.20)$$

Both the above methods can be applied for the same system for validating the stiffness obtained or it can also be used to estimate the viscosity of an unknown environment. The stiffness depends also on the shape and size of the particle, laser power used, refractive index contrast between the particle and the fluid and temperature. To have a figure of merit, in the case of a spherical particle of diameter 500 nm and refractive index 1.57, the in-plane trap stiffness was experimentally determined as 14.6 pN/ μm and 21.1 pN/ μm for the x and y axis respectively. In both these cases, the input laser power was set at 10 mW [207].

3.3 Hollow photonic crystal cavities for integrated optical trapping

Photonic crystals are periodic nanostructures well known for their confinement properties of light as explained in the first two chapters of this thesis. Light confined in smaller dimensions can be very useful for applications that require large gradients of electromagnetic fields in sub-wavelength spatial dimensions. The previous section has clearly illustrated the need for increasing gradients with very low optical powers as much as possible to be able to trap smaller particles efficiently and non-invasively. PhC cavities, with their field confinement and the resulting gradients are promising candidates for such on-chip optical trapping studies amongst the various possible integrated schemes. In general, cavities in photonic crystals confine light in the medium with higher refractive index region, for example, in silicon. In the case of particle trapping, it would be beneficial to tailor the cavity modes such that the light is more confined in the lower index dielectric. Such cavities are hereby referred to as “Hollow photonic crystal cavities” (HPhC) synonymous to the hollow-core fiber terminology. These cavities are more suitable for trapping as they have a maximum field overlap with the lower dielectric medium where the particles are expected to be present and moreover they provide an in-plane geometric confinement along with a possibility of a symmetric gradient in the vertical direction. Two cavities that belong to this HPhC family are studied in detail during the course of this thesis.

3.3.1 Circular cavity

Mode profile of the cavity

The circular cavity is illustrated and shown in figure 3.7a and is one of the primary candidates amongst hollow cavities for optical trapping. This interesting cavity has also been explored by various other research groups [158, 208, 209] in previous studies. The FEM computed electric field distribution along with the SEM image of the structure is shown in figure 3.7b and c respectively. The defect diameter is approximately 700 nm while the other holes have a diameter of 250 nm. The slab thickness is set to 220 nm and the lattice constant is chosen to be 420 nm in order to obtain the resonance wavelength in the required range of operation (1.47 to 1.66 μm) that is imposed by the measurement apparatus.

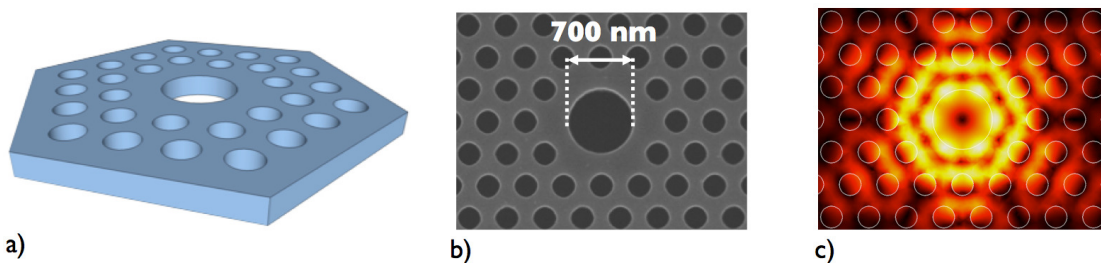


Figure 3.7: The circular cavity for resonant trapping. a) A graphic illustration of the device b) Scanning electron micrograph image of the fabricated cavity c) Finite element methods computed electric field distribution inside the cavity. *Reprinted from a publication from this thesis [125].*

3.3. Hollow photonic crystal cavities for integrated optical trapping

The formation of confined modes inside a photonic crystal cavity defect was detailed in chapter 1. In the case of a circular cavity as shown in figure 3.7, multiple modes are obtained as a result of the geometry and symmetry of the structure. In order to visualize these modes, a PWE method was employed to calculate the mode profiles lying within the bandgap of such a triangular lattice with all the before-mentioned parameters.

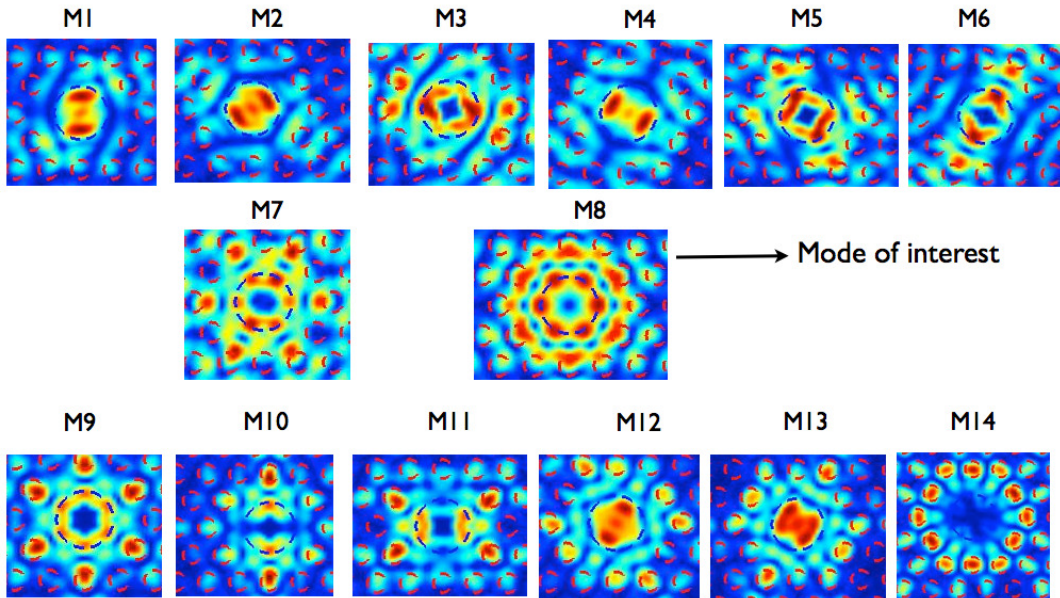


Figure 3.8: *In-plane electric field distributions of the multiple modes of a circular cavity computed with a plane wave expansion method. The modes are numbered in an increasing order of resonance wavelength. The mode that is of interest to our experiment is pointed out and is termed as M8.*

These modes are numbered (M1, M2, ..M14) in the ascending order of their resonance wavelength and are displayed in figure with their corresponding mode distributions. The mode of interest (M8) is chosen because of the combination of its high Q-factor and overlap with lower index medium as will become evident later in this chapter. Meanwhile, it is also necessary to understand the nature of all these modes in detail.

As explained in chapter 1, the symmetry of the system determines the nature of these modes. The circular defect in the lattice together with the bulk possesses a hexagonal symmetry and this is expected to be reflected in all the defect mode profiles in figure 3.8. This is visually evident only in the case of modes M7, M8, M9 and M14. In the case of all the remaining modes, the subset of degenerate modes also preserve symmetry. These degenerate pairs can be for example, M1 and M2 or M5 and M6. The orientations of these mode profiles can hence be not fixed, as they are degenerate. The mode spacings of these multiple modes were also computed with FEM and it was found that the non-degenerate modes had very distinct resonance wavelengths and were well-separated from each other while the degenerate pairs had the same frequency.

Effect of infiltration of water

In the context of investigating the circular cavity for optical trapping in an aqueous medium, it is important to check the optical properties of these devices after infiltration. The eigenmodes of the photonic crystal are perturbed when there is an addition of high refractive index content over the photonic crystal lattice. In the case of water, the global index increase causes a decrease in the refractive index contrast. This results in a corresponding decrease in the confinement of light and hence the quality factor. In the case of such a slight perturbation of the index, the eigenfrequencies displace towards the dielectric band edge resulting in a red shift of the resonance wavelength. This red shift of the wavelength is also related to the fact that there was partial or complete infiltration of the membrane and the holes. The changes in quality factors and resonance wavelengths due to infiltration (refractive index of water = 1.33) were computed with FEM and are shown in table 3.1. It can be seen that the farthest shift of 48 nm in wavelength occurs only for the case of complete infiltration. The table also shows an unusual increase in Q-factor in the case of water only inside the circular defect. This observation is attributed to two possible explanations.

1. The presence of water only in the defect results in a slight increase in the local refractive index that creates a gentler perturbation resulting in a increased confinement of light.
2. The loss components lying outside the air light line are altered in the presence of water in the defect leading to reduction in these components outside the water light line.

These observations were also reported and experimentally verified with a specialized apparatus to inject water into individual holes of the photonic crystal in a previously reported work by Intonti and co-workers [209] where this property was also used to selectively tune the cavity resonance wavelength.

Infiltration condition	Q-factor	Resonance wavelength (nm)
Air everywhere	7600	1545
Water everywhere	3300	1593
Water only in circular defect	8700	1553
Water in all holes	8800	1567

Table 3.1: Infiltration of water in the circular cavity. The effects of full and partial infiltration of water were numerically computed with finite element methods.

In order to experimentally verify the predictions of water infiltration on the cavity, the samples were infiltrated with a syringe based “local infiltration method” as shown in figure 3.9 during the initial days of the experiment. A hand-operated syringe was used to create a hanging droplet that was slowly deposited on the sample surface. There was a delay of a few seconds before each hole in the sample was infiltrated completely. The meniscus of the water droplet can also be seen in the photograph image shown in figure 3.9. The syringe infiltration method

3.3. Hollow photonic crystal cavities for integrated optical trapping

was used as a characterization tool but could not be further used for particle injection because of a number of compelling drawbacks.

- The droplet had an evaporation time of about 25 minutes that significantly reduced the possibility to conduct controlled and repeatable optical experiments.
- In some of the devices, the receding of the droplet during evaporation destroyed the waveguides and membranes either partially or completely along with the deposition of particulate content on the coupling fibers.
- The total lifetime of the sample deteriorated due to this method resulting in not more than 20 to 30 successful infiltration attempts.

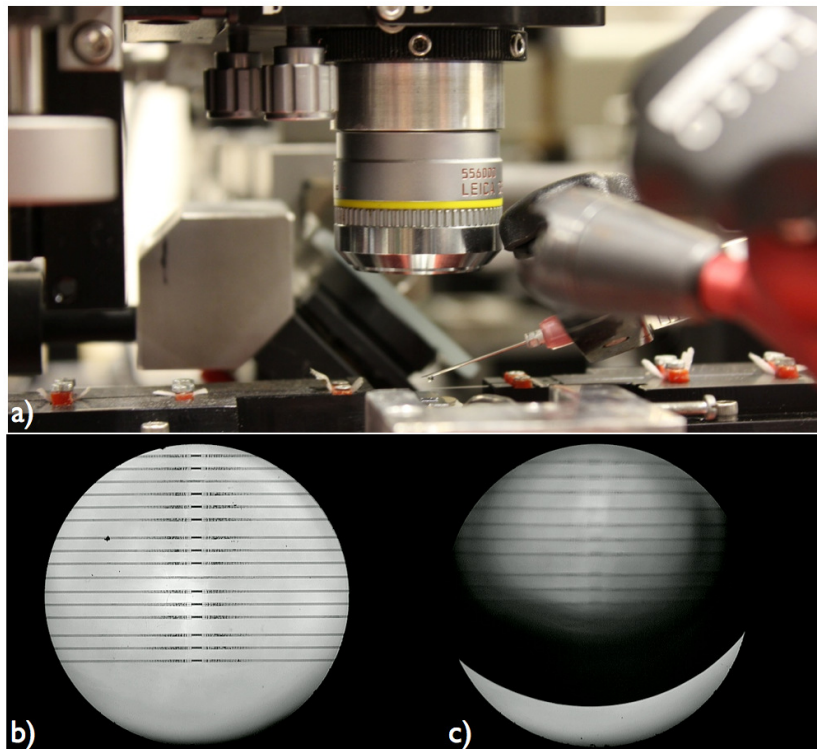


Figure 3.9: Water infiltration over the circular cavity. a) Photograph showing the basic droplet infiltration scheme implemented with a syringe. b) and c) Sample with the circular cavity devices being infiltrated before and after. The meniscus of the droplet can be seen indicating complete infiltration.

These problems were solved by the introduction of a custom-designed microfluidic membrane with pressure controls designed and built by Dr. Descharmes during his thesis work [124]. These membranes were employed for later experimental studies with the trapping of particles. The local infiltration of the droplet was simultaneously tracked with the help of the measurement of the optical transmission as shown in figure 3.10. The transmission of the cavity in atmospheric environment (is shown in red) shows a Q-factor of about 3500 around 1564 nm

in wavelength. After infiltration with the droplet, with sufficient time given to infiltrate, the broadening of the cavity resonance with a drop in Q-factor of about 800 is observed. The resonance shift in this case is around 39 nm and is seen at 1603 nm. The onset of evaporation instantaneously starts to blueshift the mode and it settles down at 4 nm redshifted than the previous value. A slight increase in Q-factor is also seen in this case and is attributed to the fact that there is a slight presence of water molecules in the holes or the circular defect. These measurements are in good agreement with the predictions of the FEM calculations of table 3.1.

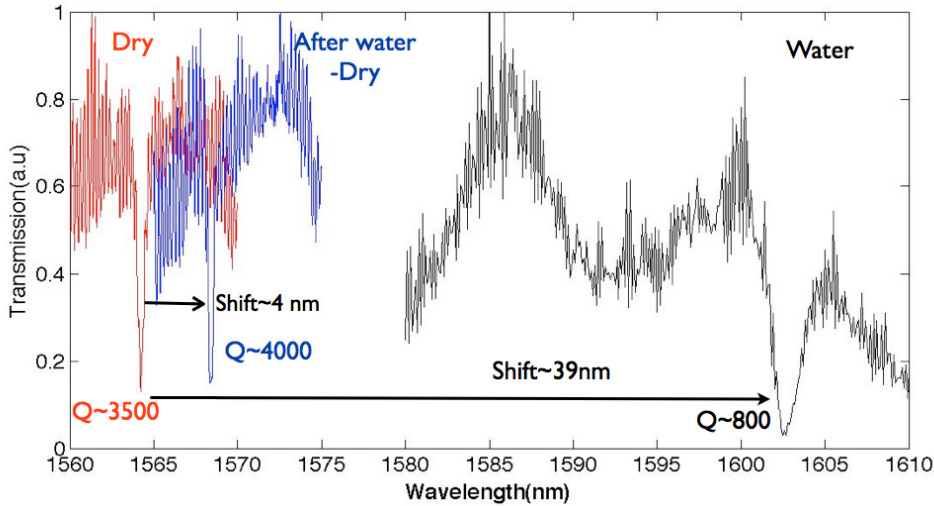


Figure 3.10: Initial experiments of water infiltration in the circular cavity using the local infiltration method. A shift of approximately 39 nm is recorded in this case with a decrease in Q-factor from 3500 to 800. A slight red shift after evaporation can also be observed indicating possible presence of water only in the holes.

The shift measurements in water are very specific to the cavity design parameters and it has been observed over numerous measurements that this number varies from 35 nm to 47 nm between different devices for the shift of resonance wavelength. This is attributed to the fact that a change in the diameter of the circular defect induces small variations in the field overlap ratio that results in a different shift value every time.

Behaviour of neighboring modes

As the circular cavity is a multiple mode system, it is important to ascertain the presence of the other modes in the system and understand their behaviour due to the presence of an external medium such as water. As a confirmation to the PWE calculations, the neighboring mode profiles were first computed with the FEM and are shown in figure 3.11. The modes are numbered similar to figure 3.8 and are in good agreement with one another in terms of spatial distributions.

The effect of infiltration of water can be different for these modes as it depends on the local field distribution of these modes. In the absence of a near-field measurement apparatus, it

3.3. Hollow photonic crystal cavities for integrated optical trapping

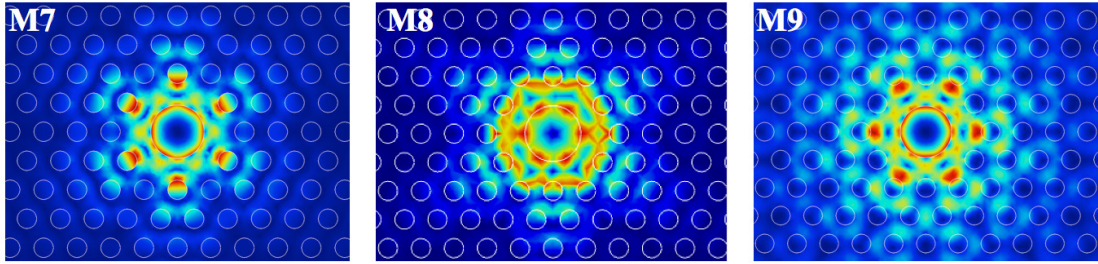


Figure 3.11: Finite element analysis of the neighboring modes. The electric field distribution of the modes M7, M8 and M9 are shown that confirm with the previously shown plane wave expansion calculations.

is not possible to ascertain these modes from their scattered field profiles. The information that is accessible during experimentation is the resonance wavelength, the quality factors and the mode spacings. In light of this problem, the above-shown modes were numerically investigated for the presence of water as can be seen in the summarized results in table 3.2.

Mode number	Wavelength	Q in water
7	1500 nm	300
8 (Mode of interest)	1593 nm	3300
9	1653 nm	800

Table 3.2: Quality factors of modes in the proximity calculated with 3D FEM.

The results clearly show that the mode of interest has the highest Q-factor in water compared to the neighboring modes. The previous mode M7 has a very low Q-factor and was not clearly visible during our measurements in the experiment. The latter mode M9 cannot be coupled with our configuration as it falls beyond the cut-off of the coupling W1 waveguide as will be explained in the next section.

Property	FEM computation
Q-factor in air	7600
Q-factor in water	3300
Spatial overlap with low index medium	0.30
Mode volume	$0.21 \mu\text{m}^3$
Sensitivity	150 nm/RIU

Table 3.3: Finite element analysis summary of circular cavity properties.

In the presence of all these numerous modes, the mode M8 is the most suited one for the trapping experiment as it has the right combination of a high Q-factor in the presence of water, a small mode volume and a larger overlap ratio with the lower index medium. These computed properties are listed in table 3.3.

3.3.2 The slot cavity

It was known from the work of Almeida and co-workers [198] that a slot structure inside a waveguide could confine light within the narrow slot in the low refractive index region. In subsequent works [155, 210], this concept was taken and implemented within a standard W1 photonic crystal waveguide and the dispersion and transmission properties of this slot PhC waveguide mode were demonstrated. The confinement properties of this slot mode had the

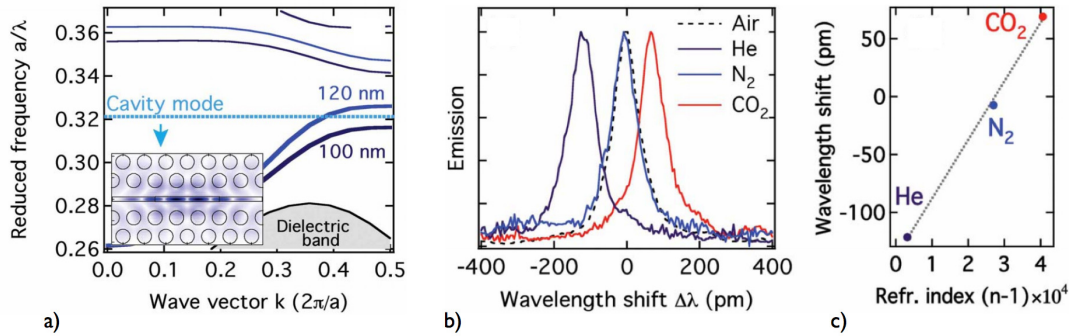


Figure 3.12: The physics behind the slot photonic crystal cavity mode. a) The two different slot widths creating the barriers shown in the dispersion of the structure. b) Resonance shift of the cavity on exposure to different gases. c) Wavelength shift as a function of refractive index change to derive sensitivity. Reprinted from [159].

compelling advantage of a maximized overlap with the low refractive index medium that was advantageous to light-matter interaction experiments. In order to achieve optical cavities with this mode, the slot propagating mode structure had to be gently perturbed like in the case of waveguide-based cavity designs where the perturbation to a W1 waveguide mode created high Q-factor cavities, for example, A1 and A3 cavities by Kuramochi and co-workers [144].

This concept was implemented in a number of successful experimental demonstrations of slotted photonic crystal cavity designs [53, 159, 211] where different approaches were used to create the “reflecting perturbation”. One approach that was implemented in our research group modified the size of the slot without changing the holes or the lattice spacing of the bulk photonic crystal as shown in figure 3.12a. This structure was then exposed to different gaseous media as shown in the emission spectra for three different gases in figure 3.12b. The large interaction overlap with the lower index medium in a volume as small as 40 attoliters results in an impressive refractive index sensitivity of 510 nm/RIU as shown in figure 3.12c [159]. The spatial dimensions of this cavity makes it a viable candidate for trapping very small particles of sizes less than 100 nm, which would lie in the range of the size of a single virus or proteins.

The cavity design was formed with a slot cavity width of 120 nm and a barrier slot width of 100 nm as shown in figure 3.13 along with its finite element calculated mode distribution. Further computations were performed to study the various parameters defining the slot cavity. This included the slot dimensions, cavity width, barrier width and the filling factor of the holes. After parametric studies with PWE, the following design parameters were used to perform

3.3. Hollow photonic crystal cavities for integrated optical trapping

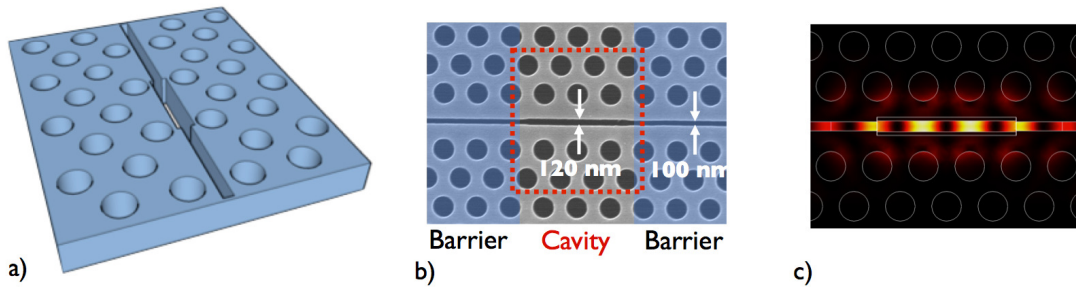


Figure 3.13: The slot cavity for resonant trapping. *a)* A graphic illustration of the device *b)* Scanning electron micrograph image of the fabricated cavity also indicating the cavity region in a red dotted line. The barrier region is shaded in blue. *c)* Finite element method computed electric field distribution inside the cavity. **Reprinted from a publication from this thesis [125].**

the FEM computations: filling factor of 40%, lattice constant of 510 nm and a cavity length of $3a$. The barrier width was taken to be about 10 lattice constants. A larger barrier results in increased confinement but also reduced coupling to the cavity mode in experimental conditions.

Property	FEM computation
Q-factor in air	51000
Q-factor in water	5500
Spatial overlap with low index medium	0.83
Mode volume	$0.05 \mu\text{m}^3$
Sensitivity	480 nm/RIU

Table 3.4: Finite element analysis summary of slot cavity properties.

These structures were fabricated and experimentally measured. The cavities were very much functional in air and displayed the predicted behaviour. Nevertheless, numerous difficulties were experienced in characterizing these devices for water infiltration. The refractive index sensitivity results in a shift of 160 nm for the case of water (in agreement with the FEM calculations), which is almost the entire range of measurement window possible with the tuneable laser. Lithographic tuning was employed to take this into account that depended on “blind” measurement of the cavity mode that was expected to appear after the infiltration was performed. Cavity modes that were expected to appear in the measurement window appeared to have extremely low quality factors and were inadequate to measure.

The reasons leading to the problems in observing the mode are yet to be fully investigated. However, as mentioned before, there are other slot cavity designs using a different mechanism to create the reflecting perturbation such as tuning the lattice holes to create a heterostructure or modulating the hole radius near the slot. It is important to note that these research groups have reported slot cavities in infiltrated environments involving liquids other than water such as sugar solution [53] and Hexane [212], albeit with a huge decrease in their Q-factors.

3.4 Resonant optical trapping in a circular cavity

3.4.1 The optofluidic sample and light coupling

The optofluidic sample was fabricated and assembled by my collaborators Dr. Descharmes and Dr. Diao and the extensive description of the process can be referred to from their respective theses [213,214]. A brief description of the processes are as follows. For the silicon chip, the dimensions of the chip were 30x12 mm as can be seen in figure 3.14. It has the devices fabricated on a SOI wafer with a 220 nm silicon layer and a 2 μm sacrificial silica layer. The PhC pattern was defined with a photoresist (ZEP520) with e-beam lithography and after development, dry etching was performed with a gas mixture of SF_6 and C_4F_8 . This was followed by the final step of HF acid wet etching that resulted in a free standing membrane.

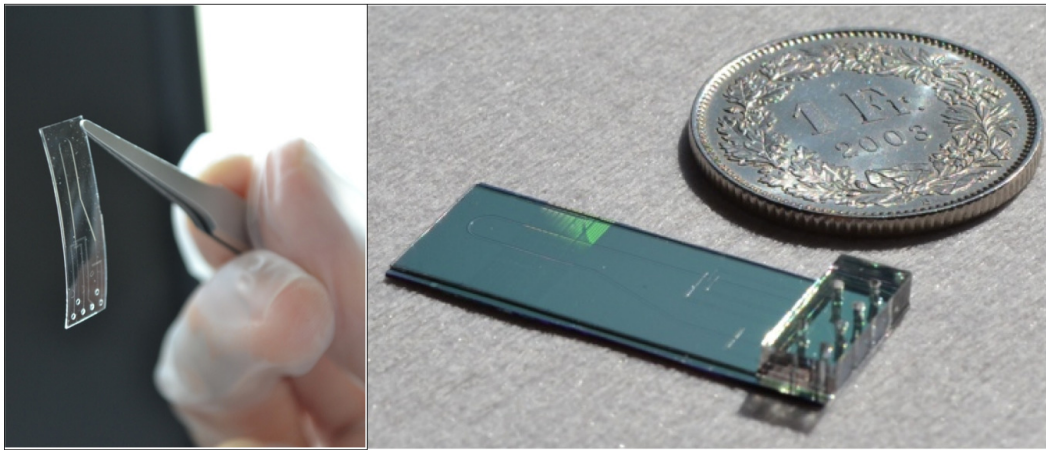


Figure 3.14: Left: Photograph of the ultrathin PDMS membrane before positioning on the silicon surface. Right: The optofluidic trapping chip after final assembly showing the input block, PDMS membrane with valves and the cavities beneath the membrane. **Reprinted from a publication from this thesis [124].**

The PDMS membrane was fabricated by a standard soft lithography process [215]. A first PDMS layer, 30 μm thick, was spin coated onto a silicon wafer comprising a positive photoresist (AZ9260) mould. Meanwhile, a second PDMS membrane, 140 μm thick, was spin coated onto a negative photoresist (SU8) mould on a silicon wafer. The thicker layer, including the control channels, was then deposited on the thinner layer, which carried the infiltration channel (120 nL). The design of the microfluidic layers along with the sample position is shown in figure 3.15. The assembled microfluidics layer was finally aligned and placed on the photonic crystal chip and a 4 mm thick PDMS interconnect was added to ensure stable injection and pressure control.

The cavities are coupled from the exterior environment with the help of a tuneable laser source. A pair of lensed fibers are used to couple the light in and out of the system in a standard end-fire configuration. Standard ridge waveguides are engineered that slowly taper down to the photonic crystal sample to match the modes of the structures. This is then coupled to a

3.4. Resonant optical trapping in a circular cavity

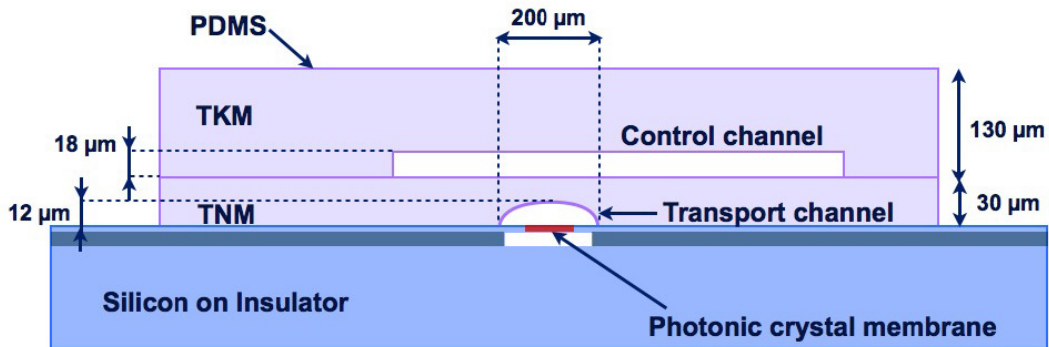


Figure 3.15: The two layers microfluidic membrane and photonic crystal sample. The full PDMS membrane has two membranes on top of each other. A thin membrane (TNM) of 30 μm with the transport channel and a thicker membrane of 130 μm with the control channels. Reprinted from [213].

propagating mode inside a photonic crystal waveguide, which in turn, couples light into the circular cavity. This arrangement is illustrated and also shown in the SEM image of figure 3.16a and b. The footprint of the device is approximately 60 μm x 10 μm . The tuneable laser diode has an operating range of 1470 nm to 1660 nm and this limits the wavelengths range allowed for the cavity design. The following conditions have to be met before the experiment can be performed on the device.

1. The even mode of the W1 waveguide falls in this measurable range of the input laser window along with its observable cut-off.
2. The cavity mode is placed in wavelength spectrum such that it is possible to observe it before and after the infiltration of water.
3. The cavity mode is placed sufficiently far from the slow light localization modes of the W1 even mode.
4. The cavity mode is coupled in the linear fast light region below the light cone to ensure maximum light coupling.

To fulfill the above-said conditions, the diameter of the circular defect, the width of the PhC waveguide, the lattice constant and the filling factor of the bulk lattice are the free parameters that are to be calculated precisely. In the case of a triangular lattice, it is found that the “useable” bandwidth in the W1 waveguide is only about 30 to 40 nm. The cavity is coupled using a side-coupling configuration where the evanescent tail of the propagating mode tunnels into the cavity mode. The strength of the coupling is determined by the spacing and three different distances were experimentally tested involving 3, 4 or 5 lattice rows between the cavity and the waveguide. The increase in distance corresponds also to an increase in the Q-factor of the cavity. On a careful consideration of all these parameters, a fully functioning device was designed and fabricated.

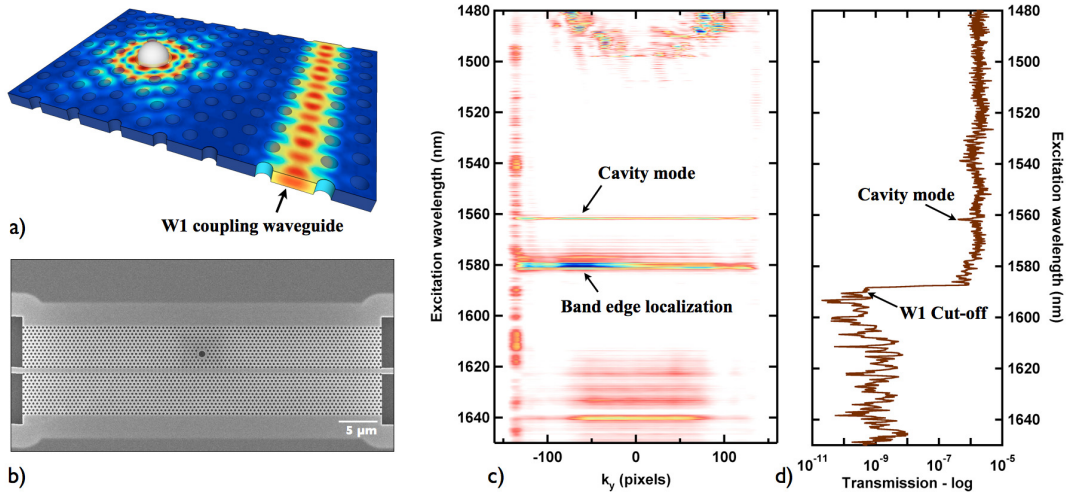


Figure 3.16: Coupling configuration of the circular cavity. *a)* Illustration of the side-coupling scheme for the optical trapping experiment. *b)* Scanning electron micrograph image showing the device footprint and the access waveguide. *c)* Fourier imaging of the modes from the top scattered light from the sample showing the cavity mode and the localized slow light modes. *d)* The simultaneous transmission spectra showing a clear dip at the cavity wavelength followed by the sharp cut-off of the W1 even mode.

In order to characterize the device, a typical end-fire transmission setup was used along with simultaneous measurement of surface light scattering from the cavity. The dispersion and transmission characteristics are shown in figure 3.16c and d respectively. The sharp line seen around 1560 nm corresponds to the cavity mode under study. This is also evident in the transmission plot where there is a slight dip observed. As the W1 mode approaches its band edge, the onset of slow light regime begins and localization effects can be seen.

The Q-factor of the cavities range from about 3000 to 7000 depending on the number of rows of coupling. The farther the cavity is, the larger the intrinsic Q and lesser the coupling Q. The dispersion of the W1-mode and the cut-off have been numerically confirmed with GME while the Q-factors were computed with FEM. The mode volume of this circular cavity as reported in chapter 2 is $0.21 \mu m^3$. This value could not be verified experimentally as it would require other methods such as a near-field characterization technique [216, 217].

However to confirm the mode symmetry, far field measurements were performed and a pattern with three planes of symmetry was obtained confirming an underlying hexapolar mode. It can be clearly seen in figure 3.16 that the device fully exhibits all the expected properties. The transmission of the device has also been further improved by the application of a TiO_2 antireflection coating on the surface of the facets to increase the light coupling and minimize the Fabry Perot reflections. The qualitative and quantitative agreements with the theoretical and experimental results has been a key enabler in advancing this experiment rapidly as it was quite useful for troubleshooting and for obtaining critical feedback.

3.4.2 Ultra low power resonant optical trapping

The resonant optical trapping experiment is performed in the following manner. A diluted solution of polystyrene particles (refractive index 1.59, diameter 500 nm) is injected inside the microfluidic channel. The velocity of the particles at this stage, without extra flow control can reach several millimeters per second. It is therefore crucial to be able to slow down and eventually arrest the flow of particles in the vicinity of the HPhC devices. A set of pneumatically controlled valves positioned above the entrance and exit of the channel has been integrated for this purpose. Typical working pressures of 7 PSI in the valves are usually more than enough to arrest the particles, leaving them in their natural Brownian motion. In the meantime, the HPhC cavities are resonantly excited through the side coupled optical fibers.

At this juncture, the particles are either free to be trapped by the confined optical field in the cavity volume or can be directed towards the HPhC cavity by auxiliary optical tweezers operating from the top. It can be seen from the calculated mode profile that the cavity field extends over a few hundred nanometers above and below the surface of the slab. This allows for the capturing of a particle in the vicinity of the circular defect. The field gradient along the vertical direction gives rise to a restoring force pulling the particle towards the central plane. For appropriate excitation powers, it can then remain stably trapped for very long times in the order of tens of minutes without any sign of apparent structural damage or photobleaching. This can be observed in figure 3.17 for the case of a 500 nm sized particle.

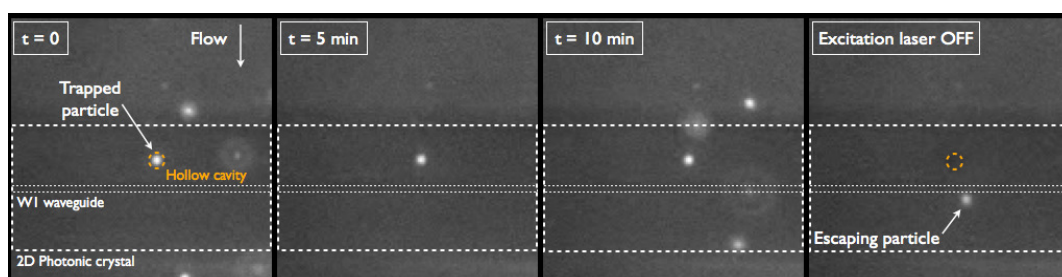


Figure 3.17: Snapshots of resonant optical trapping in a hollow cavity. A particle is guided into the trap using the auxiliary tweezers and they are switched off at $t=0$. The particle remains stably trapped for about ten minutes. The particle escapes when the tuneable laser source is turned off after ten minutes and it recovers brownian motion. *Reprinted from a publication from this thesis [123].*

The video files associated with the trapping of 500 nm sized and 250 nm sized particles can also be found in the supplementary material of these publications from this thesis [123, 124]. In the above experiments, the trapping wavelength is an important characteristic and detailed analysis shall be presented in the later section on back-action. Here, the experiment was performed on a slightly red shifted value from the unloaded wavelength. Regarding the trapping of the particle, it is to be noted that the particle remained steady in spite of a constant flow in the PDMS channel that showed the robustness of the trap. The precise measurement of the stiffness of the trap is yet to be performed and is part of ongoing experimentation. The hollow nature of the cavity permits the particle to access the inner field of the cavity where

it is suspended away from any planar surface. The particle can also be seen in constrained brownian motion during the acquisition of the video that shows that it is not attached to the inner side walls of the cavity. The transmission measurements reported in the next section throw more light on this matter.

As it can be seen in the supplementary video of [123], the circular cavity allows for the trapping of only one particle at a given time. This exclusivity arises due to three factors. Firstly, the geometric limitation imposed by the circular cavity permits only a single particle in the stable region. Secondly, the trapping volume comprises of a cylinder of radius: 350 nm, height: 600 nm, and volume: $0.2 \mu\text{m}^3$, corresponding to the volume where the particle experiences strong optical forces. Thirdly, in the presence of two or more particles, the perturbation caused by the addition of dielectric material in the cavity would cause a large shift in the resonance rendering the decoupling of optical energy that would scale down the optical forces rapidly.

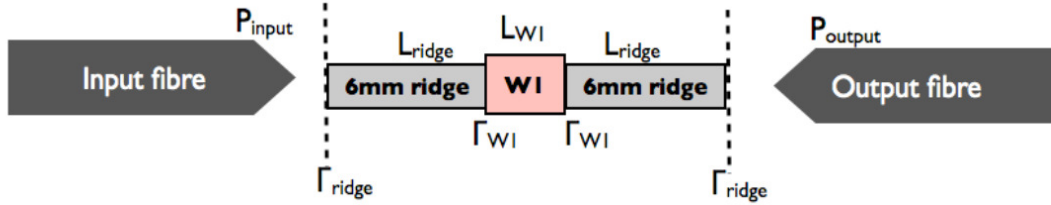


Figure 3.18: Illustration of the optical interfaces with the cavity to estimate the guided power. Reprinted from a publication from this thesis [123].

In terms of power required for trapping, stable trapping was achieved for about 2 mW of input power from the tuneable laser diode. There was no use of any optical amplifiers (like EDFAs) in the path of light coupling. It is possible to accurately evaluate the amount of guided power in the W1 waveguide next to the cavity using experimental values for waveguide propagation losses and reflection coefficients at the interfaces. The various interfaces are shown in figure 3.18. The hollow cavities are coupled via a PhC W1 waveguide, which in turn, is coupled with standard ridge waveguides through an endfire setup. In order to estimate the guided power in the middle of the W1 waveguide, the coupling fractions at the ridge-air interface (Γ_{ridge}) and at the ridge-W1 interface (Γ_{W1}) need to be ascertained. With the use of the parameters listed in table 3.5, the guided power is then calculated by using the simple algebraic expressions shown below.

$$P_{W1 \text{ guided}} = \sqrt{(\alpha_{W1} L_{W1})} \Gamma_{W1} \sqrt{(\alpha_{ridge} L_{ridge})} \Gamma_{ridge} P_{input} \quad (3.21)$$

For 1 mW input power, a guided power in the middle of the waveguide is estimated to be $62 \mu\text{W}$. However in a symmetric system, the power in the middle of the system would simply

3.4. Resonant optical trapping in a circular cavity

Parameter	Value
Length of ridge waveguide on either side	6 mm
Length of PhC W1 waveguide	60 μm
Loss in ridge waveguide: α_{ridge} (best case measured)	3 dB/cm
Loss in PhC W1 waveguide: α_{W1} (best case measured)	24 dB/cm
Coupling fraction at the ridge: Γ_{ridge} (measured)	0.13
Coupling fraction at the W1: Γ_{W1} (measured)	0.65
Output laser power: P_{input} (measured)	1 mW
Power at the output fibre: P_{output} (best case measured)	4 μW

Table 3.5: Parameters used for the estimation of guided power.

be the square root of the product of the input and output powers.

$$P_{W1\text{ guided}} = \sqrt{T}P_{input} = \sqrt{\frac{P_{output}}{P_{input}}}P_{input} = \sqrt{P_{input}P_{output}} \quad (3.22)$$

In the experimental setup, for an output power of 4 μW and input power of 1 mW, the power in the middle is 63 μW , which is in close agreement with the estimation of the previous method. Note that the previous equation can be extended to the case of an asymmetric coupling constant, if the experiment can be repeated swapping the input and output ports assuming the fact that the cavity power remains constant.

$$P_{W1\text{ guided}} = \sqrt{P_{input}^{\rightarrow} \cdot P_{output}^{\leftarrow}} = \sqrt{P_{input}^{\leftarrow} \cdot P_{output}^{\rightarrow}} \quad (3.23)$$

This procedure allows for the estimation of the trapping guided powers which is as low as 120 μW for a 500 nm particle in order to maintain stable trapping for tens of minutes. In comparison with standard optical tweezers, this corresponds to a decrease in trapping power of approximately three orders in magnitude. In some cases, it was possible to observe trapping for a few seconds for guided powers as low as 37 μW .

3.4.3 Particle-cavity perturbation

The previous subsection clearly shows the influence of the cavity field over the motion of the dielectric particle. The converse effect is the modification of the field due to the presence of the particle in the vicinity. As explained in the case of water infiltration, the addition of dielectric content to the system alters the eigenfrequencies. As the perturbation is quite small for dielectric particles or media, it does not strictly alter the field distribution. However, this will not be the case for the presence of metallic particles, which is beyond the scope of this thesis.

The addition of a single particle to a standard PhC cavity like an L3 cavity has a negligible influence on its eigenmode because of the much reduced overlap ratio between the particle

and the field. This is no longer the case for the circular cavity as can be seen in figure 3.19a. In figure 3.19b, the FEM calculated resonance wavelength shift for a single 500 nm sized

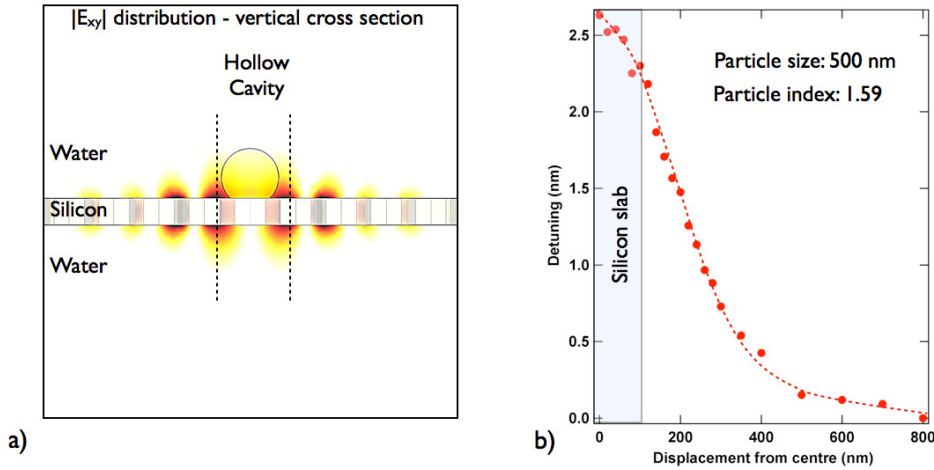


Figure 3.19: Finite element calculation of the resonance shift due to vertical displacement of particle. a) Shows the vertical extent of the field distribution in a cross section plot b) The variation in resonance wavelength is shown as a function of displacement from the center along the vertical direction from the central plane of the slab.

polystyrene particle entering the cavity is shown. The origin corresponds to the center of the slab in the vertical direction and the half silicon slab thickness of 110 nm is highlighted in shaded grey. The particle shifts the resonance wavelength to about 2.6 nm when it is placed at the center of the slab. It has to be noted that the linewidth of the cavity mode in computation is 0.4 nm. This suggests a shift of the order of 6 times the linewidth of the cavity mode. This unprecedented value for a single dielectric particle is achieved due to the specific field of this circular cavity combined with the hollow nature. The cavity mode regains its original value as the particle is displaced more than 500 nm away from the center of the slab. The tail of this shift plot also shows the extent of the influence of the cavity field over the particle. This could turn out to be a crucial parameter when back-action effects come into play as will be discussed in the next subsection. The particle is free to move in three dimensions within the cavity. The diameter of the particle is 500 nm and the diameter of the circular defect in this computed model is 640 nm. This allows for a displacement radius of 70 nm within the plane of the slab center for the particle. As the field distribution is much more stronger near the edges of the cavity walls, a larger shift on top of the before-mentioned 2.6 nm is expected for this case. A set of symmetric points were chosen in order to cover all the possible displacements within this displacement zone and the shift calculations were performed as shown in figure 3.20. The map of the shifts indicate a 0.3 nm additional shift along the edges of the cavity walls and a fluctuating shift near the center corresponding to fine changes in the overlap of the particle and the field. It can also be seen from the mode distribution of the circular cavity in figure 3.7 that exactly at the center of the cavity, there is no field present. In the case of a simple particle presence in a cavity volume, a static displacement in resonance wavelength

3.4. Resonant optical trapping in a circular cavity

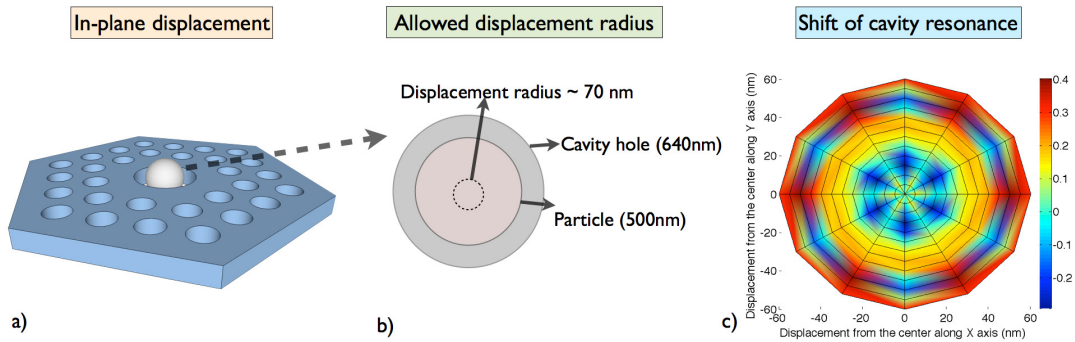


Figure 3.20: In-plane displacement and resonance shifts in circular cavity. *a)* Illustration of a 500 nm particle in the cavity allowed to move freely. *b)* The allowed displacement radius for the cavity diameter of 640 nm in the numerical model. *c)* The map of the in-plane resonance shifts for the corresponding displacements inside the hollow cavity exactly at the center of the slab.

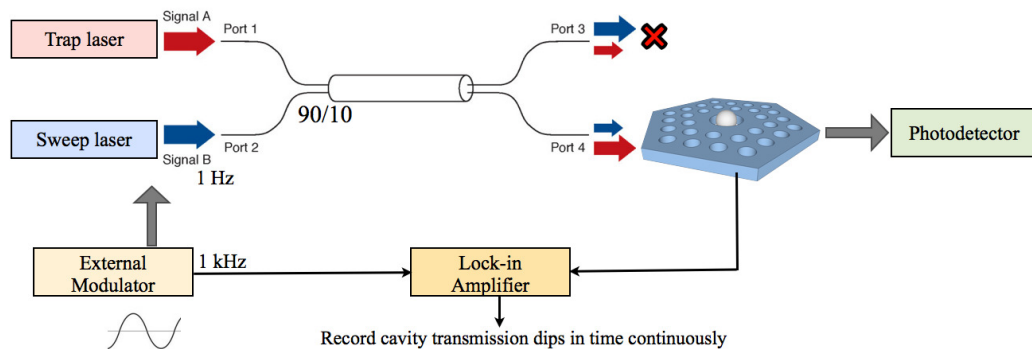


Figure 3.21: Experimental setup to probe particle cavity perturbation. Two tuneable lasers are used with a 90/10 coupler. The stronger (trap) laser is used to hold a particle while the sweep laser is used to probe the spectrum of the cavity mode with a lock-in detection scheme.

is expected. However, a particle in Brownian motion in water is expected to have Brownian motion with characteristic times of typically a millisecond. In comparison to this the cavity mode transition is instantaneous owing to the picosecond scales required to build up the photons. In order to verify these predictions experimentally, a second experiment involving two tuneable lasers was set up as shown in figure 3.21. The two lasers are coupled to the structure using a 90/10 coupler. The stronger laser is used to trap a particle and hold it in the cavity while the weaker laser is used in the scan mode with very low powers as a “non-invasive” probe to track the spectrum of the cavity mode. The spectral range was 10 nm surrounding the unloaded wavelength of the cavity. The weak signal of the sweep laser cannot be recovered from the output of the transmitted light as it is lost in the stronger trap laser signal which is also simultaneously guided out. In order to overcome this problem, a simple lock-in technique was implemented.

The scanning frequency of the sweep laser was 1 Hz and the output signal was monitored using a lock-in detection scheme. An external modulator was used to modulate the sweep

laser at 1 KHz and a one millisecond integration time was used to measure the signal. The

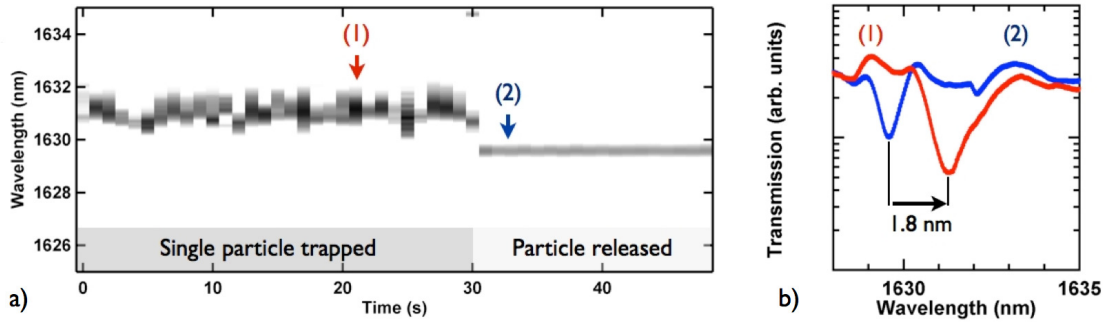


Figure 3.22: Measured resonance shift due to particle cavity perturbation. *a)* The dynamic perturbation as a function of time. A snapshot is taken every one second for 30 seconds while the particle is trapped by the trap laser. The redshifted behaviour of the resonance can be seen. The oscillation of this resonance is a result of the brownian motion of the particle *b)* Two snapshots from *a)* are seen showing a shift of 1.5 and 1.8 nm respectively. **Reprinted from a publication from this thesis [123].**

experimental measurement of this dynamic resonance shift is shown in figure 3.22a. The plot shows the transmission dips of the cavity mode in dark blue. The snapshots in time correspond to the scanning rate of the sweep laser. The particle is held within the trap for 30 seconds and a clear fluctuation can be seen in the transmission dips. After the trap laser is turned off, the particle leaves the cavity volume and the steady state initial position of the resonance wavelength is restored. These oscillations of the transmission dip clearly indicate the suspended nature of the trap and that the particle is not stuck to the inner walls of the cavity. A single snapshots in this trapping time window is shown in figure 3.22b where a shift of 1.8 nm is shown corresponding to a position of the particle within the cavity volume. The linewidth of the cavity mode in the experiment is about 0.7 nm in water. There is a visible effect of increased broadening in the snapshot and this is attributed to the slow acquisition time of the measurement setup compared to the motion of the particle. The slight discrepancy observed between the numerical shift value of 2.9 nm and experimentally measured value of 1.8 nm can be attributed to the following factors.

- It can be seen that the linewidth of the experimental and numerical modes are not similar and the overlaps are also dependent on the exact size of the circular holes that deviate during the fabrication procedure. Also the effect of the coupling waveguide has not been taken into account in the calculations.
- The particle sizes have a co-efficient of variation of about 5% corresponding to 25 nm uncertainty for a 500 nm sized particle.
- The refractive index value used for the particle during computation was 1.59. This value was characterized at 588 nm wavelength and the exact value of index at $1.55 \mu\text{m}$ is not known from the manufacturer.

3.4.4 Particle-cavity back-action

In the previous two subsections, the consequences of the effect of the field on the particle and the converse effect were studied. This leads to the expectation of the existence of a mutual coupling mechanism between these two interactions leading to “back-action” effects between the mechanics of the particle and the trapping optical field. The original term “back-action” was coined for describing the quantum mechanical problem of measurement that stated the act of measurement disturbs the system under study. A second term called “Dynamical back-action” has been used in the context of coupling between a mechanical oscillator and an optical field. This has led to interesting demonstrations of optical cooling of the mechanical oscillator [218]. In an other experiment involving 2D photonic crystals, the interaction between the mechanical vibration modes of the membrane and the cavity optical field was investigated [49]. However the interaction of a single suspended nano particle within an interacting field has never been reported even though it has been theoretically investigated [219, 220]. In our resonant optical trapping experiment, the increased interaction

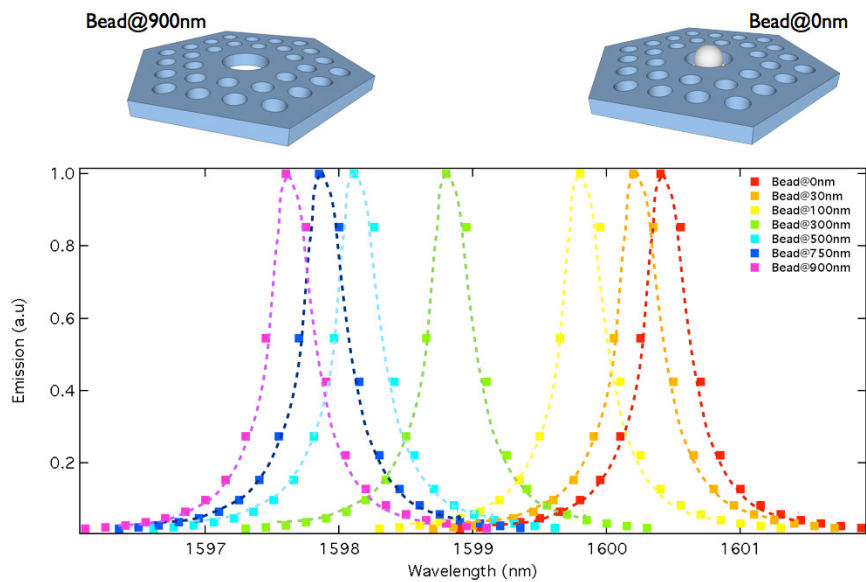


Figure 3.23: Numerical emission spectra corresponding to particle position. A snapshot of all field intensity profiles for the corresponding displacements in the vertical direction.

density between the particle and the field allows for observable back-action effects. This also leads to a situation where the particle can assist itself in the trapping process, in the so called “self induced trapping” introduced by the work of Barth and Benson [221]. The key to observing this effect is the renormalization in the field intensity due to the movement of the particle. In the simplified case of vertical displacement, this can be seen as a dynamic field build-up. A snapshot of all field intensity profiles for the corresponding displacements in the vertical direction can be seen in figure 3.23. The eigenfrequency analysis was performed for the different positions to obtain these distributions. In the next step, a constant input power

was sourced into the cavity with the help of a plane wave. A stationary analysis was performed to understand the behaviour of the forces experienced by the particle further. As explained in the section on optical forces, it is important to take into account all the fields involved in the entire system to have an accurate description of these forces using the Maxwell's stress tensor. The Maxwell's stress tensor was evaluated over the surface surrounding the particle to obtain the forces. The value of the force was then normalized to one Watt power dissipated from the cavity, which can be obtained through the following method.

$$Q = \frac{2\pi f_0 \cdot E_{Stored}}{P_{dissipation}} \quad (3.24)$$

$$E_{Stored} = \iiint_V E_{density} \quad (3.25)$$

By using the values of the numerically computed Q-factor and the energy stored in the cavity by integrating the cavity volume, we can obtain the power dissipation in the cavity, which was used as a normalizing factor. The computed behaviour of these forces can be seen in figure 3.24. It shows both the in-plane and out-of-plane force components in the same scale. The forces were obtained as the input wavelength was slowly tuned from the empty wavelength to the loaded wavelength in discrete steps. Each time the source wavelength was changed,

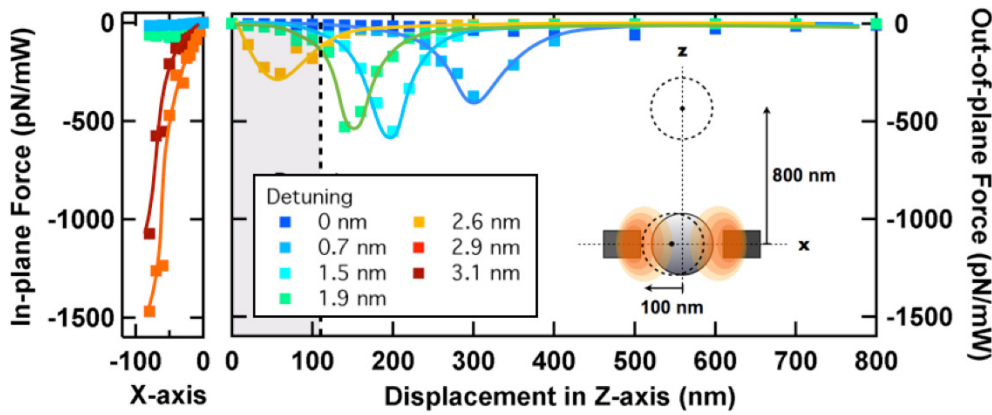


Figure 3.24: Finite elements computation of trapping forces within the hollow circular cavity. The in-plane and out-of-plane force distributions in the left and right panels respectively for various values of detuning are presented. **Reprinted from a publication from this thesis [123].**

the particle was moved from the center of the slab towards the exterior and the forces were evaluated for all these points in order to make this plot. This is also illustrated in a small graphic in the inset of figure 3.24. The detuning of 0 nm corresponds to the empty resonance wavelength in the presence of water and detuning of 2.6 nm corresponds to the case when the particle is exactly in the center of the PhC slab in reference to the z-axis. The striking feature of this plot is the anharmonic nature of the force plots (along the z-axis) that is purely a result of the renormalization of energy in the cavity. Each detuning results in a different

3.4. Resonant optical trapping in a circular cavity

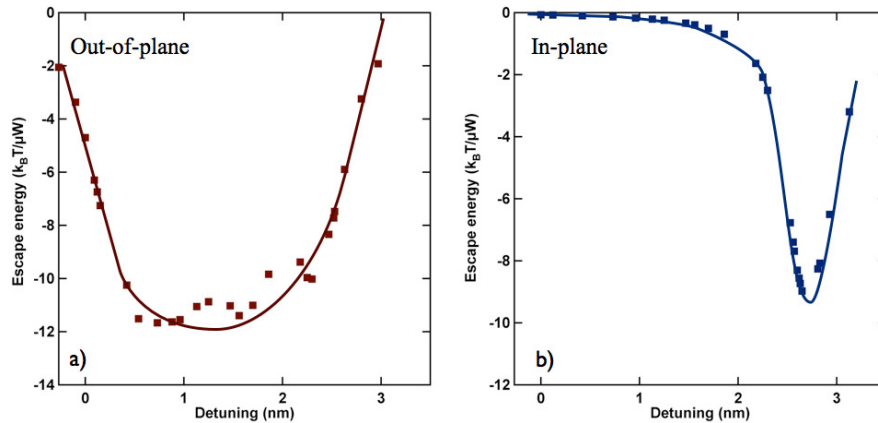


Figure 3.25: Escape energy calculation for the particle resonant trap. Contribution from a) out-of-plane force components and b) in-plane components of the respective force fields with respect to distance, calculated for a range of detuning values.

spatial position for which the force reaches a maximum value indicating the dynamic nature of the forces involved. The case of 1.5 nm detuning corresponds to the maximum restoring force obtained that is 600 pN/mW for a distance of 200 nm from the center of the slab. The detuning of 2.6 nm has a force profile along the vertical direction that looks qualitatively similar to the one that is generally obtained for a conventional tweezer. It can also be seen that for initial detuning values, only minimum forces are experienced by the particle. The

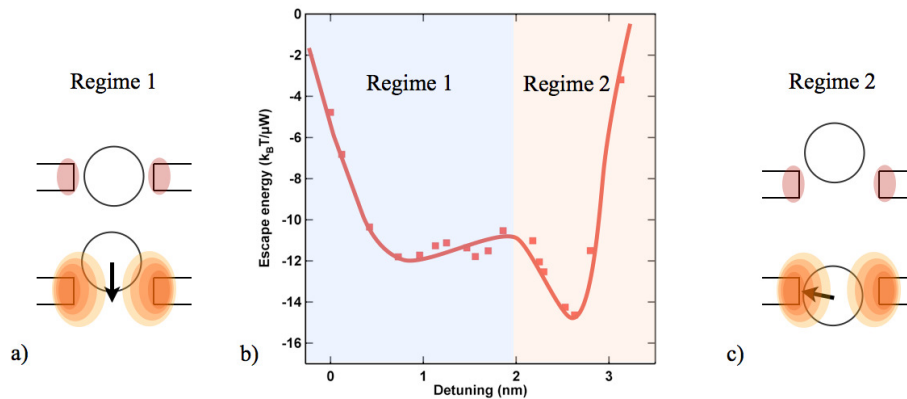


Figure 3.26: Two different trapping regimes and total escape energy. a) Illustration of the first regime of "optical cage" where the particle enters the trap and encounters no field but is pushed back to the center if it displaces outside the central volume due to field build up. b) The sum of the horizontal and vertical escape energy profiles giving a unique particle-cavity trapping signature. c) Illustration of the second regime of farther detuning values where the particle is pushed towards the field maxima near the inner walls of the cavity.

scenario with the in-plane forces is much more subtle. One can see that the absolute value of the forces themselves reach very high values, due to the fact that the gradients are much stronger for the field distribution in the plane. Nevertheless, these values are reached in

Chapter 3. Resonant optical trapping in hollow PhC cavities

very short distances and act in such a way that the particle is pulled towards the maximum field density region, i.e., towards the inner sidewalls of the cavity. In order to delve further into the mechanism of the forces, the calculation of the escape energy was performed by integrating the forces for the displacements in the vertical and horizontal directions. This is shown in figure 3.25. The sum of both the contributions is shown in figure 3.26. The plot shows

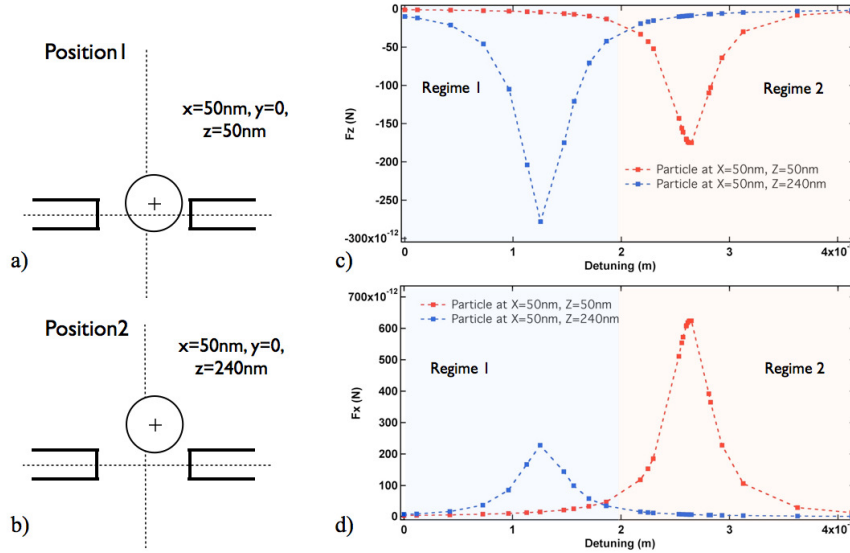


Figure 3.27: Behaviour of trapping forces with respect to position of particle. Two arbitrary positions were chosen and the horizontal and vertical force components are plotted for various detuning values. The operation in different regimes can be clearly seen.

some interesting properties of this trap. Firstly, the trap is active only for a selected range of wavelengths as is expected from a resonant nature. The width of this possible wavelengths are wider than the linewidth of the trapping cavity field. Also, the out-of-plane force component shows an inverted bell like shape centered around 1.5 nm where the particle was found to have experienced maximum force in the vertical direction. On the contrary, the in-plane escape energy has no contribution in the initial detuning values but only starts to have an effect at farther detuning values. This indicates the presence of two possible regimes as indicated in figure 3.26. In the first regime, corresponding to detuning values until 2 nm, the out-of-plane contribution is more predominant. Here, the particle also experiences forces only when it is outside the trapping cavity volume. If it is displaced into the zone, there is no field present anymore due to the renormalization resulting in free brownian motion. This behaviour is an exciting and novel property of the hollow circular cavity resulting in a so-called “one-dimensional optical cage” wherein the particle is trapped with very little optical energy. In the second regime, corresponding to detuning values of above 2 nm, the out-of-plane contribution decreases while the in-plane effect becomes more predominant and it starts pushing the particle towards the inner sidewalls of the cavity resulting in a situation that is equivalent to conventional optical tweezers. However, both these regimes qualify to be termed as “self-induced trapping” scenarios as they influence their own trapping mechanisms. The

3.4. Resonant optical trapping in a circular cavity

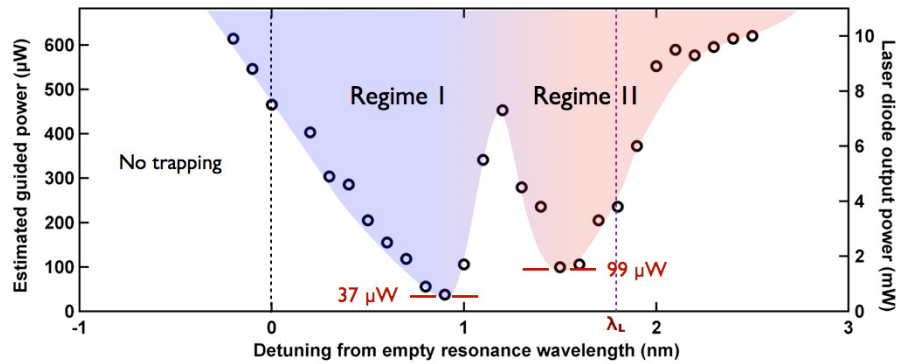


Figure 3.28: Experimental measurement of the wavelength dependent escape power. The minimum power required to maintain the trap is measured for various detuning values. Two trapping regimes are seen with very low trapping powers in their minima. **Reprinted from a publication from this thesis [123].**

behaviour of the regimes is further elucidated in the specific case of two arbitrarily chosen positions as shown in figure 3.27. In the case of position 1, the out-of-plane component attains its maximum value for farther detunings, while this is reversed for the case of position 2. Similar behaviour can be seen for the in-plane components confirming the optical-cage behaviour explained before. The complex shape of this escape energy profile is extremely specific to the combination of the cavity field and particle size and refractive index. This unique signature needs to be further explored for the understanding of the trapping stiffness and possible presence of non-conservativity in the system [222].

The realization of an experiment to demonstrate the back-action phenomena is non-trivial and requires careful thought on the measurement parameters involved. It is also true that several other experiments could in principle be performed to explore this mutual coupling between the particle and the cavity. In our version, the power required to keep the particle until escape was chosen as the quantity to measure in the lab. This measurement is done as follows. A 500 nm particle is captured and held with the trapping laser at a chosen input wavelength corresponding to a detuning value. The input power is slowly decreased until the trap breaks down and the particle leaves in free brownian motion. This power value is termed as "Escape threshold power" and is plotted as a function of detuning in figure 3.28. The detuning values were chosen from -1 nm to 3 nm. The graph shows that a minimum of $37\mu W$ is sufficient to trap a particle for a detuning value of 0.8 nm. It also shows remarkable similarities to the observations predicted in the numerical model regarding its shape and the existence of regimes even though a direct correlation of the numerical and experimental graphs cannot be rigorously made. The experimental graph also clearly shows three features. Firstly, only a restricted range of wavelengths that allows for trapping that springs from the resonant nature of the field. Secondly, the trapping range is red shifted from the empty cavity wavelength indicating the presence of additional dielectric media. Thirdly, the two distinct minima and an indication of the presence of two separate trapping regimes.

3.4.5 Single particle analysis and manipulation

The particle induced perturbation can be used to design a simple and efficient single particle detector. The prior knowledge of this interaction allows us to excite the device at a slightly redshifted value. In the presence of a single particle, the perturbation is instantaneously detected and the original wavelength is restored after the event. This leads to a large and clear spike in the transmission measurement of the cavity as shown in figure 3.29. This output can be fed to a simple Schmitt trigger counter leading to a very efficient on-chip particle counter.

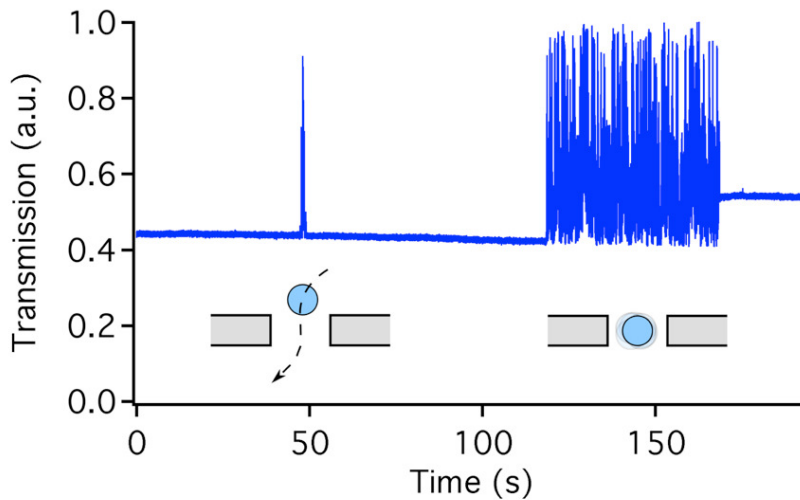


Figure 3.29: An all-optical single particle detector. A large spike is observed at the passage of a particle when the input wavelength is detuned from the cavity resonance.

This transmission signal can also be used to track the position of the particle within the cavity volume and can later enable a particle-position tracked feedback trapping scheme. This will be undertaken in the future experimental developments in our research group. In order to extend the capabilities of the resonant optical trap in an integrated environment, arrays of hundreds of these devices are envisaged.

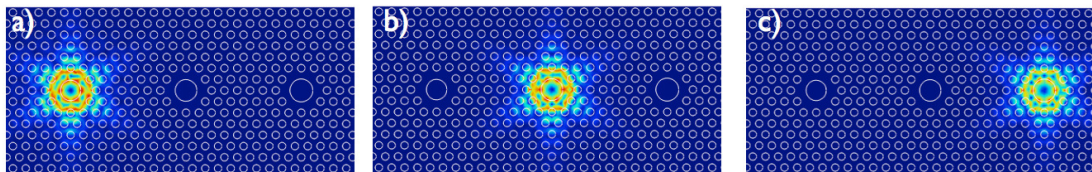


Figure 3.30: Calculation of array of optical traps with circular cavity. a) to c) showing the cavity field profile remaining fairly unchanged but a different resonance wavelength (1597 nm, 1572 nm and 1545 nm respectively) as the defect radius is increased.

To design this array, the minimum separation of hole distance without affecting the mode profile and quality factor had to be assessed. A parametric numerical study was performed with finite elements that allowed us to determine that six columns of holes were sufficient

3.4. Resonant optical trapping in a circular cavity

to have functional cavities. The wavelength of operation was tuned by slightly varying the diameter of the large circular defect. In figure 3.30 the diameter was progressively increased by 40 nm for the three cavities. The diameters of the defect hole are 685 nm, 725 nm and 765 nm respectively. This resulted in the wavelength of operation as 1597 nm, 1572 nm and 1547 nm respectively for the three cavities. It can be seen that the larger diameter defect blue shifts the cavity resonance wavelength as the mode slowly moves towards the air band in the bulk dispersion of the photonic crystal. This can also translate to the fact that there is a compromise between the Q-factor achievable and the increase of the diameter of the hole as it leads to more losses and hence a lower Q-factor.

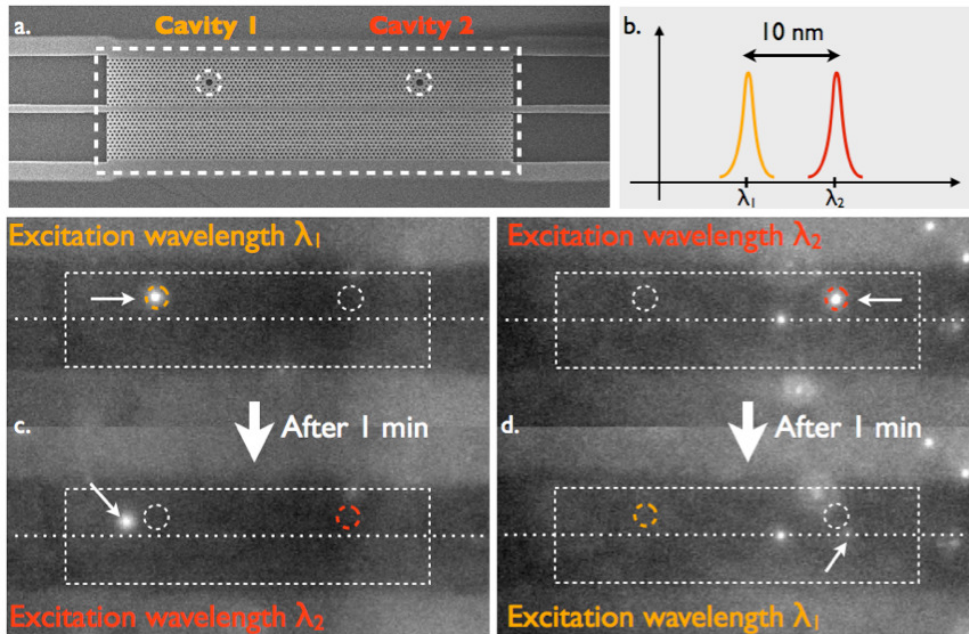


Figure 3.31: Wavelength selective resonant trapping scheme. a) SEM micrograph of a PhC structure comprising of two independent cavities, 720 nm and 700 nm in the diameter for cavity 1 and 2 respectively. b) Schematic illustration of the spectral separation of the two resonant wavelengths 1568 nm and 1578 nm. c) Snapshots demonstrating a particle being trapped in cavity 1 until the excitation wavelength is switched to second wavelength, leading to the release of the particle. d) Similar demonstration as in c) with cavity 2. **Reprinted from a publication from this thesis [124].**

The amount of perturbation caused by the particle to the cavity is central to the above-demonstrated features. The differentiation of this perturbation gives access to detecting and trapping particles by merely adjusting the excitation wavelength. In figure 3.32 the variation of the cavity resonance to particle size, refractive index and shape has been numerically computed and clearly illustrates this trend. The FEM solver solves for the global eigenfrequency of the cavity-particle system by solving the Maxwell's equations in the computational volume. It is possible to obtain the resonance shifts by tracking this global eigenfrequency for different values of refractive index of the particle. It is important to note that in the case of a single 500 nm particle, the resonance shift lies in the order of the experimental cavity linewidth of 0.8 nm. This is well within the reach of the achievable resolution limit for state-of-the-art on-chip

spectrometers [223, 224].

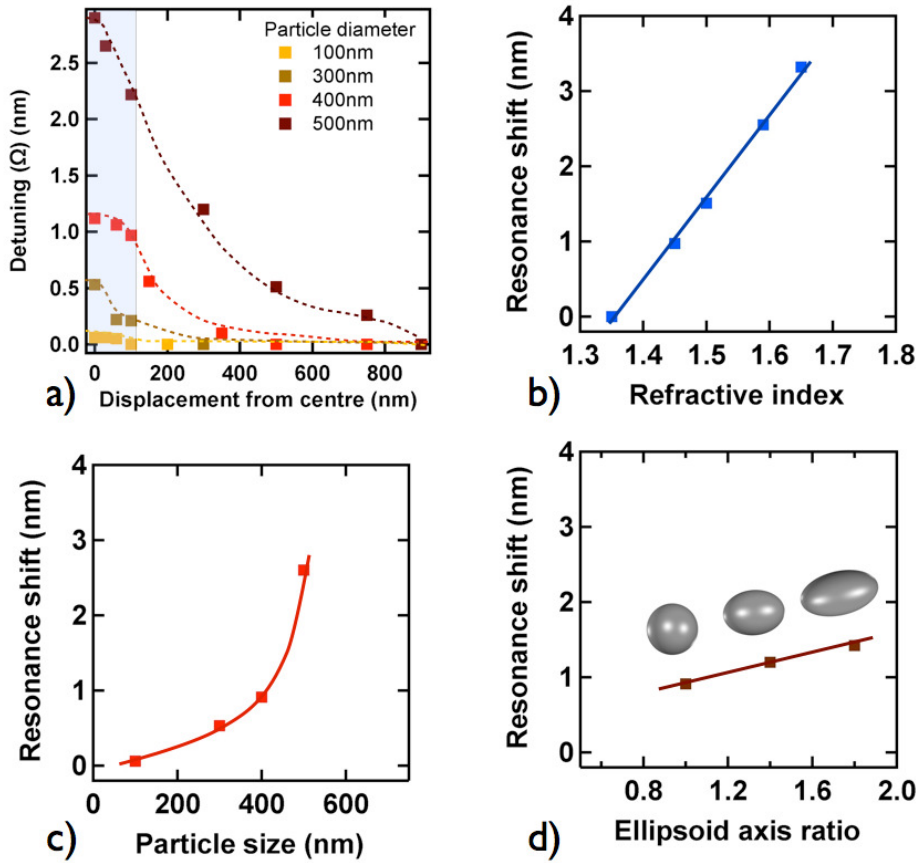


Figure 3.32: Effect of refractive index and size variation of particles. The particle-induced perturbation resulting in a resonance shift is computed for a). Particles of a similar refractive index (1.59) but varying diameters b). A 500 nm particle with varying refractive index and c) resonance shift associated with ellipsoidal particles with different aspect ratios but with a constant refractive index (1.59) and volume. The first point on the left corresponds to a 400 nm sphere. **Reprinted from a publication from this thesis [124].**

This property can be used to separate particles of different sizes or to separate particles of identical sizes but different refractive indices. In the case of the range of values shown in figure 3.32, the induced perturbation remains quite small and the shift response is a linear function. From this figure, the single particle sensitivity for the detection of a 500 nm particle shows a value of 11 nm/RIU. From this number, the minimum refractive index change that could be measured with the cavity lies in the order of 0.02 RIU assuming a half-linewidth resolution (numerical $Q=3300$). This also shows that such a system might also be capable of separating particles that are identical in volume and refractive index but with different form factors. By performing refractive index measurements, we demonstrate a completely label-free single particle detector platform.

3.5 Discussions and outlook

3.5.1 Summary of developments from this work

The contributions of this work to the optical trapping domain are summarized below.

- Resonant optical trapping of a single dielectric nanoparticle (sized from 250 nm to 500 nm in diameter) has been demonstrated in a hollow circular (diameter:700 nm) 2D photonic crystal cavity. The properties of this cavity allows for the input powers to be as low as 120 μ W for the permanent trapping of 500 nm sized particles.
- The perturbation of a single 500 nm particle on the cavity eigenmode gives an unprecedented experimental shift in the resonance wavelength of 1.8 nm, which is more than twice the linewidth of the cavity mode itself.
- The existence of mutual coupling between the trapped particle and the cavity mode leads to interesting back-action assisted trapping effects. This coupling has been probed via the wavelength dependency of trapping powers around the cavity resonance wavelength.
- The existence of two distinct trapping regimes depending on the detuning from the native resonance has been revealed. One of these regimes behaves like the conventional optical tweezer while the other exhibits a new behaviour (1D optical cage), wherein there is no optical power in the cavity when the particle is trapped in the cavity volume.
- A simple scheme involving the transmission signal of the device has been used to detect single particle presence and count the particles based on the input detuning. In addition, appropriately tuned cavities were placed in the same device to demonstrate wavelength selective cavity trap arrays (separated by 10 nm in wavelength spectrum).

3.5.2 A comparison with other integrated platforms

Optical trapping and manipulation has been implemented in other integrated chip-scale platforms such as nanobeam cavities, ring resonators and microrings. The salient features of a selection of these systems are mentioned in table 3.6 for a quick comparison. The case of a conventional tweezer for a 500 nm sized particle is also mentioned for comparison purposes. The reported power values are taken from the respective references. A substantial drop in the trapping powers from the mW regime (conventional tweezers) to the μ W regime (integrated traps) in all the cases underlines the importance of integrated trapping platforms in general. It can also be seen that the hollow cavity based trap from this thesis performs extremely well in terms of both extended trapping time and lower input trapping power as this stems from the advantage offered by the inner field of the hollow cavity volume. The hollow cavity also offers

Chapter 3. Resonant optical trapping in hollow PhC cavities

exclusive trapping as there can be only one particle present inside the cavity volume at any given time, which is not the case with other systems.

Type of device	Power	Trapping time	Particle size	Measured properties
Conventional tweezer [225]	10 mW to 100 mW	-	500 nm	Trapping
Silicon microring resonator [199]	3 mW guided power	several minutes	1.1 μm	Resonance shift, trapping
Nanobeam cavity [202]	300 μW input power	1 minute	1 μm	Trapping
Hollow circular cavity [This thesis]	120 μW guided power	> 20 minutes	500 nm	Resonance shift, trapping, back-action, array trap

Table 3.6: A comparison of various integrated single-particle trapping platforms.

3.5.3 Future directions

This resonant optical trapping platform has opened up a lot of exciting paths in terms of both theoretical and experimental work.

Theoretical aspects of back-action trapping

In order to understand the resonant trapping mechanism during this thesis, optical forces computed via the Maxwell's stress tensor using FEM was used. It is important to investigate whether the back-action effects seen in the system leads to a complete theoretical model that incorporates all the effects, such as the models used in atom traps or optomechanical systems with back-action. It has been shown in this thesis that the trapping field intensity is changed by the particle position resulting in a process of irreversible exchange of momentum and energy between the particle and the optical field. In a second point of view, it can be also viewed analogously to a parametric oscillator, in which energy can be transferred between the pump and the signal. The physics behind these non-conservative trapping forces [222] remains to be explored. This will eventually lead to the understanding of the particle lifetime in the trap and if it fits the Kramer's escape rate or if alternate descriptions will be required. A more detailed calculation is to be performed to understand the dynamic response of the system along with hydrodynamic effects as was attempted in the case of a trapped particle in Brownian motion [226].

Optical cooling schemes

There are two possible mechanisms to cool down a particle: active and passive cooling. The

basic approach involves locking of the trapping laser frequency with the shift of the particle in the trap. This will result in a stiffening of the trap and with additional dephasing, an effective viscous force can be generated that can increase the trap stiffness if the particle goes away and decreases when the particle moves inside the trap. It is to be investigated whether the current system where the particle in a fluid environment can allow this possibility. On the other hand, cooling of a particle in vacuum with the feedback method [227] can also be investigated if the setup can be extended to spray single dielectric particles into the cavity region in a controlled manner.

Cavity design

The circular cavity was the only case implemented thoroughly during this thesis. However, more specifically suited designs need to be explored that can maximize overlap or have other special properties such as concentration of field in the center of the cavity. As it is important to preserve the overlap ratio, high quality factor in water and also the mode volume, the parametric optimization space was quite limited. For example, in the case of figure 3.33a, a single hole was moved towards the circular defect by 100 nm and it resulted in the shown field distribution with a computed Q in water of 1200. In the case of figure 3.33b, three holes in

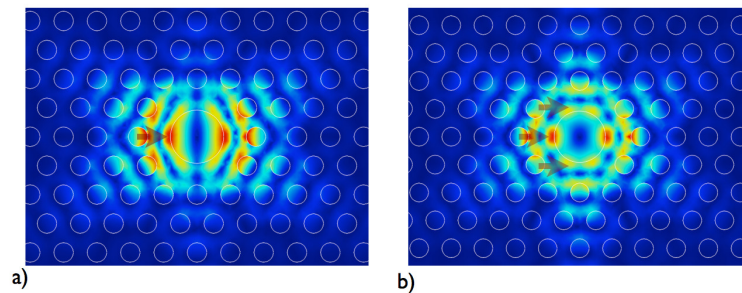


Figure 3.33: Variation of the hollow circular cavity design by modification of surrounding holes resulting in a modified field profile and slightly increasing the field overlap ratio with the circular defect.

the vicinity (six together including symmetric holes) as shown with arrows were displaced by 50 nm towards the circular defect. This resulted in the field distribution shown there with a Q-factor in water of about 1400. Both these modes are of interest because their overlap ratio over the low-refractive index part inside the circular defect is increased and can be explored for further perturbation experiments. A novel method to obtain these designs in an extremely fast manner is discussed in chapter 4 using evolutionary optimization. This method will also allow for checking the effect of disorder on the cavity before fabrication is performed.

Resonant trap characterization

The properties of the trapping forces are yet to be determined in the trap and this could be achieved either by observing the transmission signature out of the device or by performing a finer centroid analysis of the positions of the particle. This could also confirm the nature of

the two trapping regimes and throw more light into how the transition happens and in the quantitative understanding of trap stiffness and stability. The power spectrum measurement [228] of the optical transmission and optical scattering from the surface is being investigated in this regard. This spectral analysis along with the resonance-shift measurement can be performed on different types of particles (varying sized and indices) and can be used as a unique “particle-cavity” trap characteristic for differentiation. In addition to that, the near field imaging of the mode profile with and without the presence of the particle could yield new insights into the perturbation physics as the index and shape of the particle is gradually changed.

Feedback-assisted trapping

The particle-position induced resonance shift can be independently accessed through the transmission of the access waveguide and a lock-in system can be implemented to tune the input laser frequency accordingly. This is crucial for the case of high-Q cavities because the expected back-action effects will shift the cavity mode very far from the native cavity position resulting in a difficulty to use these cavities. With this feedback-assisted trapping technique, high-Q-factor hollow cavities (such as the slot cavity) can be used to trap smaller particles with further decrease in the trapping power.

Applications in Biology

Given the nature of the suspended trap and the low powers required, it is possible to trap biological particles such as cell organelles, DNA strands, small bacteria and large viruses. A recent report has shown trapping of E-coli bacteria on top of photonic crystal cavities at $1.5\mu\text{m}$ [229]. The rod-like tobacco mosaic virus (30x300nm in dimensions) for example, is a good candidate in this regard. In order to extend the usage of the resonant trap to biology, wide bandgap material systems are essential as most of the fluorescent markers function in the visible wavelengths. In this context, photonic crystals in Gallium Nitride are being considered strongly as will be shown in chapter 5 of this thesis. The scalability of Maxwell's equations will also allow us to extend the cavities to be adapted for visible wavelengths and hence smaller particles.

Integrated Lab-on-a-chip systems

The basic functionalities such as single particle detection and wavelength selective trapping has been shown in the thesis. However, there is work to be done to reach a completely functional diagnostic optical lab-on-a-chip. This can include optical waveguides for transporting the particles [201] to the cavities and specialized microfluidic chambers for collecting sorted particles etc. The current device also requires the usage of an auxiliary tweezers from the top to assist the particles to the vicinity of the cavity region. This can be changed by the use of new designs of a micro/nano fluidic transport system.

4 Ultrahigh Q-factor H0 nano cavity and nonlinear effects

This chapter shows the design and characterization of a novel ultrahigh Q-factor H0 type photonic crystal nanocavity. Section 1 gives an overview of the different optimization methods used for designing high-Q cavities. Section 2 introduces the novel H0 cavity design along with the coupling schemes and the fabrication procedures for the device. The experimental measurement of the Q-factors and nonlinear effects are reported in section 3. Section 4 presents a brief summary and outlook.

Contributions:

This work was performed as a collaborative effort with the group of Prof. Vincenzo Savona (LTPN). The 3D finite element modelling, device layout design and the experimental characterization were performed by myself. The genetic algorithm based optimization of the design was performed by Momchil Minkov (LTPN). The photonic crystal samples were fabricated in SOI by Mario Tonin (LOEQ).

Publication of results:

The results obtained during the course of this research are currently under review in Nature Photonics and a version is submitted at the arXiv [230].

4.1 Optimization of photonic crystal cavities for high Q-factors

The merit of a photonic crystal cavity, as has been emphasized repeatedly in this thesis, is highly dependent on the specific experiment it is designed for. However, in many cases, the two quantities: Quality factor (Q) and the modal volume (V) play a significant role in differentiating the performance of these cavities. A higher Q-factor translates to a high degree of light confinement paving the way for enhancement of any interactions with matter. It has been proposed that [231]

- A maximum Q/V is desired for experiments requiring spontaneous emission rate enhancement through the Purcell effect.
- A maximum Q^2/V is desired for the enhancement of some nonlinear optical effects (depending on the nonlinearity) in the photonic crystal cavity.
- A maximum \sqrt{Q}/V is desired for achieving the strong coupling regime in cavity quantum electrodynamics.

As it can be seen, the two quantities that are mentioned above are also mutually coupled in an inverse manner. A smaller cavity also results in an increased radiation loss and hence lowers the Q-factor. In this essence, the design of such high-Q cavities can be very tricky. The different methodologies that have been frequently used for achieving significantly high quality factor cavities are summarized below.

4.1.1 Optimizing leaky light cone components

In an interesting work reported in 2005, Akahane and coworkers [160] published a method that is based on the optimization of the light cone components arising from the emission pattern of the cavity mode. An L3 cavity (3 missing holes) was chosen and the position of three holes on either side of this defect were tuned appropriately. As can be seen in figure 4.1b and c, the

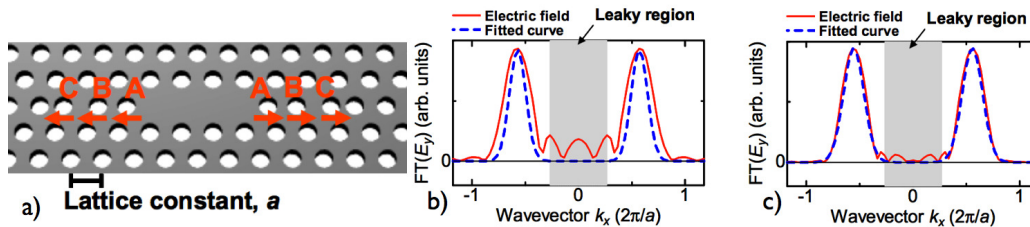


Figure 4.1: Fourier transform optimization of Q-factors in L3 cavity. a) Schematic of L3 cavity and holes to be moved b) The Fourier transform of electric field component before optimization showing leaky components in the light cone. c) The Fourier transform of electric field component after optimization showing the suppression of the leaky components in the light cone. Reprinted from [160].

4.1. Optimization of photonic crystal cavities for high Q-factors

electric field components have two peaks outside the leaky light cone region. It is understood that the abrupt change in the cavity region due to the removal of the three air holes causes the leaky light cone components. In the case of the parametric tuning of hole positions, this abrupt transition was transformed to a smooth Gaussian like transition that decreases the components falling inside the light cone and hence increasing the Q-factor. The outcome of this interesting method is the idea of “gently modulating” the cavity geometry in order to create higher Q-factors which has also been utilized by several other groups afterwards. It has to be noted that the parametric optimization of the hole positions was still a crude subset and highly limited by the computational complexities of the 3D methods used. In this work, by using this method, the maximum Q-factor achieved was of the order of 100,000 with a modal volume of $0.7 \left(\frac{\lambda}{n}\right)^3$.

4.1.2 Tuning the mode-gap of PhC waveguides

In recent studies, a method based on local modulation of the waveguide mode has been pursued as shown in [144, 162, 232] by Notomi and coworkers. The basic method works on the basis of creating a cavity region surrounded by barrier region that does not support the propagating mode. Since it was explained in chapter 1 regarding the formation of waveguide defects, it is easily understood that decreasing or increasing the waveguide width can push or pull the mode away from the dielectric band. If a normal W1 waveguide is sandwiched between a narrowed waveguide on either side for a finite direction, this barrier acts as a cavity boundary and allows the light to be coupled through evanescent modes. This mode-gap can be

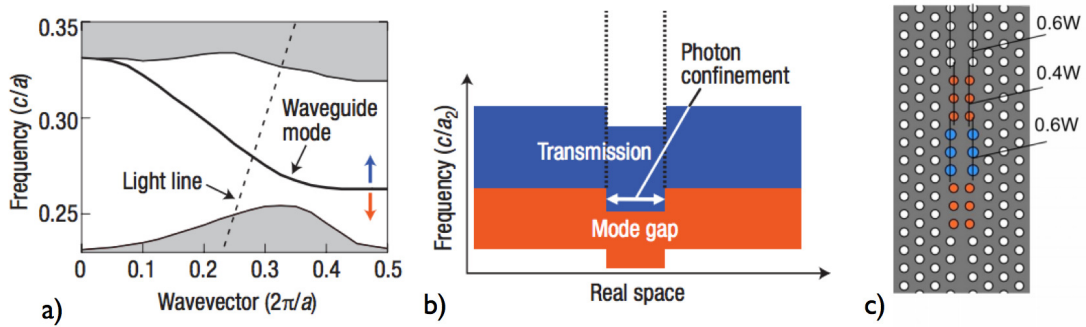


Figure 4.2: Schematic of mode-gap cavity confinement based cavities. a) Waveguide mode and the bandgap in a triangular lattice photonic crystal. b) The mode-gap based confinement by creating a barrier with the tuning the waveguide mode positions [162]. Similar design shown with a W1 waveguide along with a barrier and cavity region indicated [232].

implemented in two ways, by changing the lattice constant and creating a heterostructure [162] or by modulating the local position of the holes adjacent to a W1 waveguide [232]. The electric field distribution of these cavities resemble an ideal Gaussian envelope that also explains the higher Q-factors obtained and the gradation of the heterostructure can be tuned in order to maximize this value. In this heterostructure based work [162], a measured Q-factor of

600,000 is found and theoretical Q-factors upto 24 million were predicted. Similarly, in a waveguide width modulation cavity reported here [144], measured Q-factors of up to 800,000 and theoretical Q-factors up to 70 million were predicted. The drawback in these types of cavities is the increased mode volume due to the nature of the waveguide-based mode.

4.1.3 Analytic or semi-analytic designs of cavity mode

In contrast to the previous methods where the cavity parameters were obtained through heuristic optimization of individual hole positions, a few methods have reported analytical designs of cavities [163, 233, 234]. A detailed analysis based on the symmetry of the photonic crystal lattice, the point groups and the leaky light cone components was performed to optimize for the vertical losses for both the square lattice and triangular lattice photonic crystals that resulted in theoretical Q-factors of up to 0.5 million [233]. In the work by Englund and coworkers, a general expression for cavity radiation loss was derived and it was found that the cavity mode with a *sinc* like field envelope should completely eliminate the components from the light cone [163].

In an other work by Felici [234], a semi-analytical relationship was accomplished between the desired field distribution and the dielectric constant of the cavity system. By assuming a Gaussian envelope function, a Q-factor of 17.5 million was estimated for this design with the aid of a 3D FDTD method. It has to be also noted that there are a number of other designs that have been theoretically proposed by parametrically tuning the PhC parameters but are yet to be experimentally measured and confirmed such as this work that proposed a Q-factor of 1 billion [235]. In the past two decades, there have been numerous experimental reports showing the confinement of light inside the structures using the above-mentioned methods for reducing losses from the cavity mode resulting in the term “ultrahigh-Q” PhC cavities that have measured Q-factors of the order of a few hundred thousand.

The above-mentioned arguments reaffirm the fact that the achievement of ultrahigh-Q-factors depends on:

- The design of the cavity defect leading to a very high confinement of optical energy and hence a high intrinsic Q-factor.
- Robustness of the Q-factor of the cavity in the presence of structural disorder induced by fabrication.
- The ease of fabrication of the design and the necessary fabrication processes for achieving the proposed design parameters

The following sections in this thesis will elaborate on how this thesis has shown a novel ultrahigh-Q cavity design experimentally that addresses all these issues.

4.2 Evolutionarily optimized ultrahigh-Q H0 cavity

4.2.1 Design optimization

The primary objective of this work is to maximize the Q/V ratio of a PhC nanocavity keeping the cavity design compact while retaining the robustness to disorder and the ease of reproducibility. To fulfill this purpose, the H0 design was chosen, which has the smallest known modal volume among the various 2D PhC structures. The thickness of our PhC slab is set to $0.5a$ while the radius of each hole is $0.25a$ (a is the lattice constant) and the refractive index of the slab is set to 3.46. The basic H0 design consists of two holes shifted away from their original positions by an amount $S1x$ as shown in figure 4.3. The optimization is carried out by allowing for four more shifts of neighboring holes along the x-axis and two shifts along the y-axis. The objective function of the evolutionary optimization was the cavity Q-factor, while reasonable restrictions were imposed on the magnitudes of the shifts in order to limit the variations in modal volume.

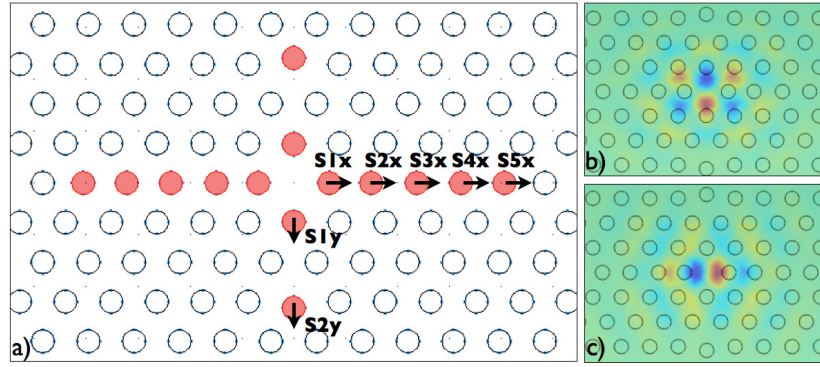


Figure 4.3: Schematic and electric field distribution of optimized H0 cavity. a) The holes whose positions are displaced are highlighted in red. b) and c) FEM computed electric field distributions, E_x and E_y respectively.

The Q-factor was first computed with the guided-mode expansion method [142] for a single realization of hole positions. It should be noted that this choice is not unique but rather highly customizable. Since a single computation yields both the Q-factor and the electromagnetic mode profile, it would be equally straightforward to optimize Q/V for example, or even more specific quantities like the amount of electric field penetrating into air. The stochastic evolutionary algorithm used here is the one that is included in the MATLAB Global Optimization Toolbox, which starts from a random initial population and goes on to create a sequence of generations where the fittest (highest-Q) individuals are kept. Reasonable constraints on the shifts can be imposed. In the case of the initial H0 optimization, the absolute value of the shift was set to be smaller than $0.3a$. For the design with a smaller mode volume, this boundary was decreased to $0.25a$. For both designs, a rough optimization was first performed with large allowed fluctuations of all parameters, which was then followed by a fine-tuning optimization in which small variations around the rough optimal values were allowed. This

ensured convergence within approximately 200 generations in total, with 120 individuals in each generation.

Parameter	Value
S1x	0.280a
S2x	0.193a
S3x	0.194a
S4x	0.162a
S5x	0.113a
S1y	-0.016a
S2y	0.134a

Table 4.1: Optimized parameters for the proposed H0 cavity. The negative sign means an inward shift towards the centre.

The final optimized device parameters are presented in table 4.1, bringing a GME-computed Q-factor of 1.95 million. Optimization attempts allowing for additional shifts of the off-axis holes and/or variation of the hole-radii did not bring significant improvement. The optimal design is thus mostly determined by variations of positions of the holes only, which are also the structural features over which the fabrication process ensures the highest precision. The computed mode profile as shown in figure 4.3 resembles that of the basic H0 design, and most importantly the modal volume remains extremely small at $0.34(\frac{\lambda}{n})^3$. The optimal structure was

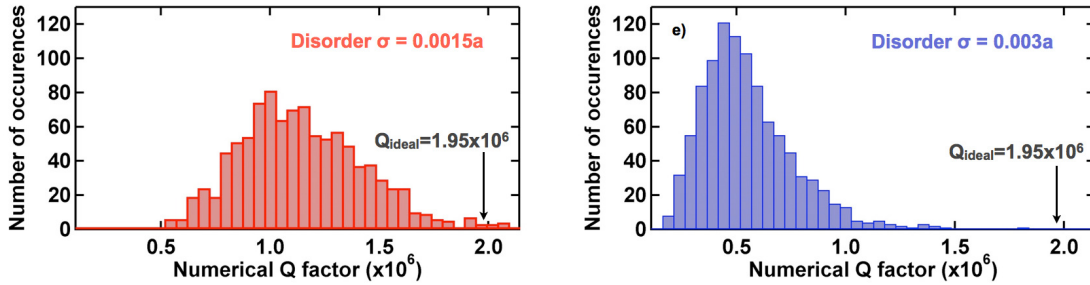


Figure 4.4: Influence of disorder on the Q-factors. Two different values of disorder corresponding to 0.0015a(left) and 0.003a(right) were used to obtain the histograms. *Reprinted from a publication from this thesis [230].*

additionally modeled using a 3D finite element method solver (COMSOL), which essentially confirmed the GME-computed values of Q and V. The theoretical Q-factor of the presented design is nearly one order of magnitude larger than the previously highest reported value [236], which was obtained through sequential optimization of individual hole-positions. This fact highlights the importance of the global optimization algorithm that helps us to attain the maximum possible Q for a particular type of configuration within the set predetermined boundary conditions. In order to assess the robustness of this design, random disorder is introduced in the form of fluctuations in the hole positions and radii, drawn from a Gaussian random distribution with zero mean and a standard deviation σ . The histograms shown in

figure 4.4 are each obtained from the simulation of 1000 disorder realizations. Figure 4.4 shows the probability distribution of Q-values for two different values of σ ($0.0015a$ and $0.003a$). The assumption of this value is based on the realistic assumption of disorder in our structures which was investigated in an earlier work by a previous co-worker of our group [170]. Disorder reduces the Q-factor on average, as intuitively expected. However, very high quality factors for a reasonable fabrication disorder are predicted by these histograms, proving the robustness of this design in terms of practical applications. It is important to note that this optimized design is made possible owing to the fast computations performed by the GME that evaluates the 24000 evaluations required for all the disorder computations within a week on a computer with 12 CPUs and 32 GB of memory. In an estimation using a 3D FEM solver, these optimization computations will require approximately 10 years to complete.

4.2.2 Coupling to the cavity

The efficient coupling of light into photonic crystal cavities is very important in integrated optics applications and in this context, it is important to optimize the coupling suitable for each type of cavity design. The relevant parameters are the spatial overlap ratio between the cavity mode and the coupling waveguide mode as well as the symmetry matching between the two modes. An ideal coupling scheme should allow for the measurement of the intrinsic Q-factor of the cavity while also allowing for sufficient light coupling into the cavity depending on the experimental requirements. In the work of Kim and coworkers [237], the coupling

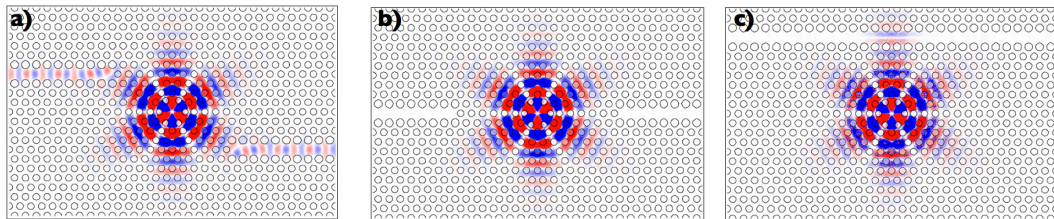


Figure 4.5: Coupling schemes to a H1 type cavity. a) shoulder-coupling b) butt-coupling and c) side-coupling configurations. Reprinted from [237].

to a H1-type photonic crystal defect was numerically studied and reported in figure 4.5. In this work, the overlap of the cavity mode with the W1 type waveguide was studied and the shoulder-coupling was reported to be the most efficient in terms of coupling light into the cavity. The problem pertaining to efficient light coupling is the increase in coupling Q-factor which brings down the measured Q-factor of the cavity mode. In the case of a more popular L3 cavity system, Faraon and coworkers showed in 2007 [238] that the best coupling is achieved by a 60 degrees tilt of the cavity with respect to the waveguide mode as shown in figure 4.6. As it can be seen in figure 4.6e, the explanation to the abnormal increase in waveguide quality factor for specific separation distance is attributed to the change in overlap integral depending on if it is a node or an antinode in space. To resolve these differences, extremely fine numerical simulations are to be constructed, which are generally cumbersome and memory consuming.

Chapter 4. Ultrahigh Q-factor H0 nano cavity and nonlinear effects

Analytical models using coupled mode theory has also been used to explain the effects of the waveguide mode on the cavity mode [239], [160]. In the case of the H0 design presented in this thesis, the coupling was studied through the implementation of three different schemes: side coupling, cross coupling and bent coupling. Each of these schemes were experimentally characterized with respect to the spatial separation between the cavity and the waveguide.

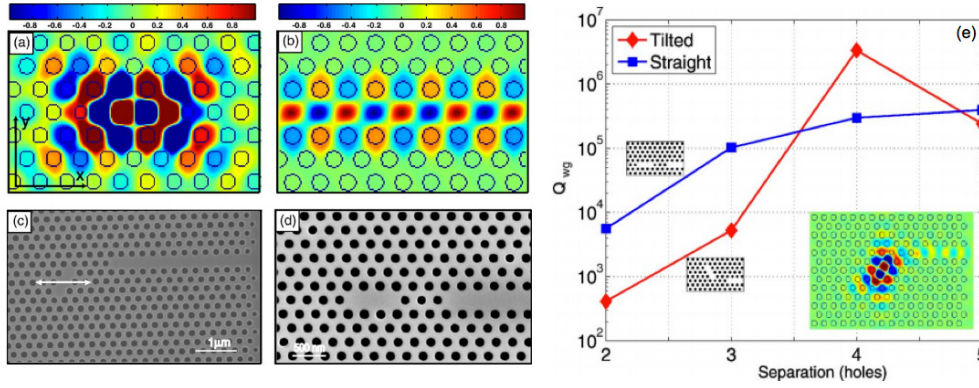


Figure 4.6: Coupling optimization for the L3 cavity a) and b) Computed mode profile of the L3 cavity and W1 waveguide even mode respectively. c) SEM image of the device with "tilted" coupling by tilting the cavity with respect to the waveguide. d) SEM image of the device with "straight" coupling of the cavity. e) Variation of Q-factor with the increase in the waveguide cavity separation Reprinted from [238].

4.2.3 Fabrication of the cavities

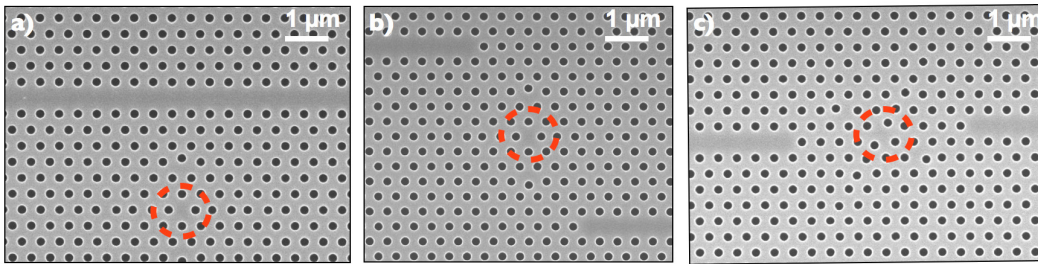


Figure 4.7: Scanning electron micrograph of H0 cavity with different coupling schemes. a) Side coupling b) Cross coupling c) Bent coupling.

The cavities were fabricated on a SOITEC Silicon-On-Insulator wafer, which consisted of a 220 nm thick silicon layer and a 2 μm thick silica (SiO_2) layer on a Silicon substrate. The PhC pattern was defined with e-beam lithography (VISTEC EBPG5000) on an electro-sensitive resist (ZEP520) and the developed pattern was further transferred into the Si layer with an inductively coupled plasma (ICP) AMS200 dry etcher with a SF_6 and C_4F_8 gas mixture. The last step is the removal of the sacrificial SiO_2 layer with buffered HF (BHF) wet etching. The SEM images of the cavities with different coupling configurations can be seen in figure 4.7.

4.3 Experimental characterization results

4.3.1 Q-factor measurement

The cavities were measured using a standard end-fire coupled setup as shown in figure 4.8. The diameter of the focal spot at the facet of the device is about $3\ \mu\text{m}$ and has to be mode matched with that of the mode of the PhC W1 waveguide. The ridge waveguides were gradually tapered down to the photonic crystal that acted as a mode convertor. A tuneable input laser (Yenista Optics - TUNICS T100S) was used to couple the light into the waveguides. This laser has a wavelength range from 1480 nm to 1570 nm with a minimum tunable wavelength step of 1 pm. The fine scanning mode (FSC) available in the tuneable laser allows for accurately scanning the wavelength over a 40 pm range with a resolution of 0.1 pm. A set of neutral density filters were also employed to control and characterize the exact amount of power input into the device. The emission of the cavity was captured with the aid of an infrared camera (by XenICs), which is sensitive between 900 nm and 1700 nm. The 320x256 pixel array of the camera comes with a pixel pitch of $30\ \mu\text{m}$ and is thermo-electrically cooled to 263K, offering a 12-bit dynamic range. The emission was also detected with an InGaAs type FPM-8200 power meter which has a wavelength range from 800 nm to 1600 nm and a power range from -75 to 1.5 dBm.

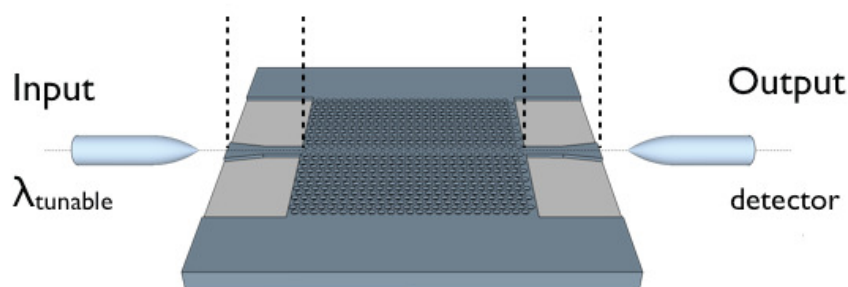


Figure 4.8: Schematic of the end-fire measurement set-up showing the input and output facets and tapered fibres

The Q-factors were measured for the cavities coupled via the three schemes explained in the previous section. A converged Q-value was reached after the measurement of the emission spectra for increasing values of input power at very low power values (around a few μW). This was necessary to eliminate additional losses due to nonlinearity in the device. The initial measurement to study the effect of coupling can be seen in figure 4.9. As expected, the bent coupling scheme which had a very large mode matching with the waveguide mode achieves much lower measured Q-values compared to the other schemes. The side coupling and the cross coupling schemes start to show significantly lower coupling losses when the distance to the cavity is increased and hence increase in measured-Q. In addition to this, the scattering losses at the cross coupling facets were much larger that lead to a significant drop in coupling

for larger distances from the cavity. In this context, the side coupling scheme was found to be the most efficient scheme for the measurement of the intrinsic Q-factor.

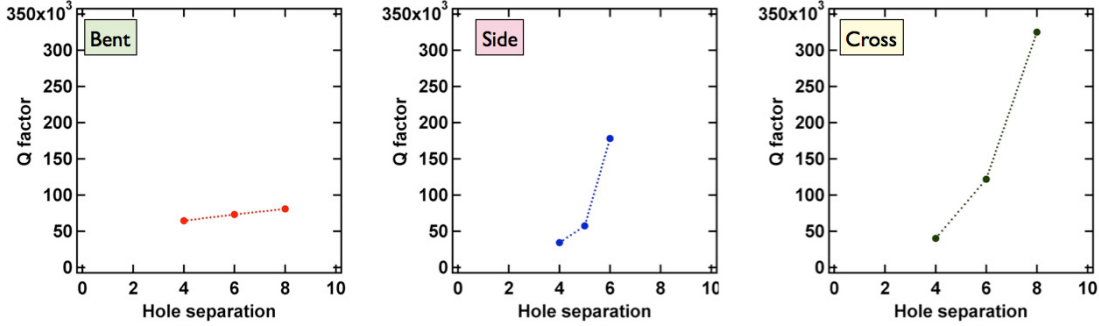


Figure 4.9: Initial measurement of Q-factors for various coupling schemes. Left: Bent coupling Centre: Side coupling and Right: Cross coupling configurations.

Figure 4.10 shows the change in measured Q-factor, for the side-coupled cavities, as the distance to the waveguide is increased. The initial points clearly show that the Q-factor of the cavity is greatly affected by the proximity of the coupling waveguide.

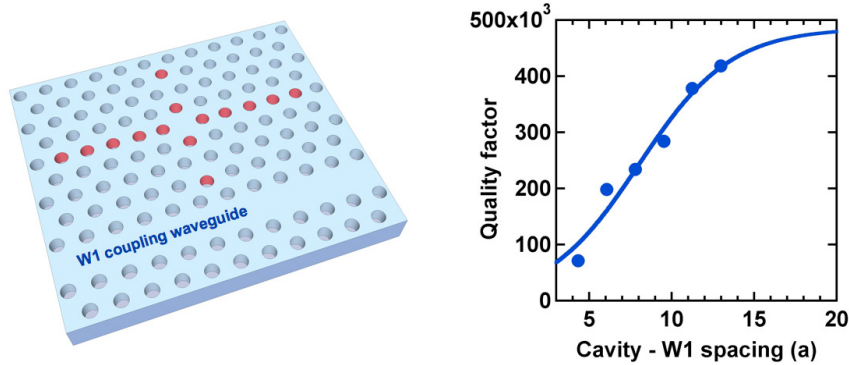


Figure 4.10: Q-factor measured in emission vs. waveguide separation showing the gradual increase in quality factors as the coupling strength decreases. The continuous line is a theoretical fit taking into account an exponential decay of the W1 mode. Reprinted from a publication from this thesis [230].

A maximum value of 418000 for the distance corresponding to 13a was measured. The data in figure 4.10 suggests clearly that even at large distances from the cavity, the coupling waveguide still affects the measured Q-factor. A conservative way of extrapolating the unloaded Q-factor consists in assuming an exponential decay with distance for the cavity-waveguide coupling. More precisely, we assume that

$$Q^{-1} = Q_{UL}^{-1} + Ce^{-\alpha D} \tag{4.1}$$

where Q_{UL} is the unloaded Q-factor along with constants C and α . A fit of the measured Q-

values (with Q_{UL} , C and α as free parameters), as plotted in figure 4.10, yields a value of 485000, which should be taken as a lower bound to the actual unloaded Q-factor. This value is in very good agreement with the maximum value found in the histogram of figure 4.4, computed for a disorder amplitude of $\sigma = 0.003a$, which is a very reasonable estimate for the largest fluctuations introduced in the fabrication process. It can also be seen that at short distances, where the Q-factor is still very high (100000), losses are largely dominated by coupling into the waveguide channel, thus highlighting the potential for photonic circuit applications.

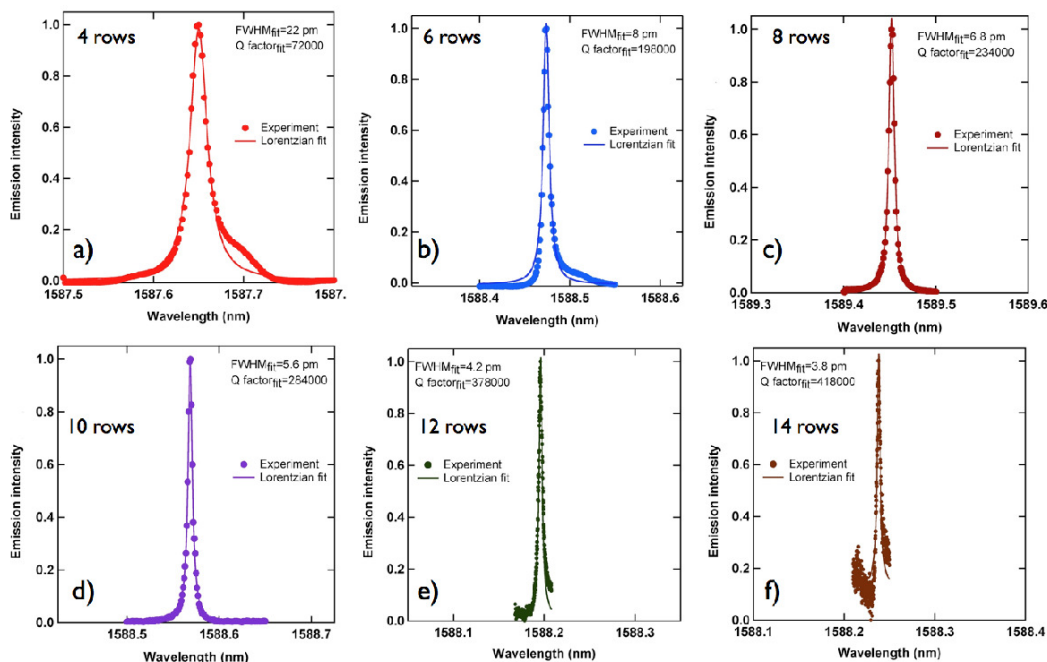


Figure 4.11: Measured Q-factors of optimized H0 cavity through side coupling. a) to f) show the emission measurements performed on the cavities with their corresponding Lorentzian fits and Q-factors as the distance to the coupling waveguide is increased.

The individual emission spectra corresponding to the six points shown in figure 4.10 are later shown in figure 4.11. The linewidth narrowing is clear and quite visually evident between the measured spectra. The resolution of the last two spectrums are different due to the fact that they were measured using the fine scanning mode of the tuneable laser, resulting in highly resolvable spectral measurements. The Q-factors shown in the figure are computed from the lorentzian fits of the corresponding measurements.

In order to further understand the effect of the coupling waveguide, the transmission plots corresponding to the emission spectra are shown in figure 4.12. In the case of shorter cavity-waveguide spacings, the transmission plots correspond to the emission spectra in dropped energy and can be understood as the manifestation of coupling loss. In the case of farther distances, the transmission spectra show no observable difference despite the fact that there is an emission spectra recorded from the cavity. If there is no influence of the waveguide on the cavity, one can expect the convergence of the observed Q-factor saturating towards

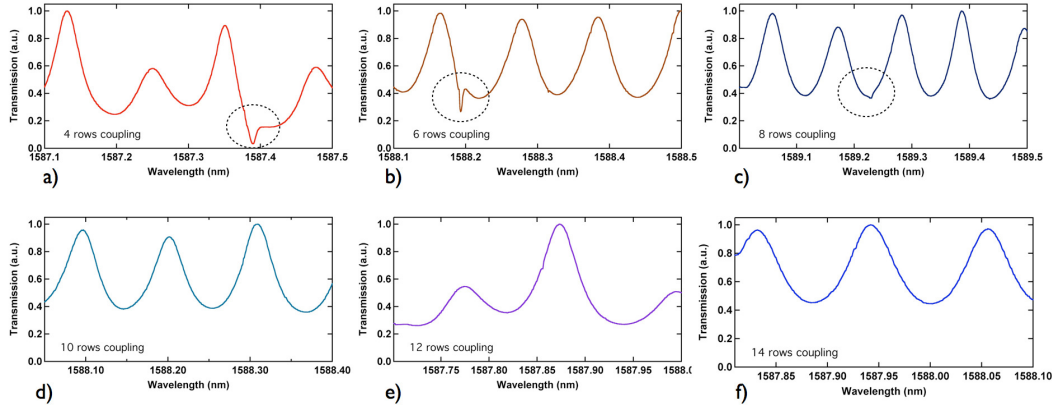


Figure 4.12: Transmission measurements of H0 cavity through side coupling. a) to f) show the transmission measurements corresponding the 6 cavities shown in the emission measurements. The cavity dropped transmission is highlighted in circles for the measurements in a) to c).

the intrinsic value. Nevertheless, this is not observed in this experiment for the two farthest distances measured.

The extremely weak coupling has also additional influences from the coupling due to scattering and disorder in the lattice which can tunnel the energy from the waveguide mode. It is to be also noted that the PhC device is also truncated in both lateral dimensions, which could possibly influence this coupling strength. As it was already explained before, for farther cavity-waveguide spacings, the position of the node and antinode of the waveguide mode becomes quite significant as the cavity mode linewidth is much smaller than the waveguide resonance width. Though the finesse of such a Fabry Perot resonator in the waveguide is quite low, this could still be an issue for coupling of ultrahigh-Q cavities.

In order to qualitatively explain the observed emission and transmission spectra, a 2D finite element study was performed for different waveguide-cavity distances and the transmission spectra were computed. A plane wave is sourced on the left side of the model and is used to couple to the cavity mode. Figure 4.13 shows the effect clearly. The images show the norm of the electric field distribution computed at the resonance wavelength of the cavity mode. As one can easily observe, the strength of the cavity mode at resonance drastically drops as the waveguide distance is increased. This also reflects in the transmission spectra that are plotted beneath the respective electric field distribution plots. This behaviour is in close agreement with the experimental graphs shown previously. With a measured quality factor of 418000 and a modal volume of $0.34(\frac{\lambda}{n})^3$, this H0 nanocavity has the highest Q/V ratio ever reported for 2D PhC cavities with modal volumes that are smaller than 1 in units of $(\frac{\lambda}{n})^3$ as shown in table 4.2.

The measured Q-value exceeds all others by at least one order of magnitude. Amongst cavities with a larger modal volume, only the heterostructure cavity has shown a larger $\frac{Q}{V}$ ratio (Q=3.9 million and $V=1.3(\frac{\lambda}{n})^3$). Nanobeam cavities [241] have displayed a comparable value, but at the expense of a structure that can less easily be integrated in a two-dimensional photonic

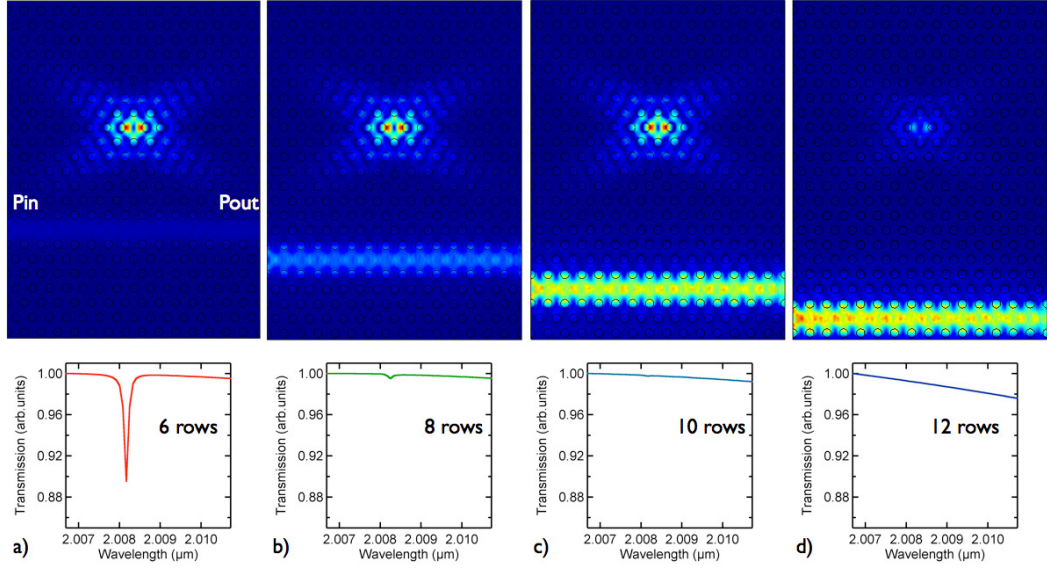


Figure 4.13: Numerical study of transmission in H0 cavity through side coupling. a) to d) show the cavity field profile and waveguide mode intensity along with the corresponding transmission plots for increasing waveguide-cavity distances.

Cavity type	Measured Q	Modal volume in $(\frac{\lambda}{n})^3$	$\frac{Q}{V}$	Reference
H0 (InGaAsP)	6500	0.26	24000	[87]
H1 (GaAs)	17000	0.39	44000	[240]
r-modulation (Si)	47000	0.9	52000	[84]
L3 (Si)	88000	0.71	120000	[160]
Optimized H0	420000	0.35	1200000	This thesis

Table 4.2: Comparison of Q-factors and mode volumes recently demonstrated in ultra-small photonic crystal cavities with modal volumes that are smaller than 1 in units of $(\frac{\lambda}{n})^3$.

circuit. The presented design has the advantage of being spatially compact, reproducible and is extremely robust to fabrication imperfections. As a further illustration of the effectiveness of the evolutionary optimization method, an alternate optimal H0 cavity has been designed with the requirement of a smaller modal volume, imposed by introducing a stricter upper bound in the shift $S1x$. This resulted in a design with the design parameters: $S1x=0.216a$, $S2x=0.103a$, $S3x=0.123a$, $S4x=-0.017a$, $S5x=0.067a$, $S1y=0.004a$ and $S2y=0.194a$. This design yielded an ideal Q-factor 1.05 million and a smaller modal volume of $0.26(\frac{\lambda}{n})^3$. This design was also fabricated and experimentally characterized. A maximum Q-factor of 260000 was measured. It was observed that this cavity mode was not found for waveguide-cavity distances of more than $10a$. This can be attributed to the fact that this cavity has a smaller modal volume compared to our previous design. This also clearly shows the dependence of the waveguide coupling strength to the modal volume of the cavity designs. These two demonstrations clearly show the full power of the present optimization technique that could extend to a variety of cavity designs tailored for different experimental requirements.

4.3.2 Nonlinear behaviour in the H0 cavity

An high Q/V ratio is expected to enhance the light matter interactions in the cavity volume leading to nonlinear effects at very low input powers. This is also one of the possible methods to validate the large Q/V measure of the proposed H0 cavity design. The response to an incident electric field ($E(t)$) on a material is determined by the polarization field ($P(t)$) that is set up due to the dielectric susceptibility (χ) of the material. This is related through a power series expansion [242] given by:

$$P(t) = \epsilon_0(\chi^{(1)}E(t) + \chi^{(2)}E^2(t) + \chi^{(3)}E^3(t) + \dots) \quad (4.2)$$

where ϵ_0 denotes the free space permittivity and $\chi^{(i)}$ denotes the i th order susceptibility of the material. This order determines the type of nonlinear effect that takes place in the medium as summarized in table 4.3 for the case of silicon. It can be seen that the third order processes are important for silicon as they are responsible for a variety of effects. Self-phase modulation

Order of susceptibility	Nonlinear process type
1	Change in refractive index, FCA
2	Not present in silicon (lack of centrosymmetry)
3	SPM, XPM, FWM, THG, TPA, FCA, FCD

Table 4.3: Nonlinear processes in silicon and order of susceptibility

(SPM) is created by three photons and leads to an index dependent refractive change that can consequently modify the spectrum of the pulse that caused it resulting in a broadening of the spectrum. SPM can also create two-photon absorption (TPA) that generates free carriers, which eventually results in free carrier absorption (FCA) and free carrier induced dispersion (FCD). All these effects reflect on the refractive index through the relation [243]:

$$n = n_0 + n_2 I - i \frac{\lambda}{4\pi} (\alpha + \alpha_{TPA} I) \quad (4.3)$$

where n_0 is the linear refractive index, n_2 is the optical Kerr coefficient, α is the linear absorption coefficient and α_{TPA} is the TPA coefficient. In addition to all these effects, the absorption of photons also causes an increase temperature that results in thermally induced refractive index variation. The thermo-optic coefficient of silicon in room temperature gives a change of refractive index of $\Delta n = 1.8 \times 10^{-4} K^{-1}$ [244]. The combination of all these effects results in a net refractive index change that changes dynamically. These non-linear effects are of interest to the optical switching community that has been looking at both electro-optic and thermo-optic effects. A nice demonstration of low voltage modulation of up to 1 GHz using free carrier effects on a photonic crystal waveguide device was shown by Gu and coworkers [113]. The thermo optic effect has been also used to show optical switching, but is limited by the slow switching speeds.

In the case of photonic crystal cavities, the change in the refractive index results in the shifting

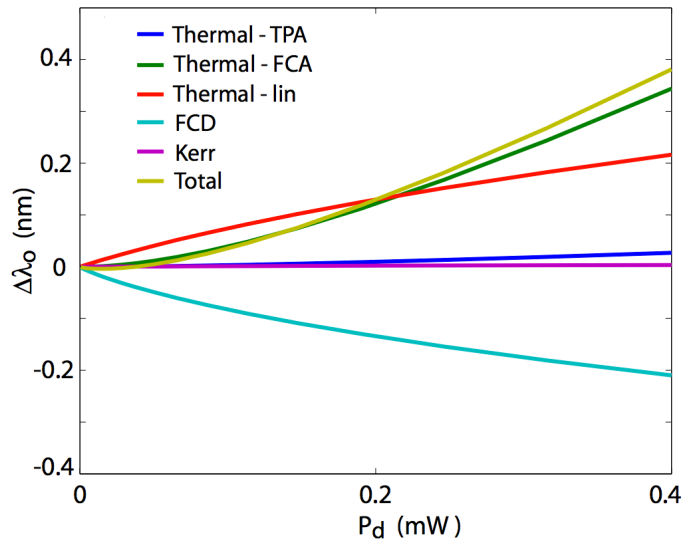


Figure 4.14: Variation of resonance wavelength in a PhC cavity due to nonlinear effects. The contributions of thermal, free carrier and Kerr effects are shown and the total resonance wavelength change is also shown. Reprinted from [84].

of the eigenmode and the shift in resonance wavelength can be calculated as [84, 88]

$$\Delta\lambda_{total} = \frac{\lambda_0}{n_0}(\Delta n_{Thermal} + \Delta n_{FCD} + \Delta n_{Kerr}) \quad (4.4)$$

where λ_0 is the cavity resonance wavelength and n_0 is the refractive index of silicon. $\Delta n_{Thermal}$, Δn_{FCD} , Δn_{Kerr} denote the change in refractive index of all the three contributions. The computation of these effects are complicated as it involves a variety of parameters to compute including the decay rates of the carriers and the effective area for each of the non-linearities involved. A complete computation has been presented for a photonic crystal cavity previously by Barclay and coworkers [84]. The computation from this work involves a high-Q-factor cavity in a square photonic crystal lattice and the numerical result is shown in figure 4.14. It can be seen that all the effects except the free carrier dispersion cause a red-shift in the resonance wavelength. The FCD effect causes a blue shift in resonance wavelength but is later dominated by the stronger effects for higher powers primarily due to the influence of thermal dispersion. In the case of the optimized H0 cavity, this experiment is performed in a cross-coupled device as shown in figure 4.15. The H0 devices are coupled to an input laser and a detector on the output side in a typical end-fire configuration.

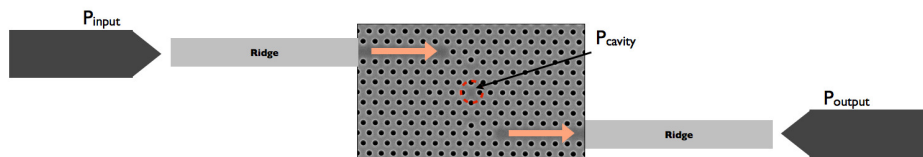


Figure 4.15: The cross-coupled device used for measuring nonlinearity

The cavities are coupled with a cross-coupling configuration as shown in figure 4.15, which creates a symmetric system with the cavity in the centre. This facilitates the use of the following method to estimate the power input to the cavity. For a known value of input power, the power in the centre of such a system is given by the following equation.

$$P_{cavity} = \sqrt{T}P_{input} = \sqrt{\frac{P_{output}}{P_{input}}}P_{input} = \sqrt{P_{input}P_{output}} \quad (4.5)$$

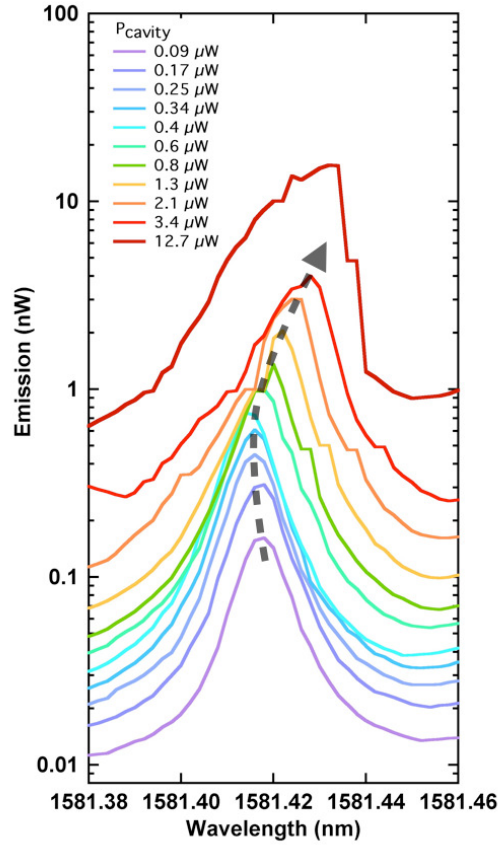


Figure 4.16: Nonlinear absorption and dispersion in the H0 nanocavity showing free carrier dispersion and thermal dispersion. The grey line is a guide to the eye. **Reprinted from a publication from this thesis [230].**

In the case of the cavity used for the characterization of nonlinear effects, we measure a transmission power $P_{output}=2$ nW in the detector, at the resonance wavelength, for an input power $P_{input}=4$ μ W, corresponding to the power coupled to the cavity $P_{cavity}=0.09$ μ W, for which the system response is still in the linear regime. The values of P_{cavity} for increasing input powers were linearly extrapolated from this value. It is to be noted that this is not an estimation of the intracavity power but only the power input to the cavity at the centre of the device. The emission Q-factor of this cavity was measured at low input powers and

was found to be 150,000. Figure 4.16 shows the nonlinear behaviour, as a function of input power. At low input powers, a slight blue shift of the cavity mode is observed and this is attributed to the presence of free carriers leading to free carrier dispersion. After a while, heating due to nonlinear absorption, and optical-Kerr nonlinearity result in a increasing redshift. At higher input powers, a clear drop in the spectral response on the red side of the resonance can be seen that indicates the onset of optical bistability. At this point, the cavity line shape does not resemble the usual Lorentzian profile but an asymmetric response due to the nonlinearities. The experimental results are in good agreement with the qualitative theoretical curves shown before. The notable fact is that these effects are achievable at very low optical powers confirming the enhanced Q/V of this newly proposed H0 nanocavity.

4.3.3 Optical bistability

As introduced in chapter 1, optical bistability is an interesting phenomena that results in a fact that the physical system has two distinct transmission states for a single input power value. To understand the bistability phenomena inside a 2D PhC cavity, the transmission through the system can be written as follows, for a symmetrically coupled simple two-port system [83].

$$\frac{P_{out}}{P_{in}} = \frac{1}{1 + [(\omega - \omega_c)/\Gamma]^2} \quad (4.6)$$

where Γ is the resonance linewidth and ω_c is the resonance frequency of the cavity for input and output powers P_{in} and P_{out} respectively. if a nonlinear material is introduced into the

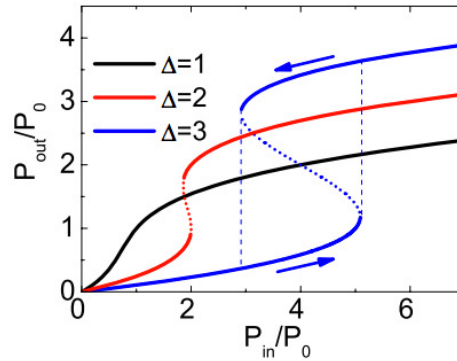


Figure 4.17: Optical bistability based on a two-port transmission model. Reprinted from [83]

resonator that modifies the refractive index such as δn is proportional to $n_2|E|^2$, where n_2 is the Kerr coefficient of the material. If there is an increase in input intensity, the resonance wavelength is shifted towards the red side of the spectrum due to the nonlinear index change. Taking this into account, the nonlinear transmission through the system is expressed as the following Lorentzian [83].

$$\frac{P_{out}}{P_{in}} = \frac{1}{1 + [(P_{out}/P_0) - \Delta]^2} \quad (4.7)$$

where P_0 is the characteristic power of the cavity and Δ is the frequency detuning normalized to the width of the resonance peak. From this expression, the behaviour of the transmission of the system for various values of Δ is plotted in figure 4.17. It is observed that for values of Δ greater than $\sqrt{3}$, bistable loops are formed. It can also be seen that the width of the hysteresis loop also increases with the increase of Δ . This enables the device to retain the past state of the system in steady state even-though the response of the material is instantaneous. This characteristic power for nonlinearity is expected to be drastically decreased for PhC based cavities due to the ultra small modal volumes and high Q-factors.

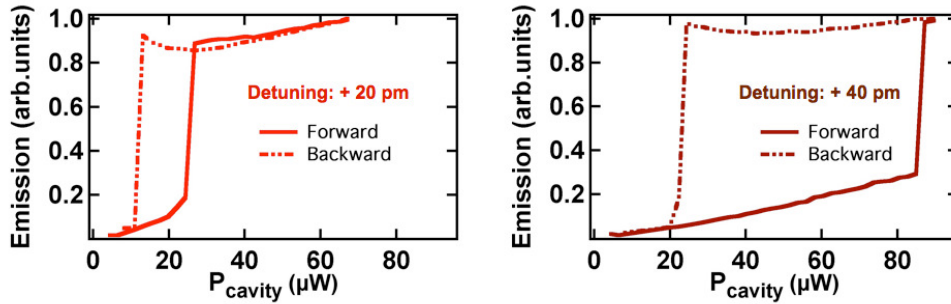


Figure 4.18: Optical bistability in the H0 nanocavity showing the hysteresis loops for detuning values a) 20 pm and b) 40 pm. *Reprinted from a publication from this thesis [230].*

Cavity type	Bistability threshold power	Year	Reference
Double heterostructure	28 μW	2005	[88]
Modified L4	26 μW	2005	[91]
Modified H1	420 μW	2007	[245]
Modified L3	26 μW	2013	[94]
Genetic H0	10 μW	2013	Our work

Table 4.4: Comparison of optical bistability threshold in 2D Si PhC cavities.

In order to characterize this bistable behaviour, the input power was gradually increased and the steady state emission intensity was recorded. Figure 4.18 shows the measured hysteresis plot for an excitation wavelength that was red-shifted by 20 pm and 40 pm from the cavity resonance. As the linewidth of this mode is close to 10 pm, the bistable behaviour occurs as expectedly for wavelengths with detuning greater than $\frac{\sqrt{3}}{2}$ as predicted by the previously said arguments. Switching power ratios of 2.0 and 4.5 along with a contrast above 70 percent are obtained for the two detuning values respectively, demonstrating the robust and controllable bistable behaviour. The present cavity also displays the lowest power threshold for optical bistability hysteresis ever measured in a 2D PhC silicon cavity as can be inferred from the comparison table 4.4.

4.4 Discussion and summary

At the time of this thesis, the highest reported Q-factor measured from a 2D PhC membrane stands at 3.9 million as reported by Taguchi and coworkers [168]. The interesting note about this particular heterostructure design is the numerical Q-factor which was reported to be at around 20 million [162]. In spite of such a high theoretical prediction, the reported measurements are far from this value, primarily due to the limitations set by fabrication induced disorder.

The discussion on the influence of disorder on cavity Q-factors was already discussed in chapter 2 of this thesis in this particular context. It can also be inferred from table 4.5 that the Q-factor of the heterostructure cavity has been improved from 0.6 million to around 4 million in a span of 6 years, primarily due to the improvements in fabrication technology.

Material	Cavity type	Measured Q-factor	Year	Reference
Silicon	Heterostructure	0.6 million	2005	[162]
Silicon	Modified W1	0.8 million	2006	[144]
Silicon	Heterostructure	2.5 million	2007	[246]
Silicon	Modified H1	0.3 million	2007	[245]
GaAs	Modified W1	0.7 million	2008	[247]
Silicon	Modified W1	0.2 million	2011	[248]
Silicon	Modified W1	1.3 million	2011	[249]
Silicon	Heterostructure	3.9 million	2011	[168]
Silicon	Modified H0	0.5 million	2013	This thesis

Table 4.5: *Ultra-high-Q 2D PhC nanocavities: A chronological compilation.*

The proposed optimized H0 designs are one of the most compact and versatile designs ever shown with 2-D photonic crystals. A high Q-factor and a small modal volume are not the only important requirements in view of applications. Many current photonic structures rely on spatial proximity between two cavities or one cavity and one waveguide, while in a longer-term perspective the density of optical elements will represent a key figure of merit of photonic circuits. The ability to produce small compact cavities with record-high Q-factors as made possible by our optimization procedure and demonstration constitutes a major advance in view of an integrated photonic technology. The design allows for the fact that two such cavities can be fabricated at approximately $5 \mu\text{m}$ distance from each other along the x-direction and much less along the y-direction without significantly affecting each other. If this is compared to the popular heterostructure design [168] for example, the minimal x-distance is $20 \mu\text{m}$. In view of the fabrication of photonic integrated circuits, the proposed H0 cavity would thus nominally allow for a 16x higher density of optical elements on the circuit. Also, the form factor of this H0 cavity is much less elongated than other well-known designs of high-Q cavities, which increases the possibilities of spatial arrangement of several cavities.

In order to show the versatility of the evolutionary design methodology, three H0 designs are

Cavity	Q_{GME}	Q_{FEM}	V_{GME} in $(\frac{\lambda}{n})^3$	V_{FEM} in $(\frac{\lambda}{n})^3$
H0 design 1	1.95 million	1.6 million	0.34	0.38
H0 design 2	1.05 million	1.0 million	0.25	0.26
H0 design 3	8.89 million	8.2 million	0.64	0.71

Table 4.6: Summary of evolutionarily optimized H0 cavity designs.

proposed and their computed Q-factors and modal volumes are shown in table 4.6. It can be seen that this method can be used to set very specific boundaries such as controlling the modal volume or the Q-factor and the required ratio can be deterministically designed. The first two designs are shown experimentally in this thesis while the third design is not attempted due to the fact that it will be dominated by disorder. This table is an important illustration of what can be achieved by optimization of a simple and compact H0 PhC nanocavity. These results are expected to set a new standard that might determine the direction along which photonic circuits could be developed in the near future.

5 Integrated photonic devices in GaN for light-matter interactions

This chapter details the study of integrated photonic devices with GaN grown on Si. Section 1 gives a brief overview of the history of GaN semiconductor technology followed by a review of the recent developments in integrated photonics based on GaN in section 2. The experimental results obtained during this thesis along with the fabrication technology that was developed are reported in section 3 and section 4, which cover the near-IR and visible wavelengths respectively. Section 5 concludes the chapter with a summary and perspectives for the future.

Contributions:

This work was performed as a collaborative effort with the group of Prof. Nicolas Grandjean (LASPE). In the case of experiments in the near-IR wavelengths, the modelling, design and optical characterization was performed by myself, the layer growth was performed by J.-F. Carlin and the sample fabrication by N. Vico Triviño (LASPE). In the case of experiments in the visible wavelengths, the layer growth was performed by J.-F. Carlin, the sample fabrication and optical characterization were completed by N. Vico Triviño and her colleagues and the modelling and post-experimental analysis of the results was performed by myself.

Publication of results:

The results obtained for the near-IR wavelength are published in Optics Letters [127] and in Applied Physics Letters [126]. The results for the visible wavelength are published in Applied Physics Letters [128].

5.1 Gallium nitride semiconductor technology

5.1.1 GaN for high power electronics

The rise and growth of semiconductor fabrication technology has strongly influenced present day life with far reaching implications in communication, computation, entertainment, security and health care. One of the fundamental building blocks of this transformation is the Integrated Circuit (IC) technology that also earned its inventor, Jack Kilby, the Nobel Prize in physics in the year 2000. Since the 1970s, there has been an increased use of Si power MOSFETs (Metal Oxide Silicon Field Effect Transistor) for high power electronics applications. The wide usage of Si has been attributed to its low fabrication costs, ease of use and reliable performance. As applications involving high temperature and high frequency began to rise, the use of wide bandgap materials was preferred over time as they could supersede the performance offered by Si owing to their superior thermal and electrical properties. The following table 5.1 from a review by Pearton [250] lists the important electrical and thermal properties of the most widely used semiconductor materials including GaN.

Property	Si	GaAS	4H-SiC	GaN
Bandgap E_g (eV)	1.12	1.42	3.25	3.44
Breakdown field E_b (MV/cm)	0.25	0.4	3.0	4.0
Electron mobility μ ($\text{cm}^2/\text{V s}$)	1350	6000	800	1300
Thermal conductivity κ (W/cm K)	1.5	0.5	4.9	1.3
Dielectric constant ϵ	11.8	12.8	9.7	9

Table 5.1: Comparison of electrical properties of semiconductors [250].

As can be easily inferred from the table, the wide bandgap materials offer a significant improvement in bandgap energies and breakdown fields compared to silicon. This would enable the achievement of simpler and more efficient high temperature circuits. This would also lower the high cost of temperature sensitive packaging that is required for Si based power electronics devices. Apart from this, GaN also has a higher mechanical and thermal stability making it robust for operation in harsh environments.

The growth of the semiconductor industry started with Si and followed with GaAs due to the ease of their fabrication technologies [250]. GaN in spite of its inherent advantages proved challenging to grow until the 1990s. Commercial applications in the power electronics industry have already seen a recent surge in the use of GaN technology. It can be seen that SiC has very similar advantages, but it is believed that the improvements in fabrication would give an edge to the GaN based power electronics devices in the near future. A detailed and extensive review on the various electronic properties of the III nitride family can also be found here [251]. Moreover it has also been recently found that GaN is compatible with biological and neural substances that would enable it for in-vivo or implant applications [252].

5.1.2 GaN for light emission and optoelectronics

Light generation for various purposes has always been of a significant importance in the lives of humans. A brief journey through modern lighting technology starts with the incandescent lamps of Edison in 1879 that were based on tungsten filaments followed by neon lamps and fluorescent tubes in the 1930s. The beginning of lighting with semiconductors goes back to 1962 with the publishing of seminal papers about Light Emitting Diodes (LED) and semiconductor lasers [253], [254]. Starting from emission of red light, LEDs were later developed for yellow portion of the spectrum with light efficiencies superior to those of incandescent lamps [255]. The evolution of the LED lighting development can also be seen visually in figure 5.1

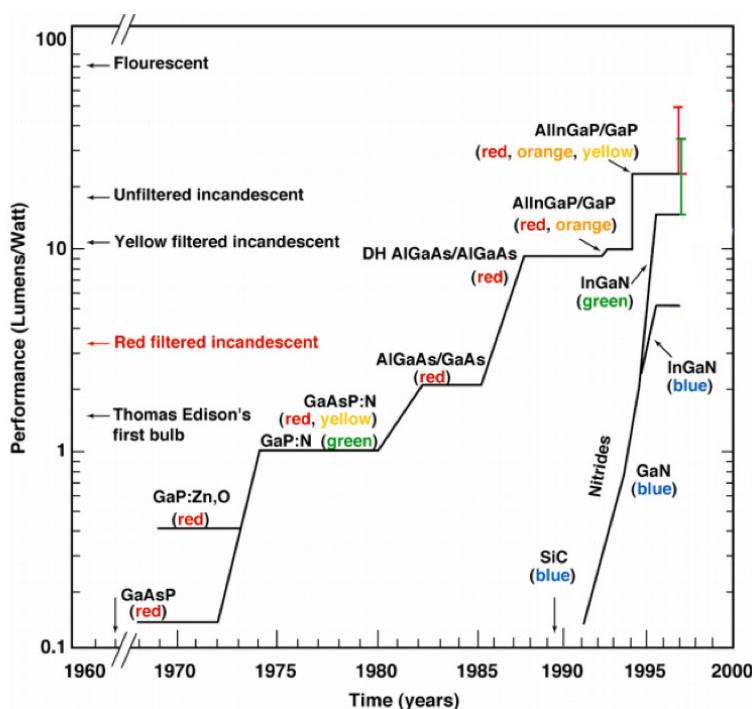


Figure 5.1: Evolution of the LED technology development until the year 2000. Reprinted from [256].

Light emission in the green to blue spectrum has so far been harder due to the lack of appropriate materials and processing techniques. SiC has been used for this purpose but has not been able to perform with satisfactory levels of efficiency compared to the red and yellow LED counterparts. A highly efficient source in the blue is required to be able to achieve a full color display or a white light LED. Due to the value of the bandgap energy, GaN is much more efficient for light emission in the UV and blue wavelengths. This is far more efficient than the previously used frequency conversion techniques for generation of blue light. The bandgap energy can be also tuned by varying the level of doping with various alloys of GaN such as Al and In. The bandgap energies for various materials used in the lighting devices are shown in figure 5.2. All these alloys also possess a direct bandgap leading to a high quantum efficiency in emission.

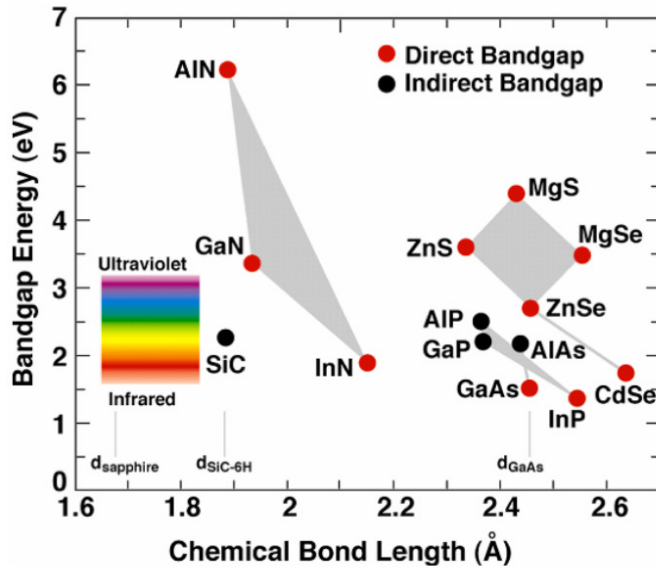


Figure 5.2: Bandgap energies for various LED materials. Reprinted from [256].

The initial demonstration of lasers came at 3.45 eV at 2K from GaN needles in 1971 from Dingle and coworkers [257]. After a number of years of progress in p-type doping and technological development by Amano and others [258, 259], the first high quality p-n junction with GaN was reported in 1991 by Nakamura and coworkers [260]. Nakamura also reported the first bright blue light LED in 1994 [261]. This was also followed up with their first demonstration of blue diode lasers in continuous wave operation in room temperatures in 1996 [262]. In 2006, these scientific breakthroughs finally lead to the first commercialization of the Blu-ray disc by Sony Corporation. There has also been a reported demonstration of a UV LED using III nitrides from Khan and coworkers in 2008 [263]. Presently, blue light LEDs display a wall plug efficiency of approximately 60% which is about 10 times that of an incandescent bulb [264]. In order to display the magnitude of difference created by the technology of the GaN blue laser diodes, table 5.1 compares the various storage technologies and their memory capacities available in the commercial market during the time of this thesis in 2013.

Type	Year	Laser wavelength (nm)	Typical storage capacity
Compact Disc (CD)	1982	780	700 MB
Digital Video Disc (DVD)	1995	650	4.7 GB (single layer)
High Density DVD (HD DVD)	2006	405	15 GB (single layer)
Blu-ray	2006	405	25 GB (single layer)

Table 5.2: Comparison of optical storage media.

It can be understood that GaN lighting devices can drastically change the paradigm of lighting and display technologies with their high power output visible wavelength performance. This is also being exploited by high density optical memory, lithography and printing technologies.

5.2 Integrated photonics with GaN: A brief overview

The development of GaN-based integrated optical devices only started a few years ago mainly due to technological challenges. The advantage of GaN to fabricate visible wavelength photonic crystals being quite obvious, owing to its near-UV bandgap and the fact that GaN is transparent in both infrared and the visible wavelength range. Furthermore, Two Photon Absorption (TPA) is non-existent at near IR wavelengths, which makes it an ideal candidate for high power operating systems. The major interest has also been in using the GaN based micro cavities towards cavity quantum electrodynamics experiments that include room temperature lasing in polaritons [265], study of strong coupling in GaN based microcavity based systems [266] amongst others. There has been only a few notable demonstrations of photonic crystals in GaN and there is a growing interest to study them. The first demonstration of PhC structures was reported in 2003 by Oder and coworkers [267] where they show enhancement of emission at 475 nm using near field optical measurements. Choi and coworkers also reported GaN PhC membranes with L7 nanocavities operating at 480 nm with experimental Q-factors of around 800 [268]. There was an experimental observation of guided resonances in GaN on Sapphire based PhC structures in 2005 [269]. A Q-factor of 2400 was reported by Arakawa's group [270] and the group of Boucaud [271] using AlN. The extraction efficiency of LEDs was also improved by the usage of III-nitride photonic crystal structures. This effect has been studied and reported by a number of research groups [272–277]. GaN based photonic crystal laser devices were also reported in the following years owing to the highly growing interest to exploit the use of the PhC properties [278], [279]. There has also been an interesting report on using GaN for making a three dimensional photonic crystal logpile structure [280]. In 2011, Xiong and coworkers also demonstrated second harmonic generation with microring devices using GaN on Si [281]. In this context, the demonstration of GaN photonic crystals cavity slabs with high quality factors and small mode volumes across the entire near-IR and visible wavelength spectrum is highly desirable, which is one of the main objectives of this thesis.

GaN growth challenges

As can be seen from the above sections, GaN is a very promising semiconductor technology for future photonics and electronics applications. The major challenges impeding the growth and development of this field are attributed to the difficulty in growing high quality GaN layers. The most widely used substrates are Sapphire, Silicon Carbide (SiC) and Silicon (Si). The growth of GaN on these alien substrates brings in a lot of disadvantages due to the processing steps that are involved. The problems mainly arise due to the mismatch in lattice, mismatch in thermal expansion coefficient etc, which finally leads to a large dislocation density in the finished layer. These defects deteriorate the optical and electronic properties of the final layer. One of the biggest breakthroughs in reducing the dislocation density problem is the use of buffer layers below the GaN layer. A summary of these growth techniques and the associated issues regarding the above-mentioned substrates can be found here [282]. In this thesis, all the devices are fabricated using GaN grown on Si substrate.

5.3 GaN photonic devices in the near-IR: Experimental results

5.3.1 Single mode operation

While working with integrated optical devices, It is important to note that single optical mode operation is often and is highly desirable. In the case of photonic crystal slabs, each mode will have its own bandgap and hence the final bandgap will be a superposition of all individual bandgaps. This has to be kept in mind before the growth process is started. In this case, it was priorly known that there would be a thin buffer layer of AlN on one side of the slab during the fabrication process. With these parameters taken into account, the study of the thickness of the membrane for various wavelengths was performed with the aid of CAMFR, an eigenmode expansion tool [283]. It can be seen from figure 5.3 that a purely single mode operation is

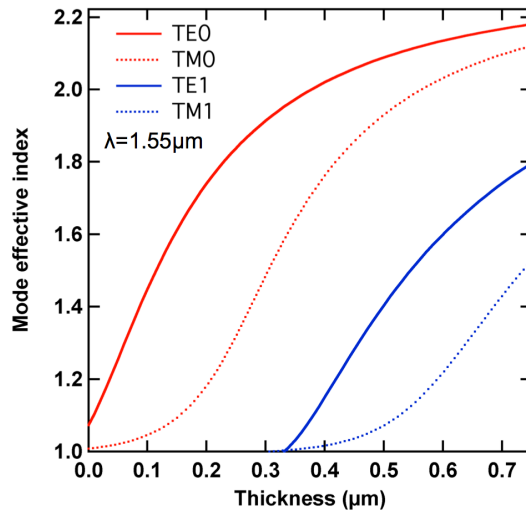


Figure 5.3: Study of thickness for single mode operation for near-IR wavelength (1.55 μm).

possible for a 330 nm thick GaN slab along with a 60 nm AlN layer on one side for the case of near-IR wavelengths. This information was taken into account for the next step, which was to grow the GaN layer.

5.3.2 Growth and fabrication of samples

In spite of the advances in GaN fabrication technology, the achievement of free standing membranes with sufficient air gaps has always remained a considerable challenge. In order to overcome the issues surrounding this problem, in this work, GaN photonic structures were fabricated by under-etching the Si substrate. The steps are listed as follows and are also summarized in figure 5.4. It can be seen that the entire structure, including the wire waveguides and the PhC lattice, is fabricated in a single lithographic step, as well as in single subsequent etching steps, which considerably reduces the time needed for the total processing.

5.3. GaN photonic devices in the near-IR: Experimental results

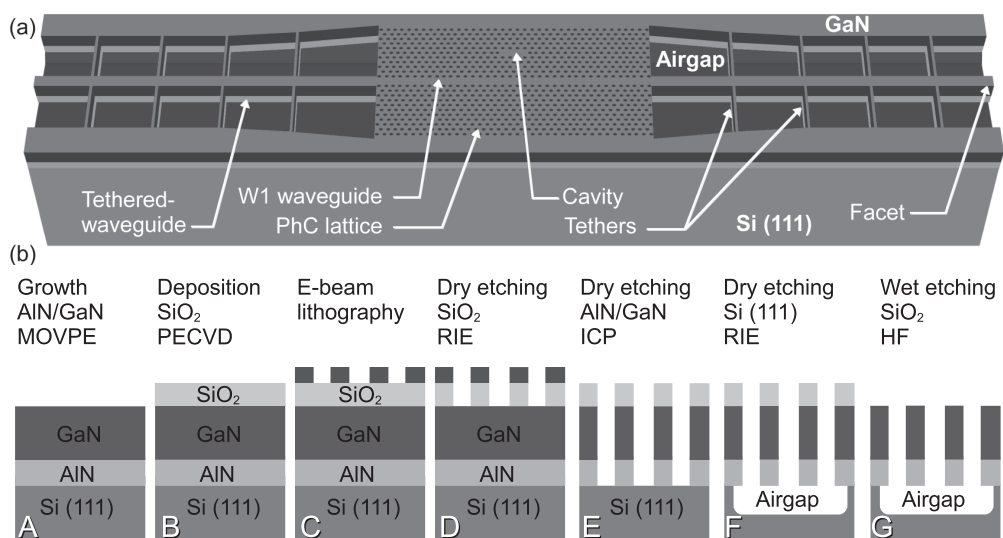


Figure 5.4: Schematic of the fabrication process in near-IR: a) Illustration of the final structure of an end-fire coupled PhC W1 waveguide. b) The sequential flow of the fabrication process steps. Reprinted from a publication from this thesis [126].

- (A) The process starts with the growth of a thin (60 nm) AlN buffer layer on Si (111) followed by 330 nm of GaN along the c-axis (0001) through Metal Organic Vapour Phase Epitaxy (MOVPE) process.
- (B) It is important to note that such thin AlN/GaN layers grown on Si are usually affected by tensile strain mainly induced by the difference in their thermal expansion coefficients. After the growth, a 100 nm thick SiO₂ layer was deposited on top of the epitaxial structure through Plasma-Enhanced Chemical Vapour Deposition (PECVD)
- (C) This layer acts as a hard-mask during the entire fabrication process protecting the GaN surface and hence avoids the degradation of the pattern. E-beam lithography was then carried out to pattern the previously spun positive photoresist ZEP-520.
- (D) Once the resist is developed, the pattern is transferred first to SiO₂ by fluorine-based Reactive Ion Etching (RIE).
- (E) The pattern is then transferred to the AlN/GaN stacked-layers using chlorine-based Inductively Coupled Plasma etching (ICP).
- (F) Finally, the membrane is released through fluorine-based RIE of the Si (111) substrate, which is a dry process. An air-gap of the order of 3 μm was achieved, which is large enough to avoid light losses through the substrate at 1.5 μm.
- (G) Finally, the SiO₂ layer was removed using a hydrofluoric acid solution. This is the most critical step due to the fragility of the self-supported structure, especially at the facets, and a very careful manipulation is required in order to prevent collapsing and peeling off of the wire waveguides.

5.3.3 Examination of structures with SEM and AFM

The various components of a single integrated PhC W1 device are shown in the collection of SEM images in figure 5.5. The images show the GaN wire waveguide that is mechanically held stable with the aid of tethers. These tethers are spaced equally with intervals of $20\ \mu\text{m}$ and in some cases also $10\ \mu\text{m}$. The tether designs are also previously implemented for an InP based wire waveguide by Talneau and coworkers [284]. This interval is chosen for the reasons concerning mechanical stability. Shorter tether spacings results in increased tether scattering losses and a larger spacing results in the peeling off of the wire waveguide. The tethers are $200\ \text{nm}$ in width and the width of the wire waveguide is $3\ \mu\text{m}$ and is slowly tapered down to $1\ \mu\text{m}$ at the beginning of the W1 waveguide as can be seen in figure 5.5c. The image also shows the smooth surface and vertical sidewalls of the wire waveguide.

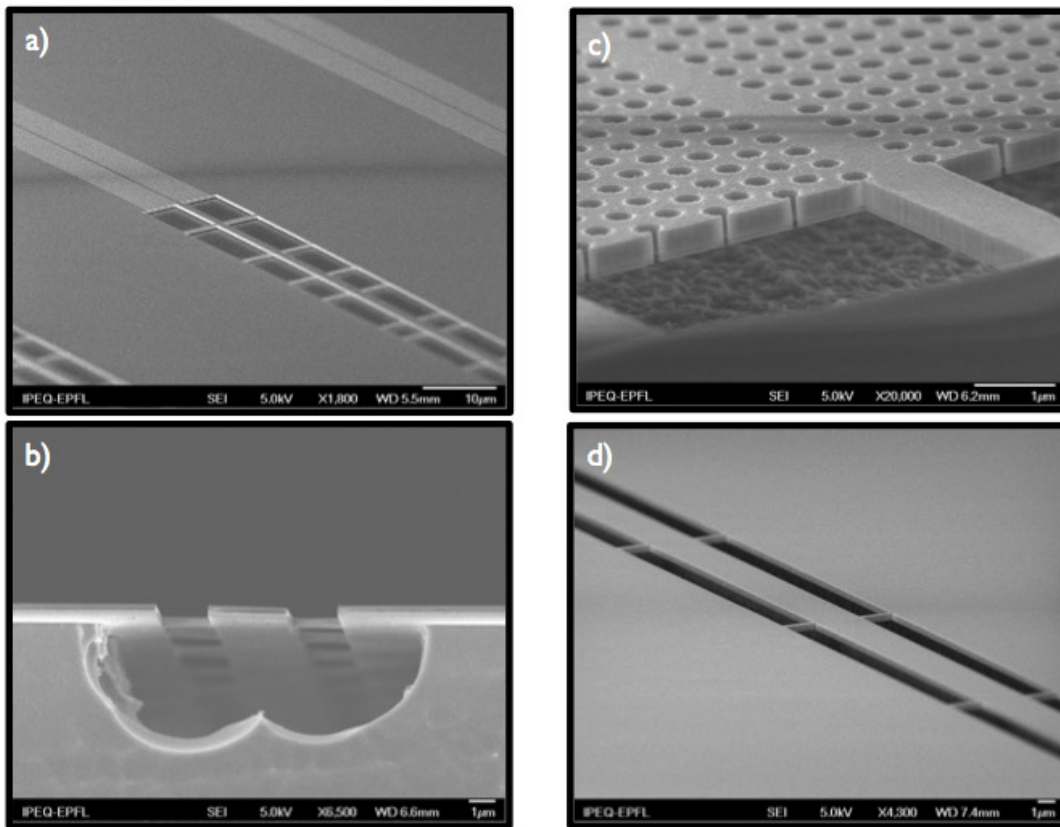


Figure 5.5: Scanning Electron Micrograph images of the GaN device. a) Image showing the freely suspended wire waveguide supported by tethers along with the suspended PhC membrane. b) The end facet of the integrated PhC device showing the smooth and well suspended wire facet with an isotropically etched air-gap. c) The entrance to the W1 waveguide and the wire termination also showing the smooth and vertical sidewalls. d) The close up view of the wire waveguide with equally spaced tethers of $20\ \mu\text{m}$.

The technology allows for the achievement of high verticality of the side walls ($<5^\circ$). A closer view at the input of the photonic crystal is shown in figure 5.5c. The PhC slab is composed of a

5.3. GaN photonic devices in the near-IR: Experimental results

GaN layer with a thickness of 330 nm and an AlN layer with a thickness of 60 nm. These two layers can be distinguished with the naked eye from the optical contrast in the cross-section of the slab owing to the difference in their refractive indices. The diameter of the air hole is 234 nm with a lattice constant of 600 nm and they form a hexagonal lattice. At the input side, the crystal is cut exactly on the edge of the hole in order to achieve a maximal coupling efficiency from the nanowire waveguide to the PhC W1 waveguide. Figure 5.5b also shows an arc like air-gap below the suspended wire that is due to the isotropic etching process involved. It is to be noted that this is the first reported demonstration of a completely free standing GaN PhC device operational with a standard end-fire setup.

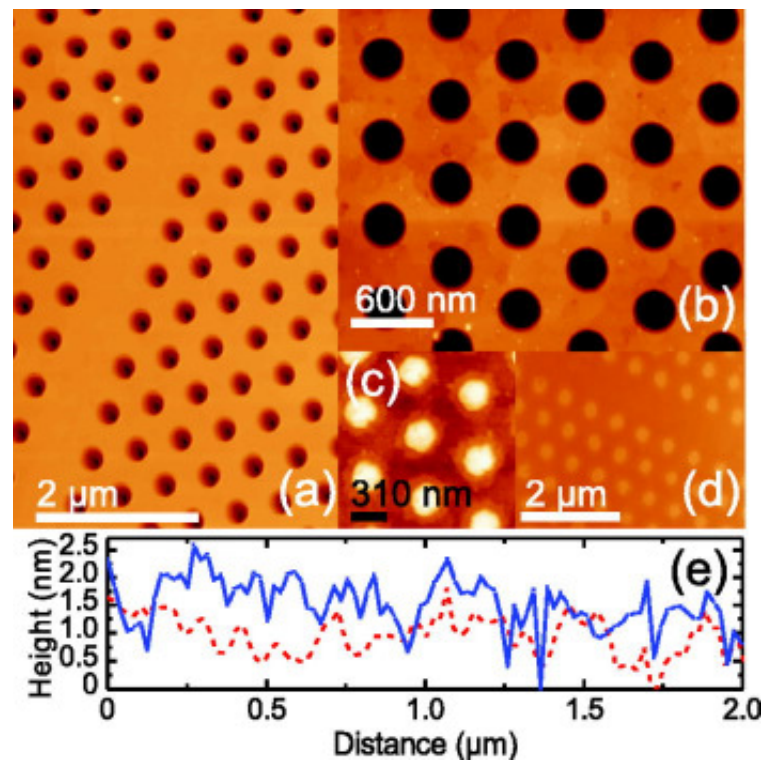


Figure 5.6: Atomic force microscope measurement of the PhC slab a) W1 waveguide b) hexagonal lattice of the PhC c) and d) AFM images of b) and a) respectively. e) Surface roughness profile of the W1 PhC waveguide. *Reprinted from a publication from this thesis [126].*

Atomic Force Microscope (AFM) measurements were also performed after the sample was fully fabricated and can be seen in figure 5.6. A slight trend for the holes resembling a hexagonal shape can be seen. The measurements show bumps on the backside of the sample that is attributed towards the adhesive tape used for sticking the membrane to the sample holder, which flows through the holes of the membrane. Nevertheless, it can be seen that the RMS roughness of the W1 was found to be lower than just 1.5 nm over a 500x500 nm² area. Figure 5.6e displays the surface roughness profile over a 2 μm distance on top of the W1 waveguide and the peak-valley height is lower than 2.5 nm.

5.3.4 Comparison of process flows: SOI vs GaN on Si in the near-IR

The results in this thesis cover photonic crystals that have been fabricated with both SOI and GaN. It is interesting to note the differences and similarities between the process flows of the two technological platforms. The schematic version of the comparison is shown in figure 5.7. A number of state-of-the-art fabrication methods are employed in both the cases that were developed in-house within the respective research groups (LOEQ and LASPE). In the case of SOI flow, 220 nm thick core Si layer and a 2 μm thick buried oxide buffer layer are supported by the base substrate. In the case of GaN, a 330 nm thick GaN core layer and a 60 nm of AlN buffer

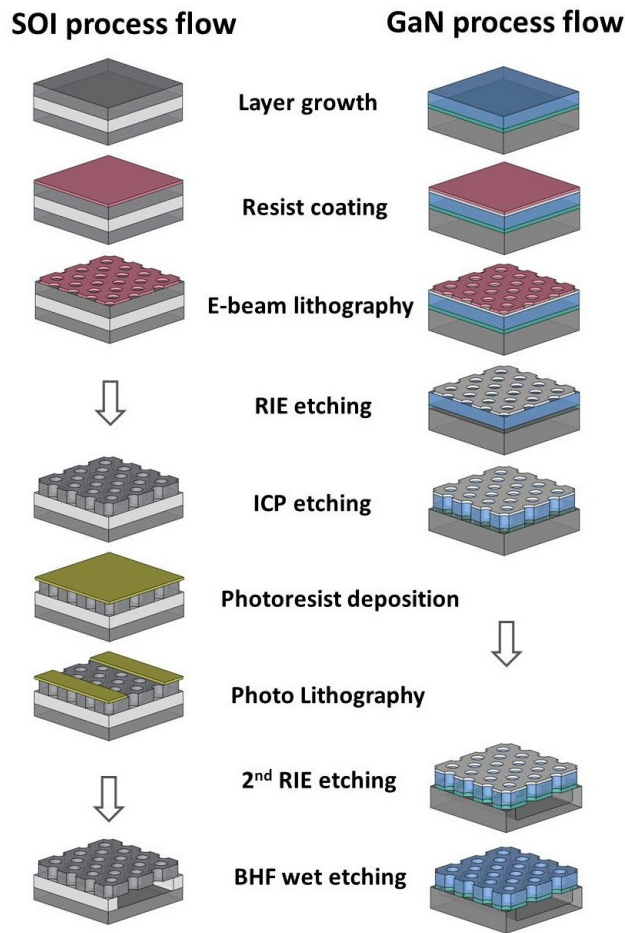


Figure 5.7: Comparison of SOI and GaN process flows (left and right). The single lithographic step advantage is clearly visible for the GaN process flow.

layer are grown on top of an Si substrate. This step is followed by the e-beam lithography that is used to achieve structures with a very high resolution of the order of 1 nm. From this point, there are differences in the fabrication flow as indicated in the schematic. The primary difference to note is that the GaN process flow results in much lesser enlargement effects on the holes compared to the SOI process flow due to the type of dry etching method used.

5.3.5 Optical characterization of the devices

Wire waveguides

The preliminary step before guiding light into a PhC device is to demonstrate guiding in a simple wire waveguide. This allows for injecting light into the photonic crystal and for collecting the transmission in a typical end-fire configuration. In the case of SOI platform, the ridge waveguide is typically created with a stripe of Si that is generally supported on top of an oxide layer. However, in the case of GaN on Si technology, the refractive index of the underlying layer has a higher value ($n_{\text{GaN}}=2.31$ and $n_{\text{Si}}=3.47$ respectively at near-IR wavelengths). This will prohibit the guiding of light through the wire waveguide leading to the use of a fully suspended wire waveguide such that the silicon layer underneath the GaN wire is completely removed through dry etching. These wire waveguides are then mechanically supported through the use of appropriately designed tethers as shown already in the previous section.

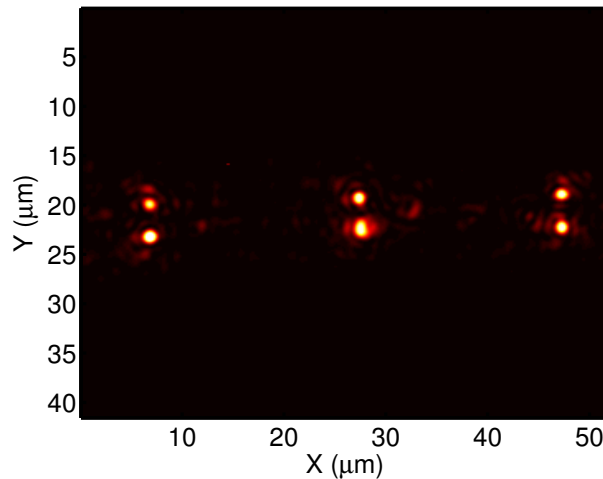


Figure 5.8: Light scattering observed from the equally spaced tethers holding the wire waveguide. Measurement was made using a microscope objective with an N.A of 0.9.

In this particular design, the nanowire width at the facet of the sample is set to $3 \mu\text{m}$ to maximize the coupling to the focussed beam from the lensed fiber tip. The width is then gradually tapered down to $1 \mu\text{m}$ next to the photonic crystal waveguide in order to couple efficiently into the W1 PhC even mode. The tethers that hold the wire waveguide are randomly or periodically distributed in different devices. The implication of this periodicity can be seen in the formation of Bragg type resonance peaks in the transmission spectrum of the device that could impede the coupling to the PhC devices. The random distribution prevents and minimizes this effect. Nevertheless, these tethers prove to be quite useful also in the optical characterization of the sample. In the first order, the tethers that are used to suspend the wire in this case can be assumed as uniform periodic scatterers that scatter the light in all directions and this scattered light can be imaged using an infrared camera from the top of

the sample as seen in figure 5.8. Three pairs of bright spots can be observed that corresponds to the scattering of guided light in the wire by the tethers. The decay of this scattered light obtained by combining frames along the nanowire propagation direction upto 2 mm was used to estimate the losses in the nanowires as shown in figure 5.9. The propagation losses are estimated to vary from 10 to 12 dB/mm, which is a first reported loss number for GaN based free standing wire waveguides of this thickness. A similar measurement was performed with a tether spacing of 10 μm spacing, and the loss was found to be around 10 dB/mm. This indicates that the tether dimensions have rather a small influence over the propagation loss in the nanowire waveguide, and it could also still serve as a useful scattering probe tool.

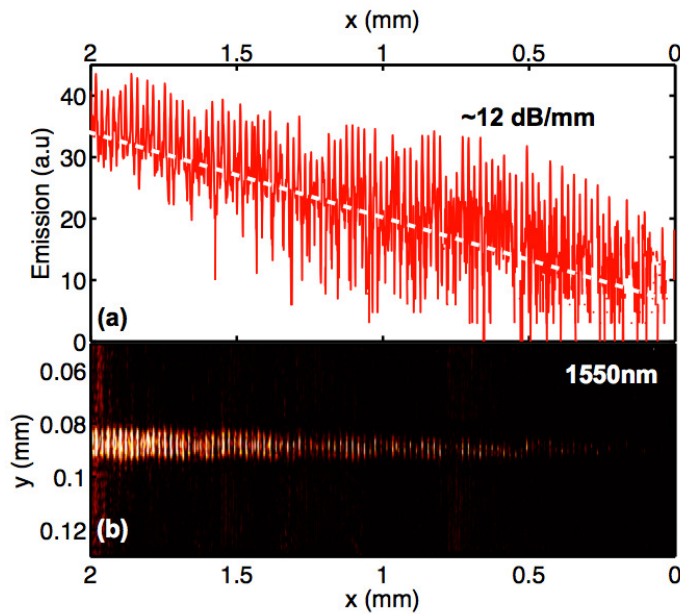


Figure 5.9: Propagation loss of a tethered nanowire (a) Integrated intensity profile of the scattered light from the tethers along the propagation direction. (b) Real space image of scattered light on top of the wire waveguide imaged with an infrared camera. **Reprinted from a publication from this thesis [127].**

The additional losses observed for the GaN wire can be due to a number of reasons such as fabrication imperfections and the presence of the AlN layer. As a consequence of these loss values, the maximal transmission power measured from the end-fire setup was about 20 nW for a 1 mW injection power from the tunable laser. Considering the fiber to fiber transmission power which is 85 μW , the total decay in a 3 mm nanowire is 36 dB. This value is in accordance with the scattered light measurement (30 dB in 3 mm) and the additional 6 dB loss is attributed to the coupling losses between the lensed fiber and the device facets. It is hard to compare the loss figures across different platforms as there are several parameters such as thickness, height etc. involved. This loss value can be compared to the reported InP nanowire [285] with a very similar tethering scheme whose propagation loss is 1.6 dB/mm. In the case of Si waveguide technology, the initial reported loss figures are around 8 dB/cm in 1991 [286]. The progress in technology over the years by improving side wall roughness and surface smoothness has

resulted in remarkable loss figures down to 0.026 dB/cm in this example [287]. This amounts almost three orders of magnitude reduction in the loss figures over two decades of technology optimization.

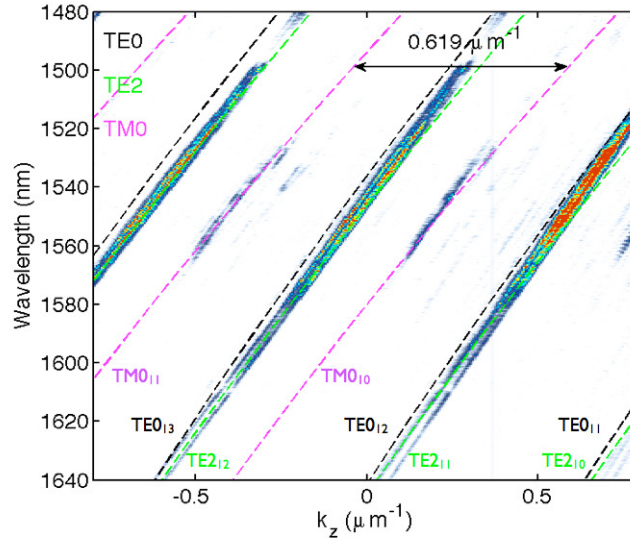


Figure 5.10: Experimental and numerical dispersion (dotted lines) of wire waveguides is shown. The folding period (G) corresponds to $0.619 \mu\text{m}^{-1}$ for all the modes. As each dispersion line is folded multiple times due to the tethers (grating), the folding order for each mode is indicated in the subscript of the mode labels (TE_{n_m} denotes the n th mode folded m times). **Reprinted from a publication from this thesis [127].**

The theoretical study of the GaN suspended waveguide dispersion was performed with the FEM not taking into the account the presence of tethers. The computations show the presence of 2 TM modes and 4 TE modes. The light emitted from the top of the sample is collected by an objective with a NA of 0.45 to perform Fourier imaging. This field of view allows for viewing several scatterers in real space and hence measuring the dispersion of the propagating modes in the reciprocal space. The spacing of the tethers in the measured device is $10 \mu\text{m}$ which gives rise to a folding period of $0.619 \mu\text{m}^{-1}$ in reciprocal space. The experimental and the superimposed theoretical results are shown in figure 5.10, and it can be clearly seen that the two strong lines representing the two TE modes are the even modes TE0 and TE2 and the weak line representing the TM mode is TM0. The mode numbering refers to lateral mode numbers, as the membrane is single mode along the vertical direction. Given the symmetric nature of the waveguide, one would expect the TM mode to be not coupled in, but the faint coupling observed in figure 5.10 is attributed to the asymmetry created in our structure due to the thin layer of AlN under the GaN layer. All the modes appearing in the dispersion are the in-plane modes that are matched strongly with the mode profile coupled from the tapered fiber. The proximity of the TE dispersion lines, for instance between TE0₁₂ and TE2₁₁ observed in figure 5.10 where TE _{n_m} denotes the n th mode folded m times, is due to the fact that the folding orders are coincidentally close to one another when they are folded into the light cone due to the chosen grating spacing, which has also been confirmed with calculations.

Device characterization: Photonic crystal waveguides

The PhC W1 waveguide is an important element in the family of devices based on photonic crystals. Apart from its properties near the band edge such as slow light, it is also used to effectively couple light to the cavities that are embedded in the PhC lattice. A simple W1 waveguide was designed and fabricated in GaN. It was optically characterized to understand its dispersion and propagation properties. A microscope objective with a high numerical aperture of 0.9 is used in order to collect light from the top of the device. The top right figure 5.11 shows the visible image of the photonic crystal W1 connected to an injection wire waveguide. The dark color is due to the membrane and indicates a freestanding structure.

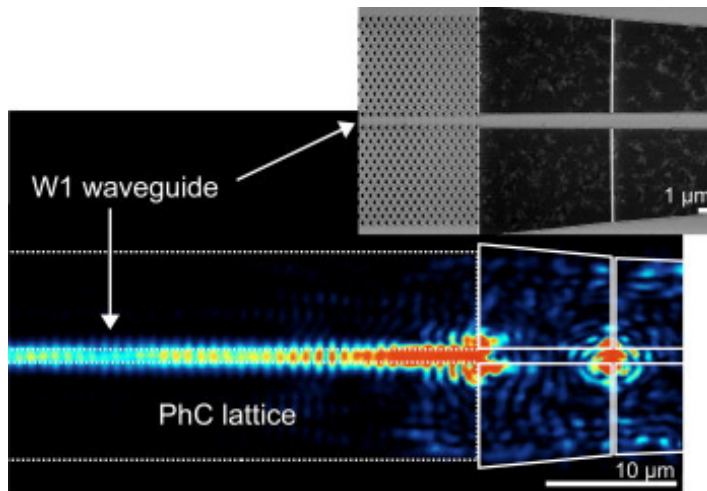


Figure 5.11: Light propagation through a GaN PhC waveguide seen with an infrared camera. The inset shows the corresponding SEM image. *Reprinted from a publication from this thesis [126].*

The interface between the wire and the PhC W1 results in a scattering loss as can be seen in the infrared image. The mode of the W1 can be also seen as it radiates outside the light line of the device. The decay of this radiated light can be used to perform a loss measurement and the propagation loss is around 82 dB/mm. These measured loss values vary from 80 to 100 dB/mm for different wavelengths in the 1.5 μm band. This is a typical propagation loss of W1 waveguide working above the light line. However, the propagation loss of a truly guided mode below the light line cannot be measured with this method because of the lack of scattered light in these wavelengths. A standard way to measure the loss below light cone is to analyze the transmitted power of devices with different lengths, but the transmission through a 3 mm device with a PhC W1 is not possible at the moment because of the heavy losses involved in the devices. Dispersion measurements were performed on the device using the Fourier imaging technique [288] and is displayed in figure 5.12. The W1 mode can be clearly observed until the cut-off of the objective light line below which the mode is truly guided and cannot be observed. The emission of the output of the W1 waveguide allows us to ascertain the cut-off of the propagating mode and the onset of the photonic bandgap, which confirms with the measured dispersion curve very well. Two dimensional Guided Mode Expansion (GME)

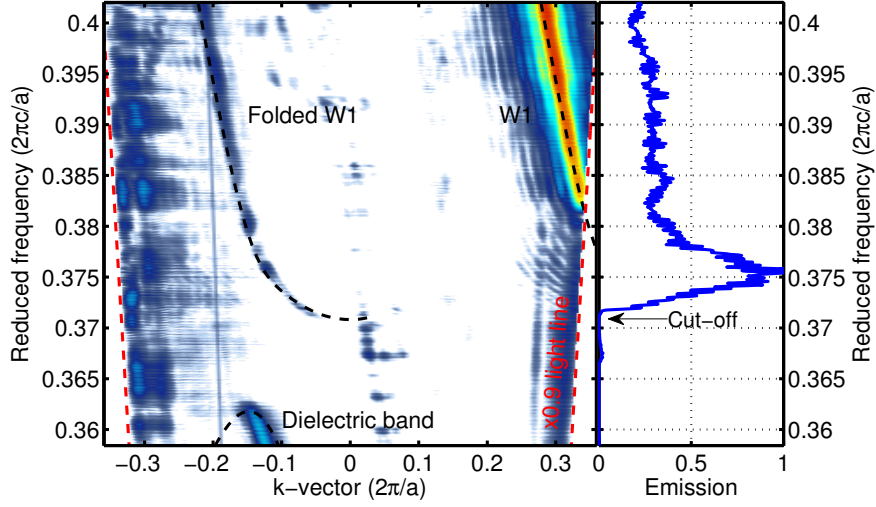


Figure 5.12: Dispersion of W1 even-mode propagation in the GaN PhC W1 waveguide with a grating. The dotted black line is the numerical computation performed with GME. **Reprinted from a publication from this thesis [127].**

based calculations are performed to compute the numerical dispersion curve using refractive indices of 2.3 and 2.1 for GaN and AlN, respectively. The lack of scattered light below light cone will also limit the measurement of dispersion. To be able to probe the dispersion of the guided modes with the Fourier imaging technique [288], we have to artificially introduce a periodic one-dimensional probe grating that enables coupling of a small portion of guided light into the radiative modes. In the case of a grating designed along the propagation direction, the dependence of the wave vector of the diffracted light k_{diff} on the propagation constant of the guided mode k_{prop} is given by the well known grating equation:

$$k_{diff} = k_{prop} + m \frac{2\pi}{\Lambda} \quad (5.1)$$

where Λ is the grating period and m is an integral number giving the order of diffraction. A linear grating in the evanescent tail of the guided field has been implemented. The dispersion and emission of light at the end of PhC is shown in figure 5.12. In principle, the linear probe grating makes it possible to reconstruct the dispersion of the entire W1 dispersion. But it can be seen that the 1st order dispersion line is neatly captured only in the fast light regime. In the slow light regime, the amount of scattered signal increases as the group index increases. This constitutes the reason why the lower parts of the W1 dispersion curve become weak and discontinuous. A further decrease in the frequency and after traversing through the photonic band gap, the dielectric band of the PhC is reached as shown in figure 5.12. In a similar manner, W0.94 and W1.02 PhC W1s are also characterized and the measurements indicated that the W1 band edge follows the fact that the mode is pushed towards the dielectric band when the width is increased.

Device characterization: Photonic crystal cavities

The interest to work with photonic crystal cavities arises from the inviting possibility of achieving cavities with a large quality factor and a small mode volume as was explained in chapter 1 in the context of various light-matter interaction experiments. In order to fabricate photonic crystal cavities with GaN for the near-infrared spectrum, three popularly used cavity designs are chosen and are optimized parametrically for the index of GaN so as to achieve a maximum theoretical Q-factor. It is to be noted that these designs have been widely studied on a free standing Si membrane that has a larger light confinement due to the higher refractive index of Si. It is advantageous if the form of the electric field distribution in the cavity is slowly varying, ideally described by a Gaussian function. This type of designing cavities is also often referred to as “gentle confinement”.

The first type is a modified L3 cavity [161] that is optimized by tuning the position of first few air holes on the left and right side of the cavity region. The second type is a width modulation of W1 type cavity [144] where the position of four holes close to the center of the waveguide are stretched perpendicular to the light propagation direction. The third type is a heterostructure type cavity [162] with a small expansion of two lattice constant widths along the light propagation direction. All these designs obey the role of gentle confinement while still keeping the small cavity size approximately. In the case of GaN, due to the differences in dielectric constant of the material, the lattice constant and the large membrane thickness compared to silicon, the optimum parameters of the cavity designs have to be recalculated and re-optimized.

Type of cavity	Optimized Q-factor
Modified L3	2900
Modified W1 - A3	66000
Heterostructure	102000

Table 5.3: Cavity designs for GaN PhC. Three designs are optimized for the refractive index of GaN and by parametrically tuning the parameters in FEM.

Two dimensional finite element methods are used to construct the cavity designs and the far fields of the planar electric field components are observed in the light cone. The components falling inside the light cone are radiated out and are lost leading to a decrease in the quality factor of the cavity. This method was the basis of the optimization as described in the initial work of Akahane and coworkers [161]. In the case of an L3 cavity without tuning of the holes, a quality factor of 2000 is numerically calculated. The Fourier spectrum contains large components inside the leaky region. This is due to the abrupt change at the cavity edges. The confinement is made gentler by slowly varying the position of the holes away from the cavity and consequently the cavity profile is considered to be close to the ideal confinement expression given by the Gaussian function. This results in a quality factor of 2900 for a displacement of $0.2a$, where a is the lattice constant of the PhC. A similar optimization is performed for both the modified W1 type and the heterostructure type cavities. The final

5.3. GaN photonic devices in the near-IR: Experimental results

optimized Q-factors are reported in table 5.3. The corresponding cross sections of the far field and the in-plane far field images of the above mentioned cavities are also shown in figure 5.13. It can be clearly seen that the A3 and heterostructure cavities exhibit very few components inside the dotted white circle, which is the leaky region out of the slab. This explains the difference in the quality factors seen between the L3 and the rest.

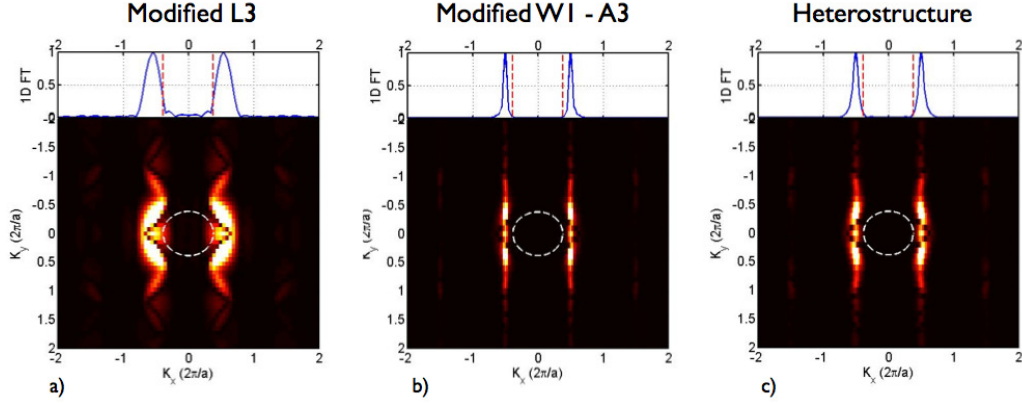


Figure 5.13: Fourier transform spectra of cavity modes of a) Modified L3 b) Modified W1 c) Heterostructure.

In the actual design of the sample, the modified L3 cavity is coupled to the W1.02 waveguide in order to avoid the coupling from the slow light regime. A varying coupling distance from the feeding waveguide is also used. In the case of the A3 and heterostructure, though the 10 nm shift is the most optimized case, a 20 nm shift was also implemented. It is also believed that the high-Q cavities are more prone to disorder in the PhC membrane than the L3 cavity. In the optical characterization of the cavities, the fundamental mode of the L3 cavity is coupled with a W1.02 waveguide to enable efficient coupling in the fast light regime under the light line.

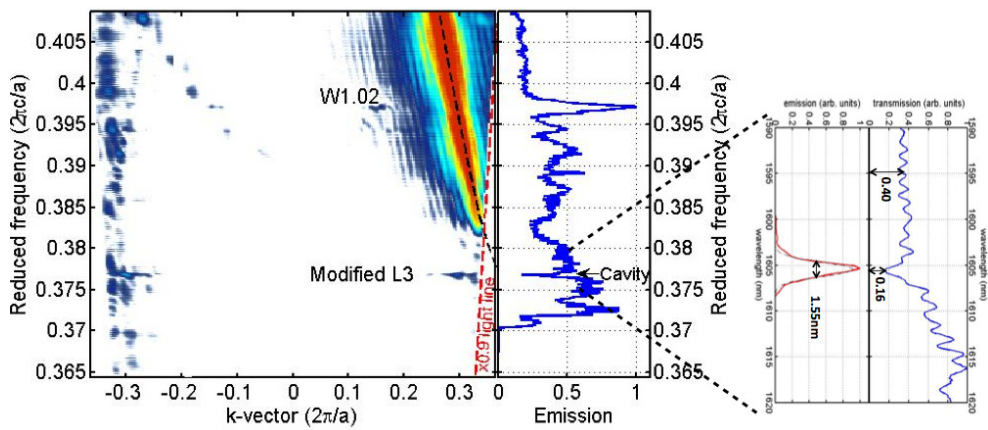


Figure 5.14: L3 cavity: Coupling and Q-factor measurement. Dispersion and transmission measurement showing the even mode of a W1.02 waveguide and the resonant dip of the L3 mode. The side inset shows the emission and transmission measurements of the cavity mode and the measured Q-factor.

This can be evidenced in the experimental measurement of the dispersion along with the cavity mode emission and transmission as shown in figure 5.14. The measured Q-factor in emission in this case is approximately close to 1000. The higher order L3 mode with a lower quality factor is also measured. As the cavity is moved far from the waveguide, the external influence on the cavity fields become smaller. The quality factor increases while the coupling strength decreases. The maximum quality factor measured in a modified L3 cavity device is 2000 where the numerical Q-factor is close to 3000.

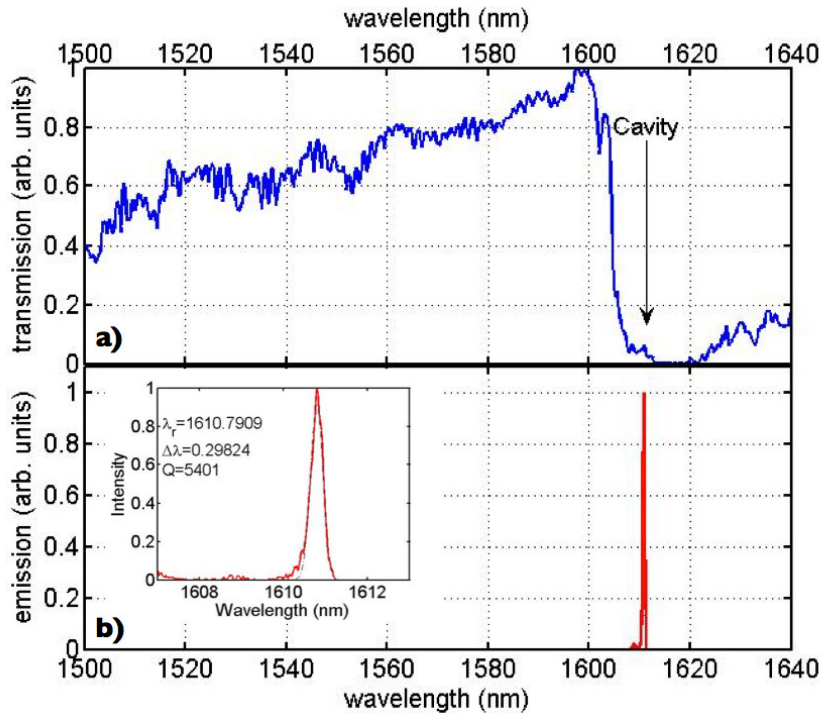


Figure 5.15: Experimental measurement of a heterostructure PhC cavity. a) The transmission through the structure showing a very negligible peak after the cut-off of the propagating mode. b) The emission measurement performed shows the presence of the cavity mode and the Q-factor is shown in the inset of the image.

The heterostructure cavity is formed by expanding two lattice constants along the propagation direction. Here, it is coupled using an in-line configuration with a W1 waveguide. The barrier is 10 lattice constants or 20 lattice constants long in different devices in the sample. The transmission properties of such a configuration is noticeably different as can be seen in figure 5.15a. The cavity mode, which is indicated by the black arrow, appears as a small peak after the cut-off frequency of the barrier. The emission spectrum of a 20 nm shifted cavity with a barrier of 20 lattice constants wide shows a quality factor as high as 5400 with a numerical Q-factor of 50000 and is shown in figure 5.15b. Other heterostructure cavities with barriers of 10 lattice constants have also been measured and their maximum quality factor is around 2000, which is consistent with the reasoning discussed with the L3 cavity regarding the proximity of the coupling waveguide.

5.4 GaN photonic crystal cavities in the visible: Experimental results

5.4.1 Growth and fabrication

The demonstration of PhC structures in the visible wavelength with a single mode optical operation demands the thickness of the slab to be around 40 nm which is currently not within the reach of growth techniques at LASPE. The growth and fabrication process used here achieves a structure shown in the schematic of figure 5.16. The fabrication steps are largely similar to the ones that are explained for the near-IR except for the presence of the additional quantum well layers, which are required for the optical characterization.

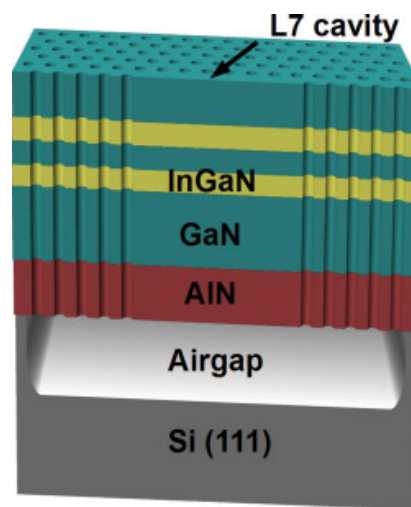


Figure 5.16: Schematic cross section of the 2D GaN PhC L7 cavity with two embedded InGaN/GaN quantum wells. *Reprinted from a publication from this thesis [128].*

1. A 60 nm thick AlN buffer layer is grown at low temperatures to reduce the dislocation density.
2. This step is followed by a growth of a 167 nm thick GaN layer and a double InGaN/GaN quantum well layer consisting of In_{0.2}Ga_{0.8}N (3.5 nm)/GaN(7 nm)/ In_{0.2}Ga_{0.8}N (3 nm) and finally a GaN layer of 21 nm is grown.
3. A 100 nm thick SiO₂ layer is then deposited on top of the structure.
4. The PhC bulk lattice with a lattice constant of 155 nm and a filling factor $r=0.35a$ is written with e-beam lithography after the spinning of photoresist. The orientation of the cavity is along $[10\bar{1}0]$.
5. The pattern is transferred via RIE and the resist is removed.
6. GaN etching is performed with a chlorine-based ICP and the membrane release is achieved through the dry under-etching of the Si substrate.

7. The SiO₂ mask is finally removed with the use of hydrofluorhydric acid solution.

The structures were later analyzed under an SEM and the images can be seen in figure 5.17. The top and side views can be seen in the left and right of figure respectively. The close-up view of one of the holes reveals the tendency towards the formation of a hexagonal shape due to the inherent crystal structure. An airgap of 1 μm can be clearly seen below the membrane in the right image and the smooth and vertical side wall of a single hole is shown in the inset of figure 5.17b.

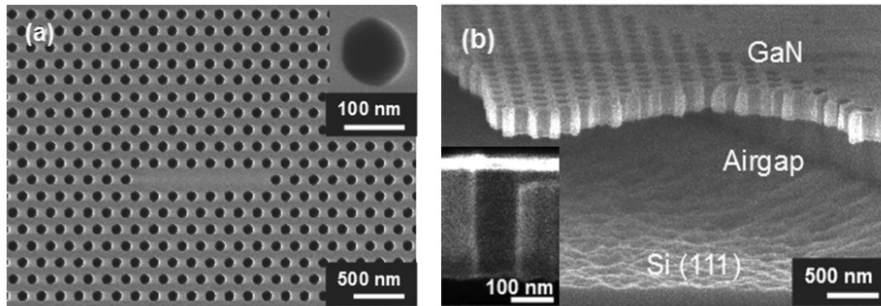


Figure 5.17: SEM images of PhC L7 cavity for visible wavelengths. a) The L7 nanocavity with an inset of a single hole on the top right corner b) Side view with a tilt angle of 15° showing the airgap below the membrane. The left inset shows the single hole cross-section and its vertical profile. *Reprinted from a publication from this thesis [128].*

It is to be noted that this is a simple case of an L7 cavity and none of the surrounding hole positions nor radii were modified for increasing the quality factor of the cavity.

5.4.2 Optical characterization and analysis

The devices are characterized at low temperature by microphotoluminescence (μPL) spectroscopy using a continuous wave Argon laser, which is focussed down to a 2 μm diameter spot at an excitation power density of 2 KW/cm^2 . The output signal is recorded by a liquid nitrogen cooled UV enhanced CCD device. The spectrum recorded is shown in figure 5.18a. There are several peaks corresponding to different modes of the cavity with one of the peaks clearly showing a high quality factor of about 5200.

To validate our analysis of the experimental spectra, the effective indices and allowed mode cut offs are first calculated for the GaN and AlN layer thicknesses used in the experiment. It is found that the system allows for the first three orders of TE and TM modes at the wavelength of interest and then, with the use of a 2D plane wave expansion method, the corresponding band gaps are calculated due to each of these mode indices. There are band gaps only for the TE1 and TE2 effective mode indices and then by creating the L7 cavity defect in the model, cavity states arising in the bandgap are computed for both these modes. A total of 13 modes for the TE1 case and 12 modes for the TE2 configuration are found. The superposition of all these states gives the final set of cavity state energies in the spectra of the sample. This

5.4. GaN photonic crystal cavities in the visible: Experimental results

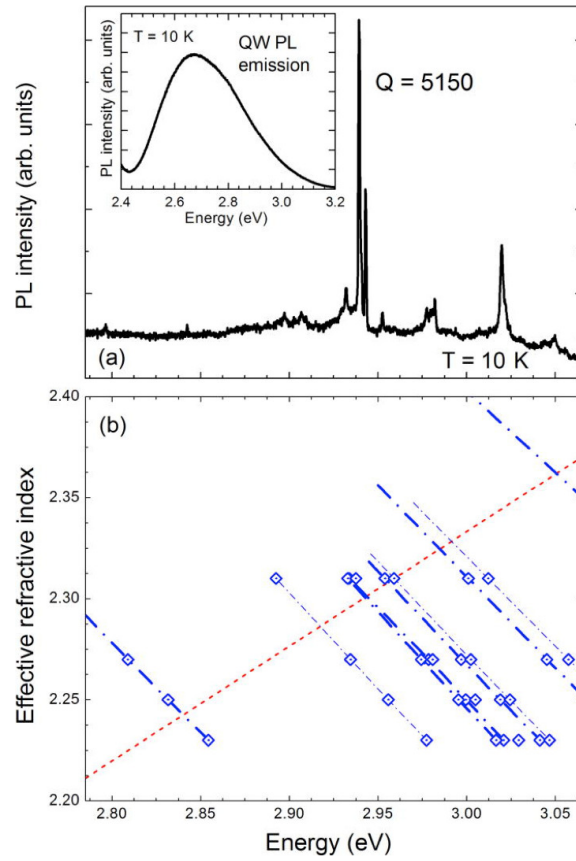


Figure 5.18: Optical characterization and numerical modeling: a) μ PL spectra showing the cavity peaks taken out from the PhC area. b) Cavity mode positions calculated for a given n_{eff} are represented in squares. Each blue dash-dotted line represents the spectral dispersion of the cavity modes from the TE1 guided mode taking into account the dispersion of the effective refractive index (red dashed line). **Reprinted from a publication from this thesis [128].**

calculation already explains the multiple peaks seen in the experimental spectra and they correspond to the modes arising due to the TE1 mode effective index. It is important to note that the mode spacing in energy is not constant when the dispersion of the GaN index is taken into account. The frequency dependence of the refractive index of GaN based devices can be found here [289] and for the frequencies of interest, it can be approximated to a linear dependence. For this linear dependence, it is possible to map the positions of the cavity modes as a function of the effective refractive index. The intersection of the GaN index spectra and that of the effective index variations of the mode positions gives the final value of the mode positions when dispersion is taken into account. This is shown in figure 5.18b where the mode positions at the intersections are superimposed on the experimental spectra and a consistent correlation can be seen between theory and experiment. 3D FEM simulations of the eigenfrequencies in the system are also performed to verify the cavity modes and several of these modes do exhibit sufficiently high Q-factors.

5.5 Summary and perspectives

Summary

In this chapter, wide bandgap photonic crystals based on Gallium Nitride technology have been explored and experimentally studied. The important results are:

- In the visible wavelength range, L7 photonic crystal cavities have been experimentally measured on a free standing GaN membrane of thickness 190 nm resulting in a Q-factor of 5150 at a wavelength of 422 nm.
- In the near-infrared wavelength range, L3 and heterostructure based photonic crystal cavities have been demonstrated showing Q-factors of up to 5400 at 1550 nm. In addition, suspended ridge waveguides and photonic crystal waveguides were also characterized for dispersion and loss propagation. The ridge waveguide propagation losses has been measured to be 10 dB/mm.

Perspectives

In the case of visible wavelengths, along with the possibility to bury quantum dots inside the device, it can be very interesting for experiments in quantum optics, quantum information and single photon emitters. The visible wavelength operation also benefits the applications involving biology due to the fluorescent markers used in this wavelength range. In terms of theory and modeling, new cavity designs have to be optimized based on the refractive index variation of GaN at different wavelengths. The effects of the underlying layer of AlN has to be also be taken into account for all calculations. Also, the optical trapping devices shown in chapter 3 of this thesis can be extended to visible wavelengths and biological species could be trapped on which spectroscopic measurements could be performed.

In the case of near-infrared wavelengths, which is widely used for telecommunications, two-photon absorption has been a major concern for high quality factor devices as has also been experimentally shown in this thesis in chapter 4. Applications involving second harmonic generation, four wave mixing or Raman amplification would be the non-linear optical effects without two-photon absorption and free-carrier absorption. GaN with its wide bandgap will have not this problem and high Q-factor cavities could be investigated in this technology. New designs of optimized cavities following the evolutionary method shown in chapter 4 could be implemented. The propagation losses and Q-factors that have been shown in this chapter could be improved by tuning the fabrication processes iteratively.

Conclusion and outlook

Conclusions

The contribution of this thesis revolves around the physics and characterization of slab photonic crystal cavities and their subsequent study for specific light-matter interaction experiments.

In the context of numerical analysis, three dimensional finite element methods were extensively used for exploring the cavity field configurations and for optimizing the quality factors through parametric optimization. Plane wave expansion and the guided mode expansion were instrumental in computing waveguide parameters and dispersion characteristics accurately. In the case of high Q-factors in photonic crystal cavities, it has been found that disorder plays a significant role in limiting the quality factor of ultra-high Q cavity designs and beyond a certain limit when the disorder-induced losses are far greater than the intrinsic losses, it is no longer beneficial to explore or optimize higher Q-factor designs. It is rather beneficial to work on reducing the disorder induced losses for existing cavities.

In the first light-matter interaction experiment, a resonant optical trapping scheme in a photonic crystal cavity has been demonstrated where a new design space using hollow cavities has been explored. The electric field maximization within the lower index dielectric has been analyzed numerically and a circular cavity with a reasonable overlap in water along with a high Q-factor was finally chosen to perform the experiment. Contrary to the evanescent trapping methods, this method experimentally confirmed the trapping of 500 nm sized dielectric particles with astonishingly low input powers in the μW range and for trapping times of about tens of minutes. 250 nm sized dielectric particles were also trapped with the cavity. Furthermore the perturbation induced by a single particle in the hollow cavity was calculated to be about 2.8 nm and an experimental value of 1.8 nm was measured. The strong perturbation induced back-action effect was numerically calculated with the maxwell stress tensor method through the forces acting on the particle predicting the existence of two separate trapping regimes and anharmonic force profiles for different detuning values. This feature was also qualitatively validated in the experiment through the evaluation of the detuning dependent escape threshold power. Furthermore, arrays of circular cavities were demonstrated for wavelength selective integrated trapping.

In the second light-matter interaction experiment, a fast and novel evolutionary optimization method using mode expansions tools has been explored and is used to demonstrate that “simple” designs can also be optimized to produce ultrahigh Q-factors. The H0 cavity was heuristically optimized to a theoretical $Q=280,000$ only three years ago. Here we demonstrate a theoretical $Q=1.95$ million and a measured Q of up to 418,000, namely twice the previous theoretical value along with modal volumes as small as $0.34 (\frac{\lambda}{n})^3$. The Q/V ratio is the most important figure of merit for photonics applications, as it determines the enhancement of optical nonlinearities and the strength of radiation-matter interaction. The crucial advantage of this design however resides in its simplicity, spatial compactness, and robustness to fabrication imperfections. In order to show the power of the optimization method, three unique H0 cavity designs with theoretical Q-factors 1.05 million, 1.95 million and 8.9 million have been proposed. The measured cavity also displayed nonlinear optical effects and bistable states due to the interaction between free carrier absorption and thermal effects at very low input powers.

In both the above experiments, Silicon was used, being the most used semiconductor optics substrate for the ease of adherence to CMOS fabrication but it suffers from two main issues. First is the spectral absorption present in the visible wavelength range that renders cavities in this wavelength highly lossy. Second is the two-photon absorption present at the near-infrared wavelength range that can be detrimental to the operation of ultra high-Q nanocavities that was also demonstrated in this thesis. To alleviate both these issues, photonic crystal devices were designed and characterized for Gallium Nitride substrates and in spite of a low refractive index contrast, reasonable quality factors of more than 5000 were witnessed in both visible and near-IR wavelengths. In the case of the infrared devices, a complete dispersion and transmission characterization was performed on fully suspended ridge waveguides, photonic crystal waveguides and high-Q cavities. A modest transmission loss of 10 dB/mm is reported for the ridges, which is mainly limited due to fabrication disorder.

Outlook

This thesis brings some exciting new results and ideas to the expanding domain of photonic crystal cavities. It opens up new experimental avenues and boundaries that have remained previously unexplored. It has to be re-iterated that photonic crystals offer a powerful platform to perform some invigorating investigations in condensed matter physics as reviewed in chapter 1 and the rest of this thesis. Apart from the novelties in physics, this thesis also showcases applications that promise commercial value in the near future for photonic crystals that have prevailed for more than two decades but are yet to find a convincing stamp in large scale industrial applications.

In terms of physics, the resonant optical trapping scheme is a completely new mechanism in integrated trapping with the perturbation specific back-action effects and trapping regimes. The experiment can be further continued in order to quantitatively measure the dynamics of the trapping behaviour for different types of particles and to evaluate the strength of the trapping forces. This can be measured through various methods, for example, by observing the power spectrum signature of the trapped particle. In an other aspect, the reported H0 nanocavity was obtained by means of a novel procedure, based on an evolutionary optimization algorithm combined with a fast simulation tool which disproves the common belief within the community, that photonic crystal cavities with Q-factors of above one million could only be realized with few specific designs, while all “simple” designs such as the L3 or H0 could never get significantly above 100,000. Global optimization revolutionizes the understanding of photonic crystal cavities, by showing that high-Q can be obtained with most cavity designs, and thus increasing the relevance of the 2-D photonic crystal paradigm within the broadest photonics community. It also holds great promise as a platform for solid-state cavity quantum electrodynamics, where a high Q/V ratio is the main requirement to achieve single-photon nonlinearities for quantum information applications.

In terms of technology and applications, the resonant trap can be extended to biological entities and size/wavelength selective integrated trap arrays can be envisaged. The GaN platform offers a number of possibilities to transfer the functionalities that were performed on Silicon. In the first step, the two experiments that have been shown in this thesis can be scaled for Gallium Nitride. The trapping circular cavity will have to be scaled to about three times smaller in diameter in order to work for visible wavelengths that could potentially trap much smaller particles of the order of 100 nm. The visible wavelength cavities could be interesting for exploring fluorescence-based devices and for nanobiosensing experiments. In the second step, the high-Q cavities that were demonstrated in this thesis can also be ported to GaN to be able to achieve very high quality factors without the influence of two photon absorption to be able to be used for high power optical applications. Finally, the evolutionary optimization method that brought this H0 design promises to play a major role in the future development of customizable PhC cavity devices for specific application requirements, thereby, opening the door to the possibilities of creating a generic library of photonic crystal cavity functions.

Publications from this thesis

Peer reviewed journals

- “Statistics of the disorder-induced losses of high-Q photonic crystal cavities”, M. Minkov, **U. Dharanipathy**, R. Houdré, and V. Savona, *Optics Express*, 21, 28233 (2013)
- “Single particle detection, manipulation and analysis with resonant optical trapping in photonic crystals”, N. Descharmes, **U. Dharanipathy**, Z. Diao, M. Tonin, and R. Houdré, *Lab Chip*, 13, 3268 (2013)
- “Observation of Backaction and Self-Induced Trapping in a Planar Hollow Photonic Crystal Cavity”, N. Descharmes, **U. Dharanipathy**, Z. Diao, M. Tonin, and R. Houdré, *Physical Review Letters*, 110, 123601 (2013)
- “Integrated photonics on silicon with wide bandgap GaN semiconductor”, N. Vico Triviño, **U. Dharanipathy**, J.-F. Carlin, Z. Diao, R. Houdré, and N. Grandjean, *Applied Physics Letters*, 102, 081120 (2013)
- “Near-infrared characterization of gallium nitride photonic-crystal waveguides and cavities”, **U. Dharanipathy**, N. Vico Triviño, C. Yan, Z. Diao, J.-F. Carlin, N. Grandjean, and R. Houdré, *Optics Letters*, 37, 4588 (2012)
- “High quality factor two dimensional GaN photonic crystal cavity membranes grown on silicon substrate”, N. Vico Triviño, G. Rossbach, **U. Dharanipathy**, J. Levrat, A. Castiglia, J.-F. Carlin, A. K. Atlasov, R. Butté, R. Houdré, and N. Grandjean, *Applied Physics Letters*, 100, 071103 (2012)
- “Numerical modelling of optical trapping in hollow photonic crystal cavities”, **U. Dharanipathy** and R. Houdré, *Optical and Quantum Electronics*, 44, 161 (2012)

International conference contributions

- N. Descharmes, **U. Dharanipathy**, Z. Diao, and R. Houdré, *Self-trapping and back-action effects in hollow photonic crystal cavity optical trap*, SPIE Photonics West, San Francisco, USA, 2013
- M. Minkov, **U. Dharanipathy**, R. Houdré, and V. Savona, *What determines the Q-factor of high-Q photonic crystal cavities*, 31st International Conference on Physics of Semiconductors (ICPS), Zurich, Switzerland, 2012
- N. Descharmes, **U. Dharanipathy**, Z. Diao, M. Tonin, and R. Houdré, *Microfluidic integrated single particle sensor based on hollow photonic crystal cavities*, Conference on Lasers and Electro-Optics (CLEO), San Jose, USA, 2012
- N. Descharmes, **U. Dharanipathy**, Z. Diao, M. Tonin, and R. Houdré, *Resonant optical trap in a photonic crystal cavity*, 31st International Conference on Physics of Semiconductors (ICPS), Zurich, Switzerland, 2012
- N. Vico Triviño, G. Rossbach, **U. Dharanipathy**, J. Levrat, A. Castiglia, J. F. Carlin, K. A. Atlasov, R. Butté, R. Houdré, and N. Grandjean, *High Quality Factor 2D GaN Photonic Crystal Cavity Membranes grown on Silicon*, 10th International Conference on Photonic and Electromagnetic Crystal Structures (PECS-X), Santa Fe, USA, 2012
- **U. Dharanipathy**, N. Vico Triviño, C. Yan, Z. Diao, J. Carlin, N. Grandjean, and R. Houdré, *Fabrication and Near-IR Measurement of GaN Photonic Crystal Membranes: Wires, Waveguides and Cavities*, 10th International Conference on Photonic and Electromagnetic Crystal Structures (PECS-X), Santa Fe, USA, 2012
- N. Descharmes, **U. Dharanipathy**, Z. Diao, and R. Houdré, *Single Particle Induced Resonance Frequency Shift in a Hollow Photonic Crystal Cavity*, 7th International Photonics Prague, Prague, Czech Republic, 2011
- **U. Dharanipathy**, N. Le Thomas, and R. Houdré, *Numerical modelling of optical trapping in hollow photonic crystal cavities*, 11th International Conference on Numerical Simulation of Optoelectronic Devices in Optical and Quantum Electronics (NUSOD), Rome, Italy, 2011
- J. Jágerská, H. Zhang, Z. Diao, N. Le Thomas, **U. Dharanipathy**, and R. Houdré, *Air-Slot Photonic Crystal Cavity for High Precision Refractive Index Sensing*, Ninth International Conference on Photonic and Electromagnetic Crystal Structures (PECS-IX), Granada, Spain, 2010

Bibliography

- [1] S. John *et al.*, “Strong localization of photons in certain disordered dielectric superlattices,” *Physical review letters*, vol. 58, no. 23, pp. 2486–2489, 1987.
- [2] E. Yablonovitch, “Inhibited spontaneous emission in solid-state physics and electronics,” *Physical review letters*, vol. 58, no. 20, p. 2059, 1987.
- [3] E. Yablonovitch and T. J. Gmitter, “Photonic band structure: The face-centered-cubic case,” *Phys. Rev. Lett.*, vol. 63, pp. 1950–1953, Oct 1989.
- [4] K. Leung and Y. Liu, “Full vector wave calculation of photonic band structures in face-centered-cubic dielectric media,” *Physical Review Letters*, vol. 65, pp. 2646–2649, 1990.
- [5] Z. Zhang and S. Satpathy, “Electromagnetic wave propagation in periodic structures: Bloch wave solution of maxwell’s equations,” *Physical review letters*, vol. 65, no. 21, p. 2650, 1990.
- [6] J. Maddox, “Photonic band-gaps bite the dust,” *Nature*, vol. 348, p. 481, 1990.
- [7] K. Ho, C. Chan, and C. Soukoulis, “Existence of a photonic gap in periodic dielectric structures,” *Physical Review Letters*, vol. 65, no. 25, p. 3152, 1990.
- [8] M. Plihal and A. Maradudin, “Photonic band structure of two-dimensional systems: The triangular lattice,” *Physical Review B*, vol. 44, no. 16, p. 8565, 1991.
- [9] S. McCall, P. Platzman, R. Dalichaouch, D. Smith, and S. Schultz, “Microwave propagation in two-dimensional dielectric lattices,” *Physical review letters*, vol. 67, no. 15, p. 2017, 1991.
- [10] E. Yablonovitch, T. Gmitter, and K. Leung, “Photonic band structure: The face-centered-cubic case employing nonspherical atoms,” *Physical review letters*, vol. 67, no. 17, p. 2295, 1991.
- [11] W. Robertson, G. Arjavalingham, R. Meade, K. Brommer, A. M. Rappe, and J. Joannopoulos, “Measurement of photonic band structure in a two-dimensional periodic dielectric array,” *Physical review letters*, vol. 68, no. 13, p. 2023, 1992.

Bibliography

- [12] S.-y. Lin, J. Fleming, D. Hetherington, B. Smith, R. Biswas, K. Ho, M. Sigalas, W. Zubrzycki, S. Kurtz, and J. Bur, "A three-dimensional photonic crystal operating at infrared wavelengths," *Nature*, vol. 394, no. 6690, pp. 251–253, 1998.
- [13] I. I. Tarhan and G. H. Watson, "Photonic band structure of fcc colloidal crystals," *Physical review letters*, vol. 76, no. 2, p. 315, 1996.
- [14] Y. Xia, B. Gates, and S. H. Park, "Fabrication of three-dimensional photonic crystals for use in the spectral region from ultraviolet to near-infrared," *Lightwave Technology, Journal of*, vol. 17, no. 11, pp. 1956–1962, 1999.
- [15] J. E. Wijnhoven and W. L. Vos, "Preparation of photonic crystals made of air spheres in titania," *Science*, vol. 281, no. 5378, pp. 802–804, 1998.
- [16] K. Busch and S. John, "Photonic band gap formation in certain self-organizing systems," *Physical Review E*, vol. 58, no. 3, p. 3896, 1998.
- [17] Y. A. Vlasov, X.-Z. Bo, J. C. Sturm, and D. J. Norris, "On-chip natural assembly of silicon photonic bandgap crystals," *Nature*, vol. 414, no. 6861, pp. 289–293, 2001.
- [18] T. F. Krauss, R. M. D. L. Rue, and S. Brand, "Two-dimensional photonic-bandgap structures operating at near-infrared wavelengths," *Nature*, vol. 383, no. 6602, pp. 699–702, 1996.
- [19] D. Labilloy, H. Benisty, C. Weisbuch, T. Krauss, R. De La Rue, V. Bardinal, R. Houdré, U. Oesterle, D. Cassagne, and C. Jouanin, "Quantitative measurement of transmission, reflection, and diffraction of two-dimensional photonic band gap structures at near-infrared wavelengths," *Physical review letters*, vol. 79, no. 21, p. 4147, 1997.
- [20] J. Knight, J. Broeng, T. Birks, and P. S. J. Russell, "Photonic band gap guidance in optical fibers," *Science*, vol. 282, no. 5393, pp. 1476–1478, 1998.
- [21] E. Yablonovitch, T. Gmitter, R. Meade, A. Rappe, K. Brommer, and J. Joannopoulos, "Donor and acceptor modes in photonic band structure," *Physical Review Letters*, vol. 67, no. 24, p. 3380, 1991.
- [22] P. R. Villeneuve, S. Fan, J. Joannopoulos, K.-Y. Lim, G. Petrich, L. Kolodziejski, and R. Reif, "Air-bridge microcavities," *Applied physics letters*, vol. 67, no. 2, pp. 167–169, 1995.
- [23] P. R. Villeneuve, S. Fan, and J. Joannopoulos, "Microcavities in photonic crystals: Mode symmetry, tunability, and coupling efficiency," *Physical Review B*, vol. 54, no. 11, p. 7837, 1996.
- [24] R. Stanley, R. Houdré, U. Oesterle, M. Ilegems, and C. Weisbuch, "Impurity modes in one-dimensional periodic systems: The transition from photonic band gaps to microcavities," *Physical Review A*, vol. 48, no. 3, p. 2246, 1993.

- [25] J. D. Joannopoulos, S. G. Johnson, J. N. Winn, and R. D. Meade, *Photonic crystals: molding the flow of light*. Princeton university press, 2011.
- [26] K. Sakoda, "Transmittance and bragg reflectivity of two-dimensional photonic lattices," *Physical Review B*, vol. 52, no. 12, p. 8992, 1995.
- [27] J. Vučković, M. Lončar, H. Mabuchi, and A. Scherer, "Design of photonic crystal microcavities for cavity qed," *Physical Review E*, vol. 65, no. 1, p. 016608, 2001.
- [28] S.-H. Kim and Y.-H. Lee, "Symmetry relations of two-dimensional photonic crystal cavity modes," *Quantum Electronics, IEEE Journal of*, vol. 39, no. 9, pp. 1081–1085, 2003.
- [29] R. D. Meade, A. Devenyi, J. Joannopoulos, O. Alerhand, D. Smith, and K. Kash, "Novel applications of photonic band gap materials: Low-loss bends and high Q cavities," *Journal of applied physics*, vol. 75, no. 9, pp. 4753–4755, 1994.
- [30] S.-Y. Lin, E. Chow, V. Hietala, P. R. Villeneuve, and J. Joannopoulos, "Experimental demonstration of guiding and bending of electromagnetic waves in a photonic crystal," *Science*, vol. 282, no. 5387, pp. 274–276, 1998.
- [31] A. Mekis, J. Chen, I. Kurland, S. Fan, P. R. Villeneuve, and J. Joannopoulos, "High transmission through sharp bends in photonic crystal waveguides," *Physical Review Letters*, vol. 77, no. 18, p. 3787, 1996.
- [32] M. Tokushima, H. Kosaka, A. Tomita, and H. Yamada, "Lightwave propagation through a 120 sharply bent single-line-defect photonic crystal waveguide," *Applied physics letters*, vol. 76, no. 8, pp. 952–954, 2000.
- [33] S. G. Johnson, P. R. Villeneuve, S. Fan, and J. Joannopoulos, "Linear waveguides in photonic-crystal slabs," *Physical Review B*, vol. 62, no. 12, p. 8212, 2000.
- [34] A. Chutinan and S. Noda, "Highly confined waveguides and waveguide bends in three-dimensional photonic crystal," *Applied Physics Letters*, vol. 75, no. 24, pp. 3739–3741, 1999.
- [35] S. Noda, K. Tomoda, N. Yamamoto, and A. Chutinan, "Full three-dimensional photonic bandgap crystals at near-infrared wavelengths," *Science*, vol. 289, no. 5479, pp. 604–606, 2000.
- [36] M. Okano, S. Kako, and S. Noda, "Coupling between a point-defect cavity and a line-defect waveguide in three-dimensional photonic crystal," *Physical Review B*, vol. 68, no. 23, p. 235110, 2003.
- [37] R. Wuest, B. C. Buchler, R. Harbers, P. Strasser, K. Rauscher, F. Robin, D. Erni, V. Sandoghdar, and H. Jackel, "Near-field optical microscopy of light propagation through photonic crystal waveguide tapers," in *Microtechnologies for the New Millennium 2005*, pp. 110–117, International Society for Optics and Photonics, 2005.

Bibliography

- [38] S. G. Johnson, S. Fan, P. R. Villeneuve, J. Joannopoulos, and L. Kolodziejski, "Guided modes in photonic crystal slabs," *Physical Review B*, vol. 60, no. 8, p. 5751, 1999.
- [39] S. Fan, P. R. Villeneuve, J. Joannopoulos, and E. Schubert, "High extraction efficiency of spontaneous emission from slabs of photonic crystals," *Physical Review Letters*, vol. 78, no. 17, p. 3294, 1997.
- [40] A. David, C. Meier, R. Sharma, F. Diana, S. DenBaars, E. Hu, S. Nakamura, C. Weisbuch, and H. Benisty, "Photonic bands in two-dimensionally patterned multimode GaN waveguides for light extraction," *Applied Physics Letters*, vol. 87, no. 10, p. 101107, 2005.
- [41] K. McGroddy, A. David, E. Matioli, M. Iza, S. Nakamura, S. DenBaars, J. Speck, C. Weisbuch, and E. Hu, "Directional emission control and increased light extraction in GaN photonic crystal light emitting diodes," *Applied physics letters*, vol. 93, no. 10, p. 103502, 2008.
- [42] J. J. Wierer, A. David, and M. M. Megens, "III-nitride photonic-crystal light-emitting diodes with high extraction efficiency," *Nature Photonics*, vol. 3, no. 3, pp. 163–169, 2009.
- [43] D. Zhou and R. Biswas, "Photonic crystal enhanced light-trapping in thin film solar cells," *Journal of Applied Physics*, vol. 103, no. 9, pp. 093102–093102, 2008.
- [44] L. Zeng, Y. Yi, C. Hong, J. Liu, N. Feng, X. Duan, L. Kimerling, and B. Alamariu, "Efficiency enhancement in si solar cells by textured photonic crystal back reflector," *Applied Physics Letters*, vol. 89, no. 11, p. 111111, 2006.
- [45] J. M. Gee, "Optically enhanced absorption in thin silicon layers using photonic crystals," in *Photovoltaic Specialists Conference, 2002. Conference Record of the Twenty-Ninth IEEE*, pp. 150–153, IEEE, 2002.
- [46] P. Bermel, C. Luo, L. Zeng, L. C. Kimerling, and J. D. Joannopoulos, "Improving thin-film crystalline silicon solar cell efficiencies with photonic crystals," *Optics Express*, vol. 15, no. 25, pp. 16986–17000, 2007.
- [47] G. Gomard, X. Meng, E. Drouard, K. El Hajjam, E. Gerelli, R. Peretti, A. Fave, R. Orobtcouk, M. Lemiti, and C. Seassal, "Light harvesting by planar photonic crystals in solar cells: the case of amorphous silicon," *Journal of Optics*, vol. 14, no. 2, p. 024011, 2012.
- [48] A. H. Safavi-Naeini, T. P. M. Alegre, M. Winger, and O. Painter, "Optomechanics in an ultrahigh-Q two-dimensional photonic crystal cavity," *Applied Physics Letters*, vol. 97, no. 18, p. 181106, 2010.
- [49] E. Gavartin, R. Braive, I. Sagnes, O. Arcizet, A. Beveratos, T. J. Kippenberg, and I. Robert-Philip, "Optomechanical coupling in a two-dimensional photonic crystal defect cavity," *Physical Review Letters*, vol. 106, no. 20, p. 203902, 2011.

- [50] C. D. Chin, V. Linder, and S. K. Sia, "Lab-on-a-chip devices for global health: past studies and future opportunities," *Lab on a Chip*, vol. 7, no. 1, pp. 41–57, 2007.
- [51] B. Troia, A. Paolicelli, F. De Leonardis, and V. M. Passaro, "Photonic crystals for optical sensing: A review," 2013.
- [52] E. Chow, A. Grot, L. Mirkarimi, M. Sigalas, and G. Girolami, "Ultracompact biochemical sensor built with two-dimensional photonic crystal microcavity," *Optics letters*, vol. 29, no. 10, pp. 1093–1095, 2004.
- [53] A. Di Falco, L. OFaolain, and T. Krauss, "Chemical sensing in slotted photonic crystal heterostructure cavities," *Applied physics letters*, vol. 94, no. 6, p. 063503, 2009.
- [54] M. Lee and P. M. Fauchet, "Two-dimensional silicon photonic crystal based biosensing platform for protein detection," *Opt. Express*, vol. 15, no. 8, pp. 4530–4535, 2007.
- [55] R. V. Nair and R. Vijaya, "Photonic crystal sensors: an overview," *Progress in Quantum Electronics*, vol. 34, no. 3, pp. 89–134, 2010.
- [56] S. Pal, E. Guillermain, R. Sriram, B. L. Miller, and P. M. Fauchet, "Silicon photonic crystal nanocavity-coupled waveguides for error-corrected optical biosensing," *Biosensors and Bioelectronics*, vol. 26, no. 10, pp. 4024–4031, 2011.
- [57] C. Karnutsch, C. L. Smith, A. Graham, S. Tomljenovic-Hanic, R. McPhedran, B. J. Eggleton, L. OFaolain, T. F. Krauss, S. Xiao, and N. A. Mortensen, "Temperature stabilization of optofluidic photonic crystal cavities," *Applied physics letters*, vol. 94, no. 23, p. 231114, 2009.
- [58] I. M. White and X. Fan, "On the performance quantification of resonant refractive index sensors," *Optics Express*, vol. 16, no. 2, pp. 1020–1028, 2008.
- [59] D. Psaltis, S. R. Quake, and C. Yang, "Developing optofluidic technology through the fusion of microfluidics and optics," *Nature*, vol. 442, no. 7101, pp. 381–386, 2006.
- [60] C. Monat, P. Domachuk, and B. Eggleton, "Integrated optofluidics: A new river of light," *Nature photonics*, vol. 1, no. 2, pp. 106–114, 2007.
- [61] T. H. Maiman, "Stimulated optical radiation in ruby," 1960.
- [62] P. Franken, A. Hill, C. Peters, and G. Weinreich, "Generation of optical harmonics," *Physical Review Letters*, vol. 7, no. 4, pp. 118–119, 1961.
- [63] R. Terhune, P. Maker, and C. Savage, "Optical harmonic generation in calcite," *Physical Review Letters*, vol. 8, no. 10, p. 404, 1962.
- [64] E. Woodbury and W. Ng, "Ruby laser operation in the near IR," *proc. IRE*, vol. 50, no. 11, p. 2367, 1962.

Bibliography

- [65] H. Gibbs, S. McCall, and T. Venkatesan, "Differential gain and bistability using a sodium-filled fabry-perot interferometer," *Physical Review Letters*, vol. 36, pp. 1135–1138, 1976.
- [66] H. M. Gibbs, "Optical bistability: controlling light with light," *Quantum electronics—principles and applications (Academic Press, 1985)*, 1985.
- [67] S. Ching, H. Lai, and K. Young, "Dielectric microspheres as optical cavities: Einstein A and B coefficients and level shift," *JOSA B*, vol. 4, no. 12, pp. 2004–2009, 1987.
- [68] H.-B. Lin and A. Campillo, "Cw nonlinear optics in droplet microcavities displaying enhanced gain," *Physical review letters*, vol. 73, no. 18, p. 2440, 1994.
- [69] H.-B. Lin and A. Campillo, "Microcavity enhanced Raman gain," *Optics communications*, vol. 133, no. 1, pp. 287–292, 1997.
- [70] D. Armani, T. Kippenberg, S. Spillane, and K. Vahala, "Ultra-high-Q toroid microcavity on a chip," *Nature*, vol. 421, no. 6926, pp. 925–928, 2003.
- [71] V. R. Almeida, C. A. Barrios, R. R. Panepucci, and M. Lipson, "All-optical control of light on a silicon chip," *Nature*, vol. 431, no. 7012, pp. 1081–1084, 2004.
- [72] G. Priem, P. Dumon, W. Bogaerts, D. Van Thourhout, G. Morthier, and R. Baets, "Optical bistability and pulsating behaviour in silicon-on-insulator ring resonator structures," *Optics express*, vol. 13, no. 23, pp. 9623–9628, 2005.
- [73] Q. Xu, S. Manipatruni, B. Schmidt, J. Shakya, and M. Lipson, "12.5 Gbit/s carrier-injection-based silicon micro-ring silicon modulators," *Opt. Express*, vol. 15, no. 2, pp. 430–436, 2007.
- [74] M. Ferrera, D. Duchesne, L. Razzari, M. Peccianti, R. Morandotti, P. Cheben, S. Janz, D.-X. Xu, B. Little, S. Chu, *et al.*, "Low power four wave mixing in an integrated, micro-ring resonator with $Q = 1.2$ million," *Optics express*, vol. 17, no. 16, pp. 14098–14103, 2009.
- [75] E. Centeno and D. Felbacq, "Optical bistability in finite-size nonlinear bidimensional photonic crystals doped by a microcavity," *Physical Review B*, vol. 62, p. 7683, 2000.
- [76] M. Soljačić, M. Ibanescu, S. G. Johnson, Y. Fink, and J. Joannopoulos, "Optimal bistable switching in nonlinear photonic crystals," *Physical Review E*, vol. 66, no. 5, p. 055601, 2002.
- [77] M. Soljačić, S. G. Johnson, S. Fan, M. Ibanescu, E. Ippen, and J. Joannopoulos, "Photonic-crystal slow-light enhancement of nonlinear phase sensitivity," *JOSA B*, vol. 19, no. 9, pp. 2052–2059, 2002.
- [78] A. Cowan and J. F. Young, "Optical bistability involving photonic crystal microcavities and fano line shapes," *Physical Review E*, vol. 68, no. 4, p. 046606, 2003.

- [79] M. Soljačić, C. Luo, J. Joannopoulos, and S. Fan, "Nonlinear photonic crystal microdevices for optical integration," *Optics letters*, vol. 28, no. 8, pp. 637–639, 2003.
- [80] M. F. Yanik, S. Fan, and M. Soljačić, "High-contrast all-optical bistable switching in photonic crystal microcavities," *Applied Physics Letters*, vol. 83, no. 14, pp. 2739–2741, 2003.
- [81] M. Martemyanov, E. Kim, T. Dolgova, A. Fedyanin, O. Aktsipetrov, and G. Marowsky, "Third-harmonic generation in silicon photonic crystals and microcavities," *Physical Review B*, vol. 70, no. 7, p. 073311, 2004.
- [82] M. Soljačić and J. D. Joannopoulos, "Enhancement of nonlinear effects using photonic crystals," *Nature materials*, vol. 3, no. 4, pp. 211–219, 2004.
- [83] J. Bravo-Abad, A. Rodriguez, P. Bermel, S. G. Johnson, J. D. Joannopoulos, and M. Soljačić, "Enhanced nonlinear optics in photonic-crystal microcavities," *Opt. Express*, vol. 15, no. 24, pp. 16161–16176, 2007.
- [84] P. Barclay, K. Srinivasan, and O. Painter, "Nonlinear response of silicon photonic crystal microresonators excited via an integrated waveguide and fiber taper," *Opt. Express*, vol. 13, no. 3, pp. 801–820, 2005.
- [85] B. Corcoran, C. Monat, C. Grillet, D. Moss, B. Eggleton, T. White, L. O’Faolain, and T. Krauss, "Green light emission in silicon through slow-light enhanced third-harmonic generation in photonic-crystal waveguides," *Nature photonics*, vol. 3, no. 4, pp. 206–210, 2009.
- [86] M. Notomi, T. Tanabe, A. Shinya, E. Kuramochi, H. Taniyama, S. Mitsugi, and M. Morita, "Nonlinear and adiabatic control of high-Q photonic crystal nanocavities," *Optics Express*, vol. 15, no. 26, pp. 17458–17481, 2007.
- [87] K. Nozaki, T. Tanabe, A. Shinya, S. Matsuo, T. Sato, H. Taniyama, and M. Notomi, "Sub-femtojoule all-optical switching using a photonic-crystal nanocavity," *Nature Photonics*, vol. 4, no. 7, pp. 477–483, 2010.
- [88] T. Uesugi, B.-S. Song, T. Asano, and S. Noda, "Investigation of optical nonlinearities in an ultra-high-Q Si nanocavity in a two-dimensional photonic crystal slab," *Optics express*, vol. 14, no. 1, pp. 377–386, 2006.
- [89] T. Tanabe, M. Notomi, S. Mitsugi, A. Shinya, and E. Kuramochi, "Fast bistable all-optical switch and memory on a silicon photonic crystal on-chip," *Optics letters*, vol. 30, no. 19, pp. 2575–2577, 2005.
- [90] T. Tanabe, M. Notomi, S. Mitsugi, A. Shinya, and E. Kuramochi, "All-optical switches on a silicon chip realized using photonic crystal nanocavities," *Applied Physics Letters*, vol. 87, no. 15, p. 151112, 2005.

Bibliography

- [91] M. Notomi, A. Shinya, S. Mitsugi, G. Kira, E. Kuramochi, and T. Tanabe, "Optical bistable switching action of Si high-Q photonic-crystal nanocavities," *Opt. Express*, vol. 13, no. 7, pp. 2678–2687, 2005.
- [92] E. Weidner, S. Combrie, A. de Rossi, N.-V.-Q. Tran, and S. Cassette, "Nonlinear and bistable behavior of an ultrahigh-Q GaAs photonic crystal nanocavity," *Applied Physics Letters*, vol. 90, no. 10, p. 101118, 2007.
- [93] X. Yang, C. Husko, C. W. Wong, M. Yu, and D.-L. Kwong, "Observation of femtojoule optical bistability involving fano resonances in high-Q/V silicon photonic crystal nanocavities," *Applied Physics Letters*, vol. 91, p. 051113, 2007.
- [94] Y. Zhang, D. Li, C. Zeng, Y. Shi, Z. Huang, J. Yu, and J. Xia, "Ultralow power nonlinear response in an si photonic crystal nanocavity," *Photonics Journal, IEEE*, vol. 5, no. 4, pp. 1–1, 2013.
- [95] C. Husko, A. De Rossi, S. Combri , Q. V. Tran, F. Raineri, and C. W. Wong, "Ultrafast all-optical modulation in GaAs photonic crystal cavities," *Applied Physics Letters*, vol. 94, no. 2, p. 021111, 2009.
- [96] M. Galli, D. Gerace, K. Welna, T. F. Krauss, L. O'Faolain, G. Guizzetti, and L. C. Andreani, "Low-power continuous-wave generation of visible harmonics in silicon photonic crystal nanocavities," *Optics express*, vol. 18, no. 25, pp. 26613–26624, 2010.
- [97] B. Maes, M. Fiers, and P. Bienstman, "Self-pulsing and chaos in short chains of coupled nonlinear microcavities," *Physical Review A*, vol. 80, no. 3, p. 033805, 2009.
- [98] E. Purcell, "Spontaneous emission probabilities at radio frequencies," *Physical Review*, vol. 69, p. 681, 1946.
- [99] T. Yoshie, A. Scherer, J. Hendrickson, G. Khitrova, H. Gibbs, G. Rupper, C. Ell, O. Shchekin, and D. Deppe, "Vacuum rabi splitting with a single quantum dot in a photonic crystal nanocavity," *Nature*, vol. 432, no. 7014, pp. 200–203, 2004.
- [100] P. Lodahl, A. F. Van Driel, I. S. Nikolaev, A. Irman, K. Overgaag, D. Vanmaekelbergh, and W. L. Vos, "Controlling the dynamics of spontaneous emission from quantum dots by photonic crystals," *Nature*, vol. 430, no. 7000, pp. 654–657, 2004.
- [101] A. Badolato, K. Hennessy, M. Atat re, J. Dreiser, E. Hu, P. M. Petroff, and A. Imamoglu, "Deterministic coupling of single quantum dots to single nanocavity modes," *Science*, vol. 308, no. 5725, pp. 1158–1161, 2005.
- [102] T. Lund-Hansen, S. Stobbe, B. Julsgaard, H. Thyrrerstrup, T. S nner, M. Kamp, A. Forchel, and P. Lodahl, "Experimental realization of highly efficient broadband coupling of single quantum dots to a photonic crystal waveguide," *Physical review letters*, vol. 101, no. 11, p. 113903, 2008.

- [103] D. Englund, D. Fattal, E. Waks, G. Solomon, B. Zhang, T. Nakaoka, Y. Arakawa, Y. Yamamoto, and J. Vučković, "Controlling the spontaneous emission rate of single quantum dots in a two-dimensional photonic crystal," *Physical Review Letters*, vol. 95, no. 1, p. 013904, 2005.
- [104] D. Gerace, H. E. Türeci, A. Imamoglu, V. Giovannetti, and R. Fazio, "The quantum-optical josephson interferometer," *Nature Physics*, vol. 5, no. 4, pp. 281–284, 2009.
- [105] W. Bogaerts, D. Taillaert, B. Luyssaert, P. Dumon, J. Van Campenhout, P. Bienstman, D. Van Thourhout, R. Baets, V. Wiaux, and S. Beckx, "Basic structures for photonic integrated circuits in silicon-on-insulator," *Opt. Express*, vol. 12, no. 8, pp. 1583–1591, 2004.
- [106] R. Nagarajan, M. Kato, D. Lambert, P. Evans, S. Corzine, V. Lal, J. Rahn, A. Nilsson, M. Fisher, M. Kuntz, *et al.*, "Terabit/s class inp photonic integrated circuits," *Semiconductor Science and Technology*, vol. 27, no. 9, p. 094003, 2012.
- [107] A. Liu, L. Liao, Y. Chetrit, J. Basak, H. Nguyen, D. Rubin, and M. Paniccia, "Wavelength division multiplexing based photonic integrated circuits on silicon-on-insulator platform," *Selected Topics in Quantum Electronics, IEEE Journal of*, vol. 16, no. 1, pp. 23–32, 2010.
- [108] <http://www.infinera.com>
- [109] W. Bogaerts, R. Baets, P. Dumon, V. Wiaux, S. Beckx, D. Taillaert, B. Luyssaert, J. Van Campenhout, P. Bienstman, and D. Van Thourhout, "Nanophotonic waveguides in silicon-on-insulator fabricated with CMOS technology," *Lightwave Technology, Journal of*, vol. 23, no. 1, pp. 401–412, 2005.
- [110] P. Dumon, W. Bogaerts, R. Baets, J.-M. Fedeli, and L. Fulbert, "Towards foundry approach for silicon photonics: silicon photonics platform ePIXfab," *Electronics letters*, vol. 45, no. 12, pp. 581–582, 2009.
- [111] H. Altug and J. V. Dirk Englund, "Ultrafast photonic crystal nanocavity laser," *Nature Physics*, vol. 2, no. 7, pp. 484–488, 2006.
- [112] Y. Takahashi, Y. Inui, M. Chihara, T. Asano, R. Terawaki, and S. Noda, "A micrometre-scale Raman silicon laser with a microwatt threshold," *Nature*, vol. 498, no. 7455, pp. 470–474, 2013.
- [113] L. Gu, W. Jiang, X. Chen, L. Wang, and R. T. Chen, "High speed silicon photonic crystal waveguide modulator for low voltage operation," *Applied physics letters*, vol. 90, no. 7, p. 071105, 2007.
- [114] C.-Y. Lin, X. Wang, S. Chakravarty, B. S. Lee, W. Lai, J. Luo, A. K.-Y. Jen, and R. T. Chen, "Electro-optic polymer infiltrated silicon photonic crystal slot waveguide modulator with 23 dB slow light enhancement," *Applied Physics Letters*, vol. 97, no. 9, p. 093304, 2010.

Bibliography

- [115] B. Corcoran, C. Monat, M. Pelusi, C. Grillet, T. White, L. O’Faolain, T. Krauss, B. Eggleton, and D. Moss, “Optical signal processing on a silicon chip at 640 Gb/s using slow-light,” *Optics express*, vol. 18, no. 8, pp. 7770–7781, 2010.
- [116] M. Notomi, A. Shinya, K. Nozaki, T. Tanabe, S. Matsuo, E. Kuramochi, T. Sato, H. Taniyama, and H. Sumikura, “Low-power nanophotonic devices based on photonic crystals towards dense photonic network on chip,” *Circuits, Devices & Systems, IET*, vol. 5, no. 2, pp. 84–93, 2011.
- [117] D. M. Beggs, T. P. White, L. O’Faolain, and T. F. Krauss, “Ultracompact and low-power optical switch based on silicon photonic crystals,” *Optics letters*, vol. 33, no. 2, pp. 147–149, 2008.
- [118] K. Nozaki, A. Shinya, S. Matsuo, Y. Suzuki, T. Segawa, T. Sato, Y. Kawaguchi, R. Takahashi, and M. Notomi, “Ultralow-power all-optical RAM based on nanocavities,” *Nat Photon*, vol. 6, pp. 248–252, 04 2012.
- [119] M. Notomi, K. Nozaki, A. Shinya, S. Matsuo, and E. Kuramochi, “Toward fJ/bit optical communication in a chip,” *Optics Communications*, 2013.
- [120] V. Zabelin, *Numerical investigation of two-dimensional photonic crystal optical properties, design and analysis of photonic crystal based structures*. PhD thesis, École Polytechnique Fédérale de Lausanne, 2009.
- [121] V. Savona, “Electromagnetic modes of a disordered photonic crystal,” *Physical Review B*, vol. 83, no. 8, p. 085301, 2011.
- [122] <http://www.comsol.com>
- [123] N. Descharmes, U. P. Dharanipathy, Z. Diao, M. Tonin, and R. Houdré, “Observation of backaction and self-induced trapping in a planar hollow photonic crystal cavity,” *Physical Review Letters*, vol. 110, no. 12, p. 123601, 2013.
- [124] N. Descharmes, U. P. Dharanipathy, Z. Diao, M. Tonin, and R. Houdré, “Single particle detection, manipulation and analysis with resonant optical trapping in photonic crystals,” *Lab Chip*, 2013.
- [125] U. P. Dharanipathy and R. Houdré, “Numerical modelling of optical trapping in hollow photonic crystal cavities,” *Optical and Quantum Electronics*, vol. 44, no. 3-5, pp. 161–167, 2012.
- [126] N. V. Triviño, U. Dharanipathy, J.-F. Carlin, Z. Diao, R. Houdré, and N. Grandjean, “Integrated photonics on silicon with wide bandgap GaN semiconductor,” *Applied Physics Letters*, vol. 102, no. 8, p. 081120, 2013.
- [127] U. Dharanipathy, N. V. Triviño, C. Yan, Z. Diao, J.-F. Carlin, N. Grandjean, and R. Houdré, “Near-infrared characterization of gallium nitride photonic-crystal waveguides and cavities,” *Opt. Lett.*, vol. 37, pp. 4588–4590, Nov 2012.

- [128] N. V. Triviño, G. Rossbach, U. Dharanipathy, J. Levrat, A. Castiglia, J.-F. Carlin, K. A. Atlasov, R. Butté, R. Houdré, and N. Grandjean, “High quality factor two dimensional GaN photonic crystal cavity membranes grown on silicon substrate,” *Applied Physics Letters*, vol. 100, no. 7, p. 071103, 2012.
- [129] M. Minkov, U. P. Dharanipathy, R. Houdré, and V. Savona, “Statistics of the disorder-induced losses of high-Q photonic crystal cavities,” *Opt. Express*, vol. 21, pp. 28233–28245, Nov 2013.
- [130] D. Fowler and E. Robson, “Square root approximations in old babylonian mathematics: YBC 7289 in context,” *Historia Mathematica*, vol. 25, no. 4, pp. 366–378, 1998.
- [131] L. F. Richardson, “The approximate arithmetical solution by finite differences of physical problems involving differential equations, with an application to the stresses in a masonry dam,” *Philosophical Transactions of the Royal Society of London. Series A, Containing Papers of a Mathematical or Physical Character*, vol. 210, pp. 307–357, 1911.
- [132] R. Courant, K. Friedrichs, and H. Lewy, “Über die partiellen differenzgleichungen der mathematischen physik,” *Mathematische Annalen*, vol. 100, no. 1, pp. 32–74, 1928.
- [133] R. Courant, “Variational methods for the solution of problems of equilibrium and vibrations,” *Bull. Amer. Math. Soc.*, vol. 49, no. 1, p. 23, 1943.
- [134] J. Von Neumann and H. H. Goldstine, “Numerical inverting of matrices of high order,” *Bulletin of the American Mathematical Society*, vol. 53, no. 11, pp. 1021–1099, 1947.
- [135] C. ping Yu and H. chun Chang, “Compact finite-difference frequency-domain method for the analysis of two-dimensional photonic crystals,” *Opt. Express*, vol. 12, pp. 1397–1408, Apr 2004.
- [136] M. Bayindir, B. Temelkuran, and E. Ozbay, “Tight-binding description of the coupled defect modes in three-dimensional photonic crystals,” *Physical Review Letters*, vol. 84, no. 10, p. 2140, 2000.
- [137] C. Chan, Q. Yu, and K. Ho, “Order-n spectral method for electromagnetic waves,” *Physical Review B*, vol. 51, no. 23, p. 16635, 1995.
- [138] P. Bienstman and R. Baets, “Optical modelling of photonic crystals and VCSELs using eigenmode expansion and perfectly matched layers,” *Optical and Quantum Electronics*, vol. 33, no. 4-5, pp. 327–341, 2001.
- [139] R. Scarmozzino, A. Gopinath, R. Pregla, and S. Helfert, “Numerical techniques for modeling guided-wave photonic devices,” *Selected Topics in Quantum Electronics, IEEE Journal of*, vol. 6, no. 1, pp. 150–162, 2000.
- [140] L. Botten, N. Nicorovici, R. McPhedran, C. M. de Sterke, and A. Asatryan, “Photonic band structure calculations using scattering matrices,” *Physical Review E*, vol. 64, no. 4, p. 046603, 2001.

Bibliography

- [141] K. Yee, "Numerical solution of initial boundary value problems involving maxwell's equations in isotropic media," *Antennas and Propagation, IEEE Transactions on*, vol. 14, no. 3, pp. 302–307, 1966.
- [142] L. C. Andreani and D. Gerace, "Photonic-crystal slabs with a triangular lattice of triangular holes investigated using a guided-mode expansion method," *Physical Review B*, vol. 73, no. 23, p. 235114, 2006.
- [143] P. A. Dirac, "The quantum theory of the emission and absorption of radiation," *Proceedings of the Royal Society of London. Series A, Containing Papers of a Mathematical and Physical Character*, vol. 114, no. 767, pp. 243–265, 1927.
- [144] E. Kuramochi, M. Notomi, S. Mitsugi, A. Shinya, T. Tanabe, and T. Watanabe, "Ultra-high-Q photonic crystal nanocavities realized by the local width modulation of a line defect," *Applied Physics Letters*, vol. 88, no. 4, p. 041112, 2006.
- [145] O. Schenk and K. Gärtner, "On fast factorization pivoting methods for sparse symmetric indefinite systems," *Electronic Transactions on Numerical Analysis*, vol. 23, pp. 158–179, 2006.
- [146] T. Baba, "Slow light in photonic crystals," *Nature Photonics*, vol. 2, no. 8, pp. 465–473, 2008.
- [147] T. F. Krauss, "Slow light in photonic crystal waveguides," *Journal of Physics D: Applied Physics*, vol. 40, no. 9, p. 2666, 2007.
- [148] J. Li, T. P. White, L. O'Faolain, A. Gomez-Iglesias, T. F. Krauss, *et al.*, "Systematic design of flat band slow light in photonic crystal waveguides," *Opt. Express*, vol. 16, no. 9, pp. 6227–6232, 2008.
- [149] Y. A. Vlasov, M. Kaliteevski, and V. Nikolaev, "Different regimes of light localization in a disordered photonic crystal," *Physical Review B*, vol. 60, no. 3, p. 1555, 1999.
- [150] S. Hughes, L. Ramunno, J. F. Young, and J. Sipe, "Extrinsic optical scattering loss in photonic crystal waveguides: role of fabrication disorder and photon group velocity," *Physical review letters*, vol. 94, no. 3, p. 033903, 2005.
- [151] J. Topolancik, B. Ilic, and F. Vollmer, "Experimental observation of strong photon localization in disordered photonic crystal waveguides," *Physical review letters*, vol. 99, no. 25, p. 253901, 2007.
- [152] N. Le Thomas, H. Zhang, J. Jágerská, V. Zabelin, R. Houdré, I. Sagnes, and A. Talneau, "Light transport regimes in slow light photonic crystal waveguides," *Physical Review B*, vol. 80, no. 12, p. 125332, 2009.
- [153] L. Sapienza, H. Thyrestrup, S. Stobbe, P. D. Garcia, S. Smolka, and P. Lodahl, "Cavity quantum electrodynamics with Anderson-localized modes," *Science*, vol. 327, no. 5971, pp. 1352–1355, 2010.

- [154] J. Jágerská, N. Le Thomas, V. Zabelin, R. Houdré, W. Bogaerts, P. Dumon, and R. Baets, "Experimental observation of slow mode dispersion in photonic crystal coupled-cavity waveguides," *Optics letters*, vol. 34, no. 3, pp. 359–361, 2009.
- [155] A. Di Falco, L. OFaolain, and T. Krauss, "Dispersion control and slow light in slotted photonic crystal waveguides," *Applied Physics Letters*, vol. 92, no. 8, p. 083501, 2008.
- [156] L. C. Andreani, D. Gerace, and M. Agio, "Gap maps, diffraction losses, and exciton-polaritons in photonic crystal slabs," *Photonics and Nanostructures-Fundamentals and Applications*, vol. 2, no. 2, pp. 103–110, 2004.
- [157] J. Foresi, P. R. Villeneuve, J. Ferrera, E. Thoen, G. Steinmeyer, S. Fan, J. Joannopoulos, L. Kimerling, H. I. Smith, and E. Ippen, "Photonic-bandgap microcavities in optical waveguides," *Nature*, vol. 390, no. 6656, pp. 143–145, 1997.
- [158] M. R. Lee and P. M. Fauchet, "Nanoscale microcavity sensor for single particle detection," *Optics letters*, vol. 32, no. 22, pp. 3284–3286, 2007.
- [159] J. Jágerská, H. Zhang, Z. Diao, N. L. Thomas, and R. Houdré, "Refractive index sensing with an air-slot photonic crystal nanocavity," *Optics letters*, vol. 35, no. 15, pp. 2523–2525, 2010.
- [160] Y. Akahane, T. Asano, B.-S. Song, and S. Noda, "Fine-tuned high-Q photonic-crystal nanocavity," *Opt. Express*, vol. 13, pp. 1202–1214, Feb 2005.
- [161] Y. Akahane, T. Asano, B.-S. Song, and S. Noda, "High-Q photonic nanocavity in a two-dimensional photonic crystal," *Nature*, vol. 425, no. 6961, pp. 944–947, 2003.
- [162] B.-S. Song, S. Noda, T. Asano, and Y. Akahane, "Ultra-high-Q photonic double-heterostructure nanocavity," *Nat Mater*, vol. 4, pp. 207–210, 03 2005.
- [163] D. Englund, I. Fushman, and J. Vučković, "General recipe for designing photonic crystal cavities," *Opt. Express*, vol. 13, no. 16, pp. 5961–5975, 2005.
- [164] T. Tanabe, M. Notomi, E. Kuramochi, A. Shinya, and H. Taniyama, "Trapping and delaying photons for one nanosecond in an ultrasmall high-Q photonic-crystal nanocavity," *Nature Photonics*, vol. 1, no. 1, pp. 49–52, 2006.
- [165] Y. Tanaka, T. Asano, Y. Akahane, B.-S. Song, and S. Noda, "Theoretical investigation of a two-dimensional photonic crystal slab with truncated cone air holes," *Applied physics letters*, vol. 82, no. 11, pp. 1661–1663, 2003.
- [166] T. Asano, B.-S. Song, and S. Noda, "Analysis of the experimental Q factors (1 million) of photonic crystal nanocavities," *Optics Express*, vol. 14, no. 5, pp. 1996–2002, 2006.
- [167] D. Gerace and L. C. Andreani, "Effects of disorder on propagation losses and cavity Q-factors in photonic crystal slabs," *Photonics and Nanostructures-fundamentals and applications*, vol. 3, no. 2, pp. 120–128, 2005.

Bibliography

- [168] Y. Taguchi, Y. Takahashi, Y. Sato, T. Asano, and S. Noda, "Statistical studies of photonic heterostructure nanocavities with an average Q factor of three million," *Opt. Express*, vol. 19, pp. 11916–11921, Jun 2011.
- [169] S. L. Portalupi, M. Galli, M. Belotti, L. C. Andreani, T. F. Krauss, and L. O'Faolain, "Deliberate versus intrinsic disorder in photonic crystal nanocavities investigated by resonant light scattering," *Physical Review B*, vol. 84, no. 4, p. 045423, 2011.
- [170] N. Le Thomas, Z. Diao, H. Zhang, and R. Houdré, "Statistical analysis of subnanometer residual disorder in photonic crystal waveguides: Correlation between slow light properties and structural properties," *Journal of Vacuum Science and Technology B: Microelectronics and Nanometer Structures*, vol. 29, no. 5, p. 051601, 2011.
- [171] M. Minkov and V. Savona, "Effect of hole-shape irregularities on photonic crystal waveguides," *Optics Letters*, vol. 37, no. 15, pp. 3108–3110, 2012.
- [172] Z. Zhang and M. Qiu, "Small-volume waveguide-section high Q microcavities in 2D photonic crystal slabs," *Optics Express*, vol. 12, no. 17, pp. 3988–3995, 2004.
- [173] H. Takagi, Y. Ota, N. Kumagai, S. Ishida, S. Iwamoto, and Y. Arakawa, "High Q H1 photonic crystal nanocavities with efficient vertical emission," *Optics express*, vol. 20, no. 27, pp. 28292–28300, 2012.
- [174] <http://solarsystem.nasa.gov>
- [175] A. Ashkin *et al.*, "Acceleration and trapping of particles by radiation pressure," *Physical review letters*, vol. 24, no. 4, pp. 156–159, 1970.
- [176] A. Ashkin, "Optical trapping and manipulation of neutral particles using lasers," *Proceedings of the National Academy of Sciences*, vol. 94, no. 10, pp. 4853–4860, 1997.
- [177] A. Ashkin, J. Dziedzic, J. Bjorkholm, and S. Chu, "Observation of a single-beam gradient force optical trap for dielectric particles," *Optics letters*, vol. 11, no. 5, pp. 288–290, 1986.
- [178] S. Block, "Optical tweezers: a new tool for biophysics," *Modern cell biology*, vol. 9, pp. 375–402, 1990.
- [179] K. Svoboda and S. M. Block, "Biological applications of optical forces," *Annual review of biophysics and biomolecular structure*, vol. 23, no. 1, pp. 247–285, 1994.
- [180] O. Brzobohatý, V. Karásek, M. Šiler, L. Chvátal, T. Čížmár, and P. Zemánek, "Experimental demonstration of optical transport, sorting and self-arrangement using a tractor beam/," *Nature Photonics*, 2013.
- [181] S. Chu, L. Hollberg, J. E. Bjorkholm, A. Cable, and A. Ashkin, "Three-dimensional viscous confinement and cooling of atoms by resonance radiation pressure," *Physical Review Letters*, vol. 55, no. 1, p. 48, 1985.

- [182] K. Davis, M.-O. Mewes, M. v. Andrews, N. Van Druten, D. Durfee, D. Kurn, and W. Ketterle, "Bose-einstein condensation in a gas of sodium atoms," *Physical Review Letters*, vol. 75, no. 22, p. 3969, 1995.
- [183] K. C. Neuman and S. M. Block, "Optical trapping," *Review of scientific instruments*, vol. 75, no. 9, pp. 2787–2809, 2004.
- [184] M. Righini, P. Ghenuche, S. Cherukulappurath, V. Myroshnychenko, F. J. García de Abajo, and R. Quidant, "Nano-optical trapping of Rayleigh particles and Escherichia coli bacteria with resonant optical antennas," *Nano letters*, vol. 9, no. 10, pp. 3387–3391, 2009.
- [185] A. H. Yang, S. D. Moore, B. S. Schmidt, M. Klug, M. Lipson, and D. Erickson, "Optical manipulation of nanoparticles and biomolecules in sub-wavelength slot waveguides," *Nature*, vol. 457, no. 7225, pp. 71–75, 2009.
- [186] S. Mandal, X. Serey, and D. Erickson, "Nanomanipulation using silicon photonic crystal resonators," *Nano letters*, vol. 10, no. 1, pp. 99–104, 2009.
- [187] L. Novotny, R. X. Bian, and X. S. Xie, "Theory of nanometric optical tweezers," *Physical Review Letters*, vol. 79, no. 4, p. 645, 1997.
- [188] O. J. Martin and C. Girard, "Controlling and tuning strong optical field gradients at a local probe microscope tip apex," *Applied Physics Letters*, vol. 70, no. 6, pp. 705–707, 1997.
- [189] K. Okamoto and S. Kawata, "Radiation force exerted on subwavelength particles near a nanoaperture," *Physical review letters*, vol. 83, no. 22, p. 4534, 1999.
- [190] M. Righini, A. S. Zelenina, C. Girard, and R. Quidant, "Parallel and selective trapping in a patterned plasmonic landscape," *Nature Physics*, vol. 3, no. 7, pp. 477–480, 2007.
- [191] M. Righini, G. Volpe, C. Girard, D. Petrov, and R. Quidant, "Surface plasmon optical tweezers: tunable optical manipulation in the femtonewton range," *Physical review letters*, vol. 100, no. 18, p. 186804, 2008.
- [192] L. Huang, S. J. Maerkl, and O. J. Martin, "Integration of plasmonic trapping in a microfluidic environment," *Opt. Express*, vol. 17, no. 8, pp. 6018–6024, 2009.
- [193] Y. Pang and R. Gordon, "Optical trapping of 12 nm dielectric spheres using double-nanoholes in a gold film," *Nano letters*, vol. 11, no. 9, pp. 3763–3767, 2011.
- [194] S. Kawata and T. Tani, "Optically driven mie particles in an evanescent field along a channeled waveguide," *Optics letters*, vol. 21, no. 21, pp. 1768–1770, 1996.
- [195] S. Gaugiran, S. Gétin, J. Fedeli, G. Colas, A. Fuchs, F. Chatelain, and J. Dérourard, "Optical manipulation of microparticles and cells on silicon nitride waveguides," *Optics Express*, vol. 13, no. 18, pp. 6956–6963, 2005.

Bibliography

- [196] G. Brambilla, G. S. Murugan, J. Wilkinson, and D. Richardson, "Optical manipulation of microspheres along a subwavelength optical wire," *Optics letters*, vol. 32, no. 20, pp. 3041–3043, 2007.
- [197] B. S. Schmidt, A. H. Yang, D. Erickson, and M. Lipson, "Optofluidic trapping and transport on solid core waveguides within a microfluidic device," *Optics Express*, vol. 15, no. 22, pp. 14322–14334, 2007.
- [198] V. R. Almeida, Q. Xu, C. A. Barrios, and M. Lipson, "Guiding and confining light in void nanostructure," *Optics letters*, vol. 29, no. 11, pp. 1209–1211, 2004.
- [199] S. Lin, E. Schonbrun, and K. Crozier, "Optical manipulation with planar silicon microring resonators," *Nano letters*, vol. 10, no. 7, pp. 2408–2411, 2010.
- [200] A. H. Yang and D. Erickson, "Optofluidic ring resonator switch for optical particle transport," *Lab on a Chip*, vol. 10, no. 6, pp. 769–774, 2010.
- [201] H. Cai and A. W. Poon, "Optical manipulation and transport of microparticles on silicon nitride microring-resonator-based add-drop devices," *Optics letters*, vol. 35, no. 17, pp. 2855–2857, 2010.
- [202] C. Renaut, J. Dellinger, B. Cluzel, T. Honegger, D. Peyrade, E. Picard, F. De Fornel, and E. Hadji, "Assembly of microparticles by optical trapping with a photonic crystal nanocavity," *Applied Physics Letters*, vol. 100, no. 10, p. 101103, 2012.
- [203] A. Ashkin, "Forces of a single-beam gradient laser trap on a dielectric sphere in the ray optics regime," *Biophysical journal*, vol. 61, no. 2, pp. 569–582, 1992.
- [204] Y. Harada and T. Asakura, "Radiation forces on a dielectric sphere in the rayleigh scattering regime," *Optics communications*, vol. 124, no. 5, pp. 529–541, 1996.
- [205] J. D. Jackson, *Classical Electrodynamics*. John Wiley & Sons: New York, 1998.
- [206] M. J. Padgett and R. W. Bowman, "Optical trapping and binding," *Reports on Progress in Physics*, vol. 76, no. 2, pp. 26401–26428, 2013.
- [207] A. Rohrbach, "Stiffness of optical traps: quantitative agreement between experiment and electromagnetic theory," *Physical review letters*, vol. 95, no. 16, p. 168102, 2005.
- [208] S. Noda, A. Chutinan, and M. Imada, "Trapping and emission of photons by a single defect in a photonic bandgap structure," *Nature*, vol. 407, no. 6804, pp. 608–610, 2000.
- [209] F. Intonti, S. Vignolini, F. Riboli, M. Zani, D. S. Wiersma, L. Balet, L. H. Li, M. Francardi, A. Gerardo, A. Fiore, *et al.*, "Tuning of photonic crystal cavities by controlled removal of locally infiltrated water," *Applied Physics Letters*, vol. 95, no. 17, p. 173112, 2009.
- [210] X. Chen, W. Jiang, J. Chen, L. Gu, and R. T. Chen, "20 dB-enhanced coupling to slot photonic crystal waveguide using multimode interference coupler," *Applied Physics Letters*, vol. 91, p. 091111, 2007.

- [211] T. Yamamoto, M. Notomi, H. Taniyama, E. Kuramochi, Y. Yoshikawa, Y. Torii, and T. Kuga, "Design of a high-Q air-slot cavity based on a width-modulated line-defect in a photonic crystal slab," *Opt. Express*, vol. 16, no. 18, pp. 13809–13817, 2008.
- [212] S. Hamed Mirsadeghi, E. Schelew, and J. F. Young, "Photonic crystal slot-microcavity circuit implemented in silicon-on-insulator: High Q operation in solvent without undercutting," *Applied Physics Letters*, vol. 102, no. 13, p. 131115, 2013.
- [213] N. Descharmes, *Resonant optical trapping in microfluidic-integrated hollow photonic crystal cavities*. PhD thesis, École Polytechnique Fédérale de Lausanne, 2013.
- [214] Z. Diao, *Investigation of 2D Photonic Crystals and Their Applications on Terahertz Quantum Cascade Lasers, Optical Trapping and Sensing*. PhD thesis, École Polytechnique Fédérale de Lausanne, 2013.
- [215] M. A. Unger, H.-P. Chou, T. Thorsen, A. Scherer, and S. R. Quake, "Monolithic microfabricated valves and pumps by multilayer soft lithography," *Science*, vol. 288, no. 5463, pp. 113–116, 2000.
- [216] K. Okamoto, M. Loncar, T. Yoshie, A. Scherer, Y. Qiu, and P. Gogna, "Near-field scanning optical microscopy of photonic crystal nanocavities," *Applied physics letters*, vol. 82, no. 11, pp. 1676–1678, 2003.
- [217] S. Mujumdar, A. Koenderink, T. Sřnner, B. Buchler, M. Kamp, A. Forchel, and V. Sandoghdar, "Near-field imaging and frequency tuning of a high-Q photonic crystal membrane microcavity," *Optics Express*, vol. 15, no. 25, pp. 17214–17220, 2007.
- [218] A. Schliesser, P. Del'Haye, N. Nooshi, K. Vahala, and T. Kippenberg, "Radiation pressure cooling of a micromechanical oscillator using dynamical backaction," *Physical Review Letters*, vol. 97, no. 24, p. 243905, 2006.
- [219] J. Hu, S. Lin, L. C. Kimerling, and K. Crozier, "Optical trapping of dielectric nanoparticles in resonant cavities," *Physical Review A*, vol. 82, no. 5, p. 053819, 2010.
- [220] Z.-q. Yin, T. Li, and M. Feng, "Three-dimensional cooling and detection of a nanosphere with a single cavity," *Physical Review A*, vol. 83, no. 1, p. 013816, 2011.
- [221] M. Barth and O. Benson, "Manipulation of dielectric particles using photonic crystal cavities," *Applied physics letters*, vol. 89, no. 25, p. 253114, 2006.
- [222] J. T. Rubin and L. Deych, "On optical forces in spherical whispering gallery mode resonators," *Opt. Express*, vol. 19, pp. 22337–22349, Oct 2011.
- [223] X. Gan, N. Pervez, I. Kymissis, F. Hatami, and D. Englund, "A high-resolution spectrometer based on a compact planar two dimensional photonic crystal cavity array," *Applied Physics Letters*, vol. 100, no. 23, p. 231104, 2012.

Bibliography

- [224] Z. Xia, A. A. Eftekhar, M. Soltani, B. Momeni, Q. Li, M. Chamanzar, S. Yegnanarayanan, and A. Adibi, "High resolution on-chip spectroscopy based on miniaturized microdonut resonators," *Opt. Express* 19 (13), pp. 12356–12364, 2011.
- [225] E. J. Peterman, F. Gittes, and C. F. Schmidt, "Laser-induced heating in optical traps," *Biophysical journal*, vol. 84, no. 2, pp. 1308–1316, 2003.
- [226] T. Franosch, M. Grimm, M. Belushkin, F. M. Mor, G. Foffi, L. Forró, and S. Jeney, "Resonances arising from hydrodynamic memory in brownian motion," *Nature*, vol. 478, no. 7367, pp. 85–88, 2011.
- [227] J. Gieseler, B. Deutsch, R. Quidant, and L. Novotny, "Subkelvin parametric feedback cooling of a laser-trapped nanoparticle," *Physical Review Letters*, vol. 109, no. 10, p. 103603, 2012.
- [228] K. Berg-Sørensen and H. Flyvbjerg, "Power spectrum analysis for optical tweezers," *Review of Scientific Instruments*, vol. 75, no. 3, pp. 594–612, 2004.
- [229] T. van Leest and J. Caro, "Cavity-enhanced optical trapping of bacteria using a silicon photonic crystal," *Lab on a Chip*, vol. 13, no. 22, pp. 4358–4365, 2013.
- [230] U. P. Dharanipathy, M. Minkov, M. Tonin, V. Savona, and R. Houdré, "Evolutionarily optimized ultrahigh-Q photonic crystal nanocavity," *arXiv preprint arXiv:1311.0997*, 2013.
- [231] J. Vučković, D. Englund, D. Fattal, E. Waks, and Y. Yamamoto, "Generation and manipulation of nonclassical light using photonic crystals," *Physica E: Low-dimensional Systems and Nanostructures*, vol. 32, no. 1, pp. 466–470, 2006.
- [232] M. Notomi, A. Shinya, S. Mitsugi, E. Kuramochi, and H. Ryu, "Waveguides, resonators and their coupled elements in photonic crystal slabs," *Optics Express*, vol. 12, no. 8, pp. 1551–1561, 2004.
- [233] K. Srinivasan and O. Painter, "Momentum space design of high-Q photonic crystal optical cavities," *Optics Express*, vol. 10, no. 15, pp. 670–684, 2002.
- [234] M. Felici, K. A. Atlasov, A. Surrente, and E. Kapon, "Semianalytical approach to the design of photonic crystal cavities," *Physical Review B*, vol. 82, no. 11, p. 115118, 2010.
- [235] Y. Tanaka, T. Asano, and S. Noda, "Design of photonic crystal nanocavity with Q-factor of 10^9 ," *Journal of Lightwave Technology*, vol. 26, no. 11, pp. 1532–1539, 2008.
- [236] M. Nomura, K. Tanabe, S. Iwamoto, and Y. Arakawa, "High-Q design of semiconductor-based ultrasmall photonic crystal nanocavity," *Opt. Express*, vol. 18, no. 8, pp. 8144–8150, 2010.

- [237] G.-H. Kim, Y.-H. Lee, A. Shinya, and M. Notomi, "Coupling of small, low-loss hexapole mode with photonic crystal slab waveguide mode," *Optics Express*, vol. 12, no. 26, pp. 6624–6631, 2004.
- [238] A. Faraon, E. Waks, D. Englund, I. Fushman, and J. Vučković, "Efficient photonic crystal cavity-waveguide couplers," *Applied Physics Letters*, vol. 90, no. 7, p. 073102, 2007.
- [239] E. Waks and J. Vučković, "Coupled mode theory for photonic crystal cavity-waveguide interaction," *Optics Express*, vol. 13, no. 13, pp. 5064–5073, 2005.
- [240] M. Shirane, S. Kono, J. Ushida, S. Ohkouchi, N. Ikeda, Y. Sugimoto, and A. Tomita, "Mode identification of high-quality-factor single-defect nanocavities in quantum dot-embedded photonic crystals," *Journal of applied physics*, vol. 101, no. 7, p. 073107, 2007.
- [241] P. B. Deotare, M. W. McCutcheon, I. W. Frank, M. Khan, and M. Loncar, "High quality factor photonic crystal nanobeam cavities," *Applied Physics Letters*, vol. 94, no. 12, p. 121106, 2009.
- [242] R. W. Boyd, "Nonlinear optics," 1992.
- [243] J. Leuthold, C. Koos, and W. Freude, "Nonlinear silicon photonics," *Nature Photonics*, vol. 4, no. 8, pp. 535–544, 2010.
- [244] J. McCaulley, V. Donnelly, M. Vernon, and I. Taha, "Temperature dependence of the near-infrared refractive index of silicon, gallium arsenide, and indium phosphide," *Physical Review B*, vol. 49, no. 11, p. 7408, 1994.
- [245] T. Tanabe, A. Shinya, E. Kuramochi, S. Kondo, H. Taniyama, and M. Notomi, "Single point defect photonic crystal nanocavity with ultrahigh quality factor achieved by using hexapole mode," *Applied physics letters*, vol. 91, no. 2, p. 021110, 2007.
- [246] Y. Takahashi, H. Hagino, Y. Tanaka, B.-S. Song, T. Asano, and S. Noda, "High-Q nanocavity with a 2-ns photon lifetime," *Opt. Express*, vol. 15, pp. 17206–17213, Dec 2007.
- [247] S. Combrié, A. D. Rossi, Q. V. Tran, and H. Benisty, "GaAs photonic crystal cavity with ultrahigh Q: microwatt nonlinearity at 1.55 μm ," *Opt. Lett.*, vol. 33, pp. 1908–1910, Aug 2008.
- [248] Z. Han, X. Checoury, L.-D. Haret, and P. Boucaud, "High quality factor in a two-dimensional photonic crystal cavity on silicon-on-insulator," *Optics letters*, vol. 36, no. 10, pp. 1749–1751, 2011.
- [249] A. Yokoo, T. Tanabe, E. Kuramochi, and M. Notomi, "Ultrahigh-Q nanocavities written with a nanoprobe," *Nano letters*, vol. 11, no. 9, pp. 3634–3642, 2011.
- [250] S. Pearton, F. Ren, A. Zhang, and K. Lee, "Fabrication and performance of GaN electronic devices," *Materials Science and Engineering: R: Reports*, vol. 30, no. 3, pp. 55–212, 2000.

Bibliography

- [251] S. Strite and H. Morkoç, "GaN, AlN, and InN: A review," *Journal of Vacuum Science & Technology B: Microelectronics and Nanometer Structures*, vol. 10, no. 4, pp. 1237–1266, 1992.
- [252] S. A. Jewett, M. S. Makowski, B. Andrews, M. J. Manfra, and A. Ivanisevic, "Gallium nitride is biocompatible and non-toxic before and after functionalization with peptides," *Acta Biomaterialia*, vol. 8, no. 2, pp. 728 – 733, 2012.
- [253] N. Holonyak and S. F. Bevacqua, "Coherent (visible) light emission from GaAs_{1-x}P_x junctions," *Applied Physics Letters*, vol. 1, no. 4, pp. 82–83, 1962.
- [254] R. N. Hall, G. E. Fenner, J. D. Kingsley, T. J. Soltys, and R. O. Carlson, "Coherent light emission from GaAs junctions," *Phys. Rev. Lett.*, vol. 9, pp. 366–368, Nov 1962.
- [255] M. Craford, "LEDs challenge the incandescents," *Circuits and Devices Magazine, IEEE*, vol. 8, no. 5, pp. 24–29, 1992.
- [256] F. Ponce and D. Bour, "Nitride-based semiconductors for blue and green light-emitting devices," *Nature*, vol. 386, no. 6623, pp. 351–359, 1997.
- [257] R. Dingle, K. L. Shaklee, R. F. Leheny, and R. B. Zetterstrom, "Stimulated emission and laser action in gallium nitride," *Applied Physics Letters*, vol. 19, no. 1, pp. 5–7, 1971.
- [258] H. Amano, M. Kito, K. Hiramatsu, and I. Akasaki, "P-type conduction in Mg-doped GaN treated with Low-Energy Electron Beam Irradiation (LEEBI)," *Japanese Journal of Applied Physics*, vol. 28, no. Part 2, No. 12, pp. L2112–L2114, 1989.
- [259] H. Amano, N. Sawaki, I. Akasaki, and Y. Toyoda, "Metalorganic vapor phase epitaxial growth of a high quality GaN film using an AlN buffer layer," *Applied Physics Letters*, vol. 48, no. 5, pp. 353–355, 1986.
- [260] S. Nakamura, T. Mukai, and M. Senoh, "High-power GaN P-N junction blue-light-emitting diodes," *Japanese Journal of Applied Physics*, vol. 30, no. Part 2, No. 12A, pp. L1998–L2001, 1991.
- [261] S. Nakamura, T. Mukai, and M. Senoh, "Candela-class high-brightness InGaN/AlGaN double-heterostructure blue-light-emitting diodes," *Applied Physics Letters*, vol. 64, no. 13, pp. 1687–1689, 1994.
- [262] S. Nakamura, M. Senoh, S. ichi Nagahama, N. Iwasa, T. Yamada, T. Matsushita, H. Kiyoku, and Y. Sugimoto, "InGaN-based multi-quantum-well-structure laser diodes," *Japanese Journal of Applied Physics*, vol. 35, no. Part 2, No. 1B, pp. L74–L76, 1996.
- [263] A. Khan, K. Balakrishnan, and T. Katona, "Ultraviolet light-emitting diodes based on group three nitrides," *Nat Photon*, vol. 2, pp. 77–84, 02 2008.
- [264] N. Grandjean and R. Butté, "Light-emitting diodes: Solid-state lighting on glass," *Nat Photon*, vol. 5, pp. 714–715, 12 2011.

- [265] S. Christopoulos, G. B. H. von Högersthal, A. J. D. Grundy, P. G. Lagoudakis, A. V. Kavokin, J. J. Baumberg, G. Christmann, R. Butté, E. Feltin, J.-F. Carlin, and N. Grandjean, “Room-temperature polariton lasing in semiconductor microcavities,” *Phys. Rev. Lett.*, vol. 98, p. 126405, Mar 2007.
- [266] G. Christmann, R. Butté, E. Feltin, A. Mouti, P. A. Stadelmann, A. Castiglia, J.-F. m. c. Carlin, and N. Grandjean, “Large vacuum Rabi splitting in a multiple quantum well GaN-based microcavity in the strong-coupling regime,” *Phys. Rev. B*, vol. 77, p. 085310, Feb 2008.
- [267] T. N. Oder, J. Shakya, J. Y. Lin, and H. X. Jiang, “III-nitride photonic crystals,” *Applied Physics Letters*, vol. 83, no. 6, pp. 1231–1233, 2003.
- [268] Y.-S. Choi, K. Hennessy, R. Sharma, E. Haberer, Y. Gao, S. P. DenBaars, S. Nakamura, E. L. Hu, and C. Meier, “GaN blue photonic crystal membrane nanocavities,” *Applied Physics Letters*, vol. 87, no. 24, p. 243101, 2005.
- [269] A. Rosenberg, M. Carter, J. Casey, M. Kim, R. Holm, R. Henry, C. Eddy, V. Shamamian, K. Bussmann, S. Shi, and D. Prather, “Guided resonances in asymmetrical GaN photonic crystal slabs observed in the visible spectrum,” *Opt. Express*, vol. 13, pp. 6564–6571, Aug 2005.
- [270] M. Arita, S. Ishida, S. Kako, S. Iwamoto, and Y. Arakawa, “AlN air-bridge photonic crystal nanocavities demonstrating high quality factor,” *Applied Physics Letters*, vol. 91, no. 5, p. 051106, 2007.
- [271] D. Néel, S. Sergent, M. Mexis, D. Sam-Giao, T. Guillet, C. Brimont, T. Bretagnon, F. Se-mond, B. Gayral, S. David, X. Checoury, and P. Boucaud, “AlN photonic crystal nanocavities realized by epitaxial conformal growth on nanopatterned silicon substrate,” *Applied Physics Letters*, vol. 98, no. 26, p. 261106, 2011.
- [272] K. Orita, S. Tamura, T. Takizawa, T. Ueda, M. Yuri, S. Takigawa, and D. Ueda, “High-extraction-efficiency blue light-emitting diode using extended-pitch photonic crystal,” *Japanese Journal of Applied Physics*, vol. 43, no. 8B, pp. 5809–5813, 2004.
- [273] J. J. Wierer, M. R. Krames, J. E. Epler, N. F. Gardner, M. G. Craford, J. R. Wendt, J. A. Simmons, and M. M. Sigalas, “InGaN/GaN quantum-well heterostructure light-emitting diodes employing photonic crystal structures,” *Applied Physics Letters*, vol. 84, no. 19, pp. 3885–3887, 2004.
- [274] D.-H. Kim, C.-O. Cho, Y.-G. Roh, H. Jeon, Y.-S. Park, J. Cho, J. S. Im, C. Sone, Y. Park, W. J. Choi, and Q.-H. Park, “Enhanced light extraction from GaN-based light-emitting diodes with holographically generated two-dimensional photonic crystal patterns,” *Applied Physics Letters*, vol. 87, no. 20, p. 203508, 2005.

Bibliography

- [275] A. D. David, T. Fujii, B. Moran, S. Nakamura, S. P. DenBaars, C. Weisbuch, and H. Benisty, "Photonic crystal laser lift-off GaN light-emitting diodes," *Applied Physics Letters*, vol. 88, no. 13, p. 133514, 2006.
- [276] A. David, T. Fujii, R. Sharma, K. McGroddy, S. Nakamura, S. P. DenBaars, E. L. Hu, C. Weisbuch, and H. Benisty, "Photonic-crystal GaN light-emitting diodes with tailored guided modes distribution," *Applied Physics Letters*, vol. 88, no. 6, p. 061124, 2006.
- [277] J. J. Wierer, A. David, and M. M. Megens, "III-nitride photonic-crystal light-emitting diodes with high extraction efficiency," *Nat Photon*, vol. 3, pp. 163–169, 03 2009.
- [278] C.-H. Lin, J.-Y. Wang, C.-Y. Chen, K.-C. Shen, D.-M. Yeh, Y.-W. Kiang, and C. C. Yang, "A GaN photonic crystal membrane laser," *Nanotechnology*, vol. 22, no. 2, p. 025201, 2011.
- [279] D. uk Kim, S. Kim, J. Lee, S.-R. Jeon, and H. Jeon, "Free-standing GaN-based photonic crystal band-edge laser," *Photonics Technology Letters, IEEE*, vol. 23, no. 20, pp. 1454–1456, 2011.
- [280] G. Subramania, Q. Li, Y.-J. Lee, J. J. Figiel, G. T. Wang, and A. J. Fischer, "Gallium nitride based logpile photonic crystals," *Nano Letters*, vol. 11, no. 11, pp. 4591–4596, 2011.
- [281] C. Xiong, W. Pernice, K. K. Ryu, C. Schuck, K. Y. Fong, T. Palacios, and H. X. Tang, "Integrated GaN photonic circuits on silicon (100) for second harmonic generation," *Opt. Express*, vol. 19, pp. 10462–10470, May 2011.
- [282] T. Paskova, D. Hanser, and K. Evans, "GaN substrates for III-nitride devices," *Proceedings of the IEEE*, vol. 98, no. 7, pp. 1324–1338, 2010.
- [283] P. Bienstman, "Camfr: cavity modelling framework software," <http://camfr.sourceforge.net/>, 2006.
- [284] A. Talneau, K. H. Lee, S. Guilet, and I. Sagnes, "Efficient coupling to W1 photonic crystal waveguide on InP membrane through suspended access guides," *Applied Physics Letters*, vol. 92, no. 6, p. 061105, 2008.
- [285] A. Talneau, K.-H. Lee, and I. Sagnes, "Spectral behavior and dispersionless propagation in indium phosphide suspended photonic wires," *Photonics Technology Letters, IEEE*, vol. 21, no. 12, pp. 775–777, 2009.
- [286] B. Weiss, G. Reed, S. K. Toh, R. Soref, and F. Namavar, "Optical waveguides in SIMOX structures," *Photonics Technology Letters, IEEE*, vol. 3, no. 1, pp. 19–21, 1991.
- [287] G. Li, J. Yao, H. Thacker, A. Mekis, X. Zheng, I. Shubin, Y. Luo, J. hyoung Lee, K. Raj, J. E. Cunningham, and A. V. Krishnamoorthy, "Ultralow-loss, high-density SOI optical waveguide routing for macrochip interconnects," *Opt. Express*, vol. 20, pp. 12035–12039, May 2012.

- [288] N. Le Thomas, R. Houdré, M. V. Kotlyar, D. O'Brien, and T. F. Krauss, "Exploring light propagating in photonic crystals with fourier optics," *JOSA B*, vol. 24, no. 12, pp. 2964–2971, 2007.
- [289] N. Antoine-Vincent, F. Natali, M. Mihailovic, A. Vasson, J. Leymarie, P. Disseix, D. Byrne, E. Semond, and J. Massies, "Determination of the refractive indices of AlN, GaN, and $\text{Al}_x\text{Ga}_{1-x}\text{N}$ grown on (111)Si substrates," *Journal of Applied Physics*, vol. 93, no. 9, pp. 5222–5226, 2003.

Acknowledgements

This PhD thesis is a massive undertaking in my life. It was also made possible due to four years of persistent and positive support by numerous people who cannot be merely thanked by words. I would like to extend my thanks to my thesis advisor, Prof. Romuald Houdré, who accepted me as an aspiring and hopeful PhD student four years ago. He has been a great source of inspiration and support and most importantly, from whom, I have learnt the art of performing rigorous scientific research. The beginning of the thesis is always marred with tough situations and I was disappointed with my own efforts on many occasions. His patience and guidance have assisted me in passing through those stormy times. His critical insights were very crucial that helped me to solve some of the persistent problems in my projects. He can also be unforgiving at times, as he constantly pushed me to get the best out of me in both scientific and non-scientific matters. He is also very accessible at work and we have discussed various topics in length all through these four years during our innumerable coffee breaks and lunch breaks. These times of sharing and exchanging knowledge from his vast experience will certainly be missed. I also thank him for encouraging me to take up skiing seriously, which has been an inspiring experience for me during my stay in Switzerland.

I would like to thank all my fellow PhD students of the past four years: Nicolas, Jana, Zhaolu and Mario. I give my heartfelt thanks to Nicolas for his constant friendship, support, encouragement and open-minded scientific attitude that has helped me in a number of aspects at work and in life. He has also spent a lot of his time acting as my “skiing coach” and “running coach” and I thank him for all the memorable times spent outside the laboratory in our usual hideouts all around Lausanne. Zhaolu has been a great team player and we have gone through some tough times together in the beginning of our thesis and he has inspired me with his patience whenever I needed it. Jana, for being a good friend and also for being my “alpine guide” and for helping me in getting familiarized with the Fourier imaging set-up and other technical aspects in the first year of my PhD. Mario, for his great enthusiasm and spirit at work and for our discussions on various aspects of science fiction literature and movies. I will also miss the annual ski weekends organized by our group that always ends up with interesting stories to remember in harsh weather conditions in the mountains. I would also offer my thanks to all the past and current members of the institute of condensed matter physics with whom I have interacted all through my thesis. I would like to thank Nicolas, Momchil and Mario for taking time to read my manuscript.

Acknowledgements

I would like to thank all the professors in my Jury who agreed to be present despite their busy schedules. I would like to especially thank both Prof. Roel Baets and Prof. Thomas Krauss who have mentored me during my photonics master program in Belgium and Scotland. It was with Thomas that I started working with photonic crystals in St-Andrews and I have continued in the topic until today. Collaborations have been an important aspect of my thesis and I have been very fortunate to work with a lot of talented colleagues from EPFL. I would like to thank Prof. Nicolas Grandjean and his group (especially Noelia) with whom we have solved some interesting challenges in the nitride photonic crystal domain. I thank Prof. Vincenzo Savona for sharing his vast knowledge on various aspects of theoretical physics and numerical physics during my study. It was a great opportunity to work with him and Momchil, with whom I have had some exciting discussions and I would like to thank him for offering to read my manuscript. I would like to thank Roger Rochat, Nicolas Leiser and Damien Trollet for their trusted technical support all through my thesis. A lot of administrative hassles were made easy due to the support from Laurence and Claire-Lyse from the LOEQ office.

I would like to thank all my friends in Lausanne, who have made my stay a memorable one. Kaja, for her constant encouragement and support through all my distressful times and my long association with the Lausanne badminton group (Viswa, Aravind, Surender and others) has given me the chance to be in touch with the sport for all the years. The Indian association at EPFL (Yuva) was instrumental in organizing a variety of events for the Indians in Lausanne that kept the connections with home alive. I also specially thank Bérengère and her family for accepting me through the Tandem program and for introducing me to various aspects of Swiss and French culture and for making me feel like part of their family. I would like to mention Balaji who has been there through all the good and bad times in my life for a very long time. My special thanks to a few of my close friends who have kept me in positive spirits through this PhD despite the distance that has separated us.

Finally, I would like to sincerely thank and dedicate this thesis to my parents in India: Dharanipathy and Sasikala. They have gone through numerous troubles and hardships in their own lives in order to educate me and support me all through my life. Their love and support has always remained with me in all my efforts.

Lausanne, 10 December 2013

Peru

Ulagalandha Perumal Dharanipathy

37, No 109, Rte Cantonale,
1025 St-Sulpice, Switzerland
dupmal@gmail.com
+41 78 956 56 44

Career objective

To utilize my photonics and microelectronics experience and participate in leading edge research and development projects across the globe to lead and demonstrate innovative technological applications.

Education

PhD in Photonics, EPFL - Switzerland	2010 - 2013
Master in Photonics, University of St Andrews - United Kingdom	2008 - 2009
Master in Photonics, Ghent University - Belgium	2007 - 2008
Bachelor in Electronics, Anna University - India	2001 - 2005

Professional & Research summary

- PhD thesis: EPFL, Switzerland (Advisor: Prof. Romuald Houdré) Jan 2010 - Dec 2013**
- Showed light propagation and high confinement cavities for the first time in Gallium Nitride based integrated photonic devices in both visible and telecom wavelengths.
 - Single particle resonant trapping in an optical cavity and its associated back-action phenomena was demonstrated experimentally and theoretically for the first time in on-chip optical tweezers.
 - Ultra-small optical nanocavities with quality factors of half a million using photonic crystals was designed and measured for silicon photonics applications.
 - Extensively collaborated with 10+ researchers and published in reputed peer-reviewed journals and presented in various international conferences involving optics and physics.
 - Planned and supervised the thesis work of 3 master students apart from undergraduate physics tutoring.
- Internship: EPFL, Switzerland (Advisor: Dr. Sandro Carrara) Jul 2009 - Dec 2009**
- Designed the CMOS analog circuitry required for the sensing of P450 molecules using electrochemical transduction.
 - Successfully performed the optimization of amplifier and comparator circuits to sense the current from the reference electrodes with Cadence EDA tools.
- Masters thesis: University of St Andrews, Scotland (Advisor: Prof. Thomas Krauss) Sep 2008 – Jun 2009**
- Fabricated and experimentally characterized high quality factor photonic crystal slot cavity devices.
 - PDMS microfluidic channels were deposited on top of the devices for use as optical biosensors in order to sense very small levels of analyte concentration.
 - Collaborated with marine biologists in order to address problems of detecting neurotoxins in seawater.
- Analog Engineer, Packaging & Interconnects, Intel Corporation, India Feb 2006 - Jul 2007**
- Performed power delivery simulations and lumped circuit analysis to solve impedance issues in the motherboard and the package of the microprocessor chip.
 - Provided circuit design recommendations for power delivery to the microprocessor chip design team.
 - Extensively used ANSOFT tool for modeling electromagnetic equations in metal interconnects in the package and the motherboard.
- Member Technical Staff, IC design, KPIT Cummins, India Jul 2005 - Jan 2006**
- Worked for the digital IC design team, which was responsible for backend flow in ASIC development.
 - Was responsible for routing of the synthesized design and performed timing analysis and layout rule violations check using the MAGMA toolset.

Summary of skills

- Participated in the complete “design to device” flow for various integrated optical devices. This included the conception of design, defining specifications, performing analytical and numerical calculations, mask design and optical characterization of devices.
- Demonstrated creative abilities by discovering new phenomena such as integrated resonant optical trapping and invented new technological methods to probe the phenomena.
- Showed accurate scientific documentation skills via authoring/co-authoring publications in reputed journals such as Physical Review Letters, Applied Physics Letters & Optics Letters.
- Demonstrated the ability to learn new technologies and design tools independently for collaborative projects across multiple teams in a multinational environment.
- Experienced in designing various analog building block circuits using SPICE and CADENCE design toolkit.
- Exposure to product oriented and time-efficient work flows at Intel Corporation and KPIT Cummins.
- Expertise in simulation and modeling with COMSOL, ANSOFT, MATLAB and CADENCE tools.
- Basic experience in the usage of scripting tools such as C++ and Perl.

Languages

English, Tamil: Fluent, Native

French, Hindi: Conversational

German, Dutch: Basic

Awards and Fellowships

- **Best master thesis award** for Master in Photonics awarded by Master in Photonics Thesis Jury 2009
- **Swiss National Science Foundation fellowship** for PhD research 2010-2013
- **Erasmus Mundus fellowship** from the European Union for the period 2007-2009

List of peer-reviewed publications

"Near-infrared characterization of gallium nitride photonic-crystal waveguides and cavities",
U. Dharanipathy, N. Vico Triviño, C. Yan, Z. Diao, J. -F. Carlin, N. Grandjean, and R. Houdré, *Optics Letters*, 37, 4588 (2012)

"Numerical modelling of optical trapping in hollow photonic crystal cavities",
U. Dharanipathy and R. Houdré, *Optical and Quantum Electronics*, 44, 161 (2012)

Single particle detection, manipulation and analysis with resonant optical trapping in photonic crystals,
N. Deschermes, **U. Dharanipathy**, Z. Diao, M. Tonin, and R. Houdré, *Lab Chip*, 13, 3268 (2013)

"Observation of Backaction and Self-Induced Trapping in a Planar Hollow Photonic Crystal Cavity",
N. Deschermes, **U. Dharanipathy**, Z. Diao, M. Tonin, and R. Houdré, *Physical Review Letters*, 110, 123601 (2013)

"Statistics of the disorder-induced losses of high-Q photonic crystal cavities",
M. Minkov, **U. Dharanipathy**, R. Houdré, and V. Savona, *Optics Express*, 23, 28233 (2013)

"Integrated photonics on silicon with wide bandgap GaN semiconductor",
N. Vico Triviño, **U. Dharanipathy**, J.-F. Carlin, Z. Diao, R. Houdré, and N. Grandjean, *Applied Physics Letters*, 102, 081120 (2013)

"High quality factor two dimensional GaN photonic crystal cavity membranes grown on silicon substrate", N. Vico Triviño, G. Rossbach, **U. Dharanipathy**, J. Levrat, A. Castiglia, J-F. Carlin, A. K. Atlasov, R. Butte, R. Houdré, and N Grandjean, *Applied Physics Letters*, 100, 071103 (2012)